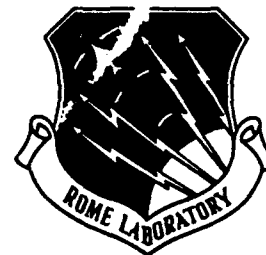


RL-TR-91-325
Final Technical Report
December 1991



2

AD-A246 090



INVESTIGATION OF KINETICS OF MOCVD SYSTEMS

University of Florida

Prof. Timothy J. Anderson

DTIC
ELECTE
FEB 20 1992
S D

APPROVED FOR PUBLIC RELEASE; DISTRIBUTION UNLIMITED.

Rome Laboratory
Air Force Systems Command
Griffiss Air Force Base, NY 13441-5700

92 2 14 064

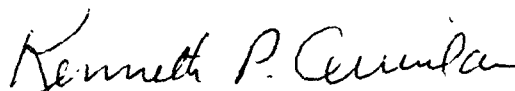
92-03953



This report has been reviewed by the Rome Laboratory Public Affairs Office (PA) and is releasable to the National Technical Information Service (NTIS). At NTIS it will be releasable to the general public, including foreign nations.

RL-TR-91-325 has been reviewed and is approved for publication.

APPROVED:



KENNETH P. QUINLAN
Project Engineer

FOR THE COMMANDER:



HAROLD ROTH, Director
Solid State Sciences
Electromagnetics & Reliability Directorate

If your address has changed or if you wish to be removed from the Rome Laboratory mailing list, or if the addressee is no longer employed by your organization, please notify RL(ERX) Hanscom AFB MA 01731-5000. This will assist us in maintaining a current mailing list.

Do not return copies of this report unless contractual obligations or notices on a specific document require that it be returned.

REPORT DOCUMENTATION PAGE

Form Approved
OMB No. 0704-0188

Public reporting burden for this collection of information is estimated to average 1 hour per response, including the time for reviewing instructions, searching existing data sources, gathering and maintaining the data needed, and completing and reviewing the collection of information. Send comments regarding this burden estimate or any other aspect of this collection of information, including suggestions for reducing this burden, to Washington Headquarters Services, Directorate for Information Operations and Reports, 1215 Jefferson Davis Highway, Suite 1204, Arlington, VA 22202-4302, and to the Office of Management and Budget, Paperwork Reduction Project (0704-0188), Washington, DC 20503.

1. AGENCY USE ONLY (Leave Blank)		2. REPORT DATE December 1991		3. REPORT TYPE AND DATES COVERED Final	
4. TITLE AND SUBTITLE INVESTIGATION OF KINETICS OF MOCVD SYSTEMS				5. FUNDING NUMBERS C - F19628-86-K-0012 PE - 61102F PR - 2306 TA - J1 WU - 47	
6. AUTHOR(S) Prof. Timothy J. Anderson					
7. PERFORMING ORGANIZATION NAME(S) AND ADDRESS(ES) University of Florida Division of Sponsored Research 219 Grinter Hall, Alachua County Gainesville FL 32611				8. PERFORMING ORGANIZATION REPORT NUMBER N/A	
9. SPONSORING/MONITORING AGENCY NAME(S) AND ADDRESS(ES) Rome Laboratory (ERY) Hanscom AFB MA 01731-5000				10. SPONSORING/MONITORING AGENCY REPORT NUMBER RL-TR-91-325	
11. SUPPLEMENTARY NOTES Rome Laboratory Project Engineer: Kenneth P. Quinlan/ERY/(617) 377-4045					
12a. DISTRIBUTION/AVAILABILITY STATEMENT Approved for public release; distribution unlimited.				12b. DISTRIBUTION CODE	
13. ABSTRACT (Maximum 200 words) Several issues related to epitaxy of III-V semiconductors by hydride VPE and MOCVD were investigated. A complex chemical equilibrium analysis was performed in order to investigate the controllability of hydride VPE. The critical control parameters for the deposition of InGaAsP Lattice matched to InP are deposition temperature, system pressure, group III Molar Ratio, Group V Molar Ratio. An experimental characterization of the Ga and In source reactors was accomplished. A MOCVD System was constructed for the deposition of AlGaAs. An investigation was performed to determine the controlling parameters of laser-enhanced deposition of GaAs and AlGaAs using an argon ion laser. Enhancement of deposition was observed when the system was operated in the reaction limited regime. The use of a Ga/In alloy source was studied for the deposition of GaInAs by the Hydride method. The system was used to produce state-of-the-art P-I-N photo-detectors.					
14. SUBJECT TERMS Epitaxy, III-V Semiconductors, MOCVD, Hydride VPE				15. NUMBER OF PAGES 266	
				16. PRICE CODE	
17. SECURITY CLASSIFICATION OF REPORT UNCLASSIFIED	18. SECURITY CLASSIFICATION OF THIS PAGE UNCLASSIFIED	19. SECURITY CLASSIFICATION OF ABSTRACT UNCLASSIFIED	20. LIMITATION OF ABSTRACT UL		

Table of Contents

Project Summary	1
List of Publications and Presentations	14
Appendix A: Complex Chemical Equilibrium Analysis in the In/Ga/As/P/H/Cl System	16
Formulation and Method of Calculation	16
Solution Thermodynamics of InGaAsP	51
Process Controllability and Optimum Operation Condition Issues	73
Process Controllability Study	82
Process Sensitivity Analysis	89
List of Figures	94
Appendix B: Investigation of the Reaction of HCl with Ga and In	109
Introduction	109
Experimental	111
Data Analysis	112
Results and Discussion	119
Conclusions	123
List of Figures	125
Appendix C: Experimental Study of Gallium and Indium Source Transport at Normal Pressure	139
Introduction	139
Experimental Method	140
Data Analysis	142
Results and Discussion	143
List of Figures	150
Appendix D: Laser Enhanced Selective Deposition of GaAs and AlGaAs by MOCVD	166
Introduction	166
Mechanisms Involved in Laser CVD	168
Routes to Compositional Control by Laser CVD	170
Review of Photon Assisted GaAs Epitaxy	173
Experimental Studies of Laser-Enhanced GaAs MOCVD	177
Experimental Studies of GaAs Substrate Damage	186
Experimental Studies of Laser-Enhanced MOCVD of AlGaAs	187
Evaluation of the Temperature Increase Induced by Laser Irradiation	189
Discussion	196
List of Figures	200

Appendix E: Process Characterization and Evaluation of Hydride VPE Grown Ga _x In _{1-x} As Using a Ga/In Alloy Source . . .	227
Introduction	227
Experimental	228
Results and Discussion of Parametric Studies	230
Source Zone Performance	234
Photodetectors Fabricated with the VPE-Hydride Alloy Technique	237
Summary	237
List of Figures	240
References	253



Accession For	
NTIS CRA&I	<input checked="" type="checkbox"/>
DTIC TAB	<input type="checkbox"/>
Unannounced	<input type="checkbox"/>
Justification	
By	
Distribution/	
Availability Codes	
Dist	Avail and/or Special
A-1	

Project Summary

This report summarizes the research results of three Ph.D. students investigating various aspects of epitaxial deposition of Group III-V compound semiconductors. Julian Hsieh investigated process design issues in hydride VPE of InGaAsP on both a theoretical and experimental basis. Jim Edgar studied the use of laser-assisted deposition of AlGaAs by MOCVD. Chinho Park is currently examining composition and temperature profiles in the gas phase using laser Raman spectroscopy. The results obtained by each graduate student are summarized below.

Julian Hsieh initiated his studies during the previous grant period and finished his studies in 1988. His work examined process design issues in hydride VPE, particularly with the group III source zone. This work complimented the work of a previous student, Doug Meyer, who investigated the thermal decomposition of Group V hydrides. These two studies represent a significant contribution to understanding epitaxy by hydride VPE.

The suitability of employing hydride vapor phase epitaxy to prepare quaternary compound semiconductor $\text{In}_{1-x}\text{Ga}_x\text{As}_y\text{P}_{1-y}$ is judged by the material quality the process can deliver. The composition and thickness of the epitaxial layer are the most important material quality factors for InGaAsP devices. Two layers of process design considerations decide the controllability and reproducibility of these two material factors. The first layer concerns how the material quality is dictated by process thermodynamics and the nonequilibrium mechanisms (mass transfer and reaction kinetics) and the second layer concerns how to design process equipment and process operation conditions in order to achieve the desired thermodynamic, mass transfer, and reaction kinetic environment. Three process design issues that have been identified are (1) the investigation of optimum process operation range, (2) the investigation of source zone reaction kinetics, and (3) the investigation of deposition reaction kinetics. Resolution of these issues will complete the required information for process design considerations.

Fourteen process parameters can influence the complex chemical equilibrium in hydride vapor phase epitaxy; namely, the input hydrogen flowrates in the gallium source zone, the indium source zone, and the mixing zone, the input HCl flowrates in the gallium source zone and the

indium source zone, the temperatures of the gallium source zone, the indium source zone, the mixing zone, and the deposition zone, the system pressure, and the transport factors of the gallium source zone and the indium source zone. Except for the source zone transport factors, which are determined by the mass transfer and reaction kinetics, the rest of the process parameters can be selected by process engineers before each run. The fourteen process parameters collectively influence the thermodynamics in the deposition zone through a smaller set of "equilibrium parameters."

Thirty nine chemical species were considered in the development of complex chemical equilibrium calculation for the In/Ga/As/P/H/Cl system and their thermochemical data was compiled. Four solid solutions models, the ideal solution model, the strictly regular solution model, the delta lattice parameter model and the quasi-chemical model, were reviewed for $\text{In}_{1-x}\text{Ga}_x\text{As}_{1-y}\text{P}_y$. The characteristic feature of this solid solution is that the distribution of the nearest neighbor pairs is not uniquely determined by the apparent composition (x, y). Only the quasi-chemical model considers this unique feature and the preferential occupation of lattice sites by short range clustering of like-atoms and was adopted in the subsequent calculations.

Complex chemical equilibrium calculations were used to resolve the first process design issue. Two target compositions of practical importance were studied. In the preparation of composition $\text{In}_{.53}\text{Ga}_{.47}\text{As}$ (lattice-matched to InP) ternary compound, the deposition zone temperature, system pressure, and the Ga/III molar ratio in the deposition zone are apparently the critical control parameters. At $T = 973\text{K}$, $P_{\text{tot}} = 1 \text{ atm}$, $\text{Cl/H} = \text{III/H} = \text{V/H} = 0.001$, and $\text{Ga/III} = 0.605$, the target solid solution composition, $\text{In}_{.53}\text{Ga}_{.47}\text{As}$, results at equilibrium. At this process condition, composition control to within 2% of the target composition could be achieved when the temperature control was within 0.5K, the pressure control was within 10% of the preset value, and the Ga/III ratio could be controlled to within 0.1% of the specified value. Different process conditions gave different degrees of process controllability and could be objectively compared by relative sensitivities. For the calculated condition for InGaAs (lattice-matched to InP) growth, the process controllability could be improved by lowering Cl/H ratio, increasing V/H ratio and

lowering the deposition zone temperature. In another case of preparation of $\text{In}_{.74}\text{Ga}_{.26}\text{As}_{.56}\text{P}_{.44}$, lattice-matched to InP, the critical control parameters are the deposition zone temperature T , the system pressure, Ga/III ratio and As/V ratio in the deposition zone. Equilibrium at $T = 973\text{K}$, $P_{\text{tot}} = 1 \text{ atm}$, $\text{Cl/H} = \text{III/H} = \text{V/H} = 0.001$, $\text{Ga/III} = 0.388$, and $\text{As/V} = 0.0039$ results in the target composition of the solid solution, $\text{In}_{.74}\text{Ga}_{.26}\text{As}_{.56}\text{P}_{.44}$. Control to within 2% of the target composition at the calculated condition could be achieved if the temperature control was within 0.5K, the pressure control was within 5% of the preset value, the Ga/III ratio was within 0.1% of the specified value and the As/V ratio could be controlled to within 0.01%. Relative sensitivities were calculated for different process conditions and the compositional controllability of these process conditions was compared. The T , Cl/H , and V/H could be varied to achieve better control of $\text{In}_{.74}\text{Ga}_{.26}\text{As}_{.56}\text{P}_{.44}$ composition. The V/H value should be increased from 0.001. The Cl/H ratio should be increased for effective reduction of compositional sensitivity to Ga/III and As/V, and the deposition temperature should be increased, at the same time, to offset the increase of sensitivity to T and P_{tot} , as a result of the increased Cl/H value. A detailed description of the calculation and results is given in Appendix A.

Characterization and modeling of gallium and indium source reactors in hydride VPE was attempted to resolve the second issue. Two transport models were developed considering the nonequilibrium mechanisms of convective diffusion and reaction kinetics in the source reactor. These models were used to reduce the experimental data and to establish the reaction rate expressions. When the input flowrates are high, the diffusion coefficients are small, a two-dimensional convective diffusion model with the consideration of only surface reactions satisfactorily described the reactor performance. The 2-D convective diffusion model met the operating condition in the study of the normal pressure experimental reactor and was subsequently used to reduce the normal pressure experimental data. When the input mass flowrates are low and the diffusion coefficients are high, axial diffusion is important, the mass transfer entrance region is short, and the transverse dependence of the concentration field does not vary much in the axial direction. With these assumptions, which are appropriate for the low pressure experimental

conditions, an axial dispersion model was developed with the considerations of both heterogeneous surface reaction and possible homogeneous reaction.

The reaction of In or Ga with HCl can be limited by either mass transfer, kinetics or thermodynamic reasons. In order to eliminate mass transfer effects, the Group III source zone was first investigated at reduced pressure. The reaction rate of HCl with liquid Ga and In, the HCl consumption, at reduced pressure was measured by mass spectrometry. A single reaction rate expression could describe the reaction of HCl with gallium and it is believed to be a heterogeneous reaction. A first-order surface reaction rate constant, k_s (cm/sec) = $3.61 \times 10^4 \exp(-3,930/T(K))$, was determined as a function of temperature for the reaction of HCl with Ga. The results of measurements with the indium source boat were somewhat different with two mechanisms apparently competing. At temperatures above 1120 K, homogeneous reaction of HCl with In vapor is proposed as the limiting reaction; the rate constant is determined to be k (sec⁻¹) = $6.2 \times 10^8 \exp(15,050/T(K))$. At temperatures below 1120 K, a heterogeneous reaction is suggested as the dominating reaction route, with the rate expression k_s (cm/sec) = $1.8 \times 10^6 \exp(-7,630/T(K))$. A full discussion of this work is given in Appendix B.

The reaction rate of HCl with liquid gallium and indium at normal pressure was studied in a flowthrough reactor. The source boat was specially designed to avoid hydrodynamic and thermal entrance region effects above the source boat. The reactor effluent exhausted into a series of three ice-bathed cold traps where gallium or indium chlorides was collected for measurement. Unreacted HCl in the exhaust was collected by bubbling the exhaust gas stream out of the cold traps through distilled water. After each experiment, the III metal chloride condensate was dissolved in aqua regia and diluted for atomic absorption spectrometric measurement, from which the total weight of group III metal in the condensate, or the transport rate of Ga or In, was deduced. The amount of Ga or In in the water bubbler was also measured by atomic absorption and used to verify the completeness of the collection of III metal chlorides by the cold traps. The amount of unreacted HCl was determined by precipitation titration of chloride ions. The transport rates were found to vary linearly with the input HCl concentration, indicating diffusion and/or first-order kinetic

limitations. The group III transport factor was found closer to the HCl conversion at low hydrogen flowrate, 1000 sccm, or high temperature, >1050K. Because of the possible chemical reactions during the course of transport and cooling of the product gas flow from the reaction zone to the sampling devices, the exact chemical composition in the reaction zone could not be easily traced. When the group III transport factor approaches the equilibrium value, however, the dominant chemical species should be group III monochlorides. The transport rate of gallium was found to be strongly dependent on the carrier gas flowrate, less on the reactor temperature, and proportional to the input HCl partial pressure. All of the above suggests a possible diffusion-limited process. With the assumption of a first-order surface rate expression, the experimental data was reduced by the two-dimensional convective diffusion model to give rate constant in the temperature range 943-1131K. The determined rate constant was close to those deduced from the data reported by Ban [28] in an independent study. The rate expression is given by, k_s (cm/sec) = $2.12 \times 10^6 \exp(-11,575/T(K))$. The indium transport rate was found to be strongly dependent upon both the carrier flowrate and the reaction temperature. Similar to gallium transport, the indium transport rate is also linearly proportional to the input HCl flowrate, which validates the assumption of a first-order rate expression. From the reduction of the indium transport rate data, the surface reaction rate constant was obtained, k_s (cm/sec) = $4.13 \times 10^6 \exp(-12,851/T(K))$. With the rate constant, the model equation could be used to predict the source reactor performance at other process conditions. Appendix C contains a more complete description of this work.

In resolving the source reaction kinetics, experiments were conducted in both normal pressure and low pressure conditions. The deduced rate expressions from these two sets of experiments were apparently different. The normal pressure experimental results agreed with the previous findings that have been reported in the literature. Also consistent with common belief in hydride process practice, the gallium reaction rate at normal pressure was found to be more efficient than the indium reaction rate. The reaction of HCl with Ga and In at reduced pressure has never been investigated before this study. The rate constants determined from this low pressure experiments were consistently higher than those found from the normal pressure experiments.

Moreover, the production of InCl seems to be more efficient than that of GaCl at low pressure conditions. Two possible explanations are speculated for this observed discrepancy. The group III transport reaction through the surface reaction route is considered to be very sensitive to the surface condition of the group III melt. If sufficient oxygen or water existed in the reactor, the liquid group III surface could be appreciably oxidized causing a decrease of the effective reaction surface area or completely changing the dominating reaction mechanisms. A low pressure reactor can be less susceptible to the oxidation problem because the reactor is under vacuum at room temperature and much lower oxygen or water content could exist in the reactor. The other possible reason is that fundamentally different reaction mechanisms exist for normal pressure and low pressure reactions. For example, the role of hydrogen may be to compete with HCl for surface adsorption or to boost the reverse reaction rate. In both cases, lower reactor pressure reduces hydrogen partial pressure in the reactor and could lead to the reaction rate enhancement as observed in this study.

Detailed experimental studies of the effects of oxygen, water and carrier gas on the reaction between HCl and Ga and In at both low pressure and normal pressure conditions are essential to resolve this discrepancy. However, from the standpoint of process design of source reactors for hydride process, it should be expected that the operation of an In source boat at elevated temperature and low pressure will present difficulties with In metal deposition in the deposition zone which is at a lower temperature.

It would be interesting and technologically important to study indium and gallium transport at normal pressure from an In/Ga alloy source boat. As was pointed out in the process controllability studies, one of the most stringent parameters in compositional control is the Ga/III ratio in the deposition zone. An alloy source presents the possibility of achieving the required gas phase makeup for a specified composition growth. The results of such a study by another student are presented later in this report.

After completing his degree program in 1988, Dr. Hsieh joined AT&T Bell Laboratories at Murray Hill in a post-doctoral capacity. In 1990, he became a member of the technical staff at IBM, Yorktown Heights.

A second Ph.D. student, Jim Edgar, was also supported by this grant. Jim spent a considerable amount of time designing and constructing a MOCVD system to deposit AlGaAs. The resulting system consisted of four main parts and is briefly described below.

The first part was the gas delivery subsystem consisting of gas pressure regulators, hydrogen purifier, constant temperature baths for the metalorganics, tubing, mass flow controllers, and valves. Constructing the gas delivery system several things were learned. Welding of the tubing should be performed with an inert gas flowing through the tubing as well as flowing on the outside of the tubing. This prevents oxidation of the interior wall which was susceptible to particulate flaking. Correct welding helps keep the system clean. It is preferred that all connections that need to be made and broken, such as connecting tubing to valves, should be of the VCR type for a good leak free system. Compression fittings and pipe threaded pieces should be avoided. No check valves should be placed in gas lines operating at atmospheric pressure as they either require a large back pressure to completely shut off or a large closing spring which results in large pressure drop across the valve.

The flow of metalorganics through the mass flow controllers should be avoided. The mass flow controllers had a tendency to clog when metalorganics were accidentally allowed to flow through the controllers.

The hydrogen purifier should be plumbed with a separate exhaust from the rest of the system to prevent the possibility of contamination from the reactor exhaust. Contamination of the hydrogen purifier results in a reduced flow of purified hydrogen. The recommended shut down procedure of the hydrogen purifier should be strictly followed to prevent contamination problems.

A second part of the system consisted of the heating system including the susceptor, thermocouple, temperature controller, and induction heater. This subsystem worked without failure. It should be noted that the susceptor should never be heated in air as this causes it to react with oxygen and decompose.

The third part of the system was the reaction chamber. Several quartz reactors were used in the experiments. From flow visualization experiments, it became clear that the entrance into the reactor should be a gradual transition from the initial to the final reactor diameter. In addition, the flow of gases over the front susceptor edge should be made as smooth as possible to avoid recirculation flow in the reactor. The insertion of a transition ramp to remove abrupt edges in the reactor seemed to improve the morphology of the deposited films.

The fourth part of the system, the reactor exhaust treatment was the most likely to cause problems. As the gas leaves the reactor and begins to cool, a fine dust was formed that was easily entrained in the gas flow for fairly long distances. This fine powder tended to clog the tubing if the inner diameter was too small, or any filter if the filter's retention was too fine and its capacity too low. In addition to the difficulties caused by the formation of a powder, the reactor did not completely decompose all arsine, so the remaining arsine had to be removed. Some general guidelines for designing the exhaust treatment include:

1. The exhaust line leaving the reactor should be as large as practical.
2. The filter to remove particulate material from the exhaust should have a large capacity so that frequent changes are not necessary.
3. A continuous filtering and degassing of the vacuum pump oil is recommended.
4. Continuous monitoring of the exhaust leaving the final absorption media is recommended.

Over 200 deposition experiments were run. Broadly deposited areas of GaAs and $\text{Al}_x\text{Ga}_{1-x}\text{As}$ were produced with a variety of reactants, gas compositions, reactor designs, temperatures, and pressures. The resulting materials were characterized primarily by film thickness, film uniformity, surface morphology, and solid composition. Some additional characterization was made using *Hall effect measurements and electrochemical carrier concentration profiling*.

For determining film thicknesses, the change in the mass of the substrate was primarily used. This method was convenient and gave consistent results. Some additional analysis was made by examining the edges of a cleaved and stained samples. The resolution of the optical microscope permitted the determination of the film thickness to within about 500 nm. Using an

optical microscope the uniformity of the deposited film across the substrate could be determined. The film thickness as determined by optical microscope were 10 to 30% lower than those determined by mass, and the uniformity of the deposit was 10% across the substrate.

Both trimethylgallium (TMG) and triethylgallium (TEG) were used as gallium sources. Trimethylaluminum (TMA) was the exclusive aluminum source. Using TEG at atmospheric pressure resulted in low reaction efficiencies and highly nonuniform film thicknesses. The resulting deposited films were thickest at the front edge of the substrate, tapering to no detectable growth on the back edge. Higher efficiencies and more uniform deposits were formed when TEG was used at reduced pressure. Film thicknesses were uniform at both atmospheric and reduced pressures using TMA and TMG. The reaction efficiencies were the same at both atmospheric and low pressures using TMA and TMG.

The initial objective was to study gas phase processes in MOCVD with laser Raman spectroscopy. Preliminary studies indicated that the signal to noise ratio was too low to obtain meaningful results at normal operating conditions since the reactant concentrations were low. In order to increase the signal to noise ratio, several design changes had to be made. Since Jim had spent considerable time designing, constructing and characterizing the system, it was decided to shift the emphasis of Jim's research to a study of selective deposition of AlGaAs in a laser enhanced mode. The results of this study are described below.

An investigation was made to determine the controlling parameters of the laser-enhanced deposition of GaAs and $\text{Al}_x\text{Ga}_{1-x}\text{As}$. The effects of temperature, pressure, reactor design, wavelength, deposition time, and reactant composition on enhanced growth rate, deposit shape, and solid composition were examined. From these studies, a basic understanding of the laser-enhanced process was made.

An enhancement of the growth rate was found to occur as long as bias temperature of the susceptor was below the transition temperature between the kinetically limited growth and mass transfer limited growth. For the deposition of GaAs from TMG and AsH_3 , the susceptor

temperature had to be below 600°C in order to observe enhanced growth due to the laser irradiation. For the deposition of GaAs from TEG and AsH₃, the susceptor temperature had to be below 500°C in order for a growth enhancement to occur. For TEG the deposition enters a mass transport limited growth regime at a temperature about 100°C lower than the case in which TMG is used as the gallium source.

Attempts to modulate the Al composition in Al_xGa_{1-x}As deposited films in the temperature range of 600 to 700°C by additional heating from the laser were not successful. A study of the Al composition in Al_xGa_{1-x}As films deposited normally showed very little change with temperature from 550 to 700°C. The possibility of spatially modifying only the material composition but not the material growth rate does not appear to be promising.

The deposit shape was found to vary with the light intensity used to deposit the spot. For high intensities, the resulting spots were volcano shaped. For low intensities, the spots were Gaussian shaped. The transition from a Gaussian shaped spot to a volcano shaped spot was dependent on the susceptor bias temperature and the gallium source, TEG or TMG. At higher susceptor temperatures the volcano shape was formed at lower light intensities than at lower susceptor bias temperatures. Volcano shaped spots were formed at lower light intensities for TEG than for TMG.

Several mechanisms have been proposed to explain the volcano shape, and each were critically examined. The most likely explanation suggests that at the spot center, the temperature is so hot that the sticking coefficients of the reactants are low. At the spot edges, the temperature is lower and the sticking coefficient is much higher. A comparison of the normal growth rate with temperature shows the growth rate goes through a maximum and decreases as the temperature is increased (above 600°C using TEG). In the case of the volcano shaped deposits, the temperature of the spot center was above this maximum growth rate while the spot edge was at the maximum growth rate.

Calculations were made to estimate the surface temperature increases induced by the laser light. A comparison of the estimated temperature increase and the predicted growth rate

enhancement with the actual growth rate enhancement showed a large discrepancy. The growth rate was much higher (by a factor of 100) than expected from the predicted temperature increase. This suggests another mechanism is responsible other than thermally induced deposition.

A dependence of the enhanced growth rate on the light wavelength was found. Higher enhanced growth rates were observed for shorter wavelengths. This behavior could not be explained by changes in the optical properties of GaAs such as the reflectivity and absorption coefficient with light wavelength. It was suggested that surface adsorbed reactants were able to absorb light and that a photochemical reaction was taking place. From the present study, the absorption spectra of such absorbed species could not be determined.

In general, the lowest possible temperature which good material can be obtained should be used. This is necessary to suppress all spurious, thermally driven large area deposition. In addition, laser-enhanced deposited material produced at high laser intensities appeared amorphous when examined by SEM. Modest laser intensities are recommended as these produce the more useful Gaussian shaped profiles. A full description of these results is given in Appendix D.

After graduating in 1987, Jim joined the Chemical Engineering faculty at Kansas State University where he has continued research in MOCVD.

A third student, Chinho Park, was partially supported by this project. The main focus of his research is an investigation of gas phase processes with laser Raman spectroscopy. The reactor has been modified in several ways to increase the signal to noise ratio. First, a multiple-pass chamber has been designed to permit the laser beam to pass 10 times through the focal point to increase the scattering. Additionally, the reactor chamber was constructed of optically flat quartz to prevent aberrations. A cylindrical quartz sleeve with vertical slits is placed inside the rectangular quartz-flat reactor to provide cylindrical flow geometry. The susceptor was also modified to allow resistance heating and thus prevent interference by the rf coils. The flow geometry is an upflow stagnation point type to allow easy numerical simulation. The susceptor is mounted on a translation stage to allow x-y-z motion in order to map out temperature and composition profiles.

The system has been used to measure temperature profiles in both H_2 and N_2 carrier gases by examining the rotational spectra. The signal to noise ratio is excellent and the measurements agree well with a numerical model. In the near future, we will examine composition profiles.

While the reactor parts were being ordered, Chinho spent 6 months at Epitaxx, Inc. investigating the use of an alloy source boat in hydride VPE. A novel, simplified hydride vapor phase epitaxy (VPE) method based on the utilization of Ga/In alloys as the group III source was studied for deposition of $Ga_xIn_{1-x}As$. The effects of a wide range of experimental variables (i.e., inlet mole fractions of HCl and AsH_3 , deposition temperature, gas velocity, Ga/In alloy composition, and reactor geometry) on the ternary composition and growth rate were investigated. The growth rate of $Ga_xIn_{1-x}As$ was found to increase with increasing deposition temperature and exhibited a maximum with inlet HCl mole fraction. The growth rate increases slightly with inlet AsH_3 mole fraction and is independent of gas velocity. The Ga composition of the deposited film increased with increasing inlet HCl mole fraction and gas velocity. Increased In concentrations were observed with increases in inlet AsH_3 mole fraction and deposition temperatures. Layers of $Ga_{0.47}In_{0.53}As$ lattice matched to InP were successfully grown from alloys containing 5 to 8 at.% Ga. These layers were used to produce state-of-the-art p-i-n photodetectors having the following characteristics: dark current, $I_d (-5V) = 10-20$ nA; responsivity, $R = 0.84-0.86$ A/W; capacitance, $C = 0.88-0.92$ pF; breakdown voltage, $V_b > 40V$. This study demonstrated for the first time that a simplified hydride VPE process with a Ga/In alloy source is capable of producing device quality epitaxial layers. Appendix E contains a detailed description of this work.

Transient behavior of source reactors during HCl turn-on/turn-off period and setpoint changes is also a great interest for achieving sharp junction at heterostructure interphase in a "single-barrel" hydride reactor. This problem is probably the single largest limitation of hydride VPE of InGaAsP. As a result, most current interest resides in MOCVD of this material. However, the growth rate and impurity concentration in hydride VPE films still remain superior. This has prompted us to investigate a merged hydride-MOCVD system in which metalorganic sources are reacted with HCl in a normal hydride VPE reactor. This source is used to replace the

liquid metal source and thus greatly lower the switching time. We are currently developing this process.

List of Publications and Presentations

Publications

1. "An Investigation of the Reaction of HCl with Ga and In," J.J. Hsieh and T.J. Anderson, *J. Crystal Growth*, **83**, 268-278 (1987).
2. "Selective Deposition of GaAs and $\text{Al}_x\text{Ga}_{1-x}\text{As}$ by Laser-Enhanced MOCVD," J.H. Edgar, S.S. Chang and T.J. Anderson, *Proc. Symp. Laser Processes for Microelectronic Applications*, J.J. Ritsko, D.J. Ehrlich, and M. Kashiwagi eds., Vol. 88-10, 203-214 (1988).
3. "Process Characterization and Evaluation of Hydride VPE Grown InGaAs using a Ga/In Alloy Source," C. Park, V.S. Ban, G.H. Olsen, T.J. Anderson and K.P. Quinlan, *Accepted J. Elect. Mat.* (1991).

Presentations

1. "Thermochemistry and Kinetics of Group III-V Semiconductors." Invited lecture at ONR Workshop on Group III-V Chemistry and Semiconductors, Buffalo, NY (1988).
2. "Phenomena and Physical Property Needs in Semiconducting Materials Processing." Invited plenary lecture at Fifth Int. Conf. on Fluid Properties and Phase Equilibria for Chemical Process Design, Banff, Alberta, Canada (1989).
3. "MOCVD of Compound Semiconductors for Optoelectronic and Photonic Devices." Invited plenary lecture at Adv. Proc. and Charact. Tech. Conf., Tokyo, Japan (1989).
4. "Chemical Vapor Deposition of Compound Semiconductors." Invited plenary lecture at Engineering Foundation Conference, Reaction Engineering III, Santa Barbara, CA (1990).
5. "Performance of Ga and In Source Boats in Hydride VPE." Presented at NATO Workshop on InP, Horwichport, MA (1986).
6. "Laser-Assisted Metalorganic Chemical Vapor Deposition of $\text{Al}_x\text{Ga}_{1-x}\text{As}$ for Fabrication of Waveguides." Presented at Annual AIChE Meeting, Miami, FL (1986).
7. "Chemical Equilibrium and Reactor Dynamics in the Hydride VPE of $\text{In}_x\text{Ga}_{1-x}\text{As}_y\text{P}_{1-y}$." Presented at 170th Electrochemical Society Meeting, San Diego, CA (1986).
8. "Selective Deposition of GaAs and $\text{Al}_x\text{Ga}_{1-x}\text{As}$ by Laser Enhanced MOCVD." Presented at 172nd Electrochemical Society Meeting, Honolulu, HI (1987).
9. "A Study of Ga and In Source Zone in Hydride Vapor Phase Epitaxy." Presented at Annual AIChE Meeting, New York, NY (1987).
10. "Laser-Enhanced Spots on Epitaxial Layers of AlGaAs." Presented at 17th Annual Symposium on Applied Vacuum Science and Technology, Clearwater, FL (1988).
11. "Thermodynamic Analysis of Chemical Vapor Deposition of $\text{Ga}_x\text{In}_{1-x}\text{As}$ by the Hydride Process." Presented at CALPHAD XVII, Berkeley, CA (1988).

12. "Process Characterization and Evaluation of Hydride VPE Grown InGaAs Using a Ga/In Alloy Source." Presented at Electronic Materials Conference, Cambridge, MA (1989).
13. "The Influence of Arsine on the Thermal Decomposition of Trimethylgallium." Presented at Annual AIChE Meeting, San Francisco, CA (1989).
14. "Complex Chemical Equilibrium Analysis of InP-based Vapor Phase Epitaxy." Presented at National AIChE Meeting, Orlando, FL (1990).

Appendix A

COMPLEX CHEMICAL EQUILIBRIUM ANALYSIS
IN THE In/Ga/As/P/H/Cl SYSTEM

A.1. Formulation and Method of Calculation

A.1.1. Chemical Species and Reactions

To consider the complex chemical equilibrium in hydride VPE of InGaAsP, the chemical species involved in the system must first be identified. In hydride VPE, three reaction zones with different sets of chemical species are encountered. Therefore, a complete complex chemical equilibrium calculation includes the calculation of complex chemical equilibrium in each of the three temperature zones.

In the source zone, where HCl in H_2 carrier gas reacts with group III metal, the three elements III, H and Cl are involved. Specifically for hydride VPE of $In_{1-x}Ga_xAs_yP_{1-y}$, the source region is composed of two independent group III source zones (the gallium source zone and the indium source zone) in which two complex chemical equilibrium systems (Ga/H/Cl and In/H/Cl) must be considered separately.

In the mixing zone, group V hydrides in hydrogen carrier gas are introduced into the reactor and mixed with the product flow from the group III source region. Since the product flow from the source zone contains group III chlorides, it is possible that the group III chlorides and the group V hydrides can react in the mixing zone to form solid deposits before the gas mixture reaches the deposition zone. Therefore, the mixing zone should always be operated at conditions to prevent parasitic reactions between group III-containing and group V-containing species and avoid extraneous deposition and loss of group III and group V nutrients. On account of this process constraint, two additional complex chemical equilibrium systems are considered,

namely, Ga/In/H/Cl and As/P/H/Cl. Finally, in the deposition zone, group III chlorides and group V species react, and chemical equilibrium of the composite system Ga/In/As/P/H/Cl is considered.

Table A-1 lists the chemical species chosen for the In/Ga/As/P/H/Cl system. At one atmosphere pressure and in the temperature range of interest to VPE, 900-1200 K, some of the chemical species are fairly unstable, thus insignificant in quantity. Mole fractions of gallium hydrides, indium hydrides, arsenic chlorides and phosphorous chlorides are typically less than 10^{-10} , hence they are excluded from consideration. The binary compound vapor species of GaAs, GaP, InAs and InP are also insignificant and do not have a great impact on the overall chemical equilibrium. Group III chlorides, Group V dimers/tetramers and group V hydrides are the dominant species in the In/Ga/As/P/H/Cl system. Kinetic studies on the growth of GaAs have shown that gallium monochloride and arsenic molecules are responsible for the epitaxial reaction in a hydrogen-rich ambient, and in addition, gallium trichloride plays a certain role in a hydrogen-deficient atmosphere. Although some of the chlorides are less important than the others, it is of strategic value to take them all into account because of their influence on the kinetics might not be known. For similar reasons, the group V molecules composed of different number of atoms should be considered. Group V hydrides, possibly competing with group V molecules in the growth reaction, are used as group V element carriers. The inclusion of all possible V-hydrides species is thus meaningful. Molecules formed from both arsenic and phosphorous atoms have not been adequately studied, and their reported thermochemical properties, at present, are missing or inconclusive. Therefore, these chemical species are discarded in the complex chemical equilibrium calculation. The thermochemical properties of the resulting 39 chemical species are reviewed and gathered.

Table A-1. Selected chemical species in the In/Ga/As/P/H/Cl system*.

Name	Symbol
Gallium	Ga, Ga(l)
Indium	In, In(l)
Gallium Chlorides	GaCl, GaCl ₂ , GaCl ₃ , Ga ₂ Cl ₂ , Ga ₂ Cl ₄ , Ga ₂ Cl ₆
Indium Chlorides	InCl, InCl ₂ , InCl ₃ , In ₂ Cl ₂ , In ₂ Cl ₄ , In ₂ Cl ₆
Arsenic	As, As ₂ , As ₃ , As ₄
Phosphorous	P, P ₂ , P ₃ , P ₄
Arsenic Hydrides	AsH, AsH ₂ , AsH ₃
Phosphorous Hydrides	PH, PH ₂ , PH ₃
Hydrogen/Chlorine	H ₂ , H, HCl, Cl, Cl ₂
Gallium Arsenide	GaAs(s)
Indium Arsenide	InAs(s)
Gallium Phosphide	GaP(s)
Indium Phosphide	InP(s)

*Unless indicated otherwise all species are in the gas phase.

(l): liquid phase

(s): solid phase

Table A-2. Selected values of standard state heat capacity,

$$C_p \text{ (cal/mole}\cdot\text{K)} = C_0 + C_1T + C_2T^2 + C_3T^3 + C_4T^{-2} + C_5\ln T \text{ (T:K)}$$

	C_0	$C_1 \cdot 10^3$	$C_2 \cdot 10^6$	$C_3 \cdot 10^9$	$C_4 \cdot 10^{-6}$	C_5	ref.
Ga	30.138	2.09	0.	0.	-0.2662	-3.812	1
Ga(l)	6.65	0.	0.	0.	0.	0.	2
In	3.575	4.426	0.	-1.689	0.	0.	1
In(l)	7.10	0.	0.	0.	0.	0.	2
GaCl	8.84749	23.287	-0.04918	0.	-0.039674	0.	3
GaCl ₂	13.7942	13.33964	-0.04050	0.	-0.083318	0.	3
GaCl ₃	19.463	0.566884	-0.21157	0.	-0.151843	0.	3
Ga ₂ Cl ₂	19.5208	0.547979	-0.23262	0.	-0.153321	0.	3
Ga ₂ Cl ₄ (298K- 600K)	17.9843	26.683	-15.7484	0.	-0.151084	0.	3
(600K- 1200K)	28.1419	4.0013	-1.27179	0.	-0.784768	0.	3
Ga ₂ Cl ₆	43.0051	0.989928	-0.37017	0.	-0.340547	0.	3
InCl	8.93	0.	0.	0.	-0.209	0.	4
InCl ₂	13.84	0.0515	0.	0.	0.08644	0.	5

(Table A-2 continued)

$$C_p \text{ (cal/mole-K)} = C_0 + C_1T + C_2T^2 + C_3T^3 + C_4T^{-2} + C_5\ln T \text{ (T:K)}$$

	C_0	$C_1 \cdot 10^3$	$C_2 \cdot 10^6$	$C_3 \cdot 10^9$	$C_4 \cdot 10^{-6}$	C_5	ref.
InCl ₃	18.00	1.7	0.	0.	0.	0.	4
In ₂ Cl ₄	26.93	1.7	0.	0.	-0.209	0.	6
In ₂ Cl ₆	40.	3.4	0.	0.	0.	0.	7
As	4.968	0.	0.	0.	0.	0.	1
As ₂	8.772	0.2571	-0.121	0.	-0.04241	0.	8,9
As ₃	13.836	-0.1365	0.	0.	-0.05889	0.172	1
As ₄	19.696	0.2834	-0.1252	0.	-0.168	0.	8,9
P	4.968	0.	0.	0.	0.	0.	10
P ₂	8.236	8.6618	0.	0.	0.06036	0.	10,11
P ₄	19.2	0.5744	0.	0.	-0.02974	0.	10,11
AsH	6.4	1.432	0.	0.	0.0108	0.	10
AsH ₃	10.07	5.42	0.	0.	-0.220	0.	12
PH	6.4	1.432	0.	0.	0.0108	0.	10

(Table A-2 continued)

$$C_p \text{ (cal/mole-K)} = C_0 + C_1T + C_2T^2 + C_3T^3 + C_4T^{-2} + C_5\ln T \text{ (T:K)}$$

	C_0	$C_1 \times 10^3$	$C_2 \times 10^6$	$C_3 \times 10^9$	$C_4 \times 10^{-6}$	C_5	ref.
PH ₂	6.524	6.237	0.	-1.506	0.	0.	10
PH ₃	4.77	14.97	-0.4388	0.	0.	0.	10
GaAs(s)	10.8	1.46	0.	0.	0.	0.	8,13
InAs(s)	10.6	2.0	0.	0.	0.	0.	8,13
Gap(s)	11.85	0.68	0.	0.	-0.14	0.	11,14
InP(s) (298K- 910K)	12.27	0.	0.	0.	-0.114	0.	11,14
(910K- 1500K)	5.89	6.4	0.	0.	0.	0.	11,14
H ₂	15.256	2.12	0.	0.	-0.05906	-1.462	10
H	4.968	0.	0.	0.	0.	0.	15
HCl	6.224	1.29	0.	0.	0.03251	0.	10
Cl	5.779	-0.4083	0.	0.	-0.0387	0.	15
Cl ₂	8.8	0.208	0.	0.	-0.067	0.	3

Table A-3. Selected values of the standard enthalpy of formation and absolute entropy at 298 K,

$\Delta H_f^\circ(298K)$ (kcal/mole)			$S^\circ(298K)$ (cal/mole-K)	
	$\Delta H_f^\circ(298K)$	ref	$S^\circ(298K)$	ref
Ga	65.0	1	40.375	1
Ga ₍₁₎	1.3	2	14.2	2
In	57.3	1	41.507	1
In ₍₁₎	0.8	2	15.53	2
GaCl	-17.1	3	57.236	3
GaCl ₂	-39.0	3	71.668	3
GaCl ₃	-102.4	3	77.515	3
Ga ₂ Cl ₂	-56.1	3	83.681	3
Ga ₂ Cl ₄	-148.5	3	103.031	3
Ga ₂ Cl ₆	-228.9	3	116.9	3
InCl	-16.7	4	59.3	4
InCl ₂	-58.4	7	73.4	7
InCl ₃	-90.0	12	82.3	12
In ₂ Cl ₄	-140.84	17	110.6	17
In ₂ Cl ₆	-208.5	7	129.7	7
As	68.7	1	41.611	1
As ₂	45.58	9	57.546	1
As ₃	52.2	1	74.121	1
As ₄	36.725	9	78.232	1
P	75.62	1	38.98	1
P ₂	34.34	1	52.11	10

(Table A-3 continued)

	$\Delta H_f^\circ(298K)$		ref	$S^\circ(298K)$		ref
P ₄	12.58	7	66.89	1		
AsH	58.	7	51.	7		
AsH ₃	16.	17	53.22	20		
PH	56.2	10	46.9	10		
PH ₂	25.9	10	50.8	10		
PH ₃	1.3	18	50.24	10		
GaAs(s)	-19.54	8	16.05	8		
InAs(s)	-14.29	8	17.84	8		
GaP(s)	-23.93	11	10.96	11		
InP(s)	-14.73	11	14.18	11		
H ₂	0.	31.207	19			
H	52.103	19	27.391	19		
HCl	-22.063	19	44.643	19		
Cl	28.992	19	39.454	19		
Cl ₂	0.	53.29	19			

Tables A-2 and A-3 provide the compilation with references to the selected values.

System reactions are determined after the chemical species are chosen. Every system reaction describes the relationship of one added chemical species to the existing ones. This also implicitly means that the system reactions are independent. Although the number of system reactions is fixed when the chemical species are chosen, the reaction formulae can be written in various forms as long as the requirement of independence is met. The system reactions of the chosen chemical species (as listed in Table A-1) are tabulated in Table A-4.

A.1.2. Complex Chemical Equilibrium Equations and Equilibrium Parameters

Gallium Source Zone

The system reactions involved in gallium source zone are listed in Table A-4. The ideal gas phase equilibrium equations for these system reactions at 1 atm pressure are written as follows

$$K_9(T) = \frac{P_{\text{GaCl}_3} P_{\text{H}_2}}{P_{\text{GaCl}} P_{\text{HCl}}^2} \quad (\text{A-1})$$

$$K_{10}(T) = \frac{P_{\text{Ga}_2\text{Cl}_4}}{P_{\text{GaCl}_3} P_{\text{GaCl}}} \quad (\text{A-2})$$

$$K_{14}(T) = \frac{P_{\text{GaCl}_2} P_{\text{H}_2}^{0.5}}{P_{\text{GaCl}} P_{\text{HCl}}} \quad (\text{A-3})$$

$$K_{16}(T) = \frac{P_{\text{Ga}_2\text{Cl}_6}}{P_{\text{GaCl}_3}^2} \quad (\text{A-4})$$

$$K_{18}(T) = \frac{P_{\text{Ga}_2\text{Cl}_2}}{P_{\text{GaCl}}^2} \quad (\text{A-5})$$

Table A-4. Chemical reactions in hydride VPE of InGaAsP

number	reaction	applicable*
		temperature zone
1	$\text{GaCl} + 1/4 \text{As}_4 + 1/2 \text{H}_2 \rightleftharpoons \text{GaAs}_{(\text{s.s.})} \# + \text{HCl}$	d
2	$\text{InCl} + 1/4 \text{As}_4 + 1/2 \text{H}_2 \rightleftharpoons \text{InAs}_{(\text{s.s.})} \# + \text{HCl}$	d
3	$\text{GaCl} + 1/4 \text{P}_4 + 1/2 \text{H}_2 \rightleftharpoons \text{GaP}_{(\text{s.s.})} \# + \text{HCl}$	d
4	$\text{InCl} + 1/4 \text{P}_4 + 1/2 \text{H}_2 \rightleftharpoons \text{InP}_{(\text{s.s.})} \# + \text{HCl}$	d
5	$2 \text{As}_2 \rightleftharpoons \text{As}_4$	m, d
6	$\text{AsH}_3 \rightleftharpoons 1/2 \text{As}_2 + 3/2 \text{H}_2$	m, d
7	$2 \text{P}_2 \rightleftharpoons \text{P}_4$	m, d
8	$\text{PH}_3 \rightleftharpoons 1/2 \text{P}_2 + 3/2 \text{H}_2$	m, d
9	$\text{GaCl} + 2 \text{HCl} \rightleftharpoons \text{GaCl}_3 + \text{H}_2$	s(Ga), m, d
10	$\text{GaCl} + \text{GaCl}_3 \rightleftharpoons \text{Ga}_2\text{Cl}_4$	s(Ga), m, d
11	$\text{InCl} + 2 \text{HCl} \rightleftharpoons \text{InCl}_3 + \text{H}_2$	s(In), m, d
12	$\text{InCl} + \text{InCl}_3 \rightleftharpoons \text{In}_2\text{Cl}_4$	s(In), m, d
13	$\text{InCl} + \text{HCl} \rightleftharpoons \text{InCl}_2 + 1/2 \text{H}_2$	s(In), m, d
14	$\text{GaCl} + \text{HCl} \rightleftharpoons \text{GaCl}_2 + 1/2 \text{H}_2$	s(Ga), m, d
15	$2 \text{InCl}_3 \rightleftharpoons \text{In}_2\text{Cl}_6$	s(In), m, d
16	$2 \text{GaCl}_3 \rightleftharpoons \text{Ga}_2\text{Cl}_6$	s(Ga), m, d
17	$2 \text{InCl} \rightleftharpoons \text{In}_2\text{Cl}_2$	s(In), m, d
18	$2 \text{GaCl} \rightleftharpoons \text{Ga}_2\text{Cl}_2$	s(Ga), m, d
19	$\text{AsH}_3 \rightleftharpoons \text{Ga}_2\text{Cl}_2$	s(Ga), m, d
20	$\text{AsH}_3 \rightleftharpoons \text{AsH} + \text{H}_2$	m, d
21	$\text{PH}_3 \rightleftharpoons \text{PH}_2 + 1/2 \text{H}_2$	m, d
22	$\text{PH}_3 \rightleftharpoons \text{PH} + \text{H}_2$	m, d

(Table A-4 continued)

number	reaction	applicable*
		temperature zone
23	$\text{As}_2 \rightleftharpoons 2 \text{As}$	m, d
24	$\text{As}_4 + \text{As}_2 \rightleftharpoons 2 \text{As}_3$	m, d
25	$\text{P}_2 \rightleftharpoons 2\text{P}$	m, d
26	$\text{P}_4 + \text{P}_2 \rightleftharpoons 2 \text{P}_3$	m, d
27	$\text{H}_2 \rightleftharpoons 2\text{H}$	s(Ga), s(In), m, d
28	$\text{HCl} \rightleftharpoons \text{H} + \text{Cl}$	s(Ga), s(In), m, d
29	$2\text{Cl} \rightleftharpoons \text{Cl}_2$	s(Ga), s(In), m, d
30	$\text{GaCl} \rightleftharpoons \text{Ga} + \text{Cl}$	s(Ga), m, d
31	$\text{InCl} \rightleftharpoons \text{In} + \text{Cl}$	s(In), m, d
32	$\text{Ga(l)} + \text{HCl} \rightleftharpoons \text{GaCl} + 1/2 \text{H}_2$	s(Ga)
33	$\text{In(l)} + \text{HCl} \rightleftharpoons \text{InCl} + 1/2 \text{H}_2$	s(In)

* s(Ga): Ga source zone
s(In): In source zone
m: mixing zone
d: deposition zone

(s.s.): InGaAsP solid solution

$$K_{27}(T) = \frac{P_H^2}{P_{H_2}} \quad (A-6)$$

$$K_{28}(T) = \frac{P_H P_{Cl}}{P_{HCl}} \quad (A-7)$$

$$K_{29}(T) = \frac{P_{Cl_2}}{P_{Cl}^2} \quad (A-8)$$

$$K_{30}(T) = \frac{P_{Ga} P_{Cl}}{P_{GaCl}} \quad (A-9)$$

$$K_{32}(T) = \frac{P_{GaCl} P_{H_2}^{0.5}}{P_{HCl}} \quad (A-10)$$

In the equations above, $K_i(T)$ is the equilibrium constant of reaction i and P_j is the partial pressure of chemical species j in the vapor phase. Since neither Cl or H is incorporated in the condensed phases, the number of chlorine atoms and hydrogen atoms in the vapor phase is constant. It is thus convenient to define the parameter $A_s(Ga)$ that represents the ratio of chlorine atoms to hydrogen atoms in the gas phase.

$$A_s(Ga) = (Cl/H) = \frac{P_{GaCl} + 2(P_{GaCl_2} + P_{Ga_2Cl_2} + P_{Cl_2}) + 3P_{GaCl_3} + 4P_{Ga_2Cl_4} + 6P_{Ga_2Cl_6} + P_{HCl} + P_{Cl}}{2P_{H_2} + P_{HCl} + P_H} \quad (A-11)$$

The summation of the vapor pressure of the twelve vapor species is equal to the total pressure, P_{tot} , i.e.

$$P_{tot} = P_{GaCl} + P_{GaCl_2} + P_{GaCl_3} + P_{Ga_2Cl_2} + P_{Ga_2Cl_4} + P_{Ga_2Cl_6} + P_{Ga} + P_{H_2} + P_{HCl} + P_H + P_{Cl} + P_{Cl_2} \quad (A-12)$$

Complex chemical equilibrium in the gallium source zone is completely defined by equations (A-1) to (A-12). When values of the gallium source zone temperature, $T_s(\text{Ga})$, total system pressure, P_{tot} , and $A_s(\text{Ga})$ are specified, equations (A-1) to (A-12) can be solved simultaneously to resolve the equilibrium partial pressure of the twelve vapor species.

Indium source zone

Similar equilibrium equations exist for the indium source zone. There are twelve equilibrium equations with three system parameters; indium source zone temperature, $T_s(\text{In})$, total system pressure, P_{tot} , and chlorine to hydrogen ratio, $A_s(\text{In})$. The twelve equilibrium equations are written as follows:

$$K_{11}(T) = \frac{P_{\text{InCl}_3} P_{\text{H}_2}}{P_{\text{InCl}} P_{\text{HCl}}^2} \quad (\text{A-13})$$

$$K_{12}(T) = \frac{P_{\text{In}_2\text{Cl}_4}}{P_{\text{InCl}_3} P_{\text{InCl}}} \quad (\text{A-14})$$

$$K_{13}(T) = \frac{P_{\text{InCl}_2} P_{\text{H}_2}^{0.5}}{P_{\text{InCl}} P_{\text{HCl}}} \quad (\text{A-15})$$

$$K_{15}(T) = \frac{P_{\text{In}_2\text{Cl}_6}}{P_{\text{InCl}_3}^2} \quad (\text{A-16})$$

$$K_{17}(T) = \frac{P_{\text{In}_2\text{Cl}_2}}{P_{\text{InCl}}^2} \quad (\text{A-17})$$

$$K_{27}(T) = \frac{P_{\text{H}}^2}{P_{\text{H}_2}} \quad (\text{A-18})$$

$$K_{28}(T) = \frac{P_{\text{H}} P_{\text{Cl}}}{P_{\text{HCl}}} \quad (\text{A-19})$$

$$K_{29}(T) = \frac{P_{\text{Cl}_2}}{P_{\text{Cl}}^2} \quad (\text{A-20})$$

$$K_{31}(T) = \frac{P_{\text{In}} P_{\text{Cl}}}{P_{\text{InCl}}} \quad (\text{A-21})$$

$$K_{33}(T) = \frac{P_{\text{InCl}} P_{\text{H}_2}^{0.5}}{P_{\text{HCl}}} \quad (\text{A-22})$$

$$A_s(\text{In}) = (\text{Cl}/\text{H}) = \frac{P_{\text{InCl}} + 2(P_{\text{InCl}_2} + P_{\text{In}_2\text{Cl}_2} + P_{\text{Cl}_2}) + 3P_{\text{InCl}_3} + 4P_{\text{In}_2\text{Cl}_4} + 6P_{\text{In}_2\text{Cl}_6} + P_{\text{HCl}} + P_{\text{Cl}}}{2P_{\text{H}_2} + P_{\text{HCl}} + P_{\text{H}}} \quad (\text{A-23})$$

$$P_{\text{tot}} = P_{\text{InCl}} + P_{\text{InCl}_2} + P_{\text{InCl}_3} + P_{\text{In}_2\text{Cl}_2} + P_{\text{In}_2\text{Cl}_4} + P_{\text{In}_2\text{Cl}_6} + P_{\text{In}} + P_{\text{H}_2} + P_{\text{HCl}} + P_{\text{H}} + P_{\text{Cl}} + P_{\text{Cl}_2} \quad (\text{A-24})$$

Mixing zone

There are 33 chemical species in the vapor phase of the mixing zone: GaCl, GaCl₂, GaCl₃, Ga₂Cl₂, Ga₂Cl₄, Ga₂Cl₆, Ga, InCl, InCl₂, InCl₃, In₂Cl₂, In₂Cl₄, In₂Cl₆, In, AsH₃, AsH₂, AsH, As, As₂, As₄, PH₃, PH₂, PH, P, P₂, P₃, P₄, H₂, HCl, H, Cl and Cl₂. A total of 27 reactions are involved with the 33 chemical species, as discussed in the previous section. Equilibrium equations can be written similar to those given for the source zone. Fifteen of the 27 equilibrium equations have been presented in the last section, the other twelve equilibrium equations are written as follows:

$$K_5(T) = \frac{P_{\text{As}_4}}{P_{\text{As}_2}^2} \quad (\text{A-25})$$

$$K_6(T) = \frac{P_{\text{As}_2}^{0.5} P_{\text{H}_2}^{1.5}}{P_{\text{AsH}_3}} \quad (\text{A-26})$$

$$K_7(T) = \frac{P_{\text{P}_4}}{P_{\text{P}_2}^2} \quad (\text{A-27})$$

30

$$K_8(T) = \frac{P_P^{0.5} P_{H_2}^{1.5}}{P_{PH_3}} \quad (A-28)$$

$$K_{19}(T) = \frac{P_{AsH_2} P_{H_2}^{0.5}}{P_{AsH_3}} \quad (A-29)$$

$$K_{20}(T) = \frac{P_{AsH} P_{H_2}}{P_{AsH_3}} \quad (A-30)$$

$$K_{21}(T) = \frac{P_{PH_2} P_{H_2}^{0.5}}{P_{PH_3}} \quad (A-31)$$

$$K_{22}(T) = \frac{P_{PH} P_{H_2}}{P_{PH_3}} \quad (A-32)$$

$$K_{23}(T) = \frac{P_{As}^2}{P_{As_2}} \quad (A-33)$$

$$K_{24}(T) = \frac{P_{As_3}^2}{P_{As_2} P_{As_4}} \quad (A-34)$$

$$K_{25}(T) = \frac{P_P^2}{P_{P_2}} \quad (A-35)$$

$$K_{26}(T) = \frac{P_{P_3}^2}{P_{P_4} P_{P_2}} \quad (A-36)$$

Define B1 as the gallium to hydrogen ratio, B2 the indium to hydrogen ratio, C1 the arsenic to hydrogen ratio, and C2 the phosphorus to hydrogen ratio. Denoting the parameters in the mixing zone by subscript m, then A_m , $B1_m$, $B2_m$, $C1_m$, and $C2_m$ can be written as follows.

$$A_m = (Cl/H)_m =$$

$$\frac{\{P_{HCl} + P_{Cl} + P_{GaCl} + P_{InCl} + 2(P_{GaCl_2} + P_{InCl_2} + P_{Ga_2Cl_2} + P_{In_2Cl_2} + P_{Cl_2}) + 3(P_{GaCl_3} + P_{In_2Cl_6})\} + 4(P_{Ga_2Cl_4} + P_{In_2Cl_4}) + 6(P_{Ga_2Cl_6} + P_{In_2Cl_6})}{2P_{H_2} + P_H + P_{HCl} + 3P_{AsH_3} + 3P_{PH_3} + 2(P_{PH_2} + P_{AsH_2} + P_{PH} + P_{AsH})} \quad (A-37)$$

$$B1_m = (Ga/H)_m =$$

$$\frac{P_{Ga} + P_{GaCl} + P_{GaCl_2} + P_{GaCl_3} + P_{Ga_2Cl_2} + 2P_{Ga_2Cl_4} + 2P_{Ga_2Cl_6}}{P_{H_2} + P_H + P_{HCl} + 3P_{AsH_3} + 3P_{PH_3} + 2P_{AsH_2} + 2P_{PH_2} + P_{AsH} + P_{PH}} \quad (A-38)$$

$$B2_m = (In/H)_m =$$

$$\frac{P_{In} + P_{InCl} + P_{InCl_2} + P_{InCl_3} + 2P_{In_2Cl_2} + 2P_{In_2Cl_4} + 2P_{In_2Cl_6}}{P_{H_2} + P_H + P_{HCl} + 3P_{AsH_3} + 3P_{PH_3} + 2P_{AsH_2} + 2P_{PH_2} + P_{AsH} + P_{PH}} \quad (A-39)$$

$$C1_m = (As/H)_m =$$

$$\frac{P_{AsH} + P_{AsH_2} + P_{AsH_3} + P_{As} + 2P_{As_2} + 3P_{As_3} + 4P_{As_4}}{P_{H_2} + P_H + P_{HCl} + 3P_{AsH_3} + 3P_{PH_3} + 2P_{AsH_2} + 2P_{PH_2} + P_{AsH} + P_{PH}} \quad (A-40)$$

$$C2_m = (P/H)_m =$$

$$\frac{P_{PH} + P_{PH_2} + P_{PH_3} + P_P + 2P_{P_2} + 3P_{P_3} + 4P_{P_4}}{P_{H_2} + P_H + P_{HCl} + 3P_{AsH_3} + 3P_{PH_3} + 2P_{AsH_2} + 2P_{PH_2} + P_{AsH} + P_{PH}} \quad (A-41)$$

The summation of partial pressure of the 33 vapor species equals to the total pressure P_{tot} .

$$\begin{aligned}
 P_{tot} = & P_{H_2} + P_{HCl} + P_H + P_{Cl} + P_{Cl_2} + P_{GaCl} + P_{GaCl_2} + P_{GaCl_3} \\
 & + P_{Ga_2Cl_2} + P_{Ga_2Cl_4} + P_{Ga_2Cl_6} + P_{Ga} + P_{InCl} + P_{InCl_2} \\
 & + P_{InCl_3} + P_{In_2Cl_2} + P_{In_2Cl_4} + P_{In_2Cl_6} + P_{In} + P_{AsH_3} \\
 & + P_{AsH_2} + P_{AsH} + P_{As} + P_{As_2} + P_{As_3} + P_{As_4} + P_{PH_3} + P_{PH_2} \\
 & + P_{PH} + P_P + P_{P_2} + P_{P_2} + P_{P_4}
 \end{aligned} \tag{A-42}$$

The complex chemical equilibrium in mixing zone is completely defined by equations (A-1) to (A-9), (A-11) to (A-15), (A-19), (A-25) to (A-36) and equations (A-37) to (A-41). When the mixing zone temperature, T_m , and the values of the parameters, A_m , $B1_m$, $B2_m$, $C1_m$, $C2_m$, and system pressure, P_{tot} , are given, the complex chemical equilibrium in the mixing zone can be calculated by solving the simultaneous equilibrium equations.

Deposition zone

All of the gaseous chemical species listed in Table A-1 are included for the discussion of complex chemical equilibrium in deposition zone. The condensed phase is the solid solution $In_{1-x}Ga_xAs_yP_{1-y}$. In addition to the 27 homogeneous system reactions for the 33 gaseous chemical species, as explained in the last section, four heterogeneous system reactions also exist in deposition zone. The equilibrium equations for these four reactions are

$$K_1(T) = \frac{a_{\text{GaAs}} P_{\text{HCl}}}{P_{\text{GaCl}} P_{\text{As}_4}^{0.25} P_{\text{H}_2}^{0.5}} \quad (\text{A-43})$$

$$K_2(T) = \frac{a_{\text{InAs}} P_{\text{HCl}}}{P_{\text{InCl}} P_{\text{As}_4}^{0.25} P_{\text{H}_2}^{0.5}} \quad (\text{A-44})$$

$$K_3(T) = \frac{a_{\text{GaP}} P_{\text{HCl}}}{P_{\text{GaCl}} P_{\text{P}_4}^{0.25} P_{\text{H}_2}^{0.5}} \quad (\text{A-45})$$

$$K_4(T) = \frac{a_{\text{InP}} P_{\text{HCl}}}{P_{\text{InCl}} P_{\text{P}_4}^{0.25} P_{\text{H}_2}^{0.5}} \quad (\text{A-46})$$

where a_i is the activity of binary component i in solid solution

$\text{In}_{1-x}\text{Ga}_x\text{As}_y\text{P}_{1-y}$. The activities are dependent upon the solid solution composition (x,y) and temperature (T) . The solution thermodynamics of solid

$\text{In}_{1-x}\text{Ga}_x\text{As}_y\text{P}_{1-y}$, which elucidate the dependence of a_i on (x,y) and T , will be discussed later in this report. Define D as the ratio of the difference between the number of group III atoms and group V atoms to the total number of hydrogen atoms in the vapor phase, so that

$$D = \frac{P_{\text{Ga}} + P_{\text{GaCl}} + P_{\text{GaCl}_2} + P_{\text{GaCl}_3} + 2P_{\text{Ga}_2\text{Cl}_2} + 2P_{\text{Ga}_2\text{Cl}_4} + 2P_{\text{Ga}_2\text{Cl}_6} + P_{\text{In}} + P_{\text{InCl}} + P_{\text{InCl}_2} + P_{\text{InCl}_3} + 2P_{\text{In}_2\text{Cl}_2} + 2P_{\text{In}_2\text{Cl}_4} + 2P_{\text{In}_2\text{Cl}_6} - P_{\text{AsH}_3} - P_{\text{AsH}_2} - P_{\text{AsH}} - P_{\text{As}} - 2P_{\text{As}_2} - 3P_{\text{As}_3} - 4P_{\text{As}_4} - P_{\text{PH}_3} - P_{\text{PH}_2} - P_{\text{PH}} - P_{\text{P}} - 2P_{\text{P}_2} - 3P_{\text{P}_3} - 4P_{\text{P}_4}}{2P_{\text{H}_2} + P_{\text{H}} + P_{\text{HCl}} + 3P_{\text{AsH}_3} + 3P_{\text{PH}_3} + 2P_{\text{AsH}_2} + 2P_{\text{PH}_2} + P_{\text{AsH}} + P_{\text{PH}}} \quad (\text{A-47})$$

When values of the deposition zone temperature, T_d , system pressure, P_{tot} , parameters D and A_d (chlorine to hydrogen ratio in the deposition zone), and solid solution composition (x,y) are given, the partial pressure of the 33 gaseous chemical species can be obtained by solving equations (A-1 to A-9, A-11 to A-15, A-19, A-25 to A-36), equation (A-37), equation (A-42), equations (A-43 to A-46), and equation (A-47) simultaneously.

Define Y as the ratio of the number of gallium atoms to the total number of group III atoms in the vapor phase, and Z the ratio of arsenic atoms to group V atom sin the vapor phase. Given values of the partial pressures, Y and Z can be readily evaluated as follows:

$$Y = \frac{P_{Ga} + P_{GaCl} + P_{GaCl_2} + P_{GaCl_3} + 2P_{Ga_2Cl_2} + 2P_{Ga_2Cl_4} + 2P_{Ga_2Cl_6}}{\{P_{Ga} + P_{GaCl} + P_{GaCl_2} + P_{GaCl_3} + 2P_{Ga_2Cl_2} + 2P_{Ga_2Cl_4} + 2P_{Ga_2Cl_6} + P_{In} + P_{InCl} + P_{InCl_2} + P_{InCl_3} + 2P_{In_2Cl_2} + 2P_{In_2Cl_4} + 2P_{In_2Cl_6}\}} \quad (A-48)$$

$$Z = \frac{P_{AsH_3} + P_{AsH_2} + P_{AsH} + P_{As} + 2P_{As_2} + 3P_{As_3} + 4P_{As_4}}{\{P_{AsH_3} + P_{AsH_2} + P_{AsH} + P_{As} + 2P_{As_2} + 3P_{As_3} + 4P_{As_4} + P_{Ph_3} + P_{PH_2} + P_{PH} + P_P + 2P_{P_2} + 3P_{P_3} + 3P_{P_4}\}} \quad (A-49)$$

Therefore, complex chemical equilibrium can also be defined by a set of chosen values of T_d , P_{tot} , A_d , D , Y , and Z . In this case, equations (A-1 to A-9, A-11 to A-15, A-19, A-25 to A-37, A-42 to A-49) are solved together for the partial pressure of the 33 vapor species and the solid solution composition (x,y).

A.1.3. Process Parameters

The parameters that have been discussed in the last section are called "equilibrium parameters," since specification of the values of these parameters defines the equilibrium condition. Table A-5 lists the equilibrium parameters and their shorthand definitions.

In open VPE reactor systems, equilibrium parameters cannot be directly controlled. Rather, process performance is controlled by changing various "process parameters," the flowrates, temperature settings and pressure set-

Table A-5. Equilibrium parameters

Zone	Equilibrium Parameters	
	Symbol	Definition
gallium source zone	$A_S(\text{Ga})$	Cl/H
	$T_S(\text{Ga})$	temperature
	P_{tot}	pressure
indium source zone	$A_S(\text{In})$	Cl/H
	$T_S(\text{In})$	temperature
	P_{tot}	pressure
mixing zone	A_m	Cl/H
	$B1_m$	Ga/H
	$B2_m$	In/H
	$C1_m$	As/H
	$C2_m$	P/H
	T_m	temperature
	P_{tot}	pressure
deposition zone	A_d	Cl/H
	D	(III-V)/H
	Y	Ga/III
	Z	As/V
	T_d	temperature
	P_{tot}	pressure

ting. In addition, the three temperature zones are connected in series since the product gasflow of upstream zone is transported into the downstream zone and becomes the input gasflow of that region. Specification of equilibrium parameters in the mixing zone is directly connected to the values of the source zone output, and similarly, equilibrium parameters in the deposition zone are dependent upon the mixing zone condition. Therefore, it is of practical value to investigate the relationship between the equilibrium parameters from one temperature zone to the other, and the relationship between the equilibrium parameters and the process parameters.

Gallium source zone

Denoting the input flowrates of HCl and H₂ into the gallium source zone by $F_{\text{HCl}}^{(\text{Ga})}$ and $F_{\text{H}_2}^{(\text{Ga})}$, then the transport rate of hydrogen atoms $F_{\text{H}}^{(\text{Ga})}$ and the transport rate of chlorine atoms $F_{\text{Cl}}^{(\text{Ga})}$ are simply

$$F_{\text{H}}^{(\text{Ga})} = 2F_{\text{H}_2}^{(\text{Ga})} + F_{\text{HCl}}^{(\text{Ga})} \quad (\text{A-50})$$

$$F_{\text{Cl}}^{(\text{Ga})} = F_{\text{HCl}}^{(\text{Ga})} \quad (\text{A-51})$$

Using the above equations, equilibrium parameter $A_{\text{S}}(\text{Ga})$ can be related to the process parameters $F_{\text{HCl}}^{(\text{Ga})}$ and $F_{\text{H}_2}^{(\text{Ga})}$ as follows:

$$A_{\text{S}}(\text{Ga}) = \frac{F_{\text{Cl}}^{(\text{Ga})}}{F_{\text{H}}^{(\text{Ga})}} \quad (\text{A-52})$$

When the process parameters $F_{\text{HCl}}^{(\text{Ga})}$, $F_{\text{H}_2}^{(\text{Ga})}$, $T_{\text{S}}(\text{Ga})$ and P_{tot} are specified, the equilibrium parameters, $A_{\text{S}}(\text{Ga})$, $T_{\text{S}}(\text{Ga})$, and P_{tot} , are also specified, and complex chemical equilibrium calculation can be carried out as discussed previously.

The result of the gallium source reactions is transport of gallium atoms via the vapor phase. Two different transport rates of gallium should be differentiated, namely the equilibrium transport rate of gallium $F_{\text{Ga}}^{(\text{Ga})*}$, and the process transport rate of gallium is the calculated gallium transport rate from complex chemical equilibrium, therefore $F_{\text{Ga}}^{(\text{Ga})*}$ can be written as

$$F_{\text{Ga}}^{(\text{Ga})*} = F_{\text{H}}^{(\text{Ga})} \frac{\{P_{\text{Ga}} + P_{\text{GaCl}} + P_{\text{GaCl}_2} + P_{\text{GaI}_3} + 2P_{\text{Ga}_2\text{Cl}_2} + 2P_{\text{Ga}_2\text{Cl}_4} + 2P_{\text{Ga}_2\text{Cl}_6}\}}{2P_{\text{H}_2} + P_{\text{HCl}} + P_{\text{H}}} \quad (\text{A-53})$$

The process transport rate of gallium is the physically obtained gallium transport in the process. Clearly, the process transport rate of gallium, which is always less than or equal to the equilibrium transport rate of gallium, is dependent upon source zone design and process operating conditions. For convenience, define $e(\text{Ga})$, the gallium transport efficiency factor as follows:

$$e(\text{Ga}) = \frac{F_{\text{Ga}}^{(\text{Ga})}}{F_{\text{Cl}}^{(\text{Ga})}} \quad (\text{A-54})$$

The value of $e(\text{Ga})$ at equilibrium equals $F_{\text{Ga}}^{(\text{Ga})*}/F_{\text{Cl}}^{(\text{Ga})}$ and is denoted $e^*(\text{Ga})$. The value of $e(\text{Ga})$ equals zero at the inlet of gallium source zone, increases in the direction of gasflow, and, given sufficient residence time, is saturated at the source zone outlet. The factor $e(\text{Ga})$ serves as an important process parameter for the mixing zone, as will be explained later in this section.

Indium source zone

Similar to gallium source zone, four process parameters exist in indium source zone, namely, HCl input flowrate, $F_{\text{HCl}}^{(\text{Ga})}$, H_2 input flowrate, $F_{\text{H}_2}^{(\text{In})}$,

indium source zone temperature, $T_s(\text{In})$, and total pressure, P_{tot} . The hydrogen transport rate, $F_H^{(\text{In})}$, and chlorine transport rate, $F_{\text{Cl}}^{(\text{In})}$, are given by

$$F_H^{(\text{In})} = 2F_{\text{H}_2}^{(\text{In})} + F_{\text{HCl}}^{(\text{In})} \quad (\text{A-55})$$

$$F_{\text{Cl}}^{(\text{In})} = F_{\text{HCl}}^{(\text{In})} \quad (\text{A-56})$$

The equilibrium parameter, $A_s(\text{In})$, is determined by $F_H^{(\text{In})}$ and $F_{\text{Cl}}^{(\text{In})}$,

$$A_s(\text{In}) = \frac{F_{\text{Cl}}^{(\text{In})}}{F_H^{(\text{In})}} \quad (\text{A-57})$$

The equilibrium transport rate of indium, $F_{\text{In}}^{(\text{In})*}$, is calculated from equilibrium partial pressures according to

$$F_{\text{In}}^{(\text{In})*} = F_H^{(\text{In})} \frac{\{P_{\text{In}} + P_{\text{InCl}} + P_{\text{InCl}_2} + P_{\text{InCl}_3} + 2P_{\text{In}_2\text{Cl}_2} + 2P_{\text{In}_2\text{Cl}_4} + 2P_{\text{In}_2\text{Cl}_6}\}}{2P_{\text{H}_2} + P_{\text{HCl}} + P_{\text{H}}} \quad (\text{A-58})$$

The indium transport $e(\text{In})$ is defined by

$$e(\text{In}) = \frac{F_{\text{In}}^{(\text{In})}}{F_{\text{Cl}}^{(\text{In})}} \quad (\text{A-59})$$

where $F_{\text{In}}^{(\text{In})}$ is the process transport rate of indium.

Mixing zone

Denote the input flowrates of H_2 , AsH_3 and PH_3 by $F_{\text{H}_2}^{(m)}$, F_{AsH_3} and F_{PH_3} , then the total transport rate of hydrogen in the mixing zone, $F_H^{(m)}$, is given by

$$F_H^{(m)} = F_H^{(Ga)} + F_H^{(In)} + 2F_{H_2}^{(m)} + 3(F_{AsH_3} + F_{PH_3}) \quad (A-60)$$

The connective nature between source zone and mixing zone is evident from the first two terms in the RHS of equation (A-60). The transport rates of chlorine, gallium, indium, arsenic and phosphorous in the mixing zone are as follows

$$F_{Cl}^{(m)} = F_{Cl}^{(Ga)} + F_{Cl}^{(In)} \quad (A-61)$$

$$F_{Ga}^{(m)} = F_{Ga}^{(Ga)} = e(Ga) F_{Cl}^{(Ga)} \quad (A-62)$$

$$F_{In}^{(m)} = F_{In}^{(In)} = e(In) F_{Cl}^{(In)} \quad (A-63)$$

$$F_{As}^{(m)} = F_{AsH_3} \quad (A-64)$$

$$F_P^{(m)} = F_{PH_3} \quad (A-65)$$

The equilibrium parameters A_m , $B1_m$, $B2_m$, $C1_m$ and $C2_m$ are related the transport rates and can be written as follows.

$$A_m = \frac{F_{Cl}^{(m)}}{F_H^{(m)}} \quad (A-66)$$

$$B1_m = \frac{F_{Ga}^{(m)}}{F_H^{(m)}} \quad (A-67)$$

$$B2_m = \frac{F_{In}^{(m)}}{F_H^{(m)}} \quad (A-68)$$

$$C1_m = \frac{F_{As}^{(m)}}{F_H^{(m)}} \quad (A-69)$$

$$C2_m = \frac{F_P^{(m)}}{F_H^{(m)}} \quad (A-70)$$

From the equations presented above, it is clear that there are seven process parameters in the mixing zone; $F_{H_2}^{(m)}$, F_{AsH_3} , F_{PH_3} , T_m , P_{tot} , $e(Ga)$ and $e(In)$. When values of $F_H^{(Ga)}$, $F_{Cl}^{(Ga)}$, $F_H^{(In)}$, $F_{Cl}^{(In)}$, and the process parameters are specified, the seven equilibrium parameters, A_m , $B1_m$, $B2_m$, $C1_m$, $C2_m$, T_m and P_{tot} can be evaluated and the complex chemical equilibrium in mixing zone is completely defined.

Since the overall reaction rate can be affected by mass transfer and kinetic effects in the process, chemical equilibrium might not be reached in the mixing zone. If the mixing zone is operated under the correct criteria prohibiting formation of any condensable reaction products, then the process transport rates of all six atomic species, equation (A-60 to A-65), will not change. Therefore, the transport rates derived for the mixing zone can be directly used in deposition zone.

Deposition zone

Equilibrium parameters A_d , D , Y and Z at the inlet of deposition zone are determined by transport rates $F_H^{(m)}$, $F_{Cl}^{(m)}$, $F_{Ga}^{(m)}$, $F_{In}^{(m)}$, $F_{As}^{(m)}$ and $F_P^{(m)}$.

$$A_d = \frac{F_{Cl}^{(m)}}{F_H^{(m)}} \quad (A-71)$$

$$D = \frac{(F_{Ga}^{(m)} + F_{In}^{(m)} - F_{As}^{(m)} - F_P^{(m)})}{F_H^{(m)}} \quad (A-72)$$

$$Y = \frac{F_{Ga}^{(m)}}{(F_{Ga}^{(m)} + F_{In}^{(m)})} \quad (A-73)$$

$$Z = \frac{F_{As}^{(m)}}{(F_{As}^{(m)} + F_P^{(m)})} \quad (A-74)$$

The reactant gas is supersaturated and deposition reaction occurs in the deposition zone. In the course of the deposition process, group III atoms (In, Ga) and group V atoms (As, P) leave the vapor phase, therefore the values of Y and Z begin to change along the flow direction. Define supersaturation, S, to be the total number of group III atoms (or equivalently the total number of group V atoms) that leave the vapor phase before equilibrium is reached. Then, at equilibrium, the equilibrium parameters Y and Z are

$$Y = \frac{(F_{Ga}^{(m)} - x S)}{(F_{Ga}^{(m)} + F_{In}^{(m)} - S)} \quad (A-75)$$

$$Z = \frac{(F_{As}^{(m)} - y S)}{(F_{As}^{(m)} + F_P^{(m)} - S)} \quad (A-76)$$

where x and y are mole fractions in the deposited compound $In_{1-x}Ga_xAs_yP_{1-y}$. Note that stoichiometry is usually assumed for the deposition of III-V compounds. Therefore, in writing equations (A-75) and (A-76) the number of deposited group III atoms has been assumed to be equal to the number of deposited group V atoms. On account of this assumption, it is clear that the value of the equilibrium parameter D is not affected by the deposition process.

The deposition zone temperature, T_d , and the system total pressure, P_{tot} , are the only process parameters in the deposition zone. With specified T_d , P_{tot} , and values of the transport rates at the deposition zone inlet, $F_H^{(m)}$, $F_{Cl}^{(m)}$, $F_{Ga}^{(m)}$, $F_{In}^{(m)}$, $F_{As}^{(m)}$, and $F_P^{(m)}$, equilibrium parameters, T_d , P_{tot} , A_d , D, Y and Z can be evaluated directly or indirectly by equations (A-71, A-72,

A-75 and A-76). With the complex chemical equilibrium defined, composition (x, y) and supersaturation S can be obtained.

Summary

Equilibrium parameters that are used to initiate complex chemical equilibrium calculation are quite different from the realistic process parameters used in process control. In order to study the effects of equilibrium on realistic processes, equilibrium parameters have to be used to bridge between process parameters and complex chemical equilibrium calculation. Table A-6 gives a complete listing of the process parameters discussed in this section. There are basically two types of process parameters. Type 1 is the "process control" parameters. Most of the process parameters (e.g., flowrate, temperature, and pressure,) belong to this group. The second type are "process design parameters" and cannot be easily tuned during process runs. For example, transport factors $e(\text{Ga})$ and $e(\text{In})$ are determined primarily as a result of source zone design. Note that there are a total of 14 process parameters in hydride VPE of $\text{In}_{1-x}\text{Ga}_x\text{As}_y\text{P}_{1-y}$ $F_{\text{H}_2}^{(\text{Ga})}$, $F_{\text{HCl}}^{(\text{Ga})}$, $T_s(\text{Ga})$, $e(\text{Ga})$, $F_{\text{H}_2}^{(\text{In})}$, $F_{\text{HCl}}^{(\text{In})}$, $T_s(\text{In})$, $e(\text{In})$, $F_{\text{H}_2}^{(m)}$, F_{AsH_3} , F_{PH_3} , T_m , T_d , and P_{tot} .

A.1.4. Computational Procedures

Equilibrium Constants

The reaction equilibrium constant K_a is given by its definition as

$$K_a = \prod_{i=1}^n a_i = \exp \left(\frac{-1}{RT} \sum_{i=1}^n v_i \mu_i^0 \right) = \exp \left(\frac{-\Delta \mu^0}{RT} \right) \quad (\text{A-77})$$

where a_i is the activity of chemical species i , v_i is the stoichiometric constant of i in the reaction, μ_i^0 is the standard Gibbs energy of i , and n equals the total number of chemical species involved in the reaction. The

Table A-6. Process parameters

Zone	Process Parameters	
	Symbol	Definition
gallium source zone	$F_{H_2}^{(Ga)}$	H ₂ input flowrate
	$F_{HCl}^{(Ga)}$	HCl input flowrate
	$T_s(Ga)$	temperature
	P_{tot}	pressure
indium source zone	$F_{H_2}^{(In)}$	H ₂ input flowrate
	$F_{HCl}^{(In)}$	HCl input flowrate
	$T_s(In)$	temperature
	P_{tot}	pressure
mixing zone	$e(Ga)$	Ga transport factor
	$e(In)$	In transport factor
	$F_{H_2}^{(m)}$	H ₂ input flowrate
	F_{AsH_3}	AsH ₃ input flowrate
	F_{PH_3}	PH ₃ input flowrate
	T_m	temperature
	P_{tot}	pressure
deposition zone	T_d	temperature
	P_{tot}	pressure

standard Gibbs energy of the reaction, $\Delta\mu^0$, at temperature T can be evaluated from the standard enthalpy of formation at 298 K, $\Delta H_f^0(298K)$, absolute entropy at 298 K, $S^0(298K)$, and high temperature heat capacity, $C_p(T)$, of the involved chemical species.

$$\Delta\mu^0 = \sum_{i=1}^n i(\Delta H_f^0(298K) - TS^0(298K) + \int_{298K}^T C_{p,i} dT - T \int_{298K}^T C_{p,i} \frac{dT}{T}) \quad (A-78)$$

Using equations (A-77) and (A-78) and the selected thermochemical data of Tables A-2 and A-3, equilibrium constants of the 33 reactions listed in Table A-4 can be calculated.

Gallium source zone

Assuming that $q_1 = P_{H_2}^{0.5}$ and $q_2 = P_{HCl} P_{H_2}^{-0.5}$, then the partial pressure of each chemical species in the gallium source zone can be rewritten in terms of q_1 , q_2 , and temperature dependent equilibrium constants.

$$P_{H_2} = q_1^2 \quad (A-79)$$

$$P_{HCl} = q_1 q_2 \quad (A-80)$$

$$P_H = K_{27}^{0.5} q_1 \quad (A-81)$$

$$P_{Cl} = K_{28} K_{27}^{-0.5} q_2 \quad (A-82)$$

$$P_{Cl_2} = K_{29} K_{28}^2 K_{27}^{-1} q_2^2 \quad (A-83)$$

$$P_{\text{GaCl}} = K_{32} q_2 \quad (\text{A-84})$$

$$P_{\text{Ga}_2\text{Cl}_2} = K_{18} K_{32}^2 q_2^2 \quad (\text{A-85})$$

$$P_{\text{GaCl}_2} = K_{14} K_{32} q_2^2 \quad (\text{A-86})$$

$$P_{\text{Ga}_2\text{Cl}_4} = K_{10} K_9 K_{32}^2 q_2^4 \quad (\text{A-87})$$

$$P_{\text{GaCl}_3} = K_9 K_{32} q_2^3 \quad (\text{A-88})$$

$$P_{\text{Ga}_2\text{Cl}_6} = K_{16} K_9^2 K_{32}^2 q_2^6 \quad (\text{A-89})$$

$$P_{\text{Ga}} = K_{30} K_{32} K_{28}^{-1} K_{27}^{0.5} \quad (\text{A-90})$$

Substituting equations (A-79 to A-90) in equations (A-11) and (A-12),

$$A_s(\text{Ga}) = \frac{\{(q_1 + K_{32} + K_{28} K_{27}^{-0.5}) q_2 + K_9 K_{32} q_2^3 + (K_{29} K_{28}^2 K_{27}^{-1} + K_{18} K_{32}^2 + K_{14} K_{32}) q_2^2 + K_{10} K_9 K_{32}^2 q_2^4 + K_{16} K_9^2 K_{32}^2 q_2^6\}}{\quad} \quad (\text{A-91})$$

$$P_{\text{tot}} = \{q_1^2 + K_{27}^{0.5} q_1 + (K_{32} + K_{28} K_{27}^{-0.5}) q_2 + (K_{29} K_{28}^2 K_{27}^{-1} + K_{18} K_{32}^2 + K_{14} K_{32}) q_2^2 + K_9 K_{32} q_2^3 + K_{10} K_9 K_{32}^2 q_2^4 + q_1 q_2 + K_{16} K_9^2 K_{32}^2 q_2^6 + K_{30} K_{32} K_{28}^{-1} K_{27}^{0.5}\} \quad (\text{A-92})$$

The nonlinear algebraic equations, equations (A-91) and (A-92), can be solved together numerically for q_1 and q_2 . Newton-Raphson method was chosen and has been found adequate for the numerical solution of this problem.

Indium source zone

The same procedure for gallium source zone calculation is used for indium source zone calculation.

$$P_{InCl} = K_{33} q_2 \quad (A-93)$$

$$P_{In_2Cl_2} = K_{17} K_{32}^2 q_2^2 \quad (A-94)$$

$$P_{InCl_2} = K_{13} K_{33} q_2^2 \quad (A-95)$$

$$P_{In_2Cl_4} = K_{12} K_{11} K_{33}^2 q_2^4 \quad (A-96)$$

$$P_{InCl_3} = K_{11} K_{33} q_2^3 \quad (A-97)$$

$$P_{In_2Cl_6} = K_{15} K_{11}^2 K_{33}^2 q_2^6 \quad (A-98)$$

$$P_{In} = K_{31} K_{33} K_{28}^{-1} K_{27}^{0.5} \quad (A-99)$$

Substitution of equations (A-79 to A-83) and (A-93 to A-99) into equations (A-23) and (A-24) and rewriting equations (A-23) and (A-24) gives,

$$\begin{aligned} & \{(q_1 + K_{33} + K_{28} K_{27}^{-0.5}) q_2 + K_{11} K_{33} q_2^3 \\ & + (K_{29} K_{28}^2 K_{27}^{-1} + K_{17} K_{32}^2 + K_{13} K_{33}) q_2^2 \end{aligned}$$

$$A_s(\text{In}) = \frac{+ K_{12}K_{11}K_{33}^2q_2^4 + K_{15}K_{11}^2K_{33}^2q_2^6}{(q_2 + K_{27}^{0.5})q_1 + q_1^2} \quad (\text{A-100})$$

$$\begin{aligned} P_{\text{tot}} = & \{q_1^2 + K_{27}^{0.5}q_1 + (K_{33} + K_{28}K_{27}^{-0.5})q_2 + \\ & (K_{29}K_{28}^2K_{27}^{-1} + K_{17}K_{33}^2 + K_{13}K_{33})q_2^2 + \\ & K_{11}K_{33}q_2^3 + K_{12}K_{11}K_{33}^2q_2^4 + q_1q_2 + \\ & K_{15}K_{11}^2K_{33}^2q_2^6 + K_{31}K_{33}K_{28}^{-1}K_{27}^{0.5}\} \end{aligned} \quad (\text{A-101})$$

Solution of equations (A-100) and (A-101) by the Newton-Raphson method gives the values of q_1 and q_2 , from which values of the partial pressure of chemical species in indium source zone at equilibrium can be calculated.

Mixing zone

Assuming that $q_3 = P_{\text{As}_4}^{0.25}$, $q_4 = P_{\text{P}_4}^{0.25}$, $q_5 = P_{\text{GaCl}}$ and $q_6 = P_{\text{InCl}}$, then the partial pressure of the chemical species in mixing zone can be written in terms of q_1 , q_2 , q_3 , q_4 , q_5 and q_6 as follows.

$$P_{\text{GaCl}} = q_5 \quad (\text{A-102})$$

$$P_{\text{Ga}_2\text{Cl}_2} = K_{18}q_5^2 \quad (\text{A-103})$$

$$P_{\text{GaCl}_2} = K_{14}q_5q_2 \quad (\text{A-104})$$

$$P_{\text{Ga}_2\text{Cl}_4} = K_{10}K_9q_5^2q_2^2 \quad (\text{A-105})$$

$$P_{\text{GaCl}_3} = K_9q_5q_2^2 \quad (\text{A-106})$$

$$P_{\text{Ga}_2\text{Cl}_6} = K_{16}K_9^2q_5^2q_2^4 \quad (\text{A-107})$$

$$P_{Ga} = K_{30} K_{28}^{-1} K_{27}^{0.5} q_5 q_2^{-1} \quad (A-108)$$

$$P_{InCl} = q_6 \quad (A-109)$$

$$P_{In_2Cl_2} = K_{17} q_6^2 \quad (A-110)$$

$$P_{InCl_2} = K_{13} q_6 q_2^2 \quad (A-111)$$

$$P_{In_2Cl_4} = K_{12} K_{11} q_6^2 q_2^2 \quad (A-112)$$

$$P_{InCl_3} = K_{11} q_6 q_2^2 \quad (A-113)$$

$$P_{In_2Cl_6} = K_{16} K_{11}^2 q_6^2 q_2^4 \quad (A-114)$$

$$P_{In} = K_{31} K_{28}^{-1} K_{27}^{0.5} q_2^{-1} q_6 \quad (A-115)$$

$$P_{As_4} = q_3^4 \quad (A-116)$$

$$P_{As_3} = K_{24}^{0.5} K_5^{-0.25} q_3^3 \quad (A-117)$$

$$P_{As_2} = K_5^{-0.5} q_3^2 \quad (A-118)$$

$$P_{As} = K_{23}^{0.5} K_5^{-0.25} q_3 \quad (A-119)$$

$$P_{AsH_3} = K_5^{-1} K_5^{-0.25} q_3 q_1^3 \quad (A-120)$$

$$P_{AsH_2} = K_{19} K_6^{-1} K_5^{-0.25} q_3 q_1^2 \quad (A-121)$$

$$P_{AsH} = K_{20} K_6^{-1} K_5^{-0.25} q_3 q_1 \quad (A-122)$$

$$P_{P_4} = q_4^4 \quad (A-123)$$

$$P_{P_3} = K_{26}^{0.5} K_7^{-0.25} q_4^3 \quad (A-124)$$

$$P_{P_2} = K_7^{-0.5} q_4^2 \quad (A-125)$$

$$P_P = K_{25}^{0.5} K_7^{-0.25} q_4 \quad (A-126)$$

$$P_{PH_3} = K_8^{-1} K_7^{0.25} q_4 q_1^3 \quad (A-127)$$

$$P_{PH_2} = K_{21} K_8^{-1} K_7^{-0.25} q_4 q_1^2 \quad (A-128)$$

$$P_{PH} = K_{22} K_8^{-1} K_7^{-0.25} q_4 q_1 \quad (A-129)$$

Substituting equations (A-79) to A-83) and (A-102 to A-129) in equations (A-37 to A-42) yields six nonlinear algebraic equations of q_1 , q_2 , q_3 , q_4 , q_5 , and q_6 , which are solved simultaneously by the Newton-Raphson method. The complex chemical equilibrium partial pressure can be readily calculated.

Deposition zone

The partial pressure of the vapor phase species can be represented by the definition of q_1 , q_2 , and q_3 presented in the last two sections,

$$P_{GaCl} = K_1^{-1} a_{GaAs} q_2 q_3^{-1} \quad (A-130)$$

$$P_{\text{Ga}_2\text{Cl}_2} = K_{18} K_1^{-2} a_{\text{GaAs}}^2 q_2^2 q_3^{-2} \quad (\text{A-131})$$

$$P_{\text{GaCl}_2} = K_{14} K_1^{-1} a_{\text{GaAs}} q_2^2 q_3^{-1} \quad (\text{A-132})$$

$$P_{\text{Ga}_2\text{Cl}_4} = K_{10} K_9 K_1^{-2} a_{\text{GaAs}}^2 q_2^4 q_3^{-2} \quad (\text{A-133})$$

$$P_{\text{GaCl}_3} = K_9 K_1^{-1} a_{\text{GaAs}} q_2^3 q_3^{-1} \quad (\text{A-134})$$

$$P_{\text{Ga}_2\text{Cl}_6} = K_{16} K_9^2 K_1^{-2} a_{\text{GaAs}}^2 q_2^6 q_3^{-2} \quad (\text{A-135})$$

$$P_{\text{Ga}} = K_{30} K_{28}^{-1} K_{27}^{0.5} K_1^{-1} a_{\text{GaAs}} q_3^{-1} \quad (\text{A-136})$$

$$P_{\text{InCl}} = K_2^{-1} a_{\text{InAs}} q_2 q_3^{-1} \quad (\text{A-137})$$

$$P_{\text{In}_2\text{Cl}_2} = K_{17} K_2^{-2} a_{\text{InAs}}^2 q_2^2 q_3^{-2} \quad (\text{A-138})$$

$$P_{\text{InCl}_2} = K_{13} K_2^{-1} a_{\text{InAs}} q_2^2 q_3^{-1} \quad (\text{A-139})$$

$$P_{\text{In}_2\text{Cl}_4} = K_{12} K_{11} K_2^{-2} a_{\text{InAs}}^2 q_2^4 q_3^{-2} \quad (\text{A-140})$$

$$P_{\text{InCl}_3} = K_{11} K_2^{-1} a_{\text{InAs}} q_2^3 q_3^{-1} \quad (\text{A-141})$$

$$P_{\text{In}_2\text{Cl}_6} = K_{15} K_{11}^2 K_2^{-2} a_{\text{InAs}}^2 q_2^6 q_3^{-2} \quad (\text{A-142})$$

$$P_{\text{In}} = K_{31} K_{28}^{-1} K_{27}^{0.5} K_2^{-1} a_{\text{InAs}} q_3^{-1} \quad (\text{A-143})$$

$$P_{\text{P}_4} = K_3^{-4} K_1^4 a_{\text{GaP}}^4 a_{\text{GaAs}}^{-4} q_3^4 \quad (\text{A-144})$$

$$P_{P_3} = K_{26}^{0.5} K_7^{-0.25} K_3^{-3} K_1^3 a_{\text{GaP}}^3 a_{\text{GaAs}}^{-3} q_3^3 \quad (\text{A-145})$$

$$P_{P_5} = K_7^{-0.5} K_3^{-2} K_1^2 a_{\text{GaP}}^2 a_{\text{GaAs}}^{-2} q_3^2 \quad (\text{A-146})$$

$$P_P = K_{25}^{0.5} K_7^{-0.25} K_3^{-1} K_1 a_{\text{GaP}} a_{\text{GaAs}}^{-1} q_3 \quad (\text{A-147})$$

$$P_{\text{PH}_3} = K_8^{-1} K_7^{-0.25} K_3^{-1} K_1 a_{\text{GaP}} a_{\text{GaAs}}^{-1} q_3 q_1^3 \quad (\text{A-148})$$

$$P_{\text{PH}_2} = K_{21} K_8^{-1} K_7^{-0.25} K_3^{-1} K_1 a_{\text{GaP}} a_{\text{GaAs}}^{-1} q_3 q_1^2 \quad (\text{A-149})$$

$$P_{\text{PH}} = K_{22} K_8^{-1} K_7^{-0.25} K_3^{-1} K_1 a_{\text{GaP}} a_{\text{GaAs}}^{-1} q_3 q_1 \quad (\text{A-150})$$

Substituting equations (A-79 to A-83, A-116 to A-122 and A-130 to A-150) into equations (A-37, A-42 and A-47) gives three nonlinear algebraic equations of q_1 , q_2 , and q_3 . When a_{GaAs} , a_{GaP} , a_{InAs} (and a_{InP}) are specified, the equations can be solved for q_1 , q_2 , and q_3 . The complex chemical equilibrium of deposition zone is calculated by an iterative algorithm.

A.2. Solution Thermodynamics of InGaAsP

A.2.1. Solution Thermodynamics

Let x_i denote the mole fraction of component i in a homogeneous solution of C components, then

$$x_1 + x_2 + x_3 + \dots + x_C = 1 \quad (\text{A-151})$$

Let W denote an extensive property of the mixture, then the intensive property w_i of component i can be derived from the basic thermodynamic relationship,

$$w_i = \left(\frac{\partial W}{\partial N_i} \right)_{T, P, N_j (j \neq i)}, \quad (\text{A-152})$$

where T is temperature, P is pressure and N_i is the amount of component in the mixture. If N_i has the unit moles, then w_i is called a partial molar property. Therefore the partial molar Gibbs energy, g_i , or chemical potential, μ_i , is simply

$$\mu_i = g_i = \left(\frac{\partial G}{\partial N_i} \right)_{T, P, N_j (j \neq i)}, \quad (\text{A-153})$$

The partial molar entropy, s_i , the partial molar enthalpy, h_i , the partial molar volume, v_i and the partial molar heat capacity, C_{p_i} , are derived from the chemical potential by classical thermodynamics.

$$s_i = - \mu_i / T \quad (\text{A-154})$$

$$h_i = \mu_i - T(\mu_i / T) \quad (\text{A-155})$$

$$v_i = \mu_i / P \quad (\text{A-156})$$

$$C_{p_i} = T(s_i / T) = -T(\mu_i / T^2) \quad (\text{A-157})$$

Besides its use of conveniently evaluating other partial properties, the chemical potential is useful in formulating phase equilibrium. Consider two homogeneous mixtures A1 and A2 of C components at equilibrium, the system of phase equilibrium equations can be written as follows:

$$T_{A1} = T_{A2} \quad (\text{A-158})$$

$$P_{A1} = P_{A2} \quad (A-159)$$

$$\mu_{i,A1} = \mu_{i,A2}, \quad i = 1, 2, 3, \dots, C \quad (A-160)$$

In the consideration of a homogeneous mixture, we are also concerned with the comparison of partial properties of the components in the mixture with those properties in pure components. Let μ_i^0 denote the chemical potential of pure component i at temperature T and pressure P of interest, then the relative activity, a_i , of component i in the mixture is defined by the relationship,

$$a_i = \exp ((\mu_i - \mu_i^0)/RT) \quad (A-161)$$

Clearly, a_i is a direct measure of the chemical potential difference of component i between the mixture and the pure component i . This quantity can be directly used in the description of phase equilibrium between two solutions.

μ_i can be rewritten in terms of μ_i^0 and a_i ,

$$\mu_i = \mu_i^0 + RT \ln(a_i) \quad (A-162)$$

Substituting equation (A-162) in equation (A-160) and cancelling μ_i^0 on both sides of the equality sign results in another form of phase equilibrium equations.

$$a_{i,A1} = a_{i,A2} \quad (A-163)$$

From the review above, it is clear that if extensive Gibbs energy $G(T, P,$

N_1, N_2, \dots, N_C) is known, all of the partial molar properties can be readily derived. Furthermore, if the standard chemical potential $\mu_i^0(T, P)$ is known, relative activity a_i is obtained.

A.2.2. Solid Solution Models

The solid solution models used for type $A_{1-x}B_xC_{1-y}D_y$ III-V quaternary compound system are reviewed in this section. The objective is to develop a mathematical representation of the extensive Gibbs energy, G , in terms of the variables, $T, P, n_{AC}, n_{BC}, n_{AD},$ and n_{BD} . A solid solution model is usually constructed from an atomic or a statistical viewpoint and its compatibility with the solution system is tested by its capability to describe the system's experimental behavior. However, when the experimental characterization of the solution is difficult, solid solution models are also employed to interpolate and extrapolate system behavior from the limited amount of available information.

The $A_{1-x}B_xC_{1-y}D_y$ type of III-V quaternary solid solution has often been treated as a pseudoquaternary mixture of binary components AC, AD, BC, and BD. The characteristic feature of this type of solution is that the distribution of the nearest neighbor pairs is not uniquely determined by the apparent composition (x, y) of the quaternary compound. Let $n_{AC}, n_{AD}, n_{BC},$ and n_{BD} represent the number of nearest neighbor pairs AC, AD, BC, and BD, respectively. These numbers are related to the number of constituent atoms, $N_A, N_B, N_C,$ and N_D , as follows

$$n_{AC} + n_{AD} = z_1 N_A \quad (A-164)$$

$$n_{BC} + n_{BD} = z_1 N_B \quad (A-165)$$

$$n_{AC} + n_{BC} = z_1 N_C \quad (A-166)$$

$$n_{AD} + n_{BD} = z_1 N_D \quad (A-167)$$

where z_1 ($i = 1, 4$) is the number of nearest neighbors for each atom in the zinc-blende lattice structure. The number of constituent atoms, N_A , N_B , N_C , and N_D , is related to the apparent composition (x , y) and the total number of group III or group V sites, N , according to:

$$N_A = (1-x) N \quad (A-168)$$

$$N_B = x N \quad (A-169)$$

$$N_C = (1-y) N \quad (A-170)$$

$$N_D = y N \quad (A-171)$$

By observing equations (A-164 to A-171), it can be seen that equations (A-164 to A-167) are a set of dependent equations and one of the four equations can be eliminated. The resulting set of three independent equations, after substitution of N_A , N_B , N_C , and N_D by equations (A-168 to A-171) into equations (A-164 to A-167), is written as follows:

$$n_{AD} = (1-x) (z_1 N) - n_{AC} \quad (A-172)$$

$$n_{BC} = (1-y) (z_1 N) - n_{AC} \quad (A-173)$$

$$n_{BD} = (x+y-1) (z_1 N) + n_{AC} \quad (A-174)$$

It is obvious from equations (A-172 to A-174) that n_{AC} , n_{AD} , n_{BC} , and n_{BD} are not uniquely determined with specified x , y , and N . This feature is characteristic for III-V compound systems with mixing on both sublattices. However, if n_{AC} , n_{AD} , n_{BC} , and n_{BD} are specified, x , y , and N can be readily calculated by

$$x = (n_{BC} + n_{BD}) / (n_{AC} + n_{AD} + n_{BC} + n_{BD}) \quad (A-175)$$

$$y = (n_{AD} + n_{BD}) / (n_{AC} + n_{AD} + n_{BC} + n_{BD}) \quad (A-176)$$

$$N = (n_{AC} + n_{AD} + n_{BC} + n_{BD}) / z_1 \quad (A-177)$$

If a completely random distribution is assumed, the number of nearest pairs is given as follows:

$$n_{AC} = (1-x) (1-y) z_1 N \quad (A-178)$$

$$n_{AD} = (1-x) y z_1 N \quad (A-179)$$

$$n_{BC} = x (1-y) z_1 N \quad (A-180)$$

$$n_{BD} = x y z_1 N \quad (A-181)$$

The molar ratio of the binary components X_{ij} ($i=A,B$; $j=C,D$) is defined by

$$X_{ij} = (n_{ij}/z_1)/N \quad (\text{A-182})$$

In the case of random mixing, X_{ij} 's are evaluated as

$$X_{AC} = (1-x)(1-y) \quad (\text{A-183})$$

$$X_{AD} = (1-x) y \quad (\text{A-184})$$

$$X_{BC} = x (1-y) \quad (\text{A-185})$$

$$X_{BD} = x y \quad (\text{A-186})$$

The extensive Gibbs energy, G , of the solid solution $A_{1-x}B_xC_{1-y}D_y$ is given as a function of n_{AC} , n_{AD} , n_{BC} , n_{BD} , and T . From equations (A-172 to A-174), it is obvious that G can also be written as a function of n_{AC} , N , x , y , and T . When completely random distribution is assumed, G is a function of N , x , y , and T only, as evidenced by equations (A-179 to A-181).

In addition to equations (A-172 to A-174), the distribution of nearest neighbor pairs is dictated by the minimization of Gibbs energy in the system. The total differential of G , dG , is written from its functional dependence as

$$dG = -SdT + (\mu_{AC}dn_{AC} + \mu_{AD}dn_{AD} + \mu_{BC}dn_{BC} + \mu_{BD}dn_{BD})/z_1 \quad (\text{A-187})$$

The Gibbs energy is minimized when dG equals to zero. Therefore, with constant temperature ($dt=0$) at thermodynamic equilibrium, equation (A-187) becomes

$$0 = \mu_{AC} dn_{AC} + \mu_{AD} dn_{AD} + \mu_{BC} dn_{BC} + \mu_{BD} dn_{BD} \quad (A-188)$$

From equations (A-172 to A-174), the relationship between the total differential of the number of nearest neighbor pairs is obtained as

$$dn_{BD} = -dn_{BC} = -dn_{AD} = dn_{AC} \quad (A-189)$$

Combining equation (A-188) and equation (A-189), we obtain

$$\mu_{AC} + \mu_{BD} = \mu_{AD} + \mu_{BC} \quad (A-190)$$

Equations (A-172 to A-174) and equation (A-190) together define the distribution of nearest neighbor pairs.

Four models will be presented in the following for type $A_{1-x}B_xC_{1-y}D_y$ III-V solid solution, namely, the ideal solution model, the strictly regular solution model, the delta lattice parameter (DLP) model and the first-order quasi-chemical model.

Ideal Solution Model

The ideal solution model assumes random mixing on both sublattices and zero enthalpy of mixing, i.e.,

$$\Delta S_{mix} = -NR(x \ln x + (1-x) \ln(1-x) + y \ln y + (1-y) \ln(1-y)) \quad (A-191)$$

$$\Delta H_{mix} = 0 \quad (A-192)$$

Therefore,

$$\begin{aligned}\Delta G_{\text{mix}} &= \Delta H_{\text{mix}} - T\Delta S_{\text{mix}} \\ &= NRT(x\ln x + (1-x)\ln(1-x) + y\ln y + (1-y)\ln(1-y))\end{aligned}\quad (\text{A-193})$$

The extensive Gibbs energy can be derived from the definition of ΔG_{mix} .

$$\Delta G_{\text{mix}} = G - (n_{\text{AC}}\mu_{\text{AC}}^0 + n_{\text{AD}}\mu_{\text{AD}}^0 + n_{\text{BC}}\mu_{\text{BC}}^0 + n_{\text{BD}}\mu_{\text{BD}}^0)/z_1 \quad (\text{A-194})$$

Therefore,

$$\begin{aligned}G &= (n_{\text{AC}}\mu_{\text{AC}}^0 + n_{\text{AD}}\mu_{\text{AD}}^0 + n_{\text{BC}}\mu_{\text{BC}}^0 + n_{\text{BD}}\mu_{\text{BD}}^0)/z_1 \\ &\quad + NRT(x\ln x + (1-x)\ln(1-x) + y\ln y + (1-y)\ln(1-y))\end{aligned}\quad (\text{A-195})$$

The chemical potential of the binary compound components can be derived by substituting equation (A-195) in equation (A-153).

$$\mu_{ij} = \mu_{ij}^0 + RT \ln (N_i N_j / N^2) \quad (\text{A-196})$$

Therefore,

$$\mu_{\text{AC}} = \mu_{\text{AC}}^0 + RT \ln((1-x)(1-y)) \quad (\text{A-197})$$

$$\mu_{\text{BC}} = \mu_{\text{BC}}^0 + RT \ln(x(1-y)) \quad (\text{A-198})$$

$$\mu_{AD} = \mu_{AD}^0 + RT \ln((1-x)y) \quad (A-199)$$

$$\mu_{BD} = \mu_{BD}^0 + RT \ln(xy) \quad (A-200)$$

With equations (A-197 to A-200), the activity of the binary compound components can be derived by its definition of equation (A-161).

$$a_{ij} = (N_i N_j / N^2) \quad (A-201)$$

$$a_{AC} = (1-x)(1-y) \quad (A-202)$$

$$a_{BC} = x(1-y) \quad (A-203)$$

$$a_{AD} = (1-x)y \quad (A-204)$$

$$a_{BD} = xy \quad (A-205)$$

Strictly Regular Solution Model

The definition of a strictly regular solution model is best described in the case of a binary mixture. Suppose the binary mixture comprises 1 and 2, with x being the molar fraction of component 1. The strictly regular solution model assumes random mixing of the two constituent components and interaction between the neighboring unlike molecules only. Suppose the volume of mixing is also negligible, then the entropy and enthalpy of mixing of N moles of the binary mixture can be expressed as follows.

$$\Delta S_{\text{mix}} = -NR (x \ln x + (1-x) \ln(1-x)) \quad (A-206)$$

$$\Delta H_{\text{mix}} = \Omega_{12} N x(1-x), \quad (\text{A-207})$$

where Ω_{12} is the interaction parameter between component 1 and 2. The interaction parameter can be a function of temperature (an assumption used in the simple solution model) or a function of composition (an assumption used in the generalized regular solution model), the strictly regular solution model dictates that the interaction parameter is assumed to be a constant value and the mixture property is symmetrical.

Jordan [21] derived the activity coefficients for strictly regular multi-component solutions in a convenient form for Gibbs energy of mixing, and also reported detailed expressions of activity coefficients in quaternary mixtures. But, it was Ilegems and Panish [22] who used the concept of regular solution for the application in type $A_{1-x}B_xC_{1-y}D_y$ solid solution.

If treated as a strictly regular solution, the quaternary solid $A_{1-x}B_xC_{1-y}D_y$ can be considered as a pseudobinary mixture of its ternary components, $AC_{1-y}D_y$ and $BC_{1-y}D_y$, or $A_{1-x}B_xD$. In terms of $AC_{1-y}D_y$ and $BC_{1-y}D_y$,

$$\begin{aligned} G = & N \left((1-x) \mu_{AC_{1-y}D_y}^0 + x \mu_{BC_{1-y}D_y}^0 \right) + \\ & N(x(1-x)\Omega_{AC_{1-y}D_y-BC_{1-y}D_y}) + \\ & NRT (x \ln x + (1-x) \ln(1-x)) \end{aligned} \quad (\text{A-208})$$

Or, in terms of $A_{1-x}B_xC$ and $A_{1-x}B_xD$,

$$G = N((1-y) \mu_{A_{1-x}B_xC}^0 + y \mu_{A_{1-x}B_xD}^0) +$$

$$N (y(1-y)\Omega_{A_{1-x}B_xC-A_{1-x}B_xD}) +$$

$$NRT (y\ln y + (1-y)\ln(1-y)) \quad (A-209)$$

The four ternary components can be considered again as pseudobinary mixtures of their binary components, and the chemical potential can be derived by strictly regular solution approach as follows:

$$\mu_{AC_{1-y}D_y}^0 = (1-y) \mu_{AC}^0 + y \mu_{AD}^0 + y(1-y) \Omega_{AC-AD}$$

$$+ RT (y\ln y + (1-y)\ln(1-y)) \quad (A-210)$$

$$\mu_{BC_{1-y}D_y}^0 = (1-y) \mu_{BC}^0 + y \mu_{BD}^0 + y(1-y) \Omega_{BC-BD}$$

$$+ RT (y\ln y + (1-y)\ln(1-y)) \quad (A-211)$$

$$\mu_{A_{1-x}B_xC}^0 = (1-x) \mu_{AC}^0 + x \mu_{BC}^0 + x(1-x) \Omega_{AC-BC}$$

$$+ RT (x\ln x + (1-x)\ln(1-x)) \quad (A-212)$$

$$\mu_{A_{1-x}B_xD}^0 = (1-x) \mu_{AD}^0 + x \mu_{BD}^0 + x(1-x) \Omega_{AD-BD}$$

$$+ RT (x\ln x + (1-x)\ln(1-x)) \quad (A-213)$$

If the interaction parameters between ternary components are assumed to obey the linear relationship,

$$\Omega_{AC_{1-y}D_y-BC_{1-y}D_y} = (1-y) \Omega_{AC-BC} + y \Omega_{AD-BD} \quad (A-214)$$

$$\Omega_{A_{1-x}B_xC-A_{1-x}B_xD} = (1-x) \Omega_{AC-AD} + x \Omega_{BC-BD} \quad (A-215)$$

Then, substitution of equations (A-210 and A-211) in equation (A-208) and substitution of equations (A-212 and A-213) in equation (A-209) result in the same equation.

$$\begin{aligned}
 G = & N((1-x)(1-y) \mu_{AC}^0 + (1-x)y \mu_{AD}^0 + x(1-y) \mu_{BC}^0 + xy \mu_{BD}^0 \\
 & + \Omega_{AC-AD} (1-x)(1-y)y + \Omega_{BC-BD} x(1-y)y + \Omega_{AD-BD} x(1-x)(1-y) \\
 & + \Omega_{AC-BC} x(1-x)(1-y) RT (x \ln x + (1-x) \ln(1-x) + y \ln y + (1-y) \ln(1-y)))
 \end{aligned}
 \tag{A-216}$$

Chemical potential of binary components can be derived from equation (A-153) by applying equation (A-216).

$$\begin{aligned}
 \mu_{AC} = & \mu_{AC}^0 + xy \Delta \mu^0 + RT \ln(1-x)(1-y)) + \Omega_{AC-AD} y(x+y-2xy) \\
 & + \Omega_{AC-BC} x(x+y-2xy) + \Omega_{BC-BD} xy(2y-1) + \Omega_{AD-BD} xy(2x-1)
 \end{aligned}
 \tag{A-217}$$

$$\begin{aligned}
 \mu_{AD} = & \mu_{AD}^0 - x(1-y) \Delta \mu^0 + RT \ln(1-x)y) + \Omega_{AC-AD} (1-y)(1-x-y+2xy) \\
 & + \Omega_{AC-BC} x(1-y)(2x-1) + \Omega_{BC-BD} x(1-y)(1-2y) + \Omega_{AD-BD} x(1-x-y+2xy)
 \end{aligned}
 \tag{A-218}$$

$$\begin{aligned}
 \mu_{BC} = & \mu_{BC}^0 - (1-x)y \Delta \mu^0 + RT \ln(x(1-y)) + \Omega_{AC-AD} (1-x)y(2y-1) \\
 & + \Omega_{AC-BC} (1-x)(1-x-y+2xy) + \Omega_{BC-BD} y(1-x-y+2xy) + \Omega_{AD-BD} (1-x)y(1-2x)
 \end{aligned}
 \tag{A-219}$$

$$\begin{aligned}
 \mu_{BD} = & \mu_{BD}^0 + (1-x)(1-y) \Delta \mu^0 + RT \ln(xy) + \Omega_{AC-AD} (1-x)(1-y)(1-2y) \\
 & + \Omega_{AC-BC} (1-x)(1-y)(1-2x) + \Omega_{BC-BD} (1-y)(x+y-2xy) + \Omega_{AD-BD} (1-x)(x+y-2xy)
 \end{aligned}
 \tag{A-220}$$

where

$$\Delta\mu^0 = \mu_{AD}^0 + \mu_{BC}^0 - \mu_{AC}^0 - \mu_{BD}^0 \quad (\text{A-221})$$

Activity of the binary components can be readily derived from equations (A-217) to A-220) straightforwardly and will not be elaborated here.

Delta Lattice Parameter Model

The Gibbs energy is considered to be equal to the Helmholtz energy, F , for condensed phases. The extensive Helmholtz energy can be derived from statistical thermodynamics by the partition function Z

$$G = F = -kT \ln Z \quad (\text{A-222})$$

where the partition function Z is given as

$$Z = \sum_i q_i \exp(-E_i/kT) \quad (\text{A-223})$$

where q_i is the number of distinguishable configurations with the same potential energy E_i .

Consider N moles of quaternary $A_{1-x}B_xC_{1-y}D_y$ mixture with lattice molecules of a single potential energy E_s , then

$$F = -kT \ln q_s + E_s = -TS_c + E_s \quad (\text{A-224})$$

where S_c is the configurational entropy. From the equation above, clearly S_c is equal to $k \ln q_s$.

For the quaternary solid solution with randomly distributed anions and cations on their sublattices,

$$S_c = k \ln \left(\frac{(N N_0)!}{(N N_0 x)! (N N_0 (1-x))!} \frac{(N N_0)!}{(N N_0 y)! (N N_0 (1-y))!} \right) \quad (\text{A-225})$$

where N_0 is the Avogadro's number. Using Stirling's approximation, equation (A-225) becomes

$$S_c = -NR (x \ln x + (1-x) \ln(1-x) + y \ln y + (1-y) \ln(1-y)) \quad (\text{A-226})$$

Since the bonding energy in semiconductors is linearly dependent on the band-gap energy and the work of Philips and Van Vetchen [23] suggested that the average bandgap energy varies with lattice parameter a_0 in III-V semiconductors according to the relationship,

$$E_g \text{ (bandgap energy)} \propto a_0^{-2.5} \quad (\text{A-227})$$

Therefore, Stringfellow [24] proposed that the enthalpy of atomization, H_{at} , (and the bonding energy) can be approximated by

$$H_{at} = K a_0^{-2.5} \quad (\text{A-228})$$

K , in the above equation, is a proportionality constant. Furthermore, if the infinitely distant atoms represent the zero potential energy state, the potential energy, E_g , of the crystal lattice is simply $-H_{at}$, or

$$E_s = 0 - H_{at} = -K a_0^{-2.5} \quad (A-229)$$

The lattice parameter of a quaternary III-V compound has usually been assumed to obey Vegard's law, therefore

$$a_0 = a_{AC}(1-x)(1-y) + a_{AD}(1-x)y + a_{BC}x(1-y) + a_{BD}xy \quad (A-230)$$

Substituting equation (A-230) for a_0 in equation (A-229) and combining equations (A-229 and A-226) with equation (A-224) results in the expression for the extensive free energy function, F

$$F = -K(a_{AC}(1-x)(1-y) + a_{AD}(1-x)y + a_{BC}x(1-y) + a_{BD}xy)^{-2.5} \quad (A-231) \\ + NRT (x \ln x + (1-x) \ln(1-x) + y \ln y + (1-y) \ln(1-y)).$$

The chemical potential of the binary components is derived from its definition.

$$\mu_{AC} = -K a_0^{-2.5} + 2.5 K a_0^{-3.5} (-x \Delta a_B - y \Delta a_D + 2xy \Delta a) \quad (A-232) \\ + RT \ln((1-x)(1-y))$$

$$\mu_{AD} = -K a_0^{-2.5} + 2.5 K a_0^{-3.5} (-x \Delta a_B + (1-y) \Delta a_D + x(2y-1) \Delta a) \quad (A-233) \\ + RT \ln(1-x)y)$$

$$\mu_{BC} = -K a_0^{-2.5} + 2.5 K a_0^{-3.5} ((1-x) \Delta a_B + y \Delta a_D + y(2x-1) \Delta a) \quad (A-234) \\ + RT \ln(x(1-y))$$

$$\mu_{BD} = -K a_0^{-2.5} + 2.5 K a_0^{-3.5} ((1-x) \Delta a_B + (1-y) \Delta a_D + (2xy-x-y) \Delta a) \quad (A-235) \\ + RT \ln(xy)$$

where

$$\Delta a_B = a_{BC} - a_{AC} \quad (\text{A-236})$$

$$\Delta a_D = a_{AD} - a_{AC} \quad (\text{A-237})$$

$$\Delta a = a_{AD} + a_{BC} - a_{AC} - a_{BD} \quad (\text{A-238})$$

To derive the activity of the binary component, the standard chemical potential μ_{ij}^0 of pure component ij is required. μ_{ij}^0 can be derived as special cases of equation (A-231) by assigning the quaternary composition (x, y) to be those in the binary compound, e.g.,

$$\mu_{AC}^0 = -K a_{AC}^{-2.5} \quad (\text{A-239})$$

The activity a_{BD} is derived as

$$a_{AC} = (1-x)(1-y) \exp \left(\frac{K(a_{AC}^{-2.5} - a_0^{-2.5}) + 2.5Ka_0^{-3.5}(2xy\Delta a - x\Delta a_B - y\Delta a_D)}{RT} \right) \quad (\text{A-240})$$

The DLP model has been found to be successful in predicting the magnitude of interaction parameters in III-V ternary (pseudobinary) compound systems and has also been used extensively in complex chemical equilibrium calculation of III-V quaternary compound systems.

First Order Quasi-Chemical Model

The ideal solution model, the strictly regular solution model and the DLP model all assumed random distribution of constituent atoms on both sublat-

tices. That is, the arrangement of group III atoms on group-III sublattice sites is independent with that of group V atoms on group-V sublattice sites. The quasi-chemical models discard the random distribution assumption by taking into account the preferential occupation of lattice sites by short range clustering of like-atoms. The short range clustering occurs because it reduces the number of neighboring unlike atom pairs and results in decreased enthalpy of mixing and lowered total free energy. As pointed out in equations (A-172 to A-174), the distribution of the number of nearest neighbor pairs is not uniquely determined by the apparent solid solution composition (x, y), but also affected by the minimization of free energy (A-188) or equation (A-190)) due to short range clustering.

Onabe [25] described the second nearest neighbor pair distribution as a function of the (first) nearest neighbor pair distribution on the basis of the Bethe lattice model, neglecting the quasi-chemical nature of the second nearest neighbor pair distribution, and developed the first-order quasi-chemical model for quaternary III-V compound systems of the $A_{1-x}B_xC_{1-y}D_y$ type.

The number of second nearest neighbor pairs of like atoms is

$$n_{iji} = \frac{z_2}{2} \frac{z_1^2}{z_1^2} \frac{n_{ij}^2}{N_j} \quad (i=A,B \text{ and } j=C,D; \text{ or } i=C,D \text{ and } j=A,B), \quad (\text{A-241})$$

where z_2 (=12) is the number of second nearest neighbor pairs for an atom in the zinc-blende lattice structure. And the number of second nearest neighbor pairs of unlike atoms is

$$n_{ijk} = \frac{z_2}{2} \frac{n_{kj}}{z_1^2} \frac{n_{ij}}{N_j} \quad (i=A,B \text{ and } j=C,D; \text{ or } i=C,D \text{ and } j=A,B) \quad (\text{A-242})$$

For example,

$$n_{ACA} = \frac{z_2}{2 z_1^2} \frac{n_{AC}^2}{N_C} \quad (A-243)$$

$$n_{ACB} = \frac{z_2}{z_1^2} \frac{n_{BC} n_{AC}}{N_C} \quad (A-244)$$

Denoting the interaction energy of (first) nearest neighbor pairs AC, AD, BC and BD by v_{AC} , v_{AD} , v_{BC} and v_{BD} , and the interaction energy of second nearest neighbor pairs ACA, ACB, etc. by v_{ACA} , v_{ACB} , etc., the potential energy of the quaternary solid solution can be derived as

$$\begin{aligned} E_s = & v_{AC} n_{AC} + v_{AD} n_{AD} + v_{BC} n_{BC} + v_{BD} n_{BD} + \\ & v_{ACA} n_{ACA} + v_{ADA} n_{ADA} + v_{BCB} n_{BCB} + v_{BDB} n_{BDB} + \\ & v_{ACB} n_{ACB} + v_{ADB} + v_{ADB} n_{ADB} + v_{CA_C} n_{CA_C} + v_{CB_C} n_{CB_C} + \\ & v_{DA_D} n_{DA_D} + v_{DB_D} n_{DB_D} + v_{CA_D} n_{CA_D} + v_{CB_D} n_{CB_D} \end{aligned} \quad (A-245)$$

Since the potential energy of (n_{ij}/z_1) moles of binary ij compound ($i=A,B$ and $j=C,D$) is

$$E_{ij} = v_{ij} n_{ij} + (v_{iji} + v_{jij}) (z_2/2z_1) n_{ij} \quad (A-246)$$

The interaction parameter in the ternary (pseudobinary) solid solutions can be considered as the difference between unlike atoms and like atoms, therefore

$$\Omega_{AB-AC} = N_0 z_2 (v_{ACB} - (v_{ACA} + v_{BCB})/2) \quad (A-247)$$

$$\Omega_{AD-BD} = N_0 z_2 (v_{ADB} - (v_{ADA} + v_{BDB})/2) \quad (A-248)$$

$$\Omega_{AC-AD} = N_0 z_2 (v_{CAD} - (v_{CAC} + v_{DAD})/2) \quad (A-249)$$

$$\Omega_{BC-BD} = N_0 z_2 (v_{CBD} - (v_{CBC} + v_{DBD})/2) \quad (A-250)$$

Rearranging equation (A-245) with the use of equations (A-246 to A-250) results in

$$\begin{aligned} E_s = & E_{AC} n_{AC} + E_{AD} n_{AD} + E_{BC} n_{BC} + E_{BD} n_{BD} + \Omega_{AC-BC} \left(\frac{1}{z_1 N_0} \frac{n_{AC} n_{BC}}{n_{AC} + n_{BC}} \right) \\ & + \Omega_{AD-BD} \left(\frac{1}{z_1 N_0} \frac{n_{AD} n_{BD}}{n_{AD} + n_{BD}} \right) + \Omega_{AC-AD} \left(\frac{1}{z_1 N_0} \frac{n_{AC} n_{AD}}{n_{AC} + n_{AD}} \right) \\ & + \Omega_{BC-BD} \left(\frac{1}{z_1 N_0} \frac{n_{BC} n_{BD}}{n_{BC} + n_{BD}} \right) \end{aligned} \quad (A-251)$$

The configurational entropy S_c takes the following form,

$$\begin{aligned} S_c = & -k \ln q \\ = & -k \left(\ln \frac{(z_1 N_0)!}{n_{AC}! n_{AD}! n_{BC}! n_{BD}!} + \ln \frac{N_0! N_0!}{N_A! N_B! N_C! N_D!} \right. \\ & \left. - \ln \frac{n_{AC}^0! n_{AD}^0! n_{BC}^0! n_{BD}^0!}{(z_1 N_0)!} \right) \end{aligned} \quad (A-252)$$

where q is the degeneracy factor and n_{ij}^0 's represent n_{ij} at completely random distribution.

$$n_{ij}^0 = z_1 \frac{N_i N_j}{N_0} \quad (\text{A-253})$$

With the potential energy, E_g , in equation (A-251) and the configurational entropy, S_c , in equation (A-252), the Helmholtz free energy can be readily obtained. The chemical potential of the binary components can be derived from its definition in equation (A-251):

$$\begin{aligned} \mu_{AC} = & \mu_{AC}^0 + RT \ln((1-x)(1-y)) + z_1 RT \ln\left(\frac{x_{AC}}{(1-x)(1-y)}\right) \\ & + \Omega_{AC-BC} \frac{x_{BC}^2}{(1-y)^2} + \Omega_{AC-AD} \frac{x_{AD}^2}{(1-x)^2} \end{aligned} \quad (\text{A-254})$$

$$\begin{aligned} \mu_{AD} = & \mu_{AD}^0 + RT \ln((1-x)y) + z_1 RT \ln\left(\frac{x_{AD}}{(1-x)y}\right) \\ & + \Omega_{AD-BD} \frac{x_{BD}^2}{y^2} + \Omega_{AC-AD} \frac{x_{AC}^2}{(1-x)^2} \end{aligned} \quad (\text{A-255})$$

$$\begin{aligned} \mu_{BC} = & \mu_{BC}^0 + RT \ln(x(1-y)) + z_1 RT \ln\left(\frac{x_{BC}}{x(1-y)}\right) \\ & + \Omega_{AC-BC} \frac{x_{AC}^2}{(1-y)^2} + \Omega_{BC-BD} \frac{x_{BD}^2}{x^2} \end{aligned} \quad (\text{A-256})$$

$$\mu_{BD} = \mu_{BD}^0 + RT \ln(xy) + z_1 RT \ln\left(\frac{x_{BD}}{xy}\right) + \Omega_{AD-BD} \frac{x_{AD}^2}{y^2} + \Omega_{BC-BD} \frac{x_{BC}^2}{x^2} \quad (\text{A-257})$$

The activity of the binary components is again readily derivable from equations (A-254 to A-257) and the definition of activity in equation (A-161). For example,

$$a_{BD} = xy \left(\frac{x_{BD}}{xy}\right) z_1 \exp\left(\frac{\Omega_{AD-BD}}{RT} \frac{x_{AD}^2}{y^2} + \frac{\Omega_{BC-BD}}{RT} \frac{x_{BC}^2}{x^2}\right) \quad (\text{A-258})$$

To calculate the activity of the binary components requires knowledge of the nearest neighbor pair distribution X_{AC} , X_{AD} , X_{BC} and X_{BD} . This can be done by solving equations (A-172 to A-174 and A-190) simultaneously. Plugging equations (A-254 to A-257) into equation (A-190) results in

$$z_1 RT \ln\left(\frac{X_{AC} X_{BD}}{X_{AD} X_{BC}}\right) = \Omega_{AC-BC} \frac{X_{AC}^2 - X_{BC}^2}{(1-y)^2} + \Omega_{AC-AD} \frac{X_{AC}^2 - X_{AD}^2}{(1-x)^2} \\ + \Omega_{BC-BD} \frac{X_{BD}^2 - X_{BC}^2}{x^2} + \Omega_{AD-BD} \frac{X_{BD}^2 - X_{AD}^2}{y^2} + \Delta\mu^0 \quad (A-259)$$

The superscript 0 in the equation (A-259) has been defined in equation (A-221). Equations of mass conservation are obtained by applying equation (A-182) in equations (A-172 to A-174).

$$X_{AD} + X_{AC} = 1-x \quad (A-260)$$

$$X_{BC} + X_{AC} = 1-y \quad (A-261)$$

$$X_{BD} - X_{AC} = x+y-1 \quad (A-262)$$

The distribution of the nearest neighbor pairs is determined by equations (A-259 to A-262).

When the apparent solid solution (x,y) of a type $A_{1-x}B_xC_{1-y}C_y$ III-V quaternary compound is specified, the activity of the binary components can be calculated by firstly solving for $(X_{AC}, X_{AD}, X_{BC}, X_{BD})$, followed by the direct calculation through the use of equations (A-254 to A-257) and equation (A-161).

A.3. Process Controllability and Optimum Operation Condition Issues

The growth of quaternary $\text{In}_{1-x}\text{Ga}_x\text{As}_y\text{P}_{1-y}$ by hydride VPE is a complex process. Since the desired band gap energy and the preferred lattice matching condition are controlled by the composition of the grown compound, composition control is of primary concern for hydride VPE users. Composition control is usually achieved in the process development stage by empirical tuning of process parameters, in conjunction with complex chemical equilibrium calculations. This approach, although not ideal, has nevertheless been successful enough to make the hydride VPE a viable process for industrial development and production of $\text{In}_{1-x}\text{Ga}_x\text{As}_y\text{P}_{1-y}$ heterostructures.

The empirical tuning method, which involves tedious procedural trial-and-error runs, is quite expensive and time-consuming. Intelligent maneuvering is crucial to obtaining fruitful results in this type of process development. The drawback of this empirical method has been that the result obtained from one system is often not directly applicable to another reactor system. In order to render the results more tractable, complex chemical equilibrium calculations have been used to predict and compare with the process behavior. Complex chemical equilibrium calculations have been reported capable of predicting solid solution composition in VPE growth of some III-V compounds. But, in general, this theoretical approach has not been able to make accurate predictions for the growth of InGaAsP solutions. The reason is simply that, although hydride VPE is a thermodynamically driven process, the process behavior can still be significantly affected by mass transfer and chemical reaction kinetics. Therefore, complex chemical equilibrium calculations, at best, give a qualitative description of process performance. Quantitative prediction is very difficult when each epitaxial reactor is designed and operated differently and the magnitude of mass transfer and kinetic effects varies.

Another problem that undermines the creditability of complex chemical equilibrium calculations is that the result of the calculation is sensitive to the choice of thermochemical data and solid solution model, which are required to initiate the calculation. Although sometimes it is possible to explain a set of experimental results by using a particular set of thermochemical data and solid solution model, the reverse exercise is usually unsatisfactory. At the present time, some important thermochemical data that are needed in the complex chemical equilibrium calculation for the hydride VPE of $\text{In}_{1-x}\text{Ga}_x\text{As}_y\text{P}_{1-y}$ are still being refined and different solid solution models are being tested for compatibility with the $\text{In}_{1-x}\text{Ga}_x\text{As}_y\text{P}_{1-y}$ solution system, therefore there is no reason to expect accurate description of process behavior by complex chemical equilibrium calculation.

In the practice of empirical tuning of process parameters, engineers observe (1) how process results change with respect to incremental setpoint change of each and every one of the process parameters, (2) the fluctuation of process parameters around their setpoints during a process run and the effects on process results, and (3) how setpoint changes affect the observations of (1) and (2). The first observation can be termed "the process sensitivity to process parameters." Since all the process parameters are interrelated, their influences on process behavior are not totally independent. "Process parameter sensitivity network" is determined from the first observation. The second observation, "the process parameter value fluctuation," is a inevitable result of process controllers' control mechanisms compounded with the changing nature of process mechanics. If the composition of the resulted epitaxial film is of primary importance, then the observations centered upon the compositional variation should be conducted. That is, we should try to determine the "compositional" process parameter sensitivity network and the magnitude

and effect of process parameter value fluctuation on "compositional control." The third and last observation is to resolve the optimum operating condition for the objective of controllability of intended process results. For the development of hydride VPE of $\text{In}_{1-x}\text{Ga}_x\text{As}_y\text{P}_{1-y}$, this observation primarily involves the determination of compositional process parameter sensitivity network and process parameter value fluctuations at various sets of process parameter setpoints.

Specifically in hydride VPE of $\text{In}_{1-x}\text{Ga}_x\text{As}_y\text{P}_{1-y}$ there are fourteen process parameters, $F_{\text{H}_2}^{(\text{Ga})}$, $F_{\text{HCl}}^{(\text{Ga})}$, $T_{\text{S}}(\text{Ga})$, $e(\text{Ga})$, $F_{\text{H}_2}^{(\text{In})}$, $F_{\text{HCl}}^{(\text{In})}$, $T_{\text{S}}(\text{In})$, $e(\text{In})$, $F_{\text{H}_2}^{(\text{m})}$, $F_{\text{AsH}_3}^{(\text{m})}$, $F_{\text{PH}_3}^{(\text{m})}$, T_{m} , T_{d} and P_{tot} . It is clear that because of the large number of process parameters, a large body of experimental runs have to be performed for the practice of empirical tuning of process parameters, which is extremely cumbersome and undesirable. What is proposed and reported in the remaining of this appendix is to apply complex chemical equilibrium calculation to simulate the empirical tuning exercise. The objective is to determine the interdependencies between process parameters, to pinpoint the most influential process parameters and to reveal the direction for the search of optimum operating conditions. With the result of such a theoretical analysis, valuable information is obtained cheaply and speedily through computer calculation and a significantly smaller body of experiments has to be conducted for compositional control studies.

The proposed approach, named "process controllability evaluation (PCE) by complex chemical equilibrium calculation," is a sound one, although it has been argued in the above that complex chemical equilibrium calculation does not accurately describe the process performance and the ambiguity related to the choice of thermodynamic data and solid solution model exists. The reason is simple, because this approach merely tries to determine the relative

merits, not the exact influence on process results, of the process parameters. It is a qualitative approach and the choice of thermochemical data and solid solution model has only slight effect on the obtained information.

In the following sections, the inter-dependencies of process parameters will be reviewed first, followed by the definitions and elaborate discussion on the ingredients in the process controllability evaluation, namely, compositional sensitivity to equilibrium parameter, range of equilibrium parameter value fluctuation and quantitative representation of process controllability. Two PCE studies are also reported in this report, deposition of $\text{In}_{.53}\text{Ga}_{.47}\text{As}$ on InP , and $\text{In}_{.74}\text{Ga}_{.26}\text{As}_{.56}\text{P}_{.44}$ on InP . Based on the results presented in these studies, the practicality of growing these ternary and quaternary compounds by hydride VPE at the studied conditions is discussed. To improve process controllability, optimum, or better, process conditions should be searched. The method of analysis aimed at elucidating the direction of search for optimum operating conditions is presented in the last section of this report. The method, readily applied to the two studied growth systems, give invaluable insight to the choice of operating conditions to gain compositional control.

A.3.1. Interdependence of Process Parameters in Hydride VPE of InGaAsP

The number of degrees of freedom in the deposition zone for the growth of InGaAsP by hydride VPE is seven. Depending upon subjective preference, different "equilibrium parameters" can be used to initiate a complex chemical equilibrium calculation. One such set of seven equilibrium parameters has been conveniently chosen and shall be used for the remaining of the discussion, namely,

T (deposition temperature)

P_{tot} (total system pressure)

Cl/H (chlorine to hydrogen ratio)

III/H (group III to hydrogen ratio)

V/H (group V to hydrogen ratio)

Ga/III (gallium to group III ratio)

As/V (arsenic to group V ratio)

Also there are fourteen process parameters in the hydride VPE of $In_{1-x}Ga_xAs_yP_{1-y}$.

$xGa_xAs_yP_{1-y}$.

$F_{H_2}^{(Ga)}$ (hydrogen flowrate in gallium source zone)

$F_{HCl}^{(Ga)}$ (HCl flowrate in gallium source zone)

$T_s(Ga)$ (gallium source zone temperature)

$e(Ga)$ (reaction efficiency factor in Ga source zone)

$F_{H_2}^{(In)}$ (hydrogen flowrate in indium source zone)

$F_{HCl}^{(In)}$ (HCl flowrate in indium source zone)

$T_s(In)$ (indium source zone temperature)

$e(In)$ (reaction efficiency factor in indium source zone)

$F_{H_2}^{(m)}$ (hydrogen input flowrate in mixing zone)

$F_{AsH_3}^{(m)}$ (arsine input flowrate in mixing zone)

$F_{PH_3}^{(m)}$ (phosphine input flowrate in mixing zone)

T_m (mixing zone temperature)

T_d (deposition zone temperature)

P_{tot} (system total pressure)

Since the degrees of freedom are less than the number of process parameters, it is self-evident that these process parameters must influence process behavior collectively. Therefore the fourteen process parameters are interdependent and can be lumped together to form a set of seven independent functional groups. If using the seven equilibrium parameters as the functional groups, then the interdependence of the fourteen process parameters can be resolved by determining the dependence of equilibrium parameters on process parameters. The interdependence of the process parameters can be written as follows.

$$A_d = (Cl/H) = \frac{F_{HCl}^{(Ga)} + F_{HCl}^{(In)}}{\{(2F_{H_2}^{(Ga)} + 2F_{H_2}^{(In)} + 2F_{H_2}^{(m)} + F_{HCl}^{(Ga)} + F_{HCl}^{(In)} + 3F_{AsH_3}^{(m)} + 3F_{PH_3}^{(m)})\}} \quad (A-263)$$

$$B1_d + B2_d = (III/H) = \frac{F_{HCl}^{(Ga)} e^{(Ga)} + F_{HCl}^{(In)} e^{(In)}}{\{2F_{H_2}^{(Ga)} + 2F_{H_2}^{(In)} + 2F_{H_2}^{(m)} + F_{HCl}^{(Ga)} + F_{HCl}^{(In)} + 3F_{AsH_3}^{(m)} + 3F_{PH_3}^{(m)}\}} \quad (A-264)$$

$$C1_d + C2_d = (V/H) = \frac{F_{AsH_3}^{(m)} + F_{PH_3}^{(m)}}{\{(2F_{H_2}^{(Ga)} + 2F_{H_2}^{(In)} + 2F_{H_2}^{(m)} + F_{HCl}^{(Ga)} + F_{HCl}^{(In)} + 3F_{AsH_3}^{(m)} + 3F_{PH_3}^{(m)})\}} \quad (A-265)$$

$$(Ga/III) = \frac{F_{HCl}^{(Ga)} e^{(Ga)}}{F_{HCl}^{(Ga)} e^{(Ga)} + F_{HCl}^{(In)} e^{(In)}} \quad (A-266)$$

$$(As/V) = \frac{F_{AsH_3}^{(m)}}{F_{AsH_3}^{(m)} + F_{PH_3}^{(m)}} \quad (A-267)$$

$$T = T_d \quad (A-268)$$

$$P_{\text{tot}} = P_{\text{tot}} \quad (\text{A-269})$$

In the above equations, the left hand side terms are the equilibrium parameters and the right hand side terms are the lumped groups of process parameters. The process parameters involved in the same lumped group are dependent in deciding process outcome.

A.3.2. Compositional Sensitivity

Define "process sensitivity to parameters" as the change of process results with respect to parameter setpoint change. If the composition of the solid solution $\text{In}_{1-x}\text{Ga}_x\text{As}_y\text{P}_{1-y}$ is chosen as the process result and the parameters are chosen to be equilibrium parameters T , P_{tot} , Cl/H , III/H , V/H , Ga/III , and As/V , then, the definition of "compositional sensitivity to equilibrium parameters" can be succinctly expressed in mathematical forms as follows.

compositional sensitivity to temperature T : dx/dT , dy/dT

compositional sensitivity to pressure P_{tot} : $dx/d(\ln P_{\text{tot}})$, $dy/d(\ln P_{\text{tot}})$

compositional sensitivity to Cl/H ratio: $dx/d(\ln \text{Cl}/\text{H})$, $dy/d(\ln \text{Cl}/\text{H})$

compositional sensitivity to III/H ratio: $dx/d(\ln \text{III}/\text{H})$, $dy/d(\ln \text{III}/\text{H})$

compositional sensitivity to V/H ratio: $dx/d(\ln \text{V}/\text{H})$, $dy/d(\ln \text{V}/\text{H})$

compositional sensitivity to Ga/III ratio: $dx/d(\text{Ga}/\text{III})$, $dy/d(\text{Ga}/\text{III})$

compositional sensitivity to As/V ratio: $dx/d(\text{As}/\text{V})$, $dy/d(\text{As}/\text{V})$

where dx/dA and dy/dA are derivatives of compositional dependence on equilibrium parameter A , and $dx/d(\ln B)$ and $dy/d(\ln B)$ are derivatives of composi-

tional dependence on the natural logarithm of equilibrium parameter B . The form of the differential dA or $d(\ln B)$ is chosen according to the expression for parameter fluctuation, which is to be discussed in the following sections. Note that the sensitivities can be evaluated for a chosen set of setpoints, or a particular operating condition, and these values change accordingly when setpoints are changed.

A.3.4. Parameter Value Fluctuation

The parameter values during a process run are not expected to obey their setpoints at all times. Ideal process controllers, which adjust parameter values to their setpoints at zero time transient, do not exist. Therefore, when the parameter values are different from their setpoints, a certain time period will elapse before the setpoints are reached. In fact, for almost all cases, the process parameter values do not really reach the setpoints, but oscillate around the intended setpoints. Depending upon the process control mechanisms, the range of fluctuation from the setpoint varies. Besides the fluctuation associated with the non-ideality of the process controllers, the process parameter values can change instantaneously during process operation even when no changes are made on the setpoints. One good example is the flowrate fluctuation during valve turn-on/turn-off cycles. The sudden change of process mechanics at a valve turn-on/turn-off cycle will change the established pressure difference across the flow controllers resulting in drastic increase or decrease of flowrates in the influenced gaslines. It should be pointed out that this is a problem of concern in all types of VPE techniques for heterostructure growth, since in the continuous growth of a heterostructure, it is unavoidable to have valve turn-on/turn-off cycles at the juncture of interphasing when a few reactant gasflows have to be interchanged between

the reactor and the bypass. The range of equilibrium parameter value fluctuation is defined as the maximum difference of equilibrium parameter value and its setpoint during the process runtime when the interested process results can be influenced by the fluctuation. In hydride VPE of InGaAsP, the interested process results are the solid solution composition x and y , and it is the range of equilibrium parameter value fluctuation during "deposition" which is of primary concern. The range of equilibrium parameter value fluctuation can also be represented as follows.

range of temperature fluctuation: dT

range of pressure fluctuation: $d(P_{tot})/(P_{tot})$ or $d(\ln P_{tot})$

range of Cl/H fluctuation: $d(Cl/H)/(Cl/H)$ or $d(\ln Cl/H)$

range of III/H fluctuation: $d(III/H)/(III/H)$ or $d(\ln III/H)$

range of V/H fluctuation: $d(V/H)/(V/H)$ or $d(\ln V/H)$

range of Ga/III fluctuation: $d(Ga/III)$

range of As/V fluctuation: $d(As/V)$

where dA is the absolute range of parameter value fluctuation of parameter A and $d(\ln B)$ is the natural logarithmic range of parameter value fluctuation of parameter B .

A.3.4. Process Controllability Evaluation

Process controllability is reflected by the range of process result fluctuation, which is decided by the magnitude of process sensitivity and the range of parameter value fluctuation. In fact, the larger the range of process result fluctuation, the harder the process is to control, and therefore the lower the process controllability. Define process control-

lability as the inverse of the range of process result fluctuation. For hydride VPE of InGaAsP process, the process result is the solid solution composition x , y . The range of composition fluctuation dx and dy are defined mathematically as follows:

$$\begin{array}{rclcl}
 \text{range of} & & \text{compositional} & & \text{range of} \\
 \text{compositional} & = & \text{sensitivity to} & \times & \text{equilibrium} \\
 \text{fluctuation} & & \text{equilibrium} & & \text{parameter} \\
 & & \text{parameter} & & \text{fluctuation} \\
 \\
 (dx, dy) & = & (dx/dA, dy/dA) & \times & (dA) \\
 \\
 & & \text{or} & & \text{or} \\
 & & (dx/d(\ln B), dy/d(\ln B)) & & (d(\ln B))
 \end{array}$$

And process controllability can be evaluated for each and every parameter by the above relationship.

A.4. Process Controllability Study

A.4.1. InGaAs Lattice-Matched to InP

The lattice matching composition of $\text{In}_{1-x}\text{Ga}_x\text{As}$ on InP is $x = 0.47$. Assuming $\text{As}/\text{V} = 1$, $T = 973\text{K}$, $P_{\text{tot}} = 1 \text{ atm}$, $\text{Cl}/\text{H} = \text{III}/\text{H} = \text{V}/\text{H} = 0.001$, iterative complex chemical equilibrium calculation by varying Ga/III gives the result that when $\text{Ga}/\text{III} = 0.605$, $x = 0.47$ is achieved with supersaturation $S/\text{H} = 0.53 \times 10^{-4}$.

Using the result of this calculation as a reference, compositional sensitivity to parameters T , P_{tot} , Cl/H , III/H , V/H , and Ga/III can be calculated successively by making an incremental change (1% of the parameter value of the reference state) on the input value of one parameter while holding others at constant. The result of this sensitivity calculation is as follows

parameter	sensitivity
T	$dx/dT = - 0.0141 \text{ K}^{-1}$
P_{tot}	$dx/d(\ln P_{\text{tot}}) = 0.044$
Cl/H	$dx/d(\ln \text{Cl/H}) = - 0.923 \times 10^{-9}$
III/H	$dx/d(\ln \text{III/H}) = 0.937 \times 10^{-6}$
V/H	$dx/d(\ln \text{V/H}) = 0.152 \times 10^{-14}$
Ga/III	$dx/d(\text{Ga/III}) = 6.94$

Note that compositional sensitivity is small to parameters Cl/H, III/H and V/H. The composition is quite sensitive to parameters T and P_{tot} , and extremely sensitive to Ga/III. The first-order quasi-chemical model was used in the calculations above.

The range of parameter value fluctuation is assumed to be as follows.

parameter	range of parameter value fluctuation
T	$dT = 0.5\text{K}$
P_{tot}	$d(P_{\text{tot}}) = 10\% P_{\text{tot}}$ or $d(\ln P_{\text{tot}}) = 0.1$
Cl/H	$d(\text{Cl/H}) = 10\% \text{Cl/H}$ or $d(\ln \text{Cl/H}) = 0.1$
III/H	$d(\text{III/H}) = 10\% \text{III/H}$ or $d(\ln \text{III/H}) = 0.1$
V/H	$d(\text{V/H}) = 10\% \text{V/H}$ or $d(\ln \text{V/H}) = 0.1$
Ga/III	$d(\text{Ga/III}) = 0.001$

With known values of sensitivity and range of parameter value fluctuation, the range of composition fluctuation and process controllability can be evaluated. The results are presented as follows:

parameter	range of composition fluctuation	process controllability
T	0.00705	141.8
P _{tot}	0.00440	227.3
Cl/H	0.923×10^{-10}	1.08×10^{10}
III/H	0.937×10^{-7}	1.07×10^7
V/H	0.152×10^{-5}	6.58×10^5
Ga/III	0.0694	144.1

Process controllability is small with respect to T, P_{tot}, Ga/III, and very large with respect to Cl/H, III/H, and V/H. The next step is to determine the acceptable process controllability level. For the growth of In_{1-x}Ga_xAs on InP, the composition x has to be close to 0.47 to avoid the generation of dislocations due to lattice mismatch. The allowable lattice mismatch depends upon the intended thickness of the InGaAs layer. For the growth of one micrometer thickness, composition control of mole fraction to within 0.01 is generally required. Therefore in this case the acceptable process controllability level is 1/0.01, or 100. All the parameters showed satisfactory process controllability levels.

In conclusion, the growth of InGaAs on InP at the specified operating condition with T = 973K, P_{tot} = 1 atm, Cl/H = III/H = V/H = 0.001, Ga/III = 0.605, and As/V = 1 should give satisfactory controllability on InGaAs composition. Three parameters T, P_{tot}, and Ga/III are most influential to compositional control. Process tuning should be carried out intensively around these three parameters. Note that in this study, the range of Ga/III fluctuation was assumed to be 0.001, and with such a strict requirement on the range of

fluctuation the process controllability level of this parameter was 144.1, which is just above the acceptable process controllability level (100). Therefore, reduction of the range of Ga/III fluctuation is important for successful development of InGaAs VPE by hydride method. It is clear that the equilibrium parameter Ga/III is determined by four process parameters, namely, $F_{\text{HCl}}^{(\text{Ga})}$, $e(\text{Ga})$, $F_{\text{HCl}}^{(\text{In})}$ and $e(\text{In})$. Accurate and responsive controllers should be implemented to control the input flowrates of HCl into gallium and indium source zones. Under equilibrium conditions, both of $e(\text{Ga})$ and $e(\text{In})$ are independent of temperature and very close to unity above 923K. Therefore, if the source zones are operated at equilibrium conditions, the range of fluctuation of $e(\text{Ga})$ and $e(\text{In})$ is effectively reduced to zero. Careful source zone design, eliminating any possible mass transfer or reaction kinetic influences to reach source zone equilibrium, is essential to successful development of hydride VPE for InGaAs growth on InP. Lastly, the search for better operating condition should also be centered on the reduction of the values of compositional sensitivity to the three most important parameters T , P_{tot} and Ga/III. Such a search by complex chemical equilibrium calculation has been completed for this system and will be presented in the last section of this appendix.

$$\begin{aligned}
 (\text{process controllability}) &= \frac{\text{range of composition fluctuation}^{-1}}{\text{compositional sensitivity}} \\
 &= 1/dx, 1/dy
 \end{aligned}
 \tag{A-271}$$

From the above equation, it is clear that process controllability can be improved when the sensitivity or parameter fluctuation is lowered. The value of compositional sensitivity changes with respect to parameter setpoint

changes. The process that runs at setpoints with the lowest values of compositional sensitivities is considered the optimum operating condition since the highest possible process controllability is realized. It is therefore important to search for this optimum condition. Besides changing operating conditions, process controllability can be boosted by lowering the range of parameter fluctuation. This is achieved by careful study of the origin of fluctuation followed by improved process design and process controllers.

A.4.2. InGaAsP Lattice-Matched to InP

Assuming that the lattice constant of $\text{In}_{1-x}\text{Ga}_x\text{As}_y\text{P}_{1-y}$ obeys Vegard's law, the lattice matching condition for InGaAsP on InP is that x equals to $0.47y$, $0 < y < 1$. Letting $T = 973\text{K}$, $P_{\text{tot}} = 1 \text{ atm}$, $\text{Cl}/\text{H} = \text{III}/\text{H} = \text{V}/\text{H} = 0.001$, iterative complex chemical equilibrium calculation by varying both Ga/III and As/V gives the result that when $\text{Ga}/\text{III} = 0.388$ and $\text{As}/\text{V} = 0.0039$, the composition of the quaternary compound is that $x = 0.26$, $y = 0.56$ and supersaturation $S/\text{H} = 0.55 \times 10^{-5}$.

Using the result of this calculation as a reference, compositional sensitivity to parameters T , P_{tot} , Cl/H , III/H , V/H and Ga/III can be calculated successively by making an incremental change on the input value of one parameter while holding others constant. The result of this sensitivity calculation is as follows

parameter	sensitivity	
T	$dx/dT = -0.802\text{e-}2 \text{ K}^{-1}$,	$dy/dT = 0.565\text{e-}2 \text{ K}^{-1}$
P_{tot}	$dx/d(\ln P_{\text{tot}}) = 0.142$,	$dy/d(\ln P_{\text{tot}}) = -0.199$
Cl/H	$dx/d(\ln \text{Cl}/\text{H}) = -0.3 \times 10^{-10}$	$dy/d(\ln \text{Cl}/\text{H}) = .5 \times 10^{-10}$
III/H	$dx/d(\ln \text{III}/\text{H}) = 0.335 \times 10^{-7}$,	$dy/d(\ln \text{III}/\text{H}) = -.5 \times 10^{-7}$
V/H	$dx/d(\ln \text{V}/\text{H}) = -0.120 \times 10^{-6}$,	$dy/d(\ln \text{V}/\text{H}) = 0.17 \times 10^{-6}$
Ga/III	$dx/d(\text{Ga}/\text{III}) = 2.27$,	$dy/d(\text{Ga}/\text{III}) = -0.429$
As/V	$dx/d(\text{As}/\text{V}) = -58.8$,	$dy/d(\text{As}/\text{V}) = 83.0$

Similar to the study of $\text{In}_{.53}\text{Ga}_{.47}\text{As}$ growth, compositional sensitivity is small to parameters Cl/H , III/H and V/H . The composition is quite sensitive to parameters T and P_{tot} , and extremely sensitive to Ga/III and As/V . In this calculation the incremental change of parameter input value was 1% of the parameter value of the reference state.

The range of parameter value fluctuation is assumed to be as follows

parameter	range of parameter value fluctuation
T	$dT = 0.5\text{K}$
P_{tot}	$d(P_{\text{tot}}) = 5\% P_{\text{tot}}$ or $d(\ln P_{\text{tot}}) = 0.05$
Cl/H	$d(\text{Cl}/\text{H}) = 10\% \text{Cl}/\text{H}$ or $d(\ln \text{Cl}/\text{H}) = 0.1$
III/H	$d(\text{III}/\text{H}) = 10\% \text{III}/\text{H}$ or $d(\ln \text{III}/\text{H}) = 0.1$
V/H	$d(\text{V}/\text{H}) = 10\% \text{V}/\text{H}$ or $d(\ln \text{V}/\text{H}) = 0.1$
Ga/III	$d(\text{Ga}/\text{III}) = 0.001$
As/V	$d(\text{As}/\text{V}) = 0.0001$

With known values of sensitivity and range of parameter value fluctuation, the range of composition fluctuation and process controllability can be evaluated. The results are presented as follows:

parameter	range of III-sublattice composition fluctuation dx	process controllability on composition x
T	0.00401	249.4
P_{tot}	0.00710	140.8
Cl/H	0.333×10^{-11}	3.00×10^{11}
III/H	0.335×10^{-8}	2.99×10^8
V/H	0.120×10^{-7}	8.33×10^7
Ga/III	0.00227	440.5
As/V	0.00588	170.1

parameter	range of V-sublattice composition fluctuation dy	process controllability on composition y
T	0.00282	354.6
P _{tot}	0.00995	100.5
Cl/H	0.466×10^{-11}	2.15×10^{11}
III/H	0.469×10^{-8}	2.13×10^8
V/H	0.170×10^{-7}	5.88×10^7
Ga/III	0.000423	2364.
As/V	0.00830	120.5

Process controllability is small with respect to T, P_{tot}, Ga/III, and As/V and very large with respect to Cl/H, III/H, and V/H. If an acceptable process controllability level is assumed to be 100, the same value as used in the study of In_{0.53}Ga_{0.47}As growth, all the parameters showed satisfactory process controllability levels.

In conclusion, the growth of In_{0.74}Ga_{0.26}As_{0.56}P_{0.44} on InP at the specified operating condition with T = 973K, P_{tot} = 1 atm, Cl/H = III/H = V/H = 0.001, Ga/III = 0.338, and As/V = 0.00339 should give satisfactory controllability on the growth composition of this quaternary compound. Four parameters T, P_{tot}, Ga/III, and As/V are most influential to compositional control. Extensive process tuning should be done around these four parameters. Again, strict control on the range of Ga/III and also As/V fluctuation are noted. The reduction of the range of Ga/III fluctuation has been discussed in the last case study. For quaternary compound growth, tight control on the input flow-rates of both arsine and phosphine, which determine the value of As/V, is a must for the compositional controllability on both group III and group V sublattices. The search for optimum operating condition will be discussed in the next section.

A.5. Process Sensitivity Analysis

Process controllability with respect to a parameter is determined by both the process sensitivity to the parameter and its range of fluctuation. Even with the best possible process design, the reduction of the range of parameter value fluctuation is still limited by the performance of the available controller devices. For the most influential parameters it is imperative to search for operating conditions that the very high degree of process sensitivity imposed by these parameters can be driven toward lower values. Suppose empirical tuning starts at a certain set of process parameter setpoints, engineers are often interested to know in which direction the setpoints should go to resolve a more controllable, less sensitive operating condition. If the starting set of setpoints is used as a reference state, it is interesting to observe how process sensitivities of each and every process parameter will change as a result of setpoint variations.

Denote the process sensitivity at the reference set of setpoints by subscript 0 as follows

parameter	reference process sensitivity
T	$(dx/dT)_0, (dy/dT)_0$
P_{tot}	$(dx/d(\ln P_{tot}))_0, (dy/d(\ln P_{tot}))_0$
Cl/H	$(dx/d(\ln Cl/H))_0, (dy/d(\ln Cl/H))_0$
III/H	$(dx/d(\ln III/H))_0, (dy/d(\ln III/H))_0$
V/H	$(dx/d(\ln V/H))_0, (dy/d(\ln V/H))_0$
Ga/III	$(dx/d(Ga/III))_0, (dy/d(Ga/III))_0$
As/V	$(dx/d(As/V))_0, (dy/d(As/V))_0$

Define relative sensitivity as the ratio of the process sensitivity after setpoints are varied to the process sensitivity at the reference set of setpoints. Mathematically, the relative sensitivity can be represented as in Table A-7.

Table A-7. Definition of relative sensitivity

parameter	relative sensitivity
T	$(dx/dT)/(dx/dT)_0,$ $(dy/dT)/(dy/dT)_0$
P_{tot}	$(dx/d(\ln P_{tot}))/ (dx/d(\ln P_{tot}))_0,$ $(dy/d(\ln P_{tot}))/ (dy/d(\ln P_{tot}))_0$
Cl/H	$(dx/d(\ln Cl/H))/ (dx/d(\ln Cl/H))_0,$ $(dy/d(\ln Cl/H))/ (dy/d(\ln Cl/H))_0$
III/H	$(dx/d(\ln III/H))/ (dx/d(\ln III/H))_0,$ $(dy/d(\ln III/H))/ (dy/d(\ln III/H))_0$
V/H	$(dx/d(\ln V/H))/ (dx/d(\ln V/H))_0,$ $(dy/d(\ln V/H))/ (dy/d(\ln V/H))_0$
Ga/III	$(dx/d(Ga/III))/ (dx/d(Ga/III))_0,$ $(dy/d(Ga/III))/ (dy/d(Ga/III))_0$
As/V	$(dx/d(As/V))/ (dx/d(As/V))_0,$ $(dy/d(As/V))/ (dy/d(As/V))_0$

The relative sensitivity can be evaluated by varying the input process parameter setpoints and observing the corresponding process sensitivity after the changes are made. If the relative sensitivity of the interested parameter is less than one, then the new setpoints give a more controllable, less sensitive condition; if it is larger than one, the new operating conditions is less controllable and therefore undesirable. The evaluation process can be carried out experimentally or by complex chemical equilibrium calculation. The approach by complex chemical equilibrium calculation is adopted here and has been used to evaluate the relative sensitivities, at a systematic variation of parameter setpoints, in hydride VPE of $\text{In}_{.53}\text{Ga}_{.47}\text{As}$ lattice-matched to InP and $\text{In}_{.74}\text{Ga}_{.26}\text{As}_{.56}\text{P}_{.44}$ lattice-matched to InP.

A.5.1. Relative Sensitivities in Hydride VPE of InGaAs

The reference setpoints for this study have been chosen to be the result reported in the previous section. Results of the study are conveniently presented in figure A-1 to A-5. In figure A-1, the relative sensitivities of parameters T , P_{tot} , Cl/H , III/H , V/H and Ga/III are reported with the variation of temperature T , while other parameter values are kept at the reference setpoints. P_{tot} , Cl/H , III/H and V/H are varied, and the relative sensitivities are calculated and presented in figures A-2, A-3, A-4 and A-5, respectively. The calculational procedure is as follows. For each setpoint variation, Ga/III value is calculated first for the composition, $x = 0.47$, followed by the calculation of compositional sensitivities. The relative sensitivities can then be calculated according to the definition. For the sake of convenience, the curves are numbered to represent each and every parameter; curve 1: T , curve 2: P_{tot} , curve 3: Cl/H , curve 4: III/H , curve 5: V/H , and curve 6: Ga/III .

Since T , P_{tot} , and Ga/III are the most influential parameters, the curves 1, 2, and 6 should be carefully studied for the search of optimum operating conditions. From figures A-1 to A-5, it is observed that, with small to mild effects on the compositional sensitivities of other parameters, (1) compositional sensitivity to temperature T is reduced if Cl/H value is lowered, or if V/H value is increased, (2) compositional sensitivity to pressure, P_{tot} , is reduced if Cl/H value is lowered, or if V/H value is lowered, and (3) reduction of compositional sensitivity to Ga/III can be achieved effectively by lowering T value or by increasing V/H value. Besides, III/H should be kept close to Cl/H , which occurs when source zones are operated at equilibrium, for lower sensitivity to all parameters.

In conclusion, for better control of InGaAs composition, Cl/H setpoint should be lowered from 0.001, V/H value should be increased from 0.001, and deposition temperature should be lowered from 700°C.

A.5.2. Relative Sensitivities in Hydride VPE of InGaAsP

The reference setpoints are reported in section A.4.2. Results of this study are presented in figures A-6 to A-10. In figures A-6 and A-7, the relative sensitivities of parameters T , P_{tot} , Cl/H , III/H , V/H , Ga/III , and As/V are reported with the variation of temperature T , while other parameter values are kept at the reference setpoints. The relative sensitivities of group III sublattice composition, x , are shown in figure A-6, and those of group V sublattice composition, y , are shown in figure A-7. P_{tot} , Cl/H , III/H and V/H are varied, and the relative sensitivities are calculated and presented in figures A-8 and A-9, A-10 and A-11, A-12 and A-13, and A-14 and A-15, respectively. The calculational procedure is as follows. For each setpoint variation, Ga/III and As/V values are calculated first for the

composition, $x = 0.26$ and $y = 0.56$, followed by the calculation of compositional sensitivities. The relative sensitivities can then be calculated according to the definition. The curves are conveniently numbered to represent each and every parameter; curve 1: T , curve 2: P_{tot} , curve 3: Cl/H , curve 4: III/H , curve 5: V/H , curve 6: Ga/III , and curve 7: As/V .

T , P_{tot} , Ga/III , and As/V are the most influential parameters, therefore the curves 1, 2, 6 and 7 were carefully studied for the search of optimum operating conditions. From figures A-6 to A-15, it is observed that (1) compositional sensitivity to temperature T is reduced if T value is increased, Cl/H value is decreased, or V/H value is increased, (2) compositional sensitivity to pressure P_{tot} is reduced with increased T , decreased Cl/H and increased V/H , (3) reduction of compositional sensitivity to Ga/III can be achieved effectively by increasing Cl/H , and (4) reduction of compositional sensitivity can be achieved with lowered T , increased Cl/H , or increased V/H . And as discussed in the previous section, III/H should again be kept close to Cl/H .

In conclusion, T , Cl/H and V/H can be varied to achieve better control of $In_{.74}Ga_{.26}As_{.56}P_{.44}$ composition. V/H value should definitely be increased from 0.001, however the direction of variation for T and Cl/H is not clear. Both temperature decrease and Cl/H value increase reduce compositional sensitivity to As/V , but increase compositional sensitivity to T and P_{tot} . Cl/H value increase also reduces compositional sensitivity to Ga/III . A tentative conclusion is to increase Cl/H from 0.001 for effective reduction of compositional sensitivity to Ga/III and As/V , and to increase deposition temperature from 973K, at the same time, to offset the increase of sensitivity to T and P_{tot} from increased Cl/H value.

List of Figures

- Figure A-1. Dependence of relative sensitivities of parameters T (curve 1), P_{tot} (curve 2), Cl/H (curve 3), III/H (curve 4), V/H (Curve 5) and Ga/III (curve 6) on T. The reference setpoint is $T = 700^{\circ}\text{C}$, $P_{tot} = 1 \text{ atm}$, $\text{Cl/H} = \text{III/H} = \text{V/H} = 0.001$ and $\text{Ga/III} = 0.605$.
- Figure A-2. Dependence of relative sensitivities of parameters T (curve 1), P_{tot} (curve 2), Cl/H (curve 3), III/H (curve 4), V/H (curve 5) and Ga/III (curve 6) on P_{tot} . The reference setpoint is $T = 700^{\circ}\text{C}$, $P_{tot} = 1 \text{ atm}$, $\text{Cl/H} = \text{III/H} = \text{V/H} = 0.001$ and $\text{Ga/III} = 0.605$.
- Figure A-3. Dependence of relative sensitivities of parameters T (curve 1), P_{tot} (curve 2), Cl/H (curve 3), III/H (curve 4), V/H (curve 5) and Ga/III (curve 6) on Cl/H with $\text{III/H} = \text{Cl/H}$. The reference setpoint is $T = 700^{\circ}\text{C}$, $P_{tot} = 1 \text{ atm}$, $\text{Cl/H} = \text{III/H} = \text{V/H} = 0.001$ and $\text{Ga/III} = 0.605$.
- Figure A-4. Dependence of relative sensitivities of parameters T (curve 1), P_{tot} (curve 2), Cl/H (curve 3), III/H (curve 4), V/H (curve 5) and Ga/III (curve 6) on III/H. The reference setpoint is $T = 700^{\circ}\text{C}$, $P_{tot} = 1 \text{ atm}$, $\text{Cl/H} = \text{III/H} = \text{V/H} = 0.001$ and $\text{Ga/III} = 0.605$.
- Figure A-5. Dependence of relative sensitivities of parameters T (curve 1), P_{tot} (curve 2), Cl/H (curve 3), III/H (curve 4), V/H (curve 5) and Ga/III (curve 6) on V/H. The reference setpoint is $T = 700^{\circ}\text{C}$, $P_{tot} = 1 \text{ atm}$, $\text{Cl/H} = \text{III/H} = \text{V/H} = 0.001$ and $\text{Ga/III} = 0.605$.
- Figure A-6. Dependence of x (group III sublattice composition) relative sensitivities of parameters T (curve 1), P_{tot} (curve 2), Cl/H (curve 3), III/H (curve 4), V/H (curve 5), Ga/III (curve 6) and As/V (curve 7) on T. The reference setpoint is $T = 700^{\circ}\text{C}$, $P_{tot} = 1 \text{ atm}$, $\text{Cl/H} = \text{III/H} = \text{V/H} = 0.001$ and $\text{Ga/III} = 0.388$ and $\text{As/V} = 0.0039$.
- Figure A-7. Dependence of y (group V sublattice composition) relative sensitivities of parameters T (curve 1), P_{tot} (curve 2), Cl/H (curve 3), III/H (curve 4), V/H (curve 5), Ga/III (curve 6) and As/V (curve 7) on T. The reference setpoint is $T = 700^{\circ}\text{C}$, $P_{tot} = 1 \text{ atm}$, $\text{Cl/H} = \text{III/H} = \text{V/H} = 0.001$ and $\text{Ga/III} = 0.388$ and $\text{As/V} = 0.0039$.
- Figure A-8. Dependence of x (group III sublattice composition) relative sensitivities of parameters T (curve 1), P_{tot} (curve 2), Cl/H (curve 3), III/H (curve 4), V/H (curve 5), Ga/III (curve 6) and As/V (curve 7) on P_{tot} . The reference setpoint is $T = 700^{\circ}\text{C}$, $P_{tot} = 1 \text{ atm}$, $\text{Cl/H} = \text{III/H} = \text{V/H} = 0.001$ and $\text{Ga/III} = 0.388$ and $\text{As/V} = 0.0039$.

- Figure A-9. Dependence of y (group V sublattice composition) relative sensitivities of parameters T (curve 1), P_{tot} (curve 2), Cl/H (curve 3), III/H (curve 4), V/H (curve 5), Ga/III (curve 6) and As/V (curve 7) on P_{tot} . The reference setpoint is $T = 700^{\circ}C$, $P_{tot} = 1$ atm, $Cl/H = III/H = V/H = 0.001$ and $Ga/III = 0.388$ and $As/V = 0.0039$.
- Figure A-10. Dependence of x (group III sublattice composition) relative sensitivities of parameters T (curve 1), P_{tot} (curve 2), Cl/H (curve 3), III/H (curve 4), V/H (curve 5), Ga/III (curve 6) and As/V (curve 7) on Cl/H with $III/H = Cl/H$. The reference setpoint is $T = 700^{\circ}C$, $P_{tot} = 1$ atm, $Cl/H = III/H = V/H = 0.001$ and $Ga/III = 0.388$ and $As/V = 0.0039$.
- Figure A-11. Dependence of y (group V sublattice composition) relative sensitivities of parameters T (curve 1), P_{tot} (curve 2), Cl/H (curve 3), III/H (curve 4), V/H (curve 5), Ga/III (curve 6) and As/V (curve 7) on Cl/H with $III/H = Cl/H$. The reference setpoint is $T = 700^{\circ}C$, $P_{tot} = 1$ atm, $Cl/H = III/H = V/H = 0.001$ and $Ga/III = 0.388$ and $As/V = 0.0039$.
- Figure A-12. Dependence of x (group III sublattice composition) relative sensitivities of parameters T (curve 1), P_{tot} (curve 2), Cl/H (curve 3), III/H (curve 4), V/H (curve 5), Ga/III (curve 6) and As/V (curve 7) on III/H . The reference setpoint is $T = 700^{\circ}C$, $P_{tot} = 1$ atm, $Cl/H = III/H = V/H = 0.001$ and $Ga/III = 0.388$ and $As/V = 0.0039$.
- Figure A-13. Dependence of y (group V sublattice composition) relative sensitivities of parameters T (curve 1), P_{tot} (curve 2), Cl/H (curve 3), III/H (Curve 4), V/H (curve 5), Ga/III (curve 6) and As/V (curve 7) on III/H . The reference setpoint is $T = 700^{\circ}C$, $P_{tot} = 1$ atm, $Cl/H = III/H = V/H = 0.001$ and $Ga/III = 0.388$ and $As/V = 0.0039$.
- Figure A-14. Dependence of x (group III sublattice composition) relative sensitivities of parameters T (curve 1), P_{tot} (curve 2), Cl/H (curve 3), III/H (Curve 4), V/H (curve 5), Ga/III (curve 6) and As/V (curve 7) on V/H . The reference setpoint is $T = 700^{\circ}C$, $P_{tot} = 1$ atm, $Cl/H = III/H = V/H = 0.001$ and $Ga/III = 0.388$ and $As/V = 0.0039$.
- Figure A-15. Dependence of y (group V sublattice composition) relative sensitivities of parameters T (curve 1), P_{tot} (curve 2), Cl/H (curve 3), III/H (Curve 4), V/H (curve 5), Ga/III (curve 6) and As/V (curve 7) on V/H . The reference setpoint is $T = 700^{\circ}C$, $P_{tot} = 1$ atm, $Cl/H = III/H = V/H = 0.001$ and $Ga/III = 0.388$ and $As/V = 0.0039$.

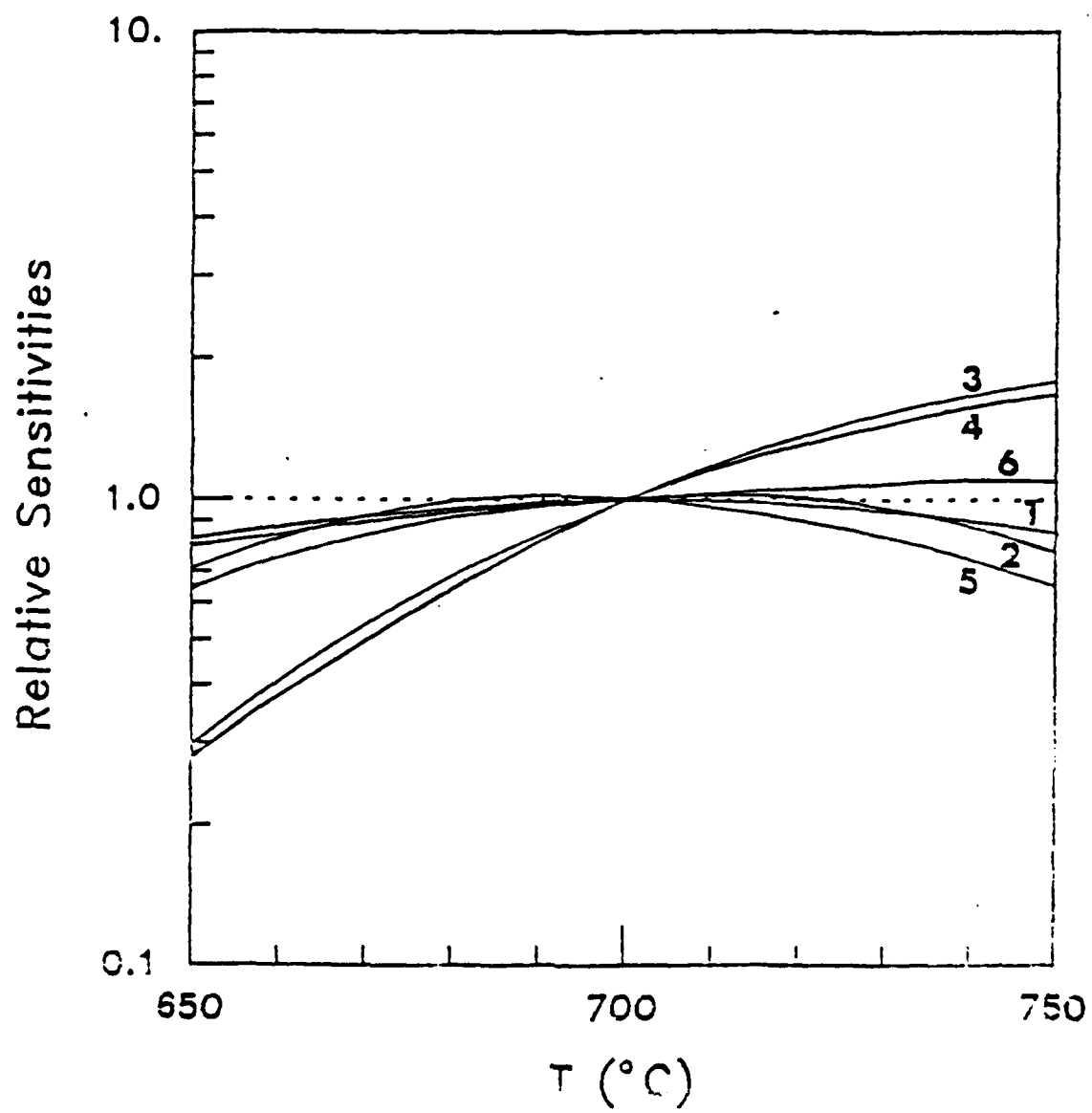


Figure A-1

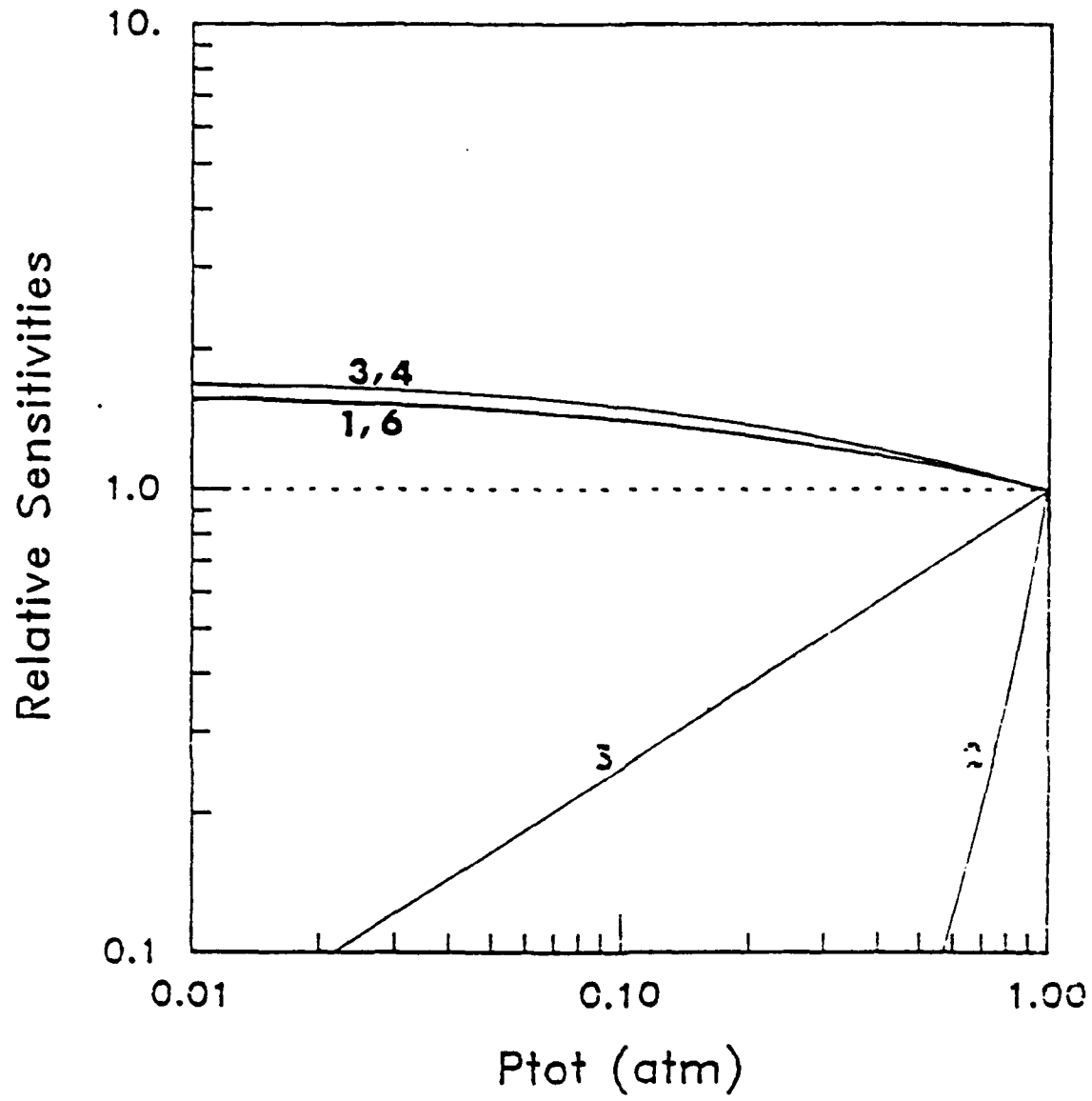


Figure A-2

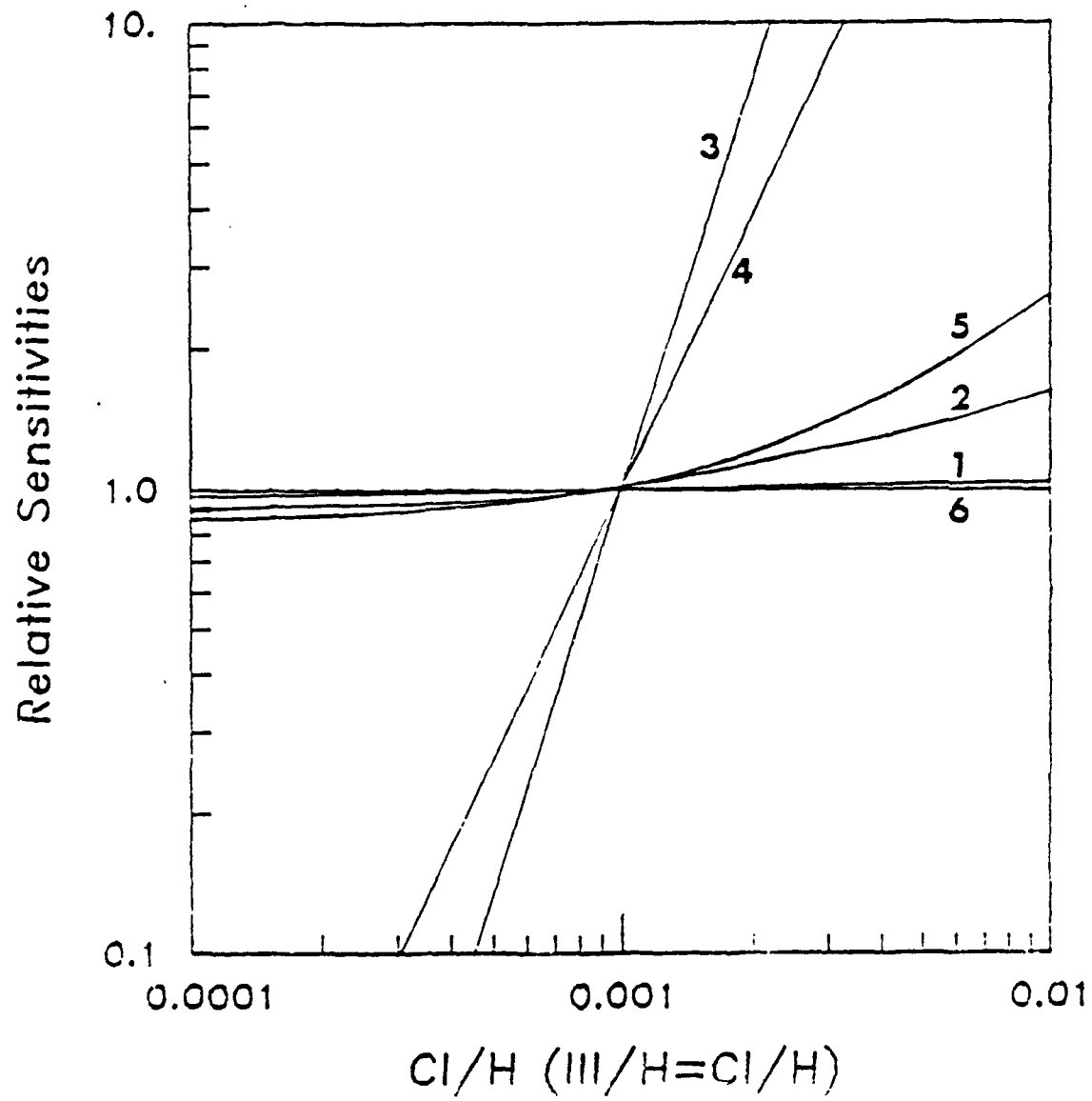


Figure A-3

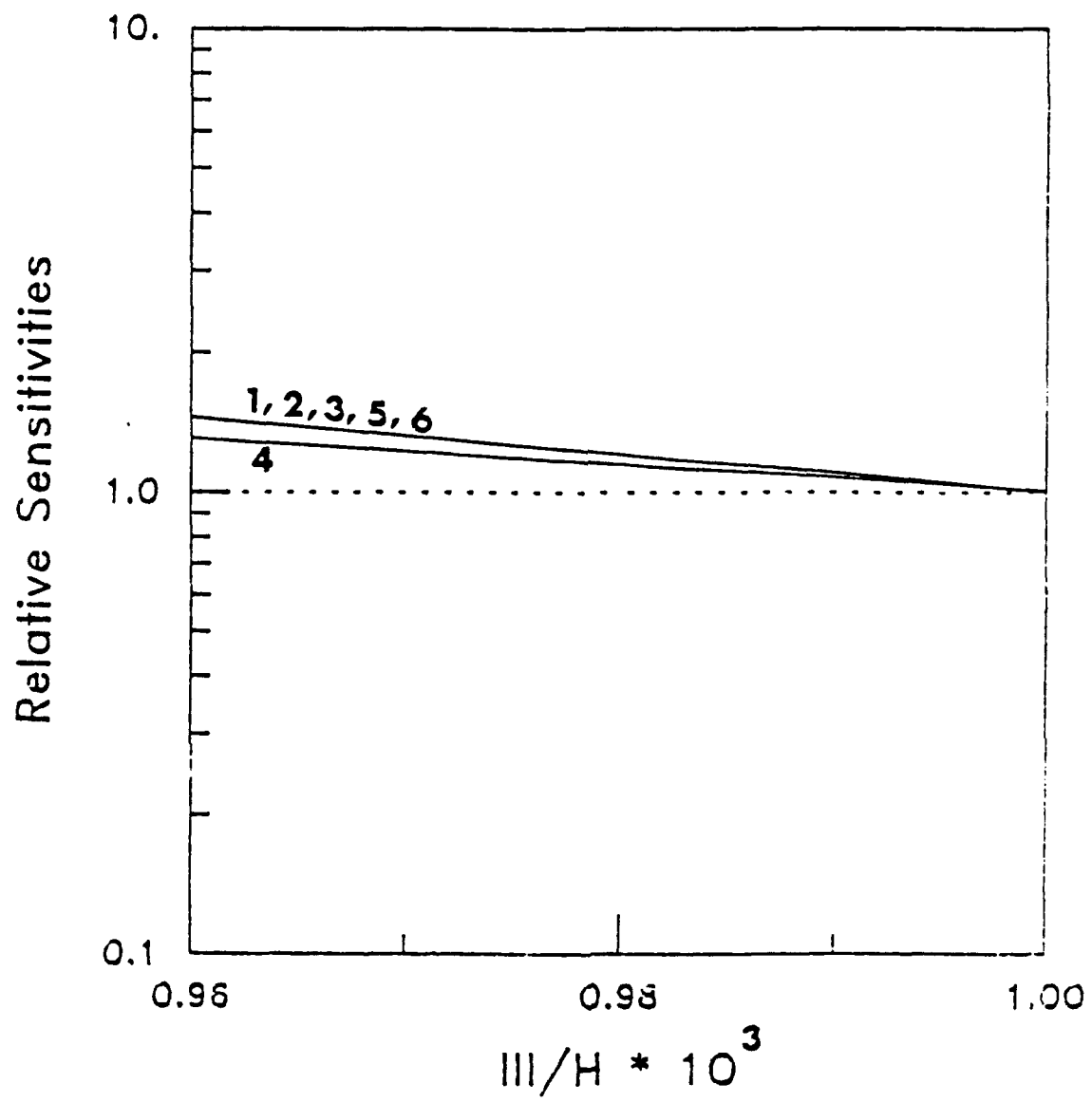


Figure A-4

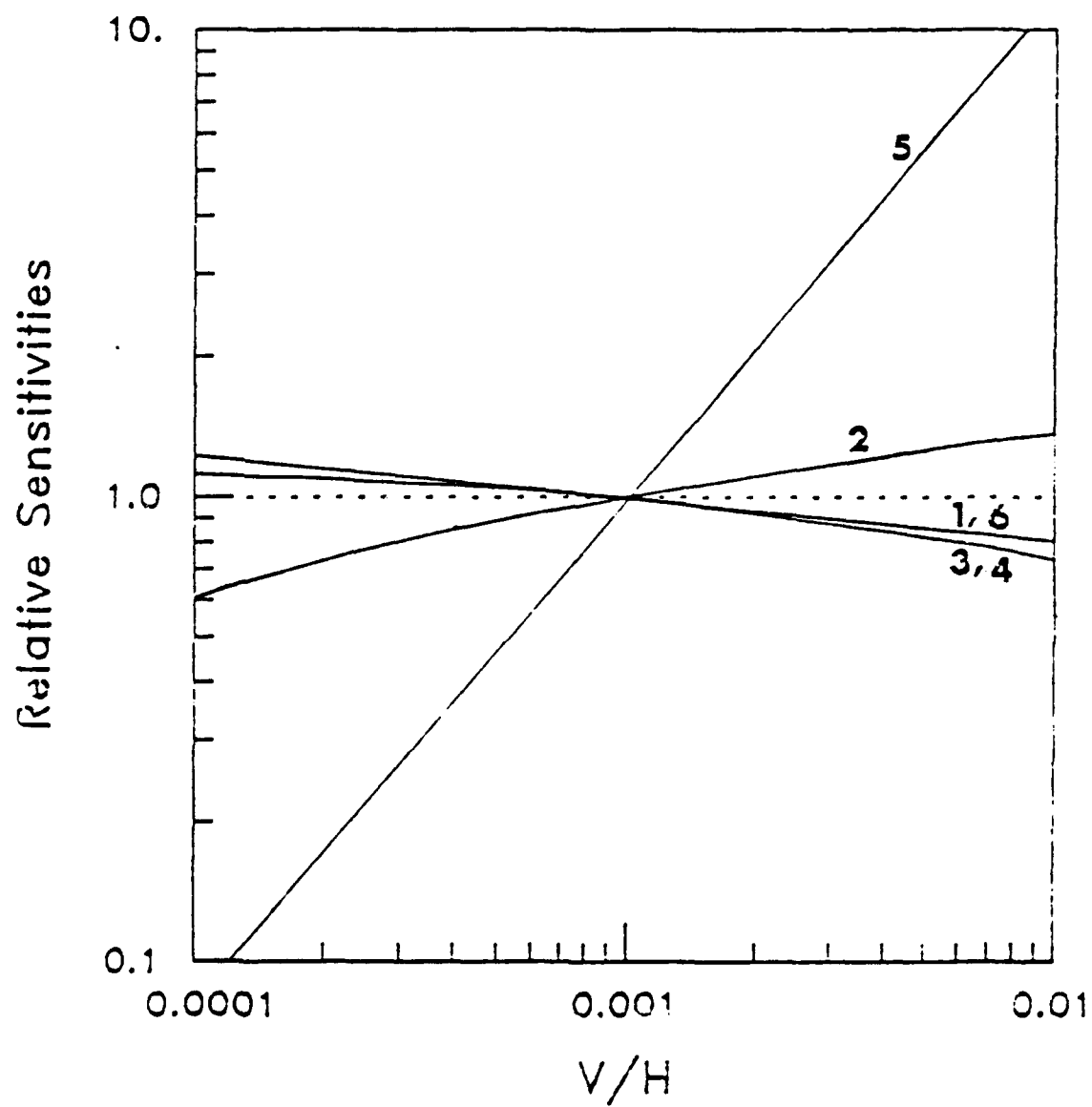


Figure A-5

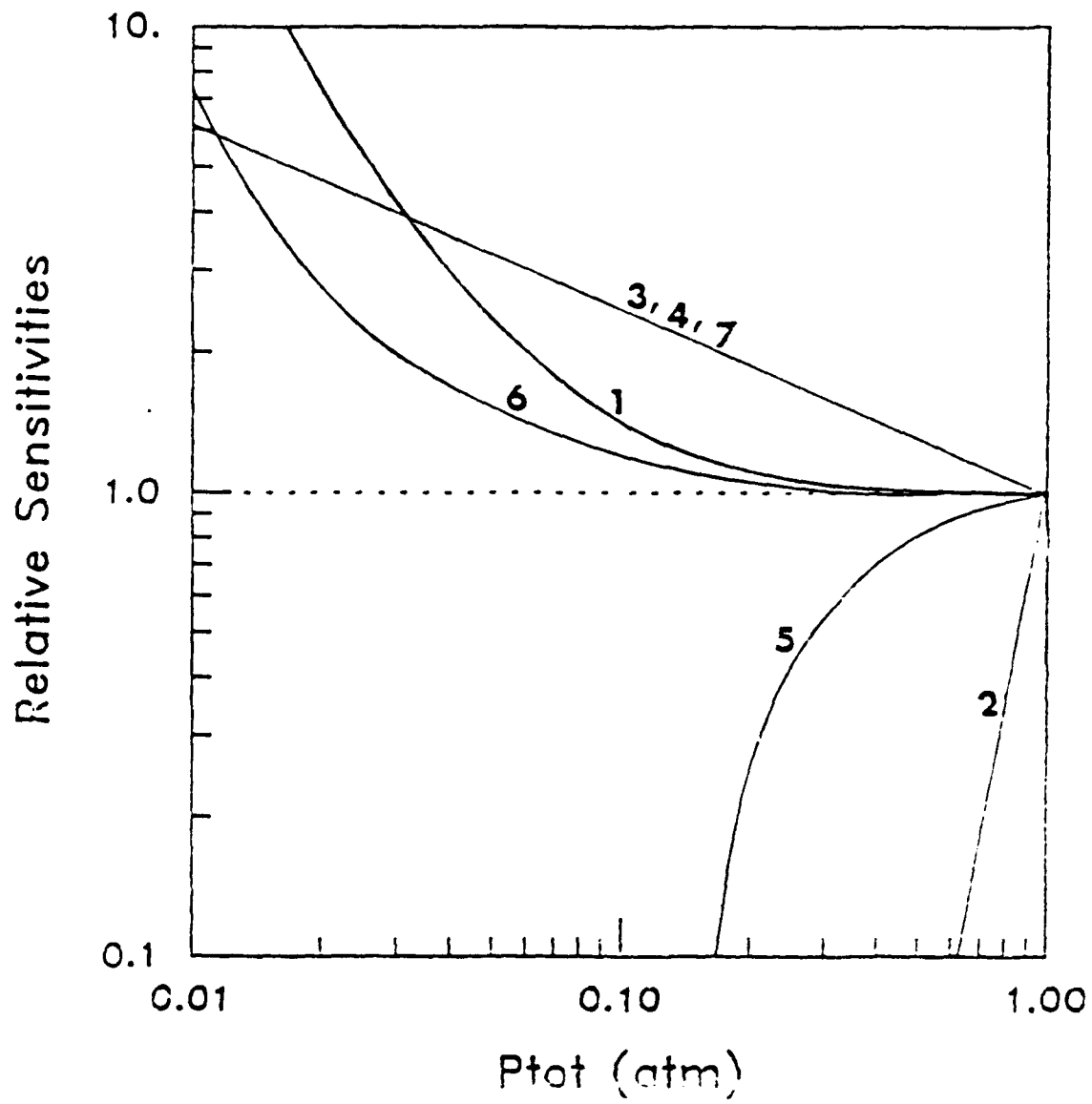


Figure A-8

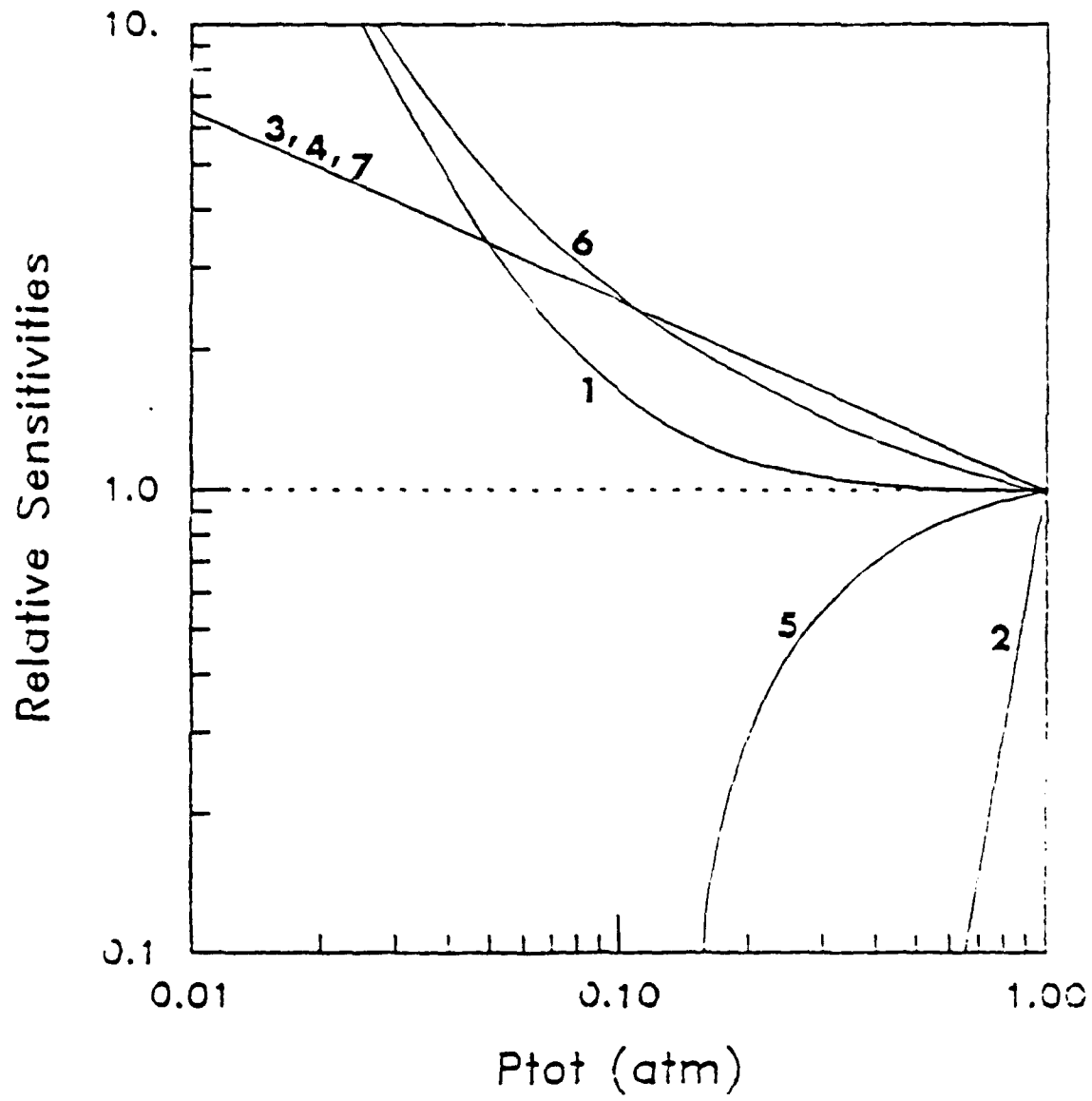


Figure A-9

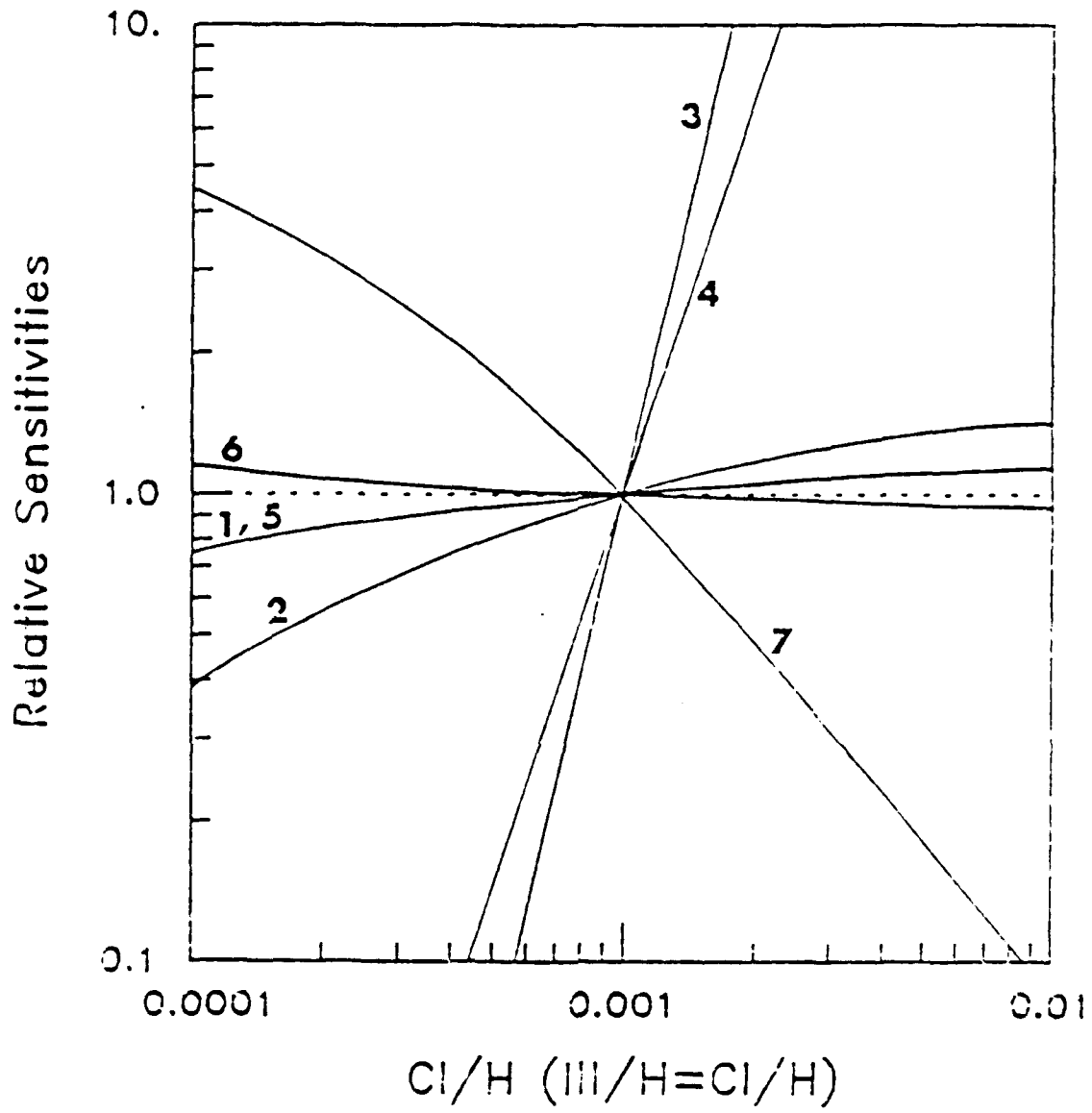


Figure A-10

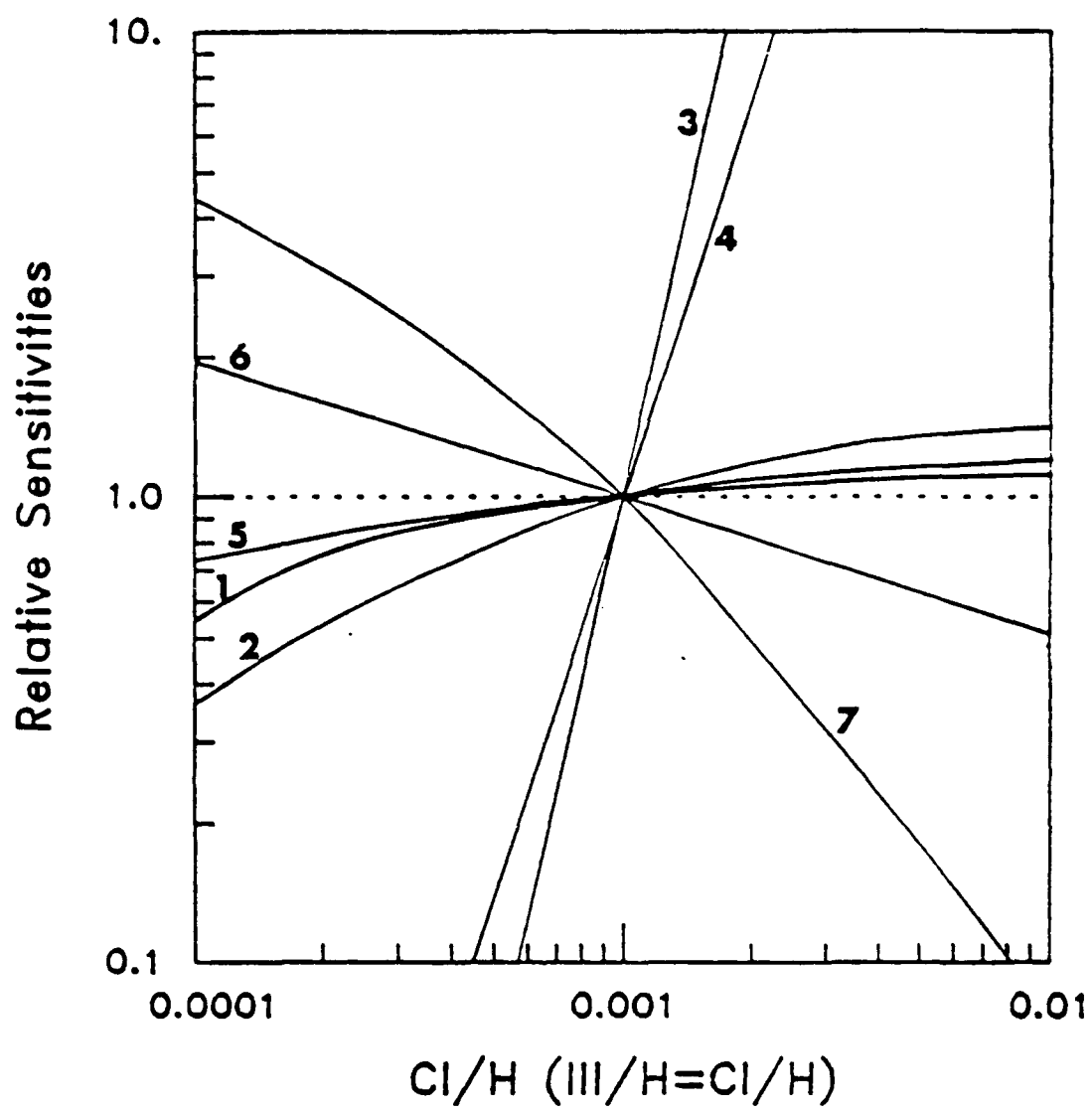


Figure A-11

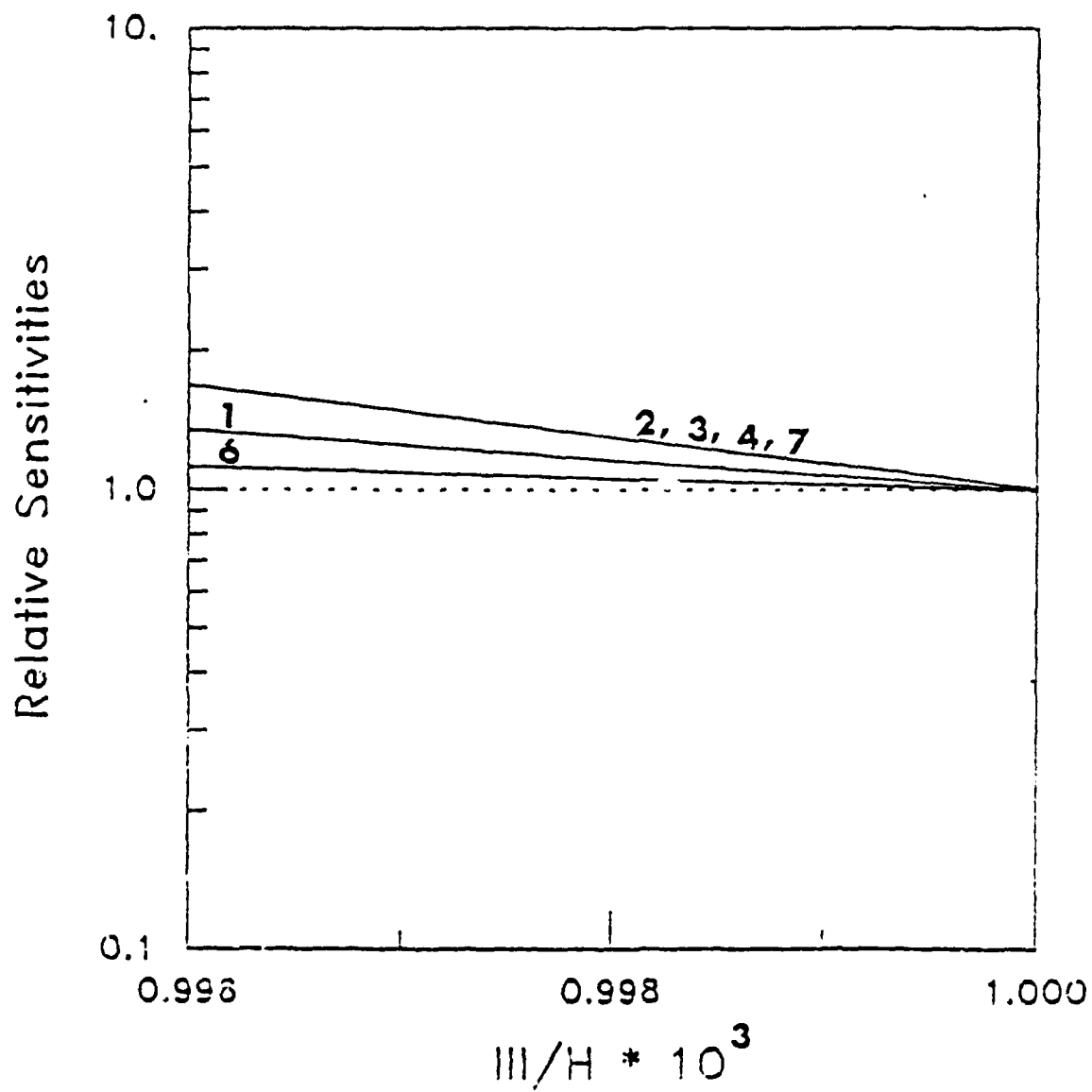


Figure A-12

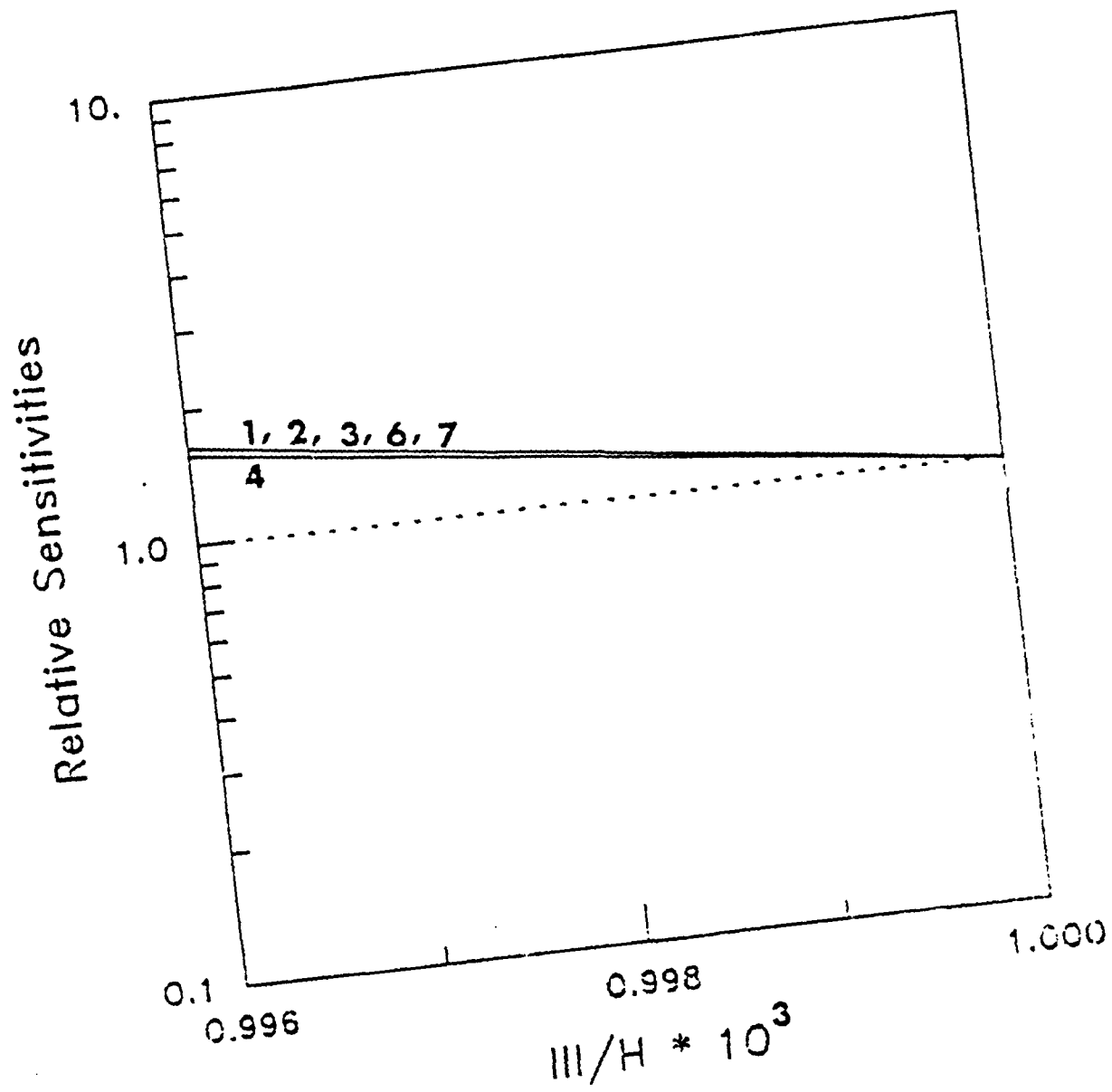


Figure A-13

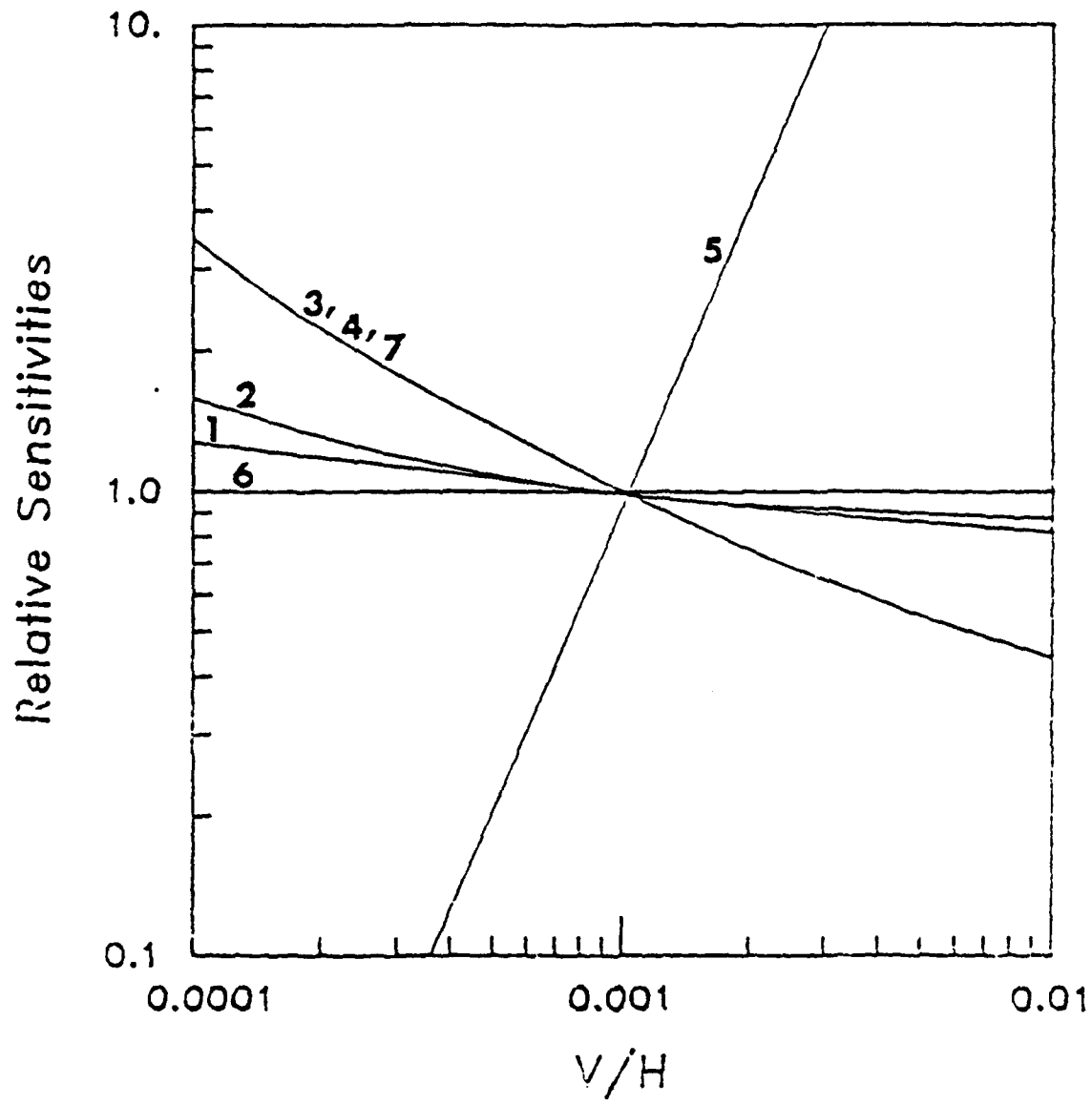


Figure A-14

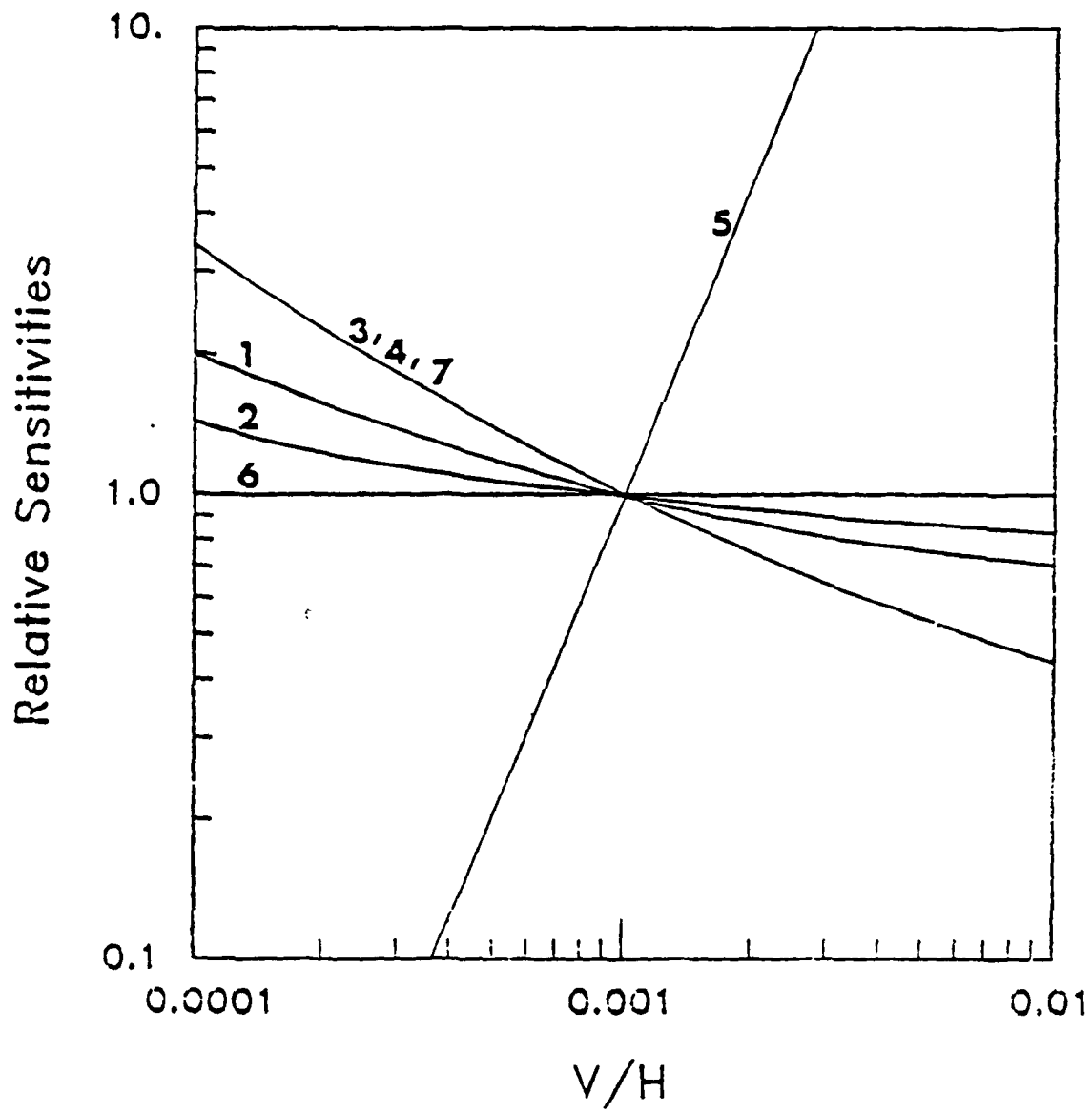


Figure A-15

Appendix B

Investigation of the Reaction of HCl with Ga and In

B.1. Introduction

Vapor phase epitaxy (VPE) of III-V compound semiconductors by the hydride process has proved to be a viable method for producing device quality films, particularly for growth of $\text{Ga}_x\text{In}_{1-x}\text{As}_y\text{P}_{1-y}$ solutions [26]. In this process the source species are gaseous group V hydrides and volatile group III chlorides, generated by reacting HCl with liquid III metal at elevated temperature.

The performance of In and Ga source reactors has been experimentally characterized by several investigators. Ban [27,28] and Ban and Ettenberg [29] sampled the outlet vapor stream of Ga [27,28] and In [29] source boats by means of a capillary coupled to a time-of-flight mass spectrometer. Measurements of HCl conversion as a function of flowrate, HCl partial pressure and temperature gave non-equilibrium conversions. More recently Donnelly and Karlicek [30] have used laser induced fluorescence to monitor the chloride transport of Ga and In. They report a non-linear dependence of InCl production rate with flowrate and HCl inlet partial pressure and a linear dependence of the GaCl production rate with respect to HCl inlet partial pressure. Under somewhat different reaction conditions Ban and Ettenberg [29] observed no dependence of the HCl conversion on HCl inlet partial pressure for an In source reaction. Karlicek and Bloemeke [31] applied UV absorption spectroscopy to measure the Ga and In source boat effluent concentrations with the results consistent with the previous fluorescence studies [30]. The results of such experimental studies on typical source boat designs indicate that the mono-chloride is the major reaction product and non-equilibrium conversions are often encountered in the range of process conditions used for hydride

deposition of In or Ga containing films. Furthermore, the non-linear behavior of InCl production rate with flow rate, temperature dependent conversions, and contrasting results with inlet HCl partial pressure suggest that both mass transfer and kinetic limitations are responsible for the non-equilibrium transport rates.

Reactor models are useful for assessing the steady state and transient performance of source boats and for developing reactor design criteria. For a given reactor geometry, a model requires knowledge of easily estimated transport properties and identification of important chemical reactions along with rate expressions. This report presents the results of an experimental determination of the rate of reaction of HCl in H_2 with liquid Ga or In at temperatures typically encountered in hydride vapor phase epitaxy. In the study of chemical reactions it is important to establish a reactor design and operating conditions where mass transfer limitations are either non-existent or small and easily determined. The experiments reported here were performed in a reactor with a geometry that was well defined with respect to modelling gas phase transport processes. In addition, the reactor was operated at reduced pressure to enhance mass transfer rates and therefore produce conditions at which reaction was the dominant limitation to group III chloride production. A molecular beam-mass spectrometer was coupled to this source boat to monitor the effluent gas-phase composition. An axial dispersion model which accounts for gas flow, gas-phase mass transfer and reaction kinetics was developed to simulate the reactor performance. This model was then used to determine values of kinetic constants from the experimental results.

B.2. Experimental

A schematic diagram of the experimental arrangement is shown in figure B-1a. The source boat was contained in a 38 mm diameter quartz tube approximately 130 cm in length and heated by a 3-zone resistance furnace. The furnace was equipped with external shunts so that a flat temperature profile across the source boat could be maintained ($\pm 2K$). In order to establish an analytically tractable reactor design, the source boats were constructed as shown in figure B-1b. The outside diameter of the semi-cylindrical quartz boats coincided with the inside diameter of the reactor tube to isolate the gas flow above the melt. The Ga source boat was 11 cm in length and the In boat was 10.5 cm in length. Two similar boats (7.5 cm length), only covered by a rectangular quartz flat, were placed adjacent to the front and back of the metal source boat. These boats served as hydrodynamic stabilizers which reduced the effects of entrance region disturbances and provided ideally axial and laminar flow conditions. The open middle boat was completely filled with Ga or In metal (99.99% purity).

The gas manifold system, constructed with stainless steel tubing and VCR fittings, accepted pure HCl and palladium-alloy diffused H_2 . Gas flows were regulated with electronic mass flow controllers. A 12 l/s mechanical pump was used to provide low pressure operation ($\sim 10^{-3}$ atm). After loading a source, the reactor was first vacuum baked and then purged with N_2 . Preliminary studies established appropriate operating conditions that gave significant reaction rate limitations in the temperature range of interest. Flowrates were 200 sccm H_2 and 10 sccm HCl with reactor pressures of 0.51 torr (Ga) and 0.68 torr (In). Under these conditions approximately 1 hour was required before a steady-state conversion was measured.

Unreacted HCl was detected by sampling the gas just beyond the third boat by a differentially-pumped mass spectrometer arrangement. Under the conditions of these experiments the transverse variation in the concentration of HCl was shown to be negligible. The sampling tube (9 mm O.D. quartz) had a tapered nozzle ($\sim 100 \mu\text{m}$ orifice) and was pumped by a 120 l/s diffusion pump. At the low reactor pressure used, molecular flow was established within a short distance after the nozzle, thus minimizing parasitic reactions in the sampling apparatus. The resulting molecular beam was collimated and directed towards the ionization chamber of quadrupole mass spectrometer (EAI Quad 250 mass spectrometer head). The electron impact energy used was 69 eV. The vacuum chamber housing the mass spectrometer head was maintained at a pressure of $\sim 10^{-8}$ torr by a 250 l/s ion pump.

Calibration of the mass spectrometer was performed by measurement of the HCl^+ ion intensity as a function of inlet HCl partial pressure and temperature at constant total flowrate without the liquid metal placed in the middle boat. The HCl^+ ion intensity was found to vary linearly with the HCl partial pressure and to be nearly independent of the sampling temperature.

B.3. Data Analysis

B.3.1. Formulation of the axial dispersion model

A general equation of change of component i in the gas phase in this reactor system is given by

$$\frac{\partial C_i}{\partial t} + V \cdot N_i = R_i \quad (\text{B-1})$$

where C_i is the concentration of component i and R_i is the rate of production per unit volume of component i . The molar flux of component i , N_i , contains

two parts; a convective flux $C_i v$, where v is the velocity, and a diffusive flux J_i . Since the source zone is operated isothermally and with an excess of carrier gas, the diffusive flux can be simplified to pseudo-binary ordinary diffusion according to

$$J_i = -CD_{i,o} \nabla x_i \quad (\text{B-2})$$

In this expression, $D_{i,o}$ is the binary molecular diffusivity of component i in carrier gas o , C is the total concentration, and x_i is the mole fraction of component i . The boundary condition along the transverse direction can be written as

$$-J_i \cdot n = R_{s,i} \quad (\text{B-3})$$

Here, n is a normal vector of unit magnitude in the direction from the transverse boundary surface to the interior of the system and $R_{s,i}$ is the production rate of component i per unit area on the liquid metal boundary surface.

Because of difficulties associated with typical reactor geometries, it is convenient to adopt an axial dispersion model to describe the reactor performance. Referring to figure B-2a, the transverse area average of a term δ in the y_1 - y_2 plane is defined as

$$\bar{\delta} = \frac{1}{A} \int_A \delta \cdot dA \quad (\text{B-4})$$

where A is the transverse area. Similarly, a transverse boundary average of δ is defined as

$$\bar{\delta} = \frac{1}{S} \int_S \delta \cdot dS \quad (B-5)$$

where S is the transverse boundary length. With these definitions the transverse average of the equation of change is

$$\frac{\partial}{\partial t} \bar{C}_i + \frac{\partial}{\partial z} \overline{v_z C_i} = - \frac{\partial}{\partial z} \bar{J}_{i,z} + \frac{S}{A} \bar{R}_{s,i} + \bar{R}_i \quad (B-6)$$

This equation is the axial dispersion model in its rigorous form.

B.3.2. Application to experimental reactor

As indicated above, the diffusive flux can be considered as the case of pseudobinary ordinary diffusion. In order to apply this relation to the experimental reactor, a statement as to the functional form of the reaction rate of HCl must be made. Given the linear dependence of GaCl formation on HCl partial pressure observed in previous studies, first-order homogeneous and heterogeneous rate expressions are assumed. The results of the measurements of this study are shown to be adequately described by first-order kinetics. With the assumptions of pseudobinary ordinary diffusion and first order kinetics, the axial dispersion equation of change is

$$\frac{\partial}{\partial t} \bar{C}_i + \frac{\partial}{\partial z} \overline{v_z C_i} = CD_{i,o} \frac{\partial^2}{\partial z^2} \bar{x}_i + \frac{S}{A} K_{s,i} \bar{C}_i + K_i \bar{C}_i \quad (B-7)$$

In this expression, $K_{s,i}$ is the first order rate constant for the heterogeneous reaction of HCl at the liquid metal surface and K_i is the first order rate constant for the disappearance of HCl by homogeneous reaction.

A dimensionless velocity and concentration based on the transverse average is defined by $\phi = v_z/\bar{v}_z$ and $\psi = C_i/\bar{C}_i$. In general ϕ and ψ are functions of the axial length. For fully developed flow, however, ϕ is not a function of z . The z dependence of ψ should be weak beyond the entrance region and no dependence exists for the case of only homogeneous reaction. Assuming that ϕ and ψ are functions of only the transverse coordinates and the reactor is operated isothermally and isobarically ($\bar{v}_z = v_a$ and C are constants), a linear equation of change with the single dependent variable \bar{C}_i results

$$\frac{\partial}{\partial t} \bar{C}_i + \bar{\phi} \bar{\psi} v_a \frac{\partial}{\partial z} \bar{C}_i = D_{i,o} \frac{\partial^2}{\partial z^2} \bar{C}_i + \left(\frac{S}{A} K_{s,i} \bar{\psi} + K_i \right) \bar{C}_i \quad (\text{B-8})$$

The reaction zone in the experimental design has a semi-circular shape (figure B-2b) and was chosen to permit a relatively straightforward development of ϕ and ψ . An orthogonal collocation procedure [32] was used to solve Poisson's equation for this geometry to give the result

$$\phi = \left(\frac{r}{R} \right) \left(1 - \frac{r}{R} \right) \left[1 + \left(\frac{2\theta}{\pi} \right)^2 \right] \left[8.71 - 1.06 \left(\frac{r}{R} \right) - 2.29 \left(\frac{2\theta}{\pi} \right)^2 + 11.54 \left(\frac{r}{R} \right) \left(\frac{2\theta}{\pi} \right)^2 \right] \quad (\text{B-9})$$

where R is the radius. Note that $\phi = 0$ at the transverse boundary and $\bar{\phi} = 1$.

The transverse boundary conditions (Eq. B-3) are

$$\text{at } \theta = 0 \quad \frac{\partial C_i}{\partial \theta} = 0 \quad (\text{B-10a})$$

$$\text{at } \theta = \pm \pi/2 \quad -D_{i,o} \frac{\partial C_i}{r \partial \theta} = \bar{\psi} K_{s,i} C_i \quad (\text{B-10b})$$

$$\text{at } r = R \quad \frac{\partial C_i}{\partial r} = 0 \quad (\text{B-10c})$$

$$\text{at } r = 0 \quad -D_{i,0} \frac{\partial C_i}{\partial r} = K_{s,i} C_i \quad (\text{B-10d})$$

ψ can be approximated from the known transverse boundary conditions and the "Taylor" procedures [33]. The "Taylor" procedures generate polynomials of (r, θ) that satisfy the transverse boundary conditions. For semi-circular geometry, the polynomial of the lowest order that satisfies the transverse boundary conditions is

$$\psi(r, \theta) = \frac{1 + \alpha \left(\frac{r}{R}\right) - \frac{\alpha}{2} \left(\frac{r}{2}\right)^2 + \left(\frac{1/3 + 3/20\alpha}{1 + \pi/8\alpha}\right) \frac{\pi}{4} \alpha \left(\frac{r}{R}\right) \left[1 + 3\left(\frac{2\theta}{\pi}\right)^2\right]}{1 + \frac{5}{12} \alpha} \quad (\text{B-11})$$

In this expression α is an axial dispersion number defined as $K_{s,i}R/D_{i,0}$ and represents the ratio of the surface reaction velocity to the transverse diffusion velocity. ψ satisfies the transverse boundary conditions and the value of the transverse average of ψ is one.

With Eq. B-9 and Eq. B-11, $\overline{\phi\psi}$ and $\bar{\psi}$ are readily obtained as

$$\overline{\phi\psi} = \frac{1 + 0.846 \alpha + 0.181 \alpha^2}{1 + 0.809 \alpha + 0.164 \alpha^2} \quad (\text{B-12})$$

and

$$\bar{\psi} = \frac{1 + 0.464 \alpha + 0.0131 \alpha^2}{1 + 0.809 \alpha + 0.164 \alpha^2} \quad (\text{B-13})$$

It is noted that if the surface reaction rate is zero, $\alpha = 0$, then both $\overline{\phi\psi}$ and $\overline{\psi}$ are unity and the concentration field is independent of the transverse directions. This situation corresponds to homogeneous reaction only and describes the reactor performance from the end of the liquid metal boat to the sampling tube. The boundary conditions in the axial-direction are of Danckwerts' type [34], and given by

$$\text{at } z = 0 \text{ (liquid metal inlet)} \quad v_a \bar{C}_i - D_{i,o} \frac{d}{dz} \bar{C}_i = v_a C_i^0 \quad (\text{B-14a})$$

$$z = l \text{ (liquid metal outlet)} \quad - D_{i,o} \frac{d}{dz} \bar{C}_i = 0 \quad (\text{B-14b})$$

C_i^0 is the mole fraction of component i in the inlet gas and l is the length of the liquid metal boat.

Three additional dimensionless numbers appear in this formulation; Peclet number (Pe), Damkoehler number (Da), and a geometric aspect ratio (β), defined by

$$\text{Pe} = v_a l / D_{i,o} \quad (\text{B-15})$$

$$\text{Da} = K_i l^2 / D_{i,o} \quad (\text{B-16})$$

$$\beta = S l / \text{AR} \quad (\text{B-17})$$

An analytical solution of the unreacted HCl as a function of dimensionless length, $\xi = z/l$, is given by

$$\frac{\bar{C}_1}{C_1^0} = \exp\left[\bar{\phi}\bar{\psi} \frac{Pe}{2} \xi\right] [d_1 \exp(-K_0 \xi) + d_2 \exp(K_0 \xi)] \quad (B-18)$$

where

$$d_1 = \frac{Pe \left(Pe \frac{\bar{\phi}\bar{\psi}}{2} + K_0 \right)}{\left[Pe \left(1 - \frac{\bar{\phi}\bar{\psi}}{2} \right) + K_0 \right] \left[Pe \left(\frac{\bar{\phi}\bar{\psi}}{2} \right) + K_0 \right] - \left[Pe \left(1 - \frac{\bar{\phi}\bar{\psi}}{2} \right) - K_0 \right] \left[Pe \left(\frac{\bar{\phi}\bar{\psi}}{2} \right) - K_0 \right] \exp(-2K_0)}$$

$$d_2 = \frac{- Pe \left(Pe \left(\frac{\bar{\phi}\bar{\psi}}{2} \right) - K_0 \right) \exp(-2K_0)}{\left[Pe \left(1 - \frac{\bar{\phi}\bar{\psi}}{2} \right) + K_0 \right] \left[Pe \left(\frac{\bar{\phi}\bar{\psi}}{2} \right) + K_0 \right] - \left[Pe \left(1 - \frac{\bar{\phi}\bar{\psi}}{2} \right) - K_0 \right] \left[Pe \left(\frac{\bar{\phi}\bar{\psi}}{2} \right) - K_0 \right] \exp(-2K_0)}$$

and

$$K_0 = \left[\left(Pe \left(\frac{\bar{\phi}\bar{\psi}}{2} \right) \right)^2 + \beta \alpha \bar{\psi} + Da \right]^{1/2}$$

At the outlet of the liquid metal boat ($z = l$), the fraction of unreacted HCl (\bar{C}_1/C_1^0) is determined by the four parameters, Pe , Da , α and β through the solved model equation (Eq. B-18). Beyond the liquid metal source to the sampling orifice, Eq. (B-18) is still applicable with $\alpha = 0$, $\bar{\phi}\bar{\psi} = \bar{\psi} = 1$, and a characteristic length equal to this additional segment. The combination of these two reactor performance equations provides a direct relation between the experimentally measured quantity (\bar{C}_1/C_1^0) and the kinetic information (Da , α) for this specific reactor design and operation (Pe , β).

B.4. Results and Discussion

B.4.1. Equilibrium calculations

In order to establish the maximum achievable HCl conversion and to identify possible reactant and product species, complex reaction equilibria in the Ga-Cl-H and In-Cl-H systems were computed. Three degrees of freedom exist in this system and the independent variables were chosen as pressure, temperature and the gas phase Cl/H ratio since these quantities are each constant during source operation. Equilibrium compositions in the Ga-Cl-H and In-Cl-H systems were computed at values of $\text{Cl/H} = 2.5 \times 10^{-2}$ and pressures of 1 and 10^{-3} atm as a function temperature in the range $950 < T < 1250$ K. A stoichiometric algorithm was used to compute values of the equilibrium partial pressures. Thirteen species were postulated to exist, including an excess of liquid metal as the only condensed species. A summary of the thermochemical data used in the calculation is given in Appendix A. It is recognized that a small solubility of metal chlorides in the melt exists, but the activity of the metal should be close to unity and therefore the slight solubility should not greatly influence the equilibrium gas phase composition.

The calculated equilibrium compositions as a function of reciprocal absolute temperature for the Ga source boat at 1 atm pressure are shown in figure B-3a and at 10^{-3} atm in figure B-3b. At both pressures the HCl conversion is high ($> 99.99\%$) and is higher at the lower pressure. For all conditions investigated, the major Ga species is the monochloride. Increasing the source temperature gave higher HCl conversions and decreased the equilibrium partial pressures of other gallium chlorides, primarily because of entropic effects. Since the equilibrium conversion of HCl was nearly complete and GaCl was the dominant Ga vapor species, the equilibrium transport rate of Ga is almost independent of source temperature and directly proportional to the

inlet HCl molar flow rate. To produce controllable and reproducible transport rates, it is therefore desirable to operate the source boat at conditions which achieve equilibrium conversions. Decreasing the pressure from the typical operating one (1 atm) to the pressure used in this experimental study, gave a decrease in the partial pressures of the minor gallium chlorides. These results suggest the overall reaction investigated in the low pressure experimental work should involve only the production of GaCl. As the temperature increased the partial pressure of elemental Ga increased, and since the vapor pressure of liquid Ga is independent of system pressure, the relative amount of elemental Ga in the vapor increased significantly with a decrease in total pressure. The inclusion of a homogeneous reaction term in the reactor performance model was motivated by this observation.

Similar calculations were performed for an In source boat and the results are given in figure B-4a (1 atm pressure) and figure B-4b (10^{-3} atm pressure). The equilibrium HCl conversion is shown to be nearly independent of temperature (~ 99.95%) but less than that calculated for Ga. The values of the equilibrium partial pressures of the other chlorides of indium were higher than those above the Ga source boat. By operating the experimental reactor at the lower pressure, the other indium chlorides were still trace species. The major difference between the Ga and In systems was the relative importance of the elemental vapor species. For the In system at 1250 K, the equilibrium In partial pressure was nearly equal to the InCl partial pressure.

B.4.2. Reaction of HCl with Ga

For the source boat design and values of operating parameters used in the experimental measurement of HCl conversions, incomplete HCl reaction was observed. The percent HCl consumed at various reaction temperatures is shown

in figure B-5 for a H_2 flowrate of 200 sccm and HCl flowrate of 10 sccm at a pressure of 0.51 torr. As expected, the HCl conversion increased with increasing source temperature.

Reaction rate constants were determined from the measured conversions by application of Eq. (B-18). The major difficulty with interpreting the rate data derived from this equation is that Da , which contains the homogeneous rate constant, and α , which is proportional to the heterogeneous rate constant, are present in a coefficient as a linear combination. Thus, it is not possible to separately determine values of both of these rate constants if they are both important. Although both reaction paths can coexist, it is highly unlikely that the rate constants have similar values of activation energy and pre-exponential factor.

The measured HCl consumption data was first reduced for the case of $Da = 0$ (negligible homogeneous reaction rate). The interdiffusion coefficient of HCl in H_2 was taken to be $D_{HCl,H_2} = 1.63 \times 10^{-4} P^{-1} T^{3/2}$ [35]. The calculated values of the first order rate constant are plotted in figure B-6 as a function of reciprocal absolute temperature. The results show a linear relation with reciprocal temperature and the values of the activation energy and pre-exponential factor, as determined by linear regression, are 32.7 KJ/mol and 3.61×10^4 cm/s, respectively. An analogous treatment of the data with the assumption of $\alpha = 0$ (negligible heterogeneous reaction rate) also showed linear behavior and the regression values of the activation energy and pre-exponential factor were determined to be 31.2 KJ/mol and 6.23×10^3 s $^{-1}$, respectively.

The reaction rate expression determined above does not identify a specific mechanism, however, the low values of the calculated pre-exponential factors suggest that the rate limiting reaction involves a heterogeneous

reaction. A possible homogeneous mechanism consists of vaporization of Ga and reaction with HCl. The maximum rate of evaporation of pure Ga is given by the Hertz-Langmuir expression. Combining this expression with the molar flux of HCl used in this study, the measured HCl conversion, and the vapor pressure of pure Ga [1], a temperature 1323 K is required to provide sufficient elemental Ga vapor to react with the inlet HCl. This temperature is greater than the measurement temperature range. Furthermore, the calculated activation energy (~ 32 KJ/mol) is considerably different from the enthalpy of vaporization of Ga (272 KJ/mol) [1]. An attempt was made to numerically deduce a first-order heterogeneous rate constant from the results of Ban [27]. An activation energy of 48 KJ/mol was calculated and the agreement with the determination of this study is considered good, given the uncertainties in the dimensions assumed for Ban's reactor [27].

B.4.3. Reaction of HCl with In

Studies similar to those performed with Ga were also made with liquid In. The measured HCl consumption is shown in figure B-7 as a function of reciprocal absolute temperature. The data was analyzed by application of Eq. (B-18). The results of the data reduction for the case of $\alpha = 0$ is given in figure B-8 and for $Da = 0$ in figure B-9. The calculated rate constants shown in figures B-8 and B-9 clearly indicate two competing reaction mechanisms exist with a crossover at 850°C. With an assumption of only homogeneous reaction (figure B-8), the calculated activation energy and pre-exponential factor are 57.7 KJ/mol and $1.04 \times 10^5 \text{ s}^{-1}$ at low temperatures and 123.6 KJ/mol and $6.2 \times 10^8 \text{ s}^{-1}$ at high temperatures. The values of the activation energy and pre-exponential factor extracted from figure B-9 (heterogeneous reaction) are 62.2 KJ/mol and $1.8 \times 10^6 \text{ cm/s}$ at low temperatures and 157.8 KJ/mol and $5.7 \times 10^{10} \text{ cm/s}$ at high temperatures.

It is believed that at low temperatures a heterogeneous reaction limitation exists and at high temperature a homogeneous one. The pre-exponential factor determined for the high temperature homogeneous reaction case is appropriate for a gas phase reaction. Furthermore, the temperature calculated from the Hertz-Langmuir expression at which there is a sufficient rate of In vaporization to react with the inlet molar flowrate of HCl flow is 846°C [1]. Above this temperature the maximum evaporation rate of In is greater than the HCl transport rate and the reduced pressure should give rapid gas phase mass transfer. This temperature value nearly coincides with the measured crossover temperature. The interpretation that reaction is limited by a homogeneous reaction at high temperatures is consistent with the experimental observation of a metallic deposit (presumably In) on the cold reactor exit parts.

The reaction of molecular chlorine with liquid In at low temperatures has been studied by Balooch et al. [36] by modulated molecular beam-mass-spectrometric methods. A reaction mechanism based on dissociative adsorption of chlorine was proposed and gives significantly higher rates than determined here. A nonlinear InCl transport rate as a function of input HCl was measured by Donnelly and Karlick [30]. For the experimental conditions used in our study, the gas phase concentration of HCl at the surface is nearly constant and thus the dependence of reaction rate on HCl concentration was not determined. These results suggest a more complex reaction mechanism exists for InCl production than for GaCl production.

B.5. Conclusions

The reaction of HCl with Ga and In was studied at temperatures and a mole fraction typically encountered in hydride VPE. Significant mass transfer limitations were eliminated by operation at reduced pressure (at 1000 K, $\alpha =$

0.1 for the Ga source). A single reaction rate expression can describe the reaction of HCl with Ga and it is believed to be a heterogeneous reaction. The results of measurements with the In source boat were somewhat different with two mechanisms apparently competing. At high temperatures the reaction is believed to be gas phase reaction of HCl with In vapor and at low temperatures a heterogeneous reaction. The operation of an In source boat at elevated temperature and low pressure is expected to give difficulties with In metal deposition in the deposition zone which is at a lower temperature. The results for Ga and In indicate that the production of InCl is more efficient for In. This is contrary to hydride growth practice, in which larger surface areas or higher operating temperatures are normally used for the In source. At atmospheric pressure operation, the InCl transport rate is largely limited by mass transport and differences in transport properties cannot explain the difference in the rates determined here and practice.

List of Figures

- Figure B-1a. Schematic diagram of the experimental apparatus.
- Figure B-1b. Enlargement of the source boat and hydrodynamic stabilizers.
- Figure B-2a. A reactor volume with arbitrary transverse area and boundary.
- Figure B-2b. Domain of the reaction zone.
- Figure B-3. Calculated equilibrium partial pressures in the Ga-Cl-H system as a function of temperature at Cl/H = 0.025. a) $P = 1$ atm, b) $P = 10^{-3}$ atm.
- Figure B-4. Calculated equilibrium partial pressures in the In-Cl-H system as a function of temperature at Cl/H = 0.0025. a) $P = 1$ atm, b) $P = 10^{-3}$ atm.
- Figure B-5. Measured percent HCl consumption versus reaction temperature in the Ga/HCl/H₂ reaction system. H₂ flowrate = 200 sccm, HCl flowrate = 10 sccm and $P = 0.51$ torr.
- Figure B-6. First order rate constant, K_s (cm/s), versus reciprocal absolute temperature as determined from reduction of data in figure 5 with equation B-18 and assuming $Da = 0$. The rate constant is given by $K_s = 3.61 \times 10^4 \exp(-3,930/T(K))$.
- Figure B-7. Measured percent HCl consumption versus reaction temperature in the In/HCl/H₂ reaction system. H₂ flowrate = 200 sccm, HCl flowrate = 10 sccm and $P = 0.68$ torr.
- Figure B-8. First order rate constant, $K(s^{-1})$, versus reciprocal absolute temperature as determined from reduction of data in figure 7 with equation B-18 and assuming $\alpha = 0$. In the high temperature range $K = 6.2 \times 10^8 \exp(-15,050/T(K))$, and in the low temperature range $K = 1.04 \times 10^5 \exp(-7,020/T(K))$.
- Figure B-9. First order rate constant, K_s (cm/s), versus reciprocal absolute temperature as determined from reduction of data in figure 7 with equation B-18 and assuming $Da = 0$. In the high temperature range $K_s = 5.7 \times 10^{10} \exp(-19,210/T(K))$ and in the low temperature range $K_s = 1.8 \times 10^6 \exp(-7,630/T(K))$.

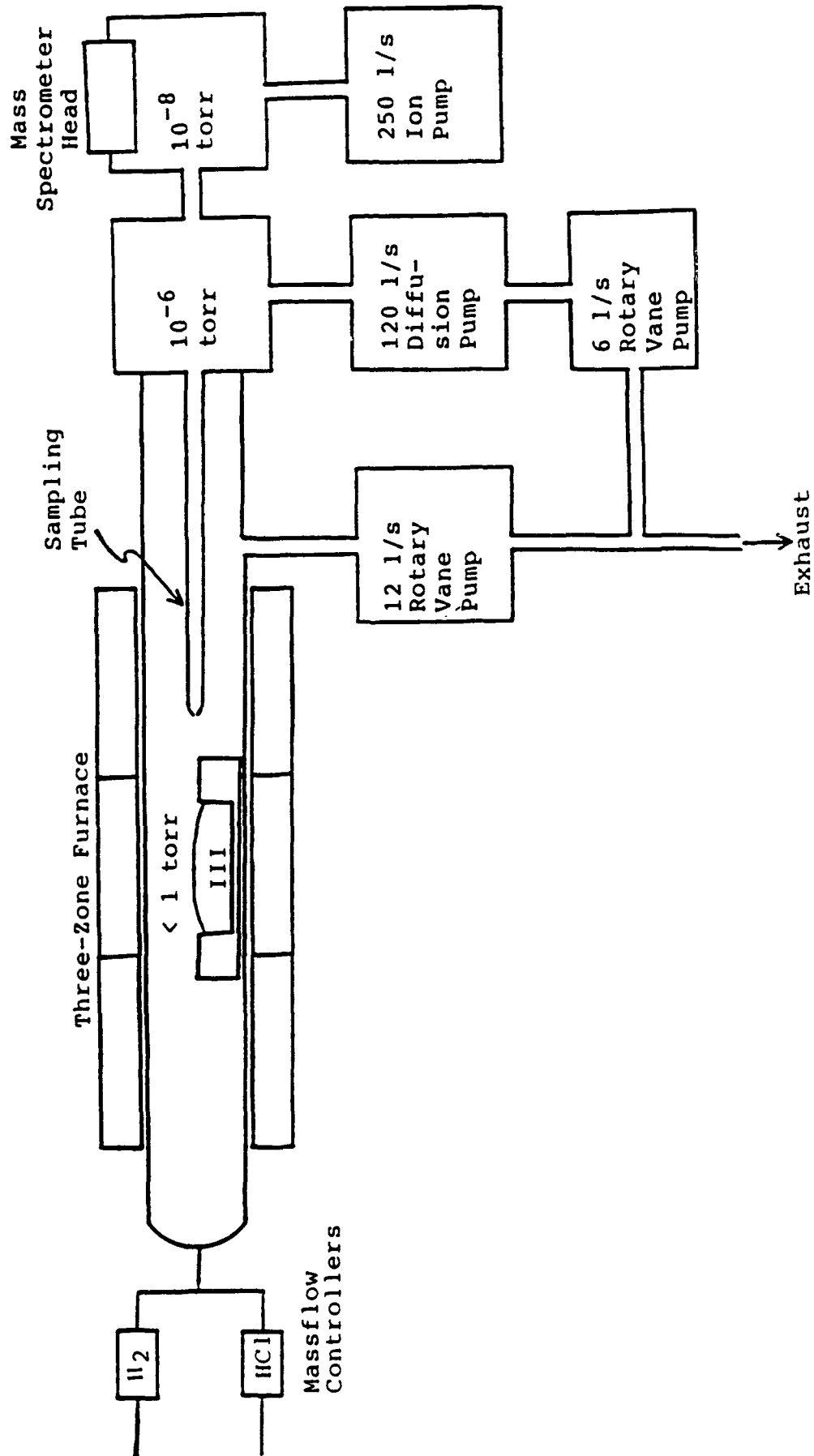


Figure B-1a

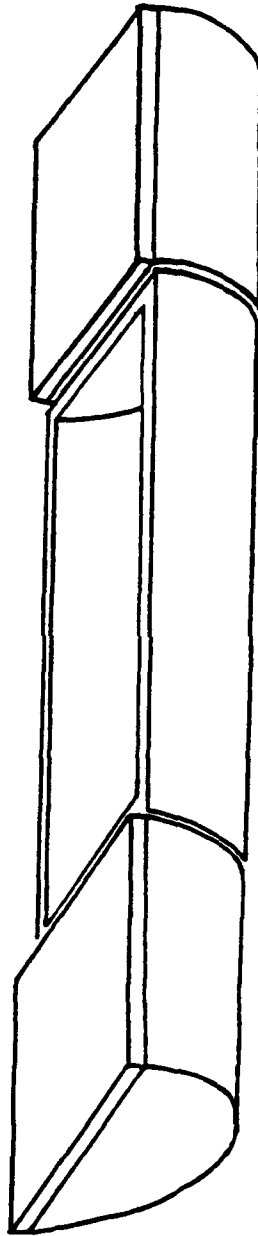


Figure B-1b

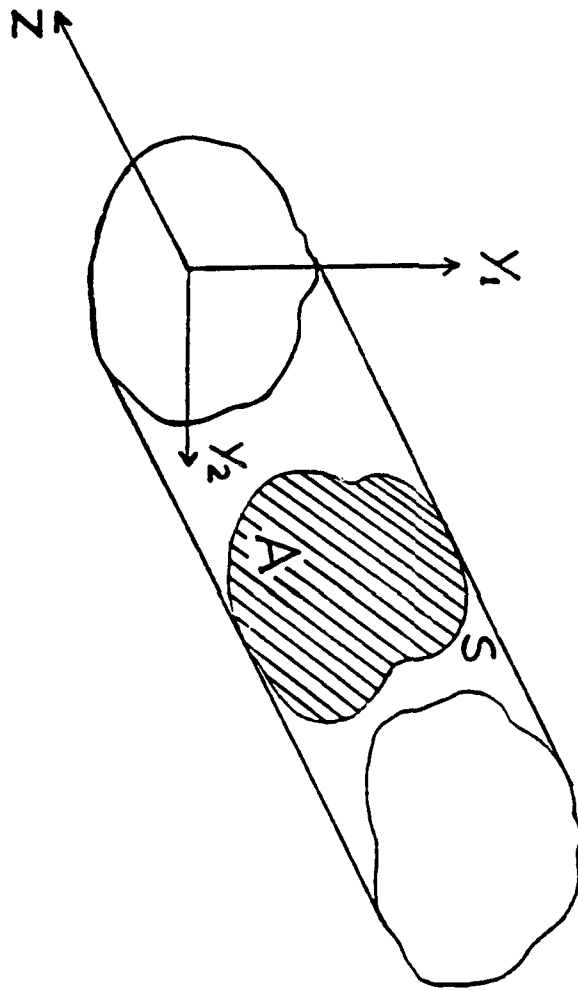


Figure B-2a

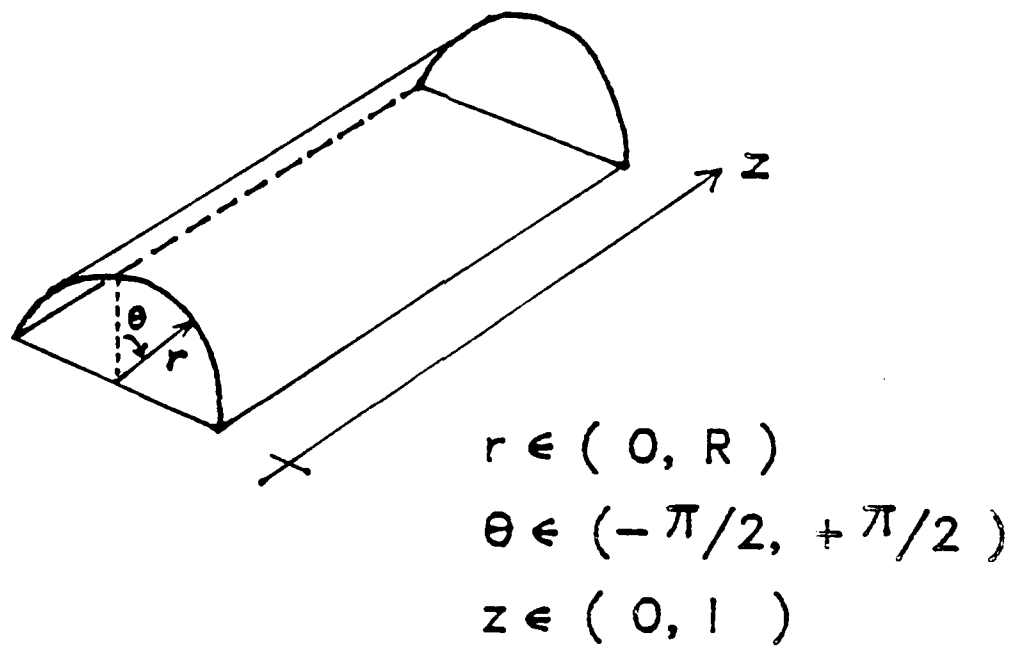


Figure B-2b

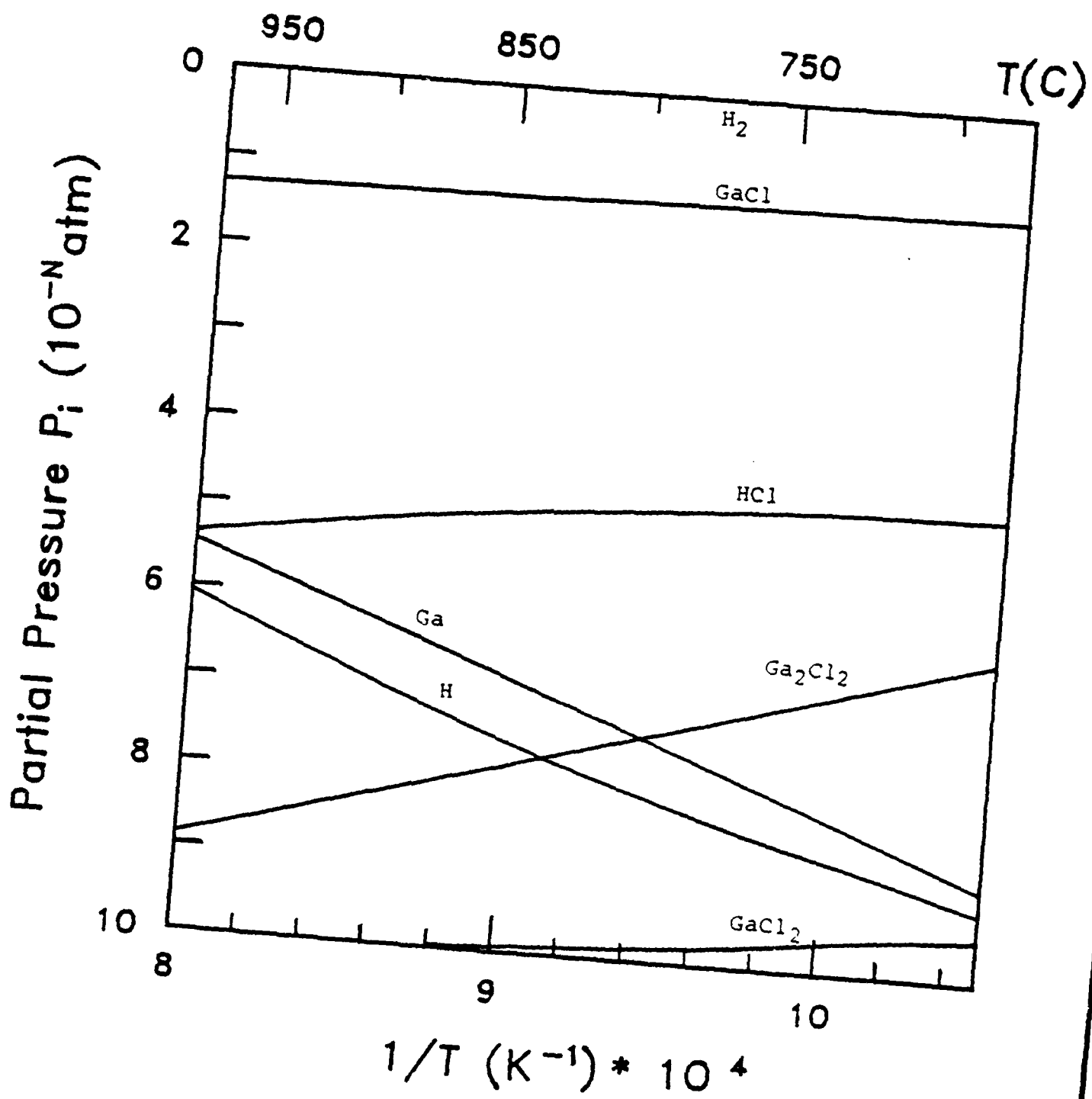


Figure B-3a

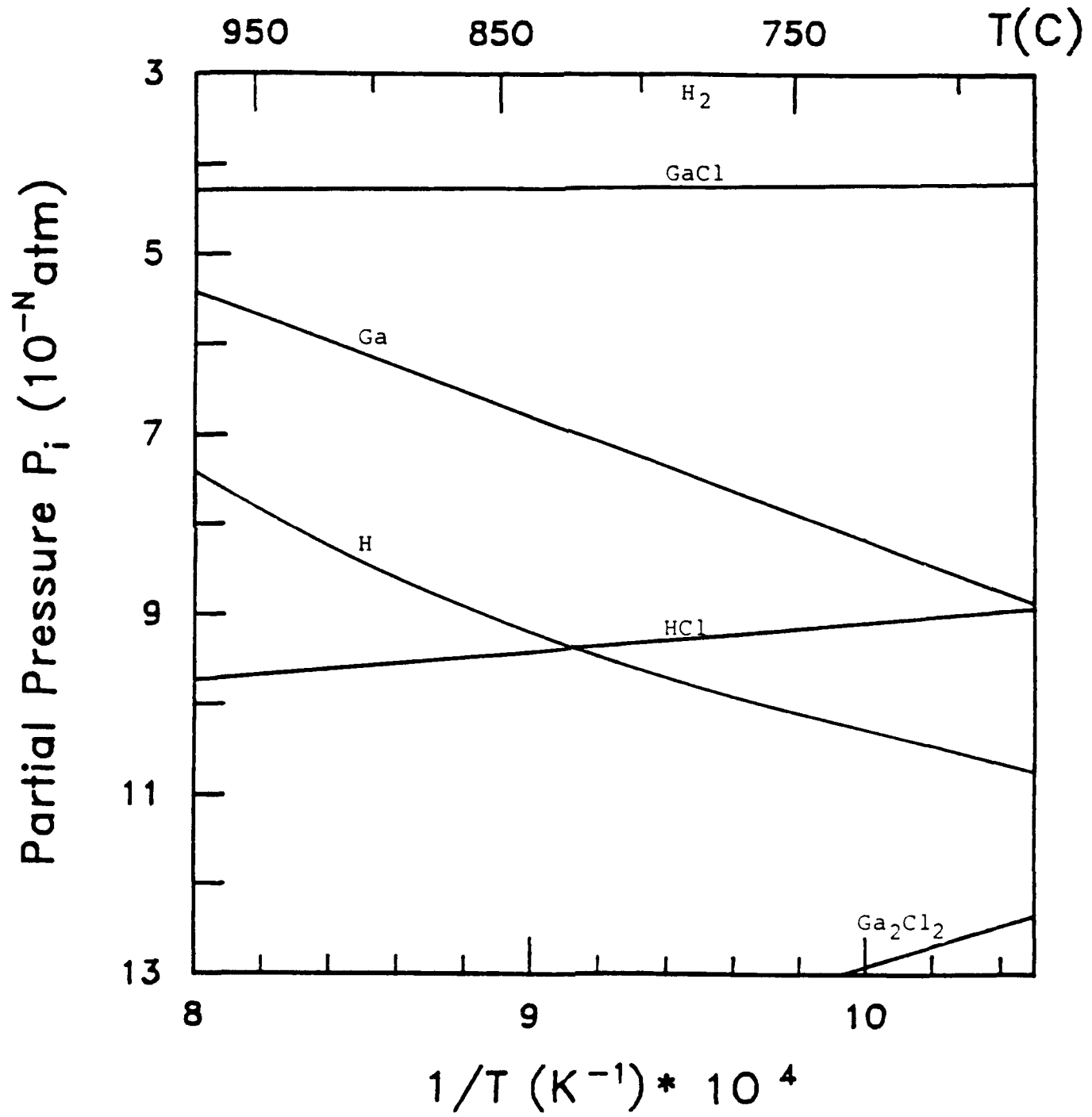


Figure B-3b

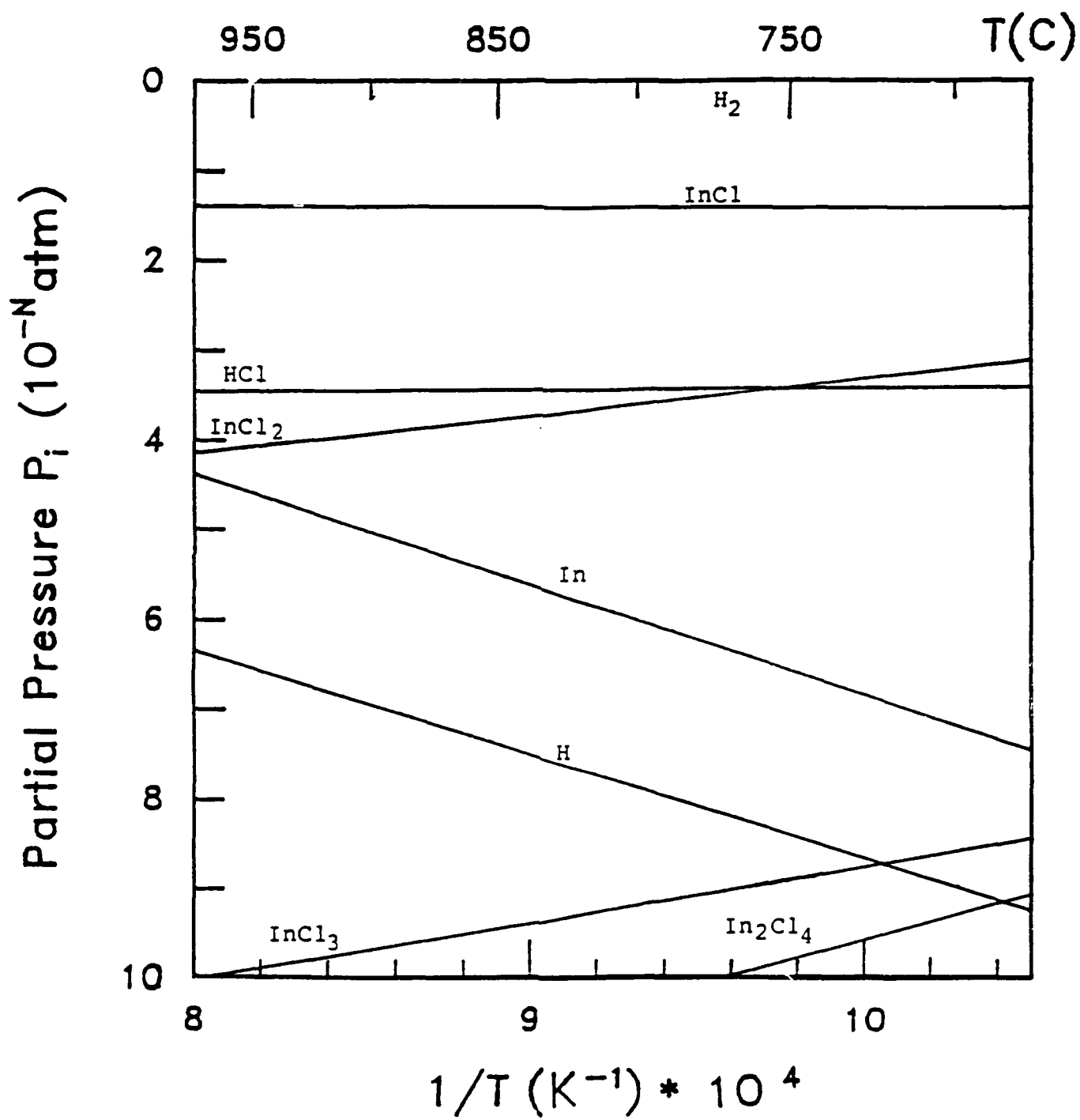


Figure B-4a

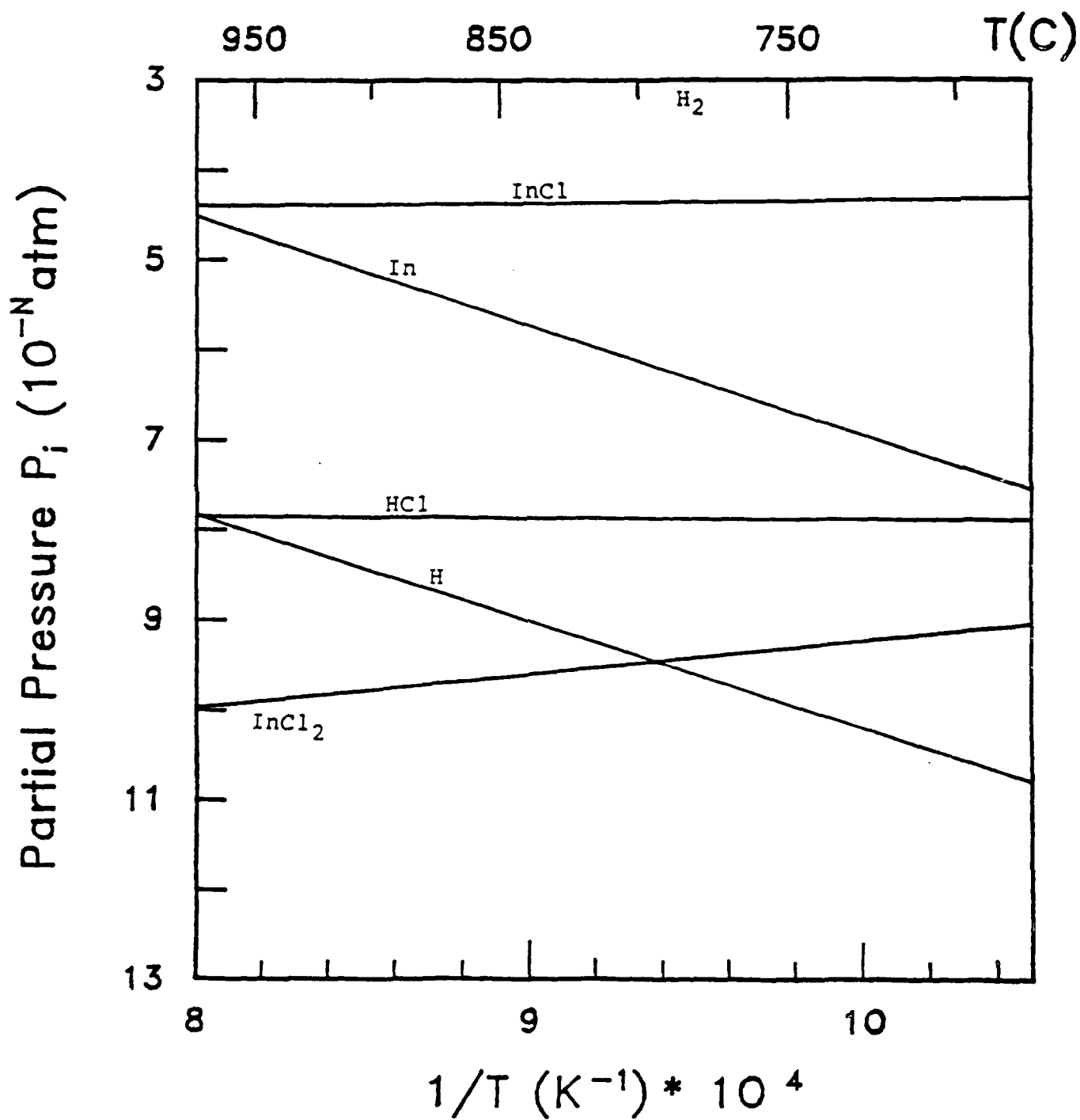


Figure B-4b

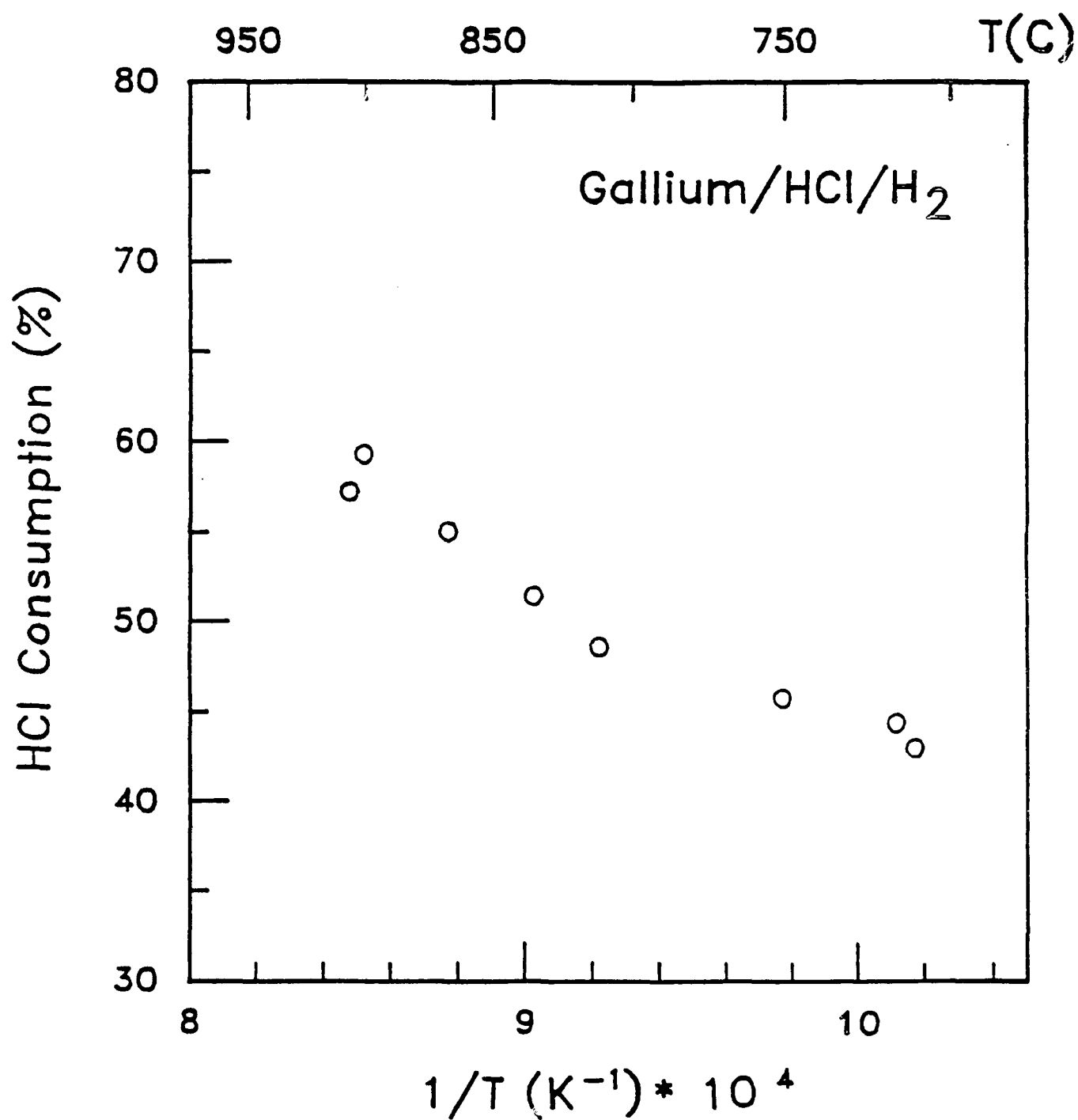


Figure B-5

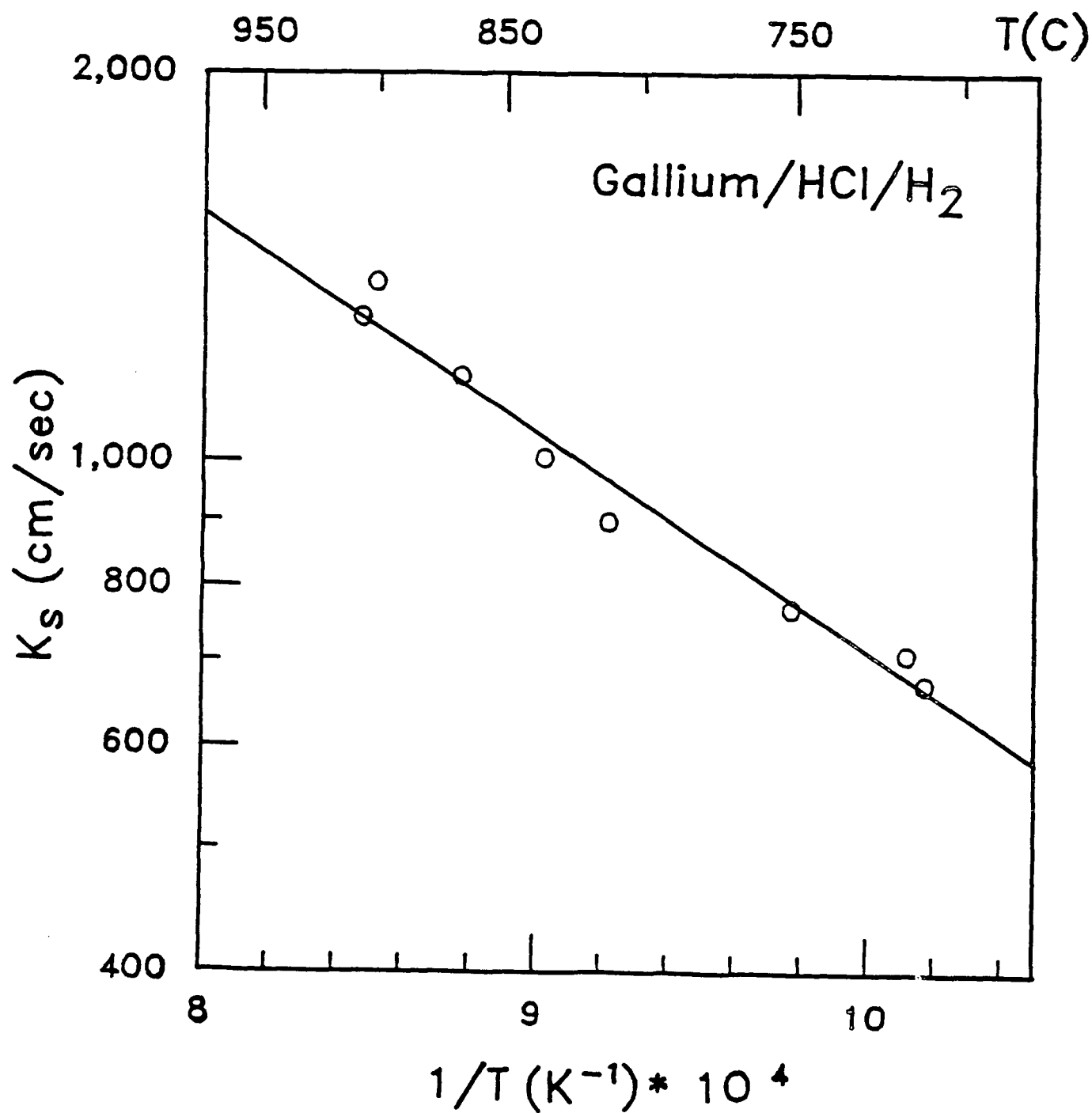


Figure B- 6

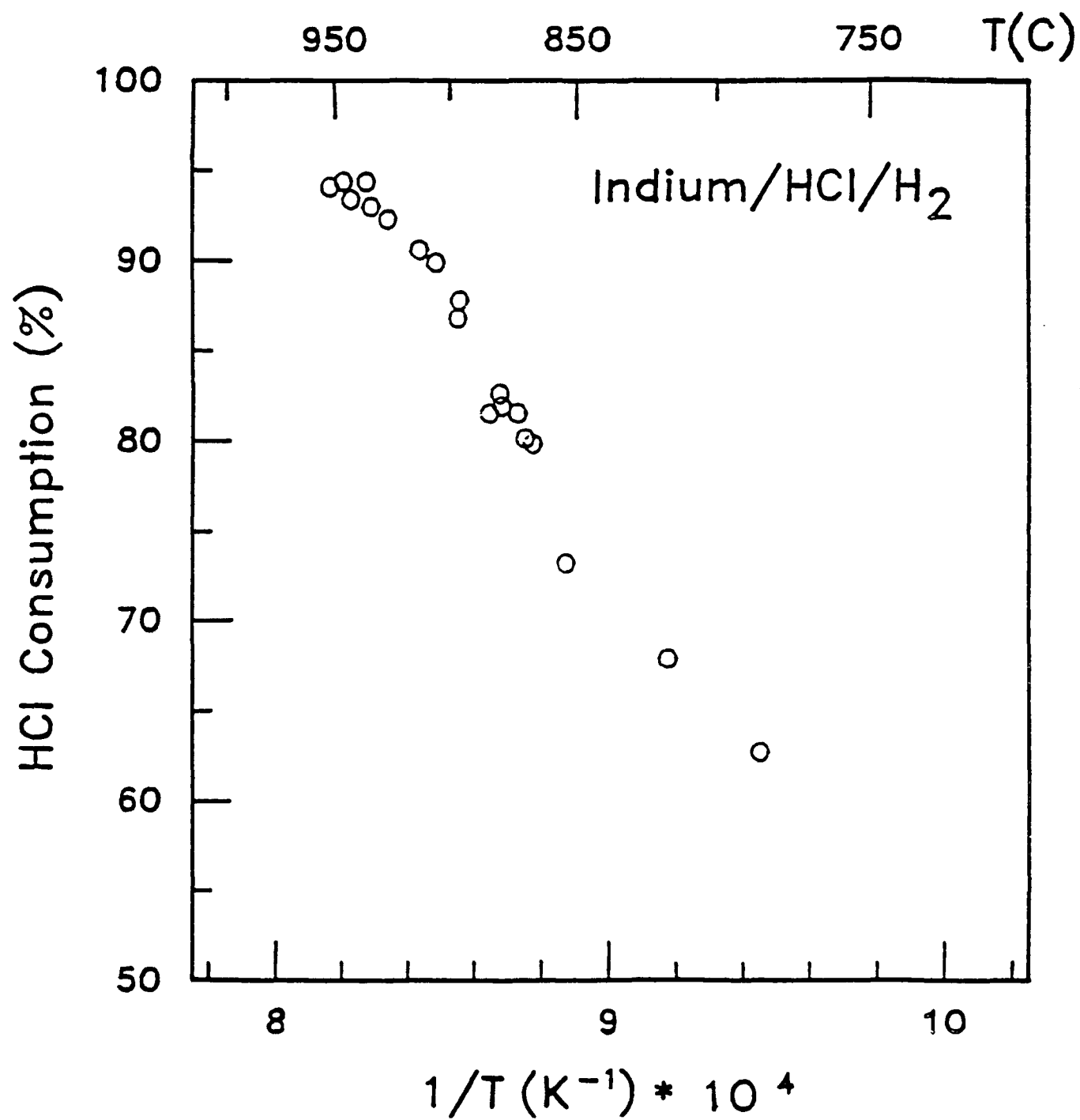


Figure B-7

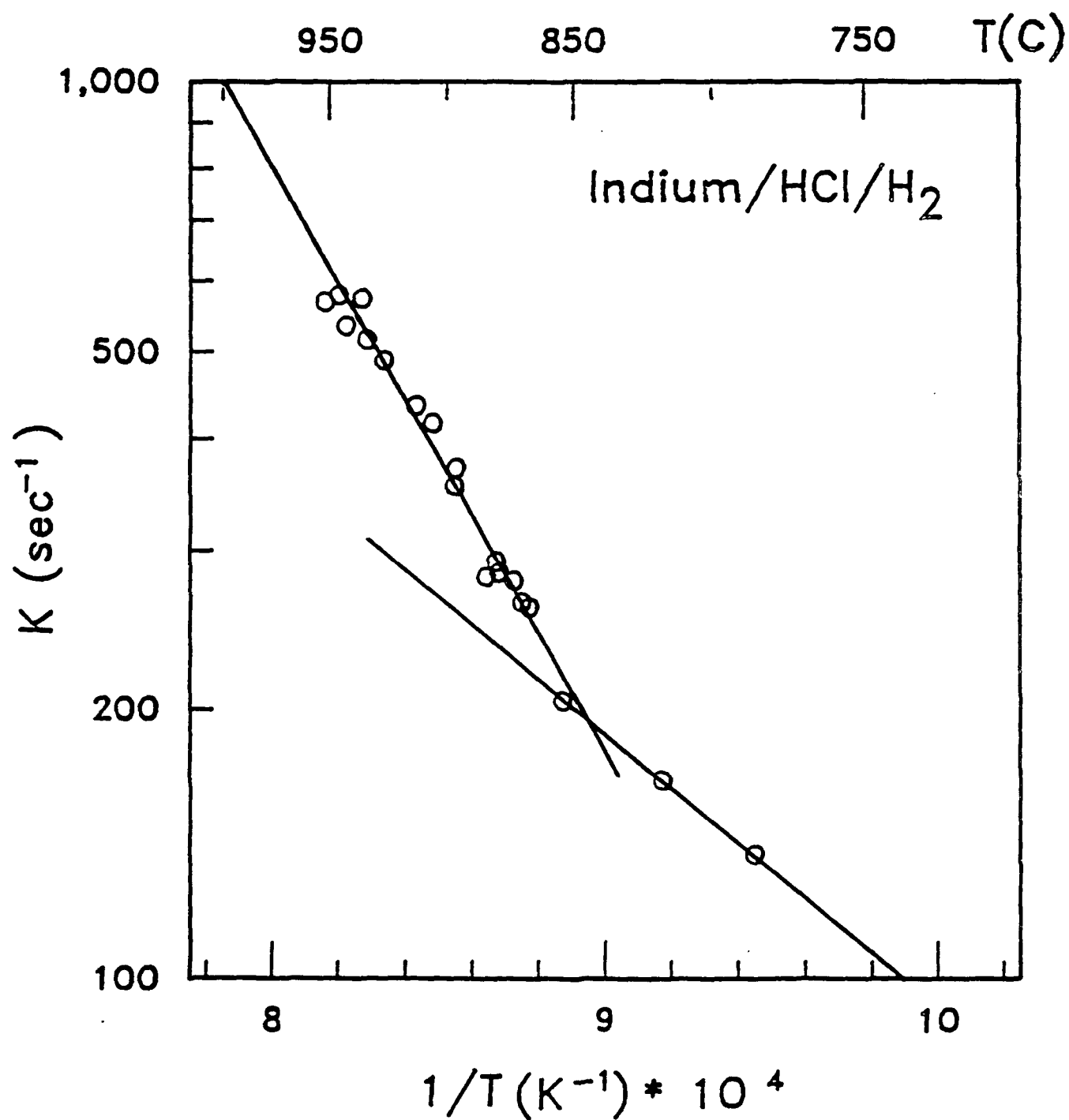


Figure B-8

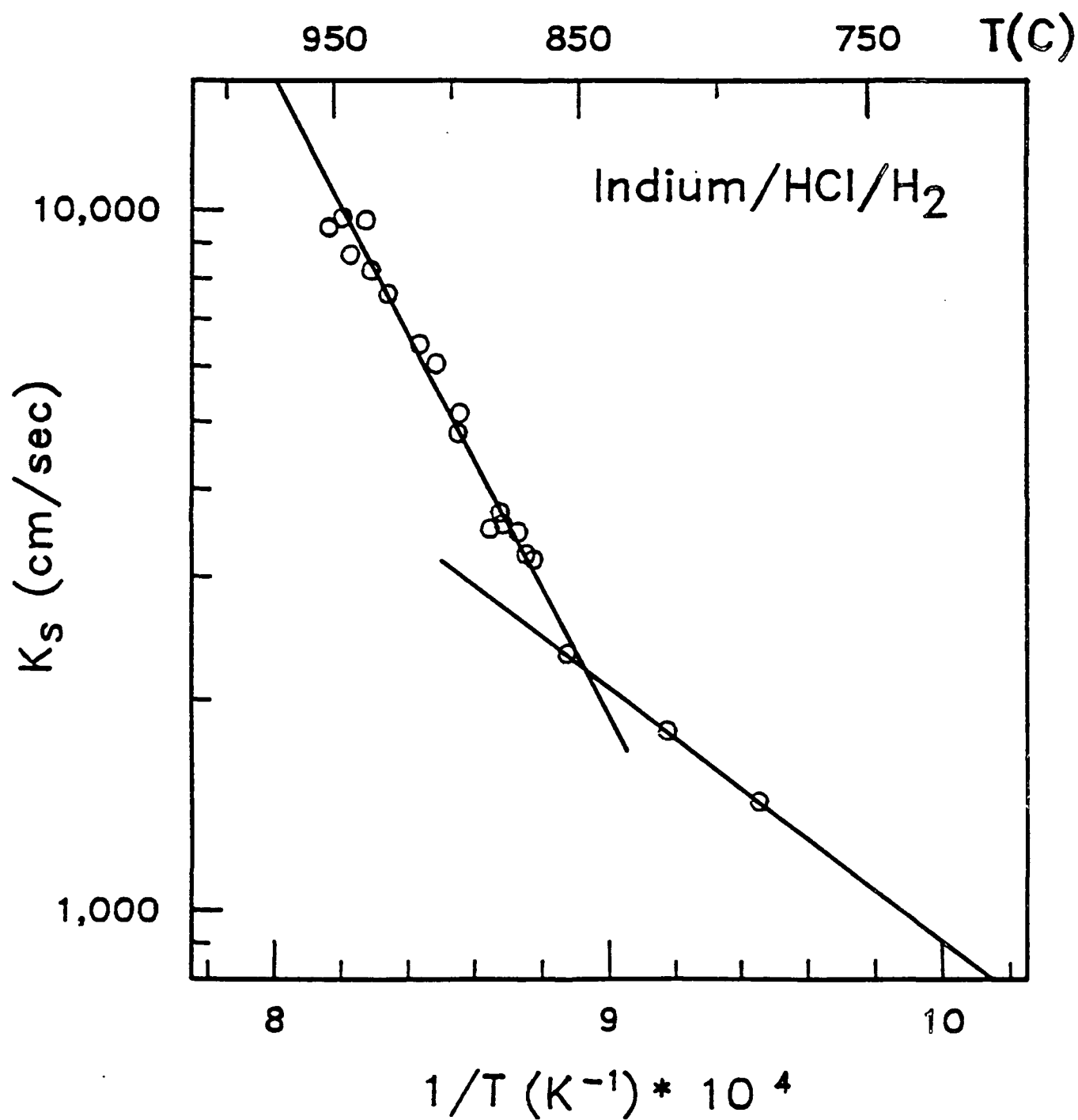


Figure B-9

Appendix C

EXPERIMENTAL STUDY OF GALLIUM AND INDIUM SOURCE TRANSPORT AT NORMAL PRESSURE

C.1 Introduction

The performance of gallium and indium source reactors at normal pressure (1 atm) has been experimentally studied by several investigators. Ban [27,28] and Ban and Ettenberg [29] sampled the outlet vapor stream of Ga and In source boats by means of a capillary coupled to a time-of-flight mass spectrometer. Measurements of HCl conversion in carrier gas H_2 as a function of flowrate, HCl partial pressure and temperature were made. The effects of the replacement of H_2 by He and of HCl by Cl_2 on the transport of Ga were also studied. The results indicated that GaCl and InCl are the only chlorides formed. Furthermore, the conversion values demonstrated that incomplete conversion of HCl occurred in their system. The Ga and In transport rates did not change when different reactants (HCl or Cl_2) or different carrier gases (He or H_2) were used.

The indium transport rate is almost always less than the gallium transport rate. The HCl conversion for an In source reactor has also been studied by Ban and Ettenberg [29] to show no dependence on HCl inlet partial pressure. Karlicek and Bloemeke [31] applied UV absorption spectroscopy to measure gallium and indium source boat effluent concentrations with results consistent with the previous fluorescence studies [30]. The transport of InCl from the indium source boat was found to continue for several minutes after the input HCl was turned off. The effect indicates an appreciable amount of InCl dissolved in the melt indium. The duration of continued InCl transport was stated to depend on the flowrate and the concentration of HCl used before the HCl was turned off. A similar effect for continued GaCl transport from

the gallium boat, though not as pronounced as for InCl, was also observed. The results of the previous investigations indicate that the mono-chloride is the major reaction product and non-equilibrium conversions are often encountered in the range of process conditions used for hydride deposition of Ga or In containing films. Furthermore, the strong dependence of conversion on temperature and flowrate suggest that both mass transfer and kinetic limitations are responsible for the non-equilibrium rates.

C.2 Experimental Method

A schematic diagram of the normal pressure experimental setup is shown in figure C-1. The source boat was contained in a 38 mm O.D. quartz tube approximately 130 cm in length and heated by a three-zone resistance furnace. The furnace was equipped with external shunts so that a flat temperature profile across the source boat could be maintained (± 2 K).

The gas manifold system, constructed with stainless steel tubing and VCR fittings, accepted pure HCl and palladium-alloy diffused H₂. Gas flows were regulated with Tylan-brand electronic mass flow controllers. A schematic representation of the gas manifold system is shown in figure C-2.

In order to eliminate hydrodynamic and thermal entrance region effects in the reaction zone, the source boats were constructed as shown in figure C-3. The outside diameter of the semi-cylindrical quartz boats coincided with the inside diameter of the reactor tube to isolate the gas flow above the melt. The source boat was 10.5 cm in length. Two similar boats (7.5 cm length), only covered by a rectangular quartz flat, were placed adjacent to the front and back of the metal source boat. These boats served as hydrodynamic and thermal stabilizers which reduced the effects of entrance region disturbances and provided axial and laminar flow conditions. Because the thermodynamic and

thermal entry lengths increase primarily with increasing flowrate, it has been calculated that the assumption of axial laminar gas flow above the melt is appropriate when the flowrate of carrier gas H_2 is less than 5,000 sccm.

The source boat was admitted into the reactor from the front open end, which was fused with a female sleeved ground-joint and could be sealed by the matching male ground-joint cap. Seal between the joints was achieved by placing rubber bands around the sleeves; Trapezon-brand grease was used to prevent gas leakage. Compression O-ring fittings was used to connect the stainless steel gas tubing and the pyrex glass tubing, fused onto the ground-joint cap.

Group III chlorides, generated as a result of the source transport reactions, were collected from the exit end of the quartz reactor by a series of three ice-bathed cold traps. Both cold traps were 25 cm long, made of 25 mm diameter pyrex glass tubing with a sealed bottom. The connection tubing between these traps was 15 mm in diameter. Size 40/50 ball-socket joints with metal clamps were used exclusively between the reactor exit end and the first cold trap and between the rest of the cold traps. The second and third cold traps were filled with glass rings, 1/4" in both diameter and length, to improve the cooling rate and condensation efficiency. It was found that if the flowrate of H_2 carrier gas was too low, then the condensation would start in the reactor and incomplete collection would result. But if the flowrate of H_2 carrier gas was too high, the condensation efficiency would decrease appreciably and part of the condensable chlorides could pass the cold traps uncollected. To allow complete collection of group III chlorides by the described collection setup, it was determined that the flowrate of H_2 carrier gas had to be between 600 sccm and 2000 sccm. The unreacted HCl in the exhaust was collected by bubbling the exhaust gas stream from the cold traps through

distilled water. The exhaust gas from the water bubbler was confirmed by mass spectrometry to contain only carrier gas H_2 .

After each experiment the group III chloride condensate in the cold traps was dissolved in aqua regia and diluted for atomic absorption spectrometric measurement, from which the total weight of group III metal in the condensate, or the transport rate of Ga or In, was deduced. The amount of gallium or indium in the water bubbler was also measured by atomic absorption and used to verify the completeness of the collection of III metal chlorides by the cold traps. The amount of unreacted HCl was determined by precipitation titration of chloride ions by the Mohr method [37].

C.3 Data Analysis

Because of the restriction imposed by the collection technique, the flowrate of H_2 carrier gas, chosen for experimental studies, was 1,000 sccm, 1,500 sccm and 2,000 sccm. The HCl flowrate was 10 sccm, 15 sccm and 20 sccm. The studied temperature range was between 999 and 1131 K.

The flowrates were low enough to insure that the hydrodynamic and thermal entrance region effects could be eliminated by the flat-quartz stabilizers, and ideal axial laminar flow was established in the reaction zone. The Peclet number at these flowrates was also high enough (larger than 10) for the axial diffusion in the reactor to be neglected. The mass transport in the reactor should be well described by the 2-D convective diffusion model, discussed in Appendix B. The following equation was used for data analysis of this experimental study.

$$\eta = \sum_{i=1}^{\infty} B_i \left\{ \frac{Pe_A + Pe_C}{\lambda_i^2} [\sin(\lambda_i \sqrt{Pe_C}) \sin(\lambda_i \sqrt{Pe_A})]^2 \exp[-\lambda_i^2 (L/l)] \right\} \quad C-1$$

C.4 Results and Discussion

C.4.1 Gallium Source Transport

Transport Rate vs. Total Flowrate The gallium transport factor $Ga/Cl,(\eta)$, was studied at $T = 1068$ K for three different total flowrates with identical input H_2 to HCl ratio. These flowrates were 1,000 sccm $H_2 + 10$ sccm HCl , 1,500 sccm $H_2 + 15$ sccm HCl and 2,000 sccm $H_2 + 20$ sccm HCl . The experimental results, presented in figure C-4, show a strong dependence on the total flowrate. Equilibrium gallium transport is also indicated in figure C-4 by the broken line, and non-equilibrium conversion was clearly observed under these experimental conditions.

Transport Rate v.s. Input HCl Concentration By fixing the H_2 flowrate and varying the input HCl flowrate, the effect of input HCl concentration on the gallium transport factor was determined. As shown in figure C-5, the input HCl concentration was varied in the range $0.5 < \%HCl < 1.0$ for H_2 flowrates of 1,500 sccm and 2,000 sccm. The transport factor showed no dependence on the input HCl concentration in both cases, indicating a linear relationship between the input HCl flowrate and the group III chloride transport rate. This result validates the assumption of the first-order rate expression, used in the development of the model equation (C-1) (see Appendix B).

Transport Rate vs. Temperature The temperature dependence of the gallium transport rate was extensively studied in the temperature range $999 < T < 1131$ K, and the gallium transport factor was calculated and shown in figure C-6. Since the gallium transport factor was found to be independent of the input HCl concentration, the HCl flowrate for the temperature dependence study was fixed at 10 sccm while different H_2 flowrates, 1,000 sccm, 1,500 sccm and 2,000 sccm, were used. As was expected, the gallium transport rate increases

with increasing temperature and decreasing H_2 flowrate. However, equilibrium conversion (the broken line in figure C-6) was not achieved even at the highest temperature and lowest flowrate used in this study.

Unreacted HCl The unreacted HCl was collected in the water bubbler and determined by precipitation titration of chloride ions. The HCl conversion is plotted in figure C-7. Similar dependencies of HCl conversion on temperature, flowrate and input HCl concentration were obtained. Theoretically, the HCl conversion should be equal to the gallium transport factor (equation (C-1)) if gallium monochloride is the only product of the source transport reaction. Results in figure C-6 and C-7 show that the gallium transport factor was closer to the HCl conversion at higher temperature and lower flowrate, or when the reactor was operated closer to equilibrium conditions. It was realized that since product sampling was performed far from the reaction zone where the reaction products had cooled considerably from the reaction temperature, the chemical composition of the product gas could have changed appreciably as a result of the chemical reactions during the course of transport. The experimentally observed HCl conversion, therefore, can be very different from that at the immediate exit of the reaction zone. The gallium transport factor was, however preserved during the transport process since no deposit was observed along the transport path between the reaction zone and the sampling devices. The exact chemical composition of the product gas was unknown, but should be primarily gallium monochloride when both the gallium transport factor and the HCl conversion were found close to equilibrium prediction, i.e. at low flowrate (1000 sccm H_2), or at a temperature higher than 1050K.

Determination of Rate Constant The experimental results in figure C-6 were reduced by equation (C-1) to determine the first-order kinetic rate constant k_g . The diffusion coefficients of HCl and GaCl in H_2 were taken [35] to be

$$D_{\text{HCl}, \text{H}_2} (\text{cm}^2/\text{sec}) = 5.32 \times 10^{-5} P(\text{atm})^{-1} T(\text{K})^{1.664} \quad (\text{C-2})$$

and

$$D_{\text{GaCl}, \text{H}_2} (\text{cm}^2/\text{sec}) = 2.87 \times 10^{-5} P(\text{atm})^{-1} T(\text{K})^{1.736} \quad (\text{C-3})$$

The calculated values of the first order rate constant are plotted in figure C-8 as a function of reciprocal absolute temperature. The results are too scattered to give a linear relationship between the rate constant and reciprocal absolute temperature. It was discovered later that the gallium transport rate in this experimental study could be explained by a diffusion-limited model and the calculation of the kinetic rate constant could be very sensitive to experimental error. The calculated rate constant in figure C-8 is, therefore, accurate only within an order of magnitude. An attempt was made to compare the results in figure C-8 with Ban's [28] experimental data. The dimension of the reactor used in Ban's experiments was estimated first. The reported HCl conversion was assumed to be equal to the gallium transport factor (equation (C-1)) and reduced by the 2-D convective diffusion model to yield the rate constant. The calculated rate constant from Ban's data, also shown in figure C-8, has the same order of magnitude as the ones from this study. A least squares fit of these calculated rate constants was finally performed and the rate constant was determined to be

$$k_s (\text{cm}/\text{sec}) = 2.12 \times 10^6 \exp(-11,575/T (\text{K})) \quad (\text{C-4})$$

Using model equation (C-1), the diffusion coefficients, equations (C-2) and (C-3), and the rate constant, equation (C-4), the reactor performance can be calculated for any given condition. The result of this calculation is given in figures C-4, C-5 and C-6 by the solid curves. These solid curves clearly demonstrate that the 2-D convective diffusion model satisfactorily fits the experimental data. The dotted curve, shown in figure C-4, is the predicted reactor performance from the diffusion-limited model, which represents a special case of equation (C-1). The closeness of the solid and the dotted curves indicates that the gallium transport process at the studied conditions is almost diffusion-limited and the reaction kinetics has only a slight effect on the transport rate.

C.4.2 Indium Source Transport

Transport Rate vs. Total Flowrate The indium transport factor, In/Cl , defined in equation (C-1), was studied at $T = 1068$ K for three different total flowrates with identical input H_2 to HCl ratio. The flowrates were 1,000 sccm $H_2 + 10$ sccm HCl , 1,500 sccm $H_2 + 15$ sccm HCl and 2,000 sccm $H_2 + 20$ sccm HCl . The experimental result, presented in figure 7-9, shows a strong dependence on the total flowrate. Equilibrium indium transport is also indicated in figure C-9 by the broken line, and non-equilibrium conversion was clearly observed at these experimental conditions.

Transport Rate vs. Input HCl Concentration By fixing the H_2 flowrate and varying the input HCl flowrate, the effect of input HCl concentration on indium transport factor was determined. As shown in figure C-10, the input HCl concentration was varied in the range $0.5 < \%HCl < 1.0$ for H_2 flowrates of 1,500 sccm and 2,000 sccm. The transport factor showed no dependence on the input HCl concentration in both cases, indicating a linear relationship be-

tween the input HCl flowrate and indium chloride transport rate. This result validates the assumption of the first-order rate expression, used in the development of model equation (C-1).

Transport Rate vs. Temperature The temperature dependence of the indium transport rate was extensively studied in the temperature range 999-1131 K, and the indium transport factor was calculated and shown in figure C-11. Since the indium transport factor was found to be independent of the input HCl concentration, the HCl flowrate for the temperature dependence study was fixed at 10 sccm while different H₂ flowrates, 1,000 sccm, 1,500 sccm and 2,000 sccm, were used. As expected, the indium transport rate increases with increasing temperature and decreasing H₂ flowrate. However, equilibrium conversion (the broken line in figure C-11) was not achieved even at the highest temperature and lowest flowrate used in this study.

Unreacted HCl The unreacted HCl was collected in the water bubbler and determined by precipitation titration of chloride ions. The HCl conversion, as defined in equation (C-1), is plotted in figure C-12. Similar dependence of HCl conversion on temperature, flowrate and input HCl concentration was obtained. Theoretically, the HCl conversion should be equal to the indium transport factor (equation (C-1)) if indium monochloride is the only product of the source transport reaction, and could be less than the indium transport factor if higher chlorides, other than monochloride, appear as reaction products. Good agreement between figures C-11 and C-12 indicates that indium monochloride should be the dominant reaction product in the studied conditions.

Determination of Rate Constant The experimental result in figure C-11 was reduced by equation (C-1) to determine the first-order kinetic rate constant k_s . Equation (C-2) was used for the diffusion coefficient of HCl in H₂. The diffusion coefficient InCl in H₂ was approximated to be

$$D_{\text{InCl}, \text{H}_2} (\text{cm/sec}) = 2.73 \times 10^{-5} P(\text{atm})^{-1} T(\text{K})^{1.7} \quad (\text{C-5})$$

The calculated values of the first order rate constant are plotted in figure C-13 as a function of reciprocal absolute temperature. The results show a linear relation with reciprocal absolute temperature and the rate constant was determined to be

$$k_s (\text{cm/sec}) = 4.13 \times 10^6 \exp(-12,851/T (\text{K})) \quad (\text{C-6})$$

Using model equation (C-1), the diffusion coefficients, equations (C-2) and (C-5), and the rate constant, equation (C-6), the reactor performance can be calculated for any given condition. The result of this calculation is given in figures C-9, C-10 and C-11 by the solid curves. It is clear that these solid curves match the experimental results satisfactorily. In order to understand the importance of both the diffusion and the kinetic mechanisms for the determination of the indium transport rate at the studied conditions, the calculated results of the kinetically-limited model and the diffusion-limited model are presented in figure C-14 by the dotted curves. The combined effect of these nonequilibrium mechanisms is realized in model equation (C-1) and described in figure C-14 by the solid curve.

The results and analysis of the normal pressure experiments shows that the 2-D convective diffusion model is adequate in describing the reactor performance in a flowthrough reactor at the studied operating conditions. The group III transport factor showed a first-order dependence on input HCl concentration which indicated that the overall reaction rate could be dominated by two possible processes; namely, molecular diffusion, and first order reac-

tion kinetics. Both processes exist in source reactors and one of the two processes can be dominant depending upon reactor design and operation. Flow-through reactor design should be carried out under two criteria, minimum material (group III metal) requirement and maximum process reproducibility. These two criteria, however, appear to be against each other since maximum process reproducibility entails long boats to ensure equilibrium conversion and incurs problems in trying to minimize material requirement. The difficulty in source reactor design is, therefore, to choose the appropriate reactor geometry and reactor length to satisfy the above criteria. With the determined rate constants for gallium (equation (C-4)) and for indium (equation (C-6)) source reactor performance can be easily simulated and reactor design can be checked numerically for improvements. In general, diffusion limitation should be eliminated or reduced to achieve efficient reactor operation which implies a kinetically controlled reactor. Since reaction kinetics only controls the local reaction rate, therefore, when the reactor residence time is long enough, equilibrium conversion is obtained and the overall reaction rate (group III transport rate) will follow the thermodynamic trend becoming temperature insensitive.

List of Figures

- Figure C-1. Schematic diagram of the normal pressure experimental apparatus.
- Figure C-2. Gas manifold for the experimental system.
- Figure C-3. Enlargement of the source boat design.
- Figure C-4. Gallium transport factor (Ga/Cl) versus total flowrate at $T = 1068$ K and HCl flowrate/ H_2 flowrate = 0.01. The broken line shows the maximum gallium transport at equilibrium. The solid curve is the result calculated from transport model equation (6-41), with rate constant k_s deduced from figure C-8. The dotted curve is the result calculated from the diffusion-limited case of transport model equation (6-41).
- Figure C-5. Gallium transport factor (Ga/Cl) versus percent HCl in the input flow at $T = 1068$ K. The broken line shows the maximum gallium transport at equilibrium. The solid curves are the results calculated from transport model equation (6-41), with rate constant k_s deduced from figure C-8.
- Figure C-6. Gallium transport factor (Ga/Cl) versus temperature at various flowrates. The broken line shows the maximum gallium transport at equilibrium. The solid curves are the results calculated from transport model equation (6-41), with rate constant k_s deduced from figure C-8.
- Figure C-7. HCl conversion versus temperature of gallium source reactor. The broken line shows the maximum gallium transport at equilibrium.
- Figure C-8. First order rate constant of gallium source reaction, k_s (cm/sec), versus reciprocal absolute temperature, deduced from experimental results in figure C-6 or Ban's data [71] and equation (6-41). The straight line approximates the temperature dependence of the rate constant, and is given by $2.12 \times 10^6 \exp(-11,575/T \text{ (K)})$.
- Figure C-9. Indium transport factor (In/Cl) versus total flowrate at $T = 1068$ K and HCl flowrate/ H_2 flowrate = 0.01. The broken line shows the maximum indium transport at equilibrium. The solid curve is the result calculated from transport model equation (6-41), with rate constant k_s deduced from figure C-13.
- Figure C-10. Indium transport factor (In/Cl) versus percent HCl in the input flow at $T = 1068$ K. The broken line shows the maximum indium transport at equilibrium. The solid curves are the results calculated from transport model equation (6-41), with rate constant k_s deduced from figure C-13.
- Figure C-11. Indium transport factor (In/Cl) versus temperature at various flowrates. The broken line shows the maximum indium transport at equilibrium. The solid curves are the results calculated

from transport model equation (6-41), with rate constant k_s deduced from figure C-13.

Figure C-12. HCl conversion versus temperature of indium source reactor.

Figure C-13. First order rate constant of indium source reaction, k_s (cm/sec), versus reciprocal absolute temperature, deduced from experimental results in figure C-11 and equation (6-41). The temperature dependence of the rate constant is given by $4.13 \times 10^6 \exp(-12,851/T \text{ (K)})$.

Figure C-14. Experimental results, obtained at H_2 flowrate = 1,000 sccm, HCl flowrate = 10 sccm and temperature range, $943 < T < 1131 \text{ K}$. The solid curve shows the calculated result from equation (6-41), considering both diffusion and kinetic limitations. The dotted curves show the calculated results from two special cases, the diffusion-limited case and the kinetically-limited case, of equation (6-41).

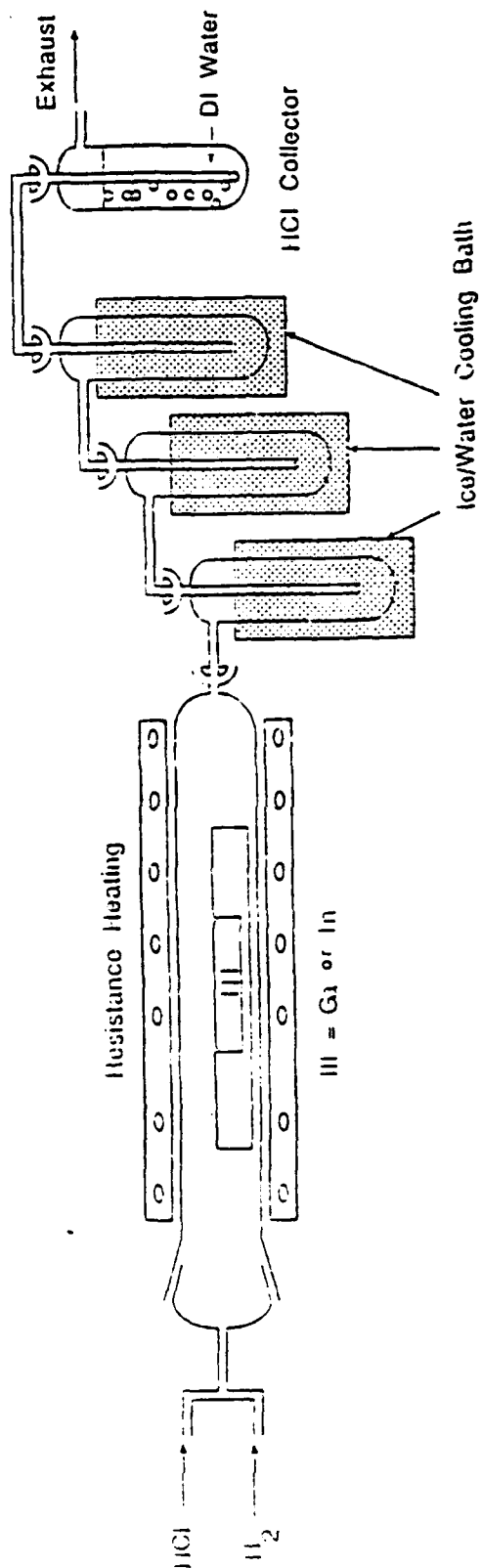


Figure C-1

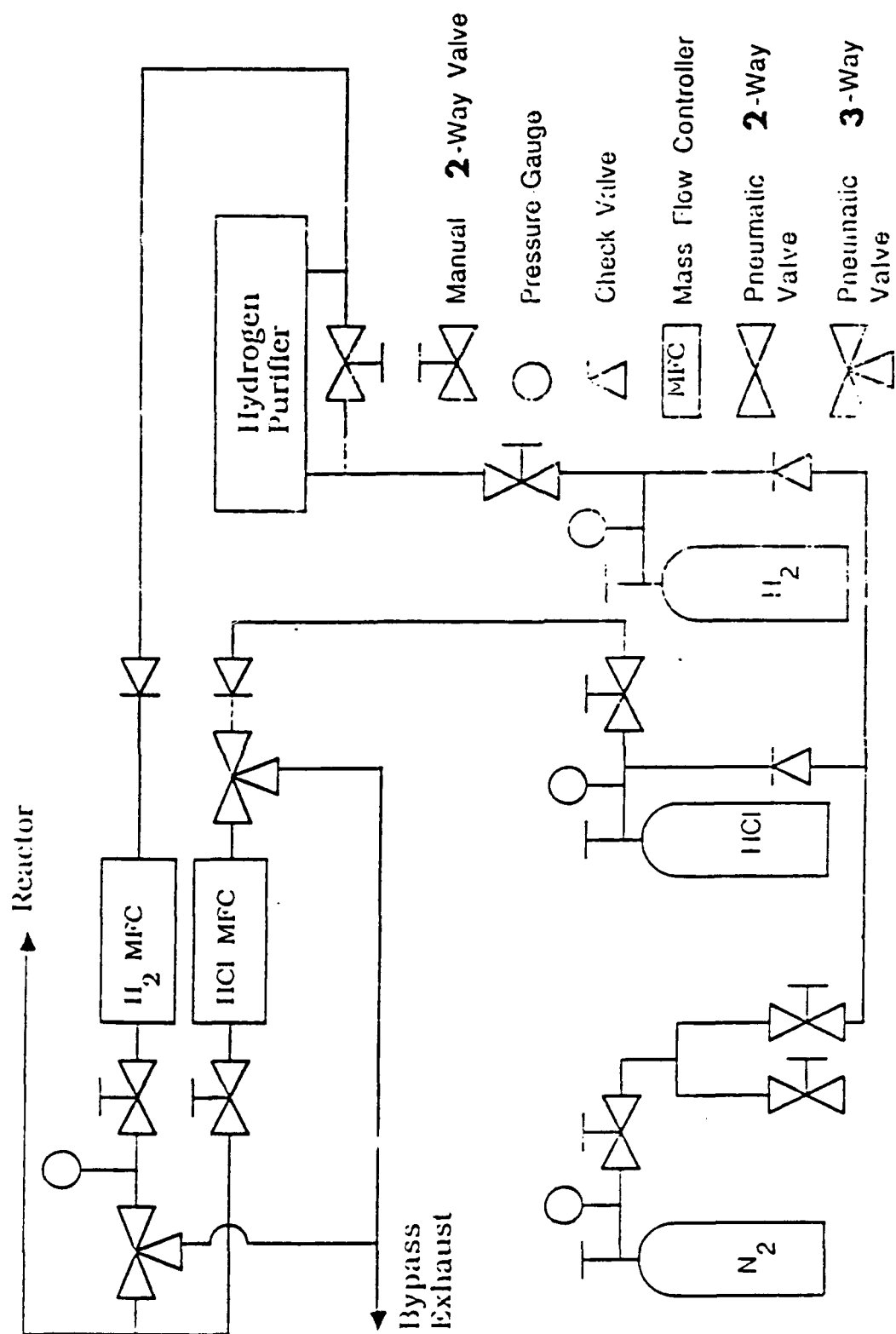


Figure C-2

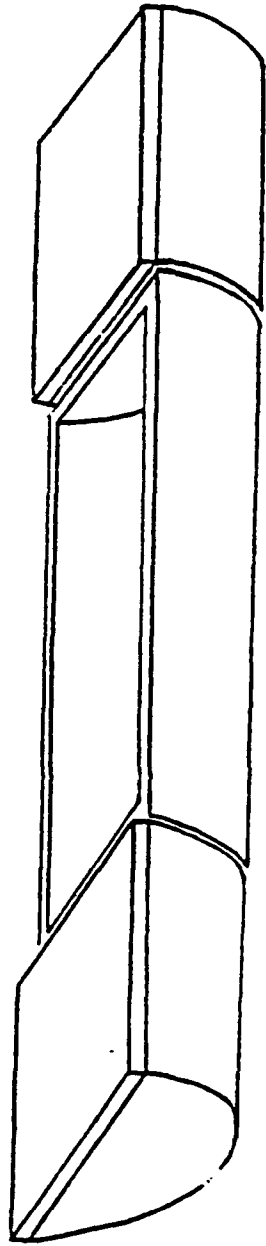


Figure C-3

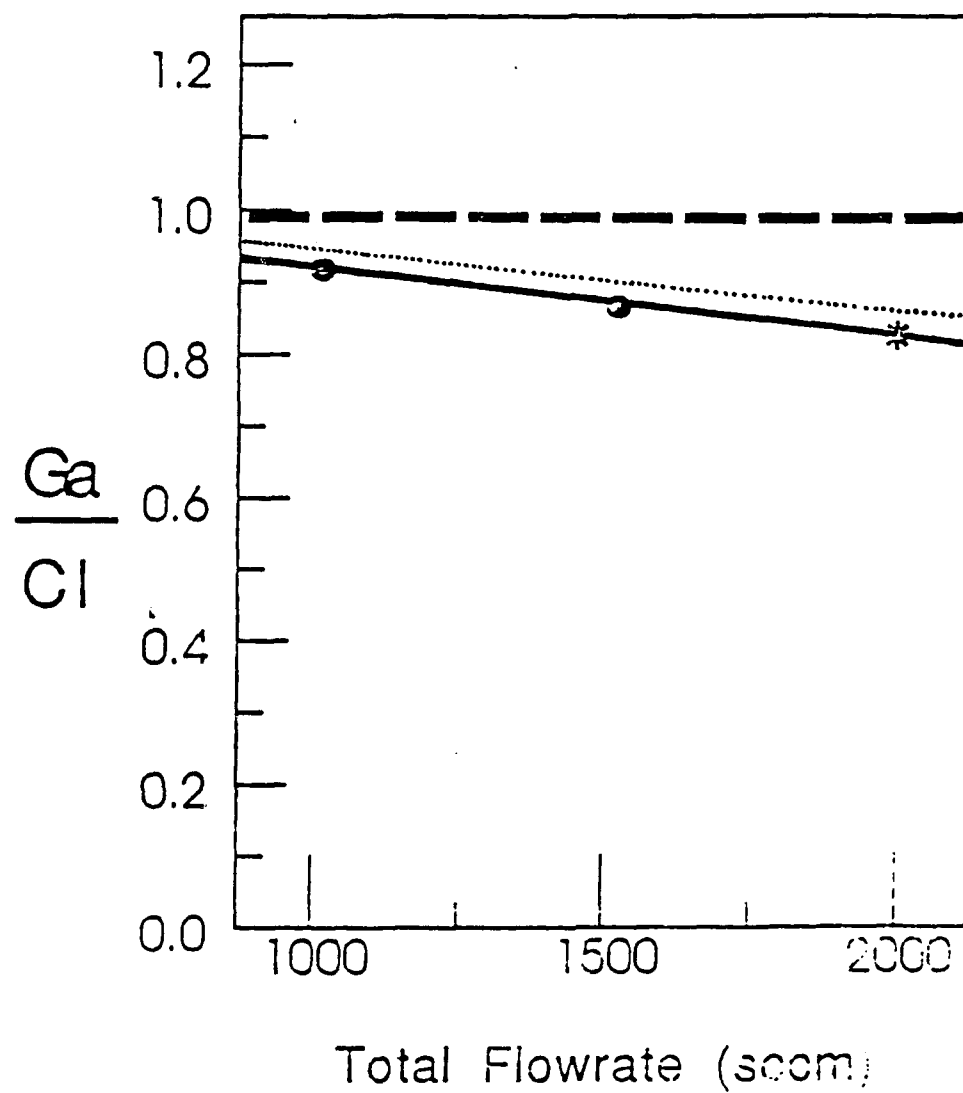


Figure C-4

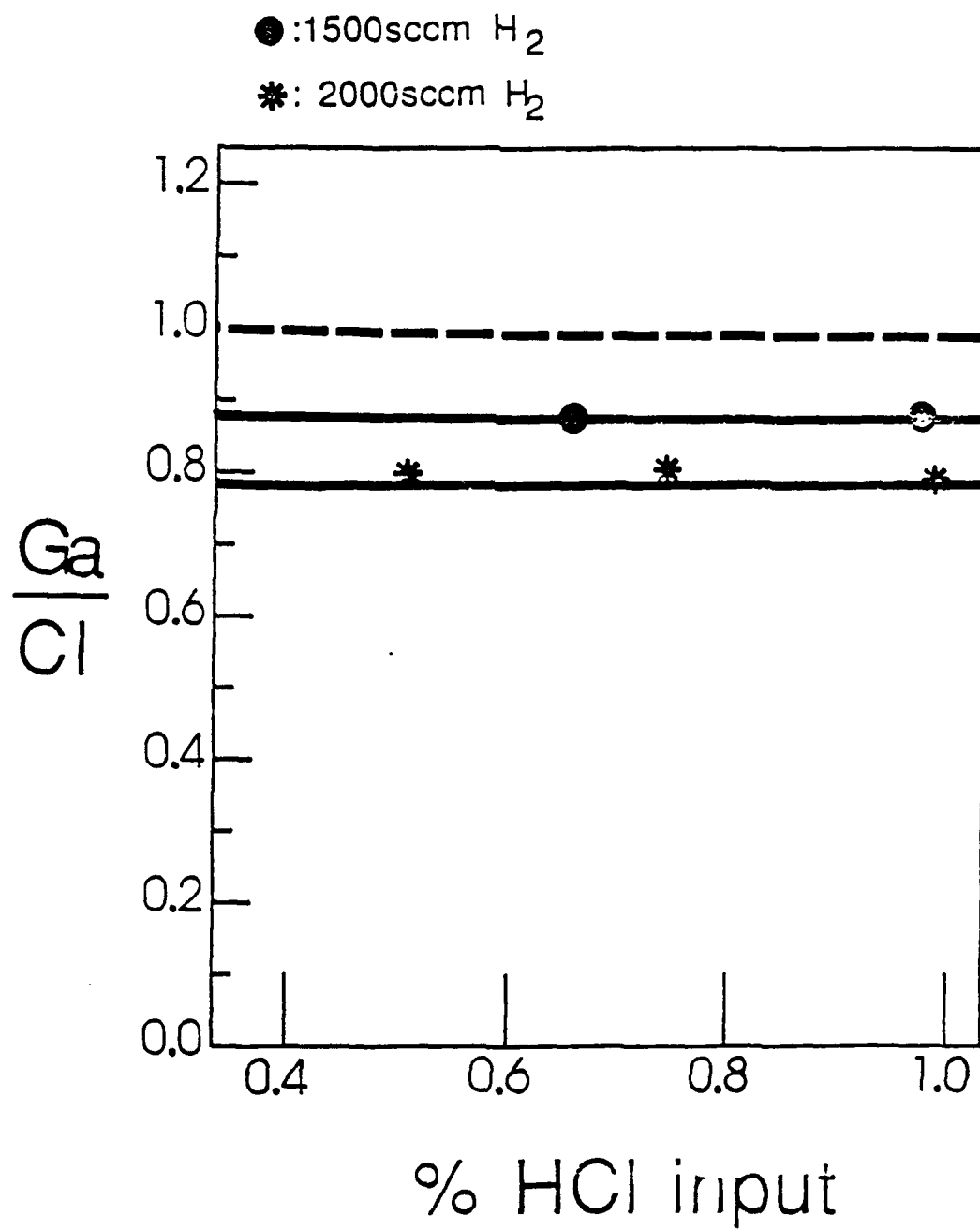


Figure C-5

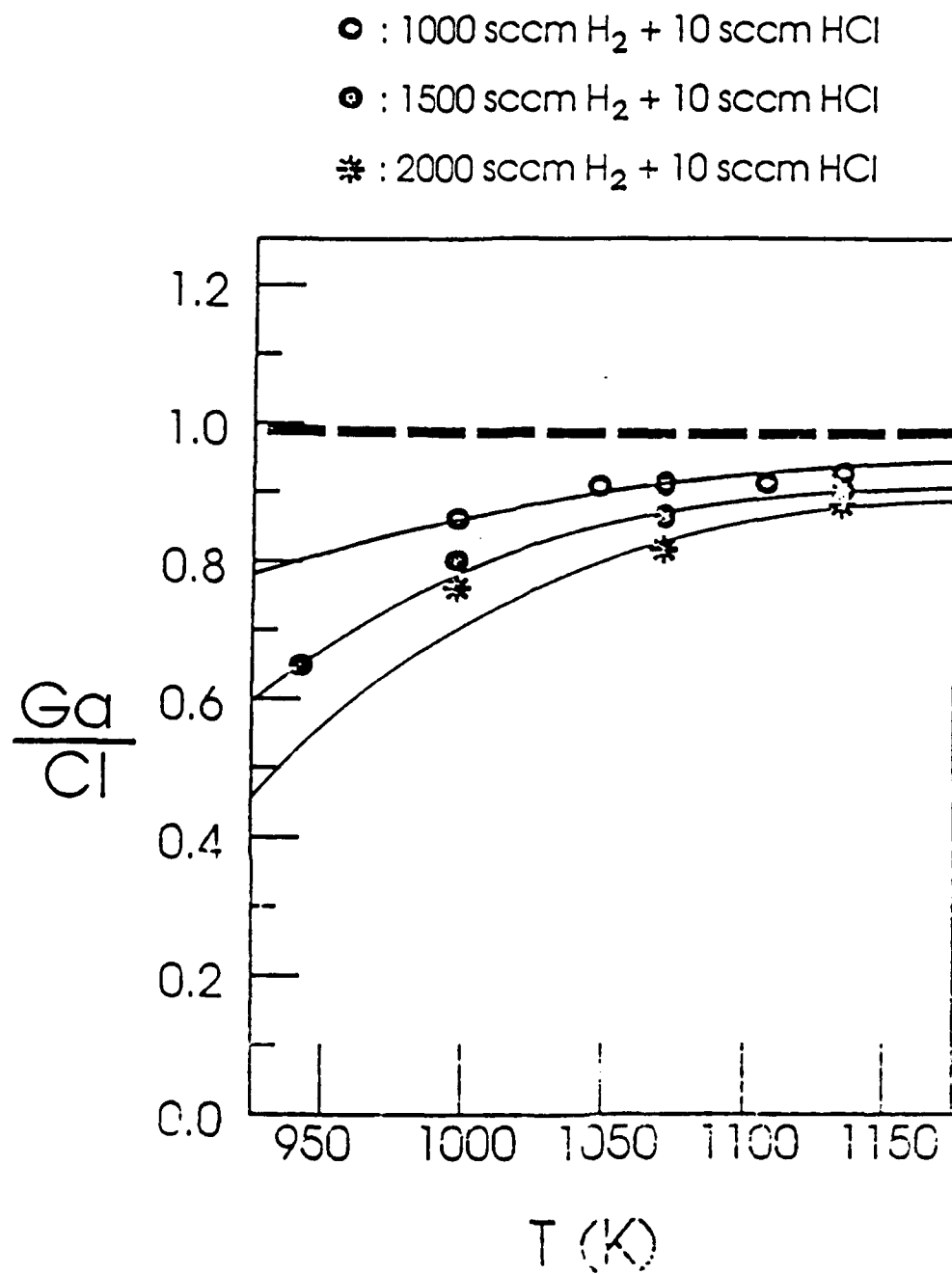


Figure C-6

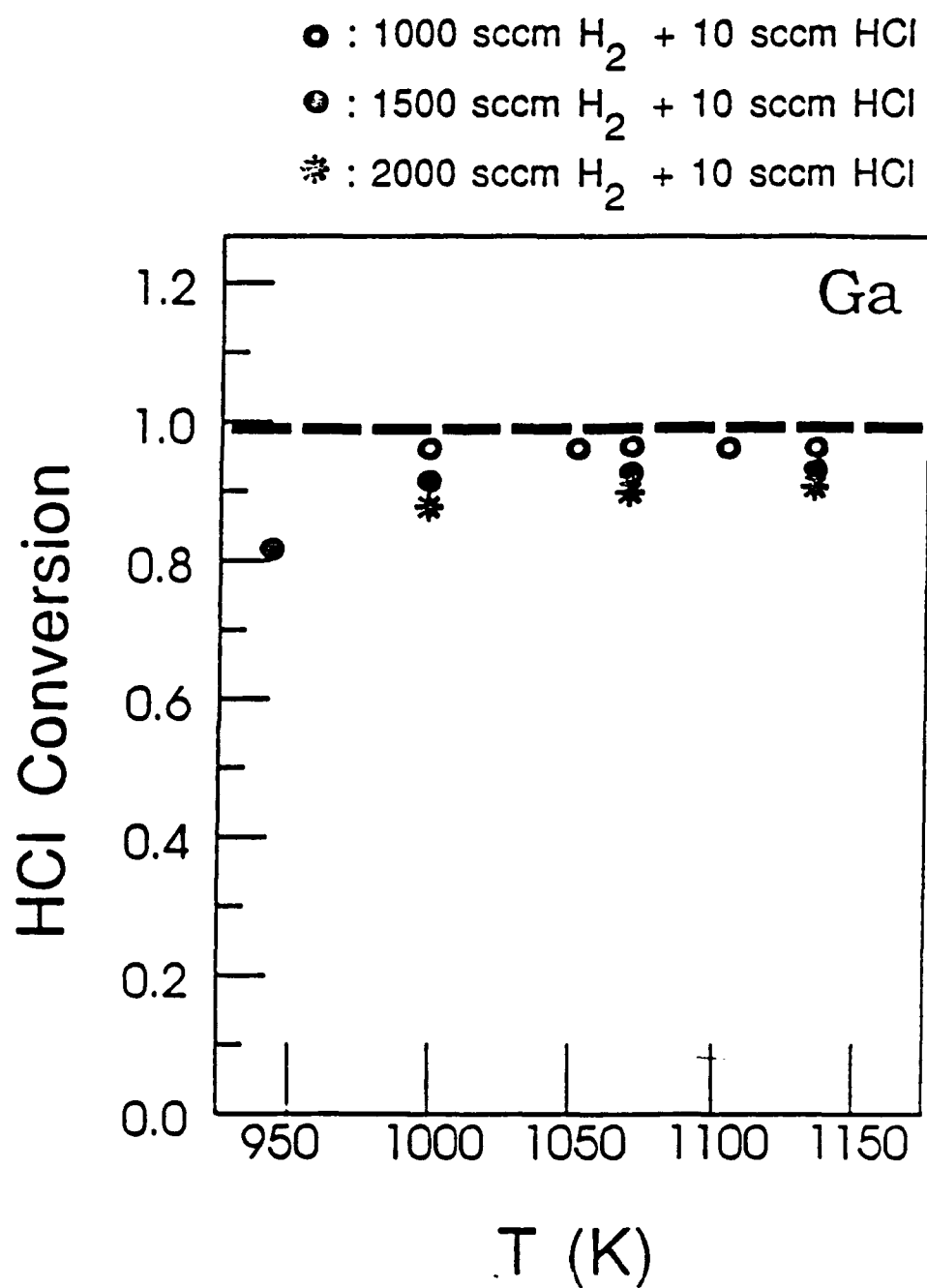


Figure C-7

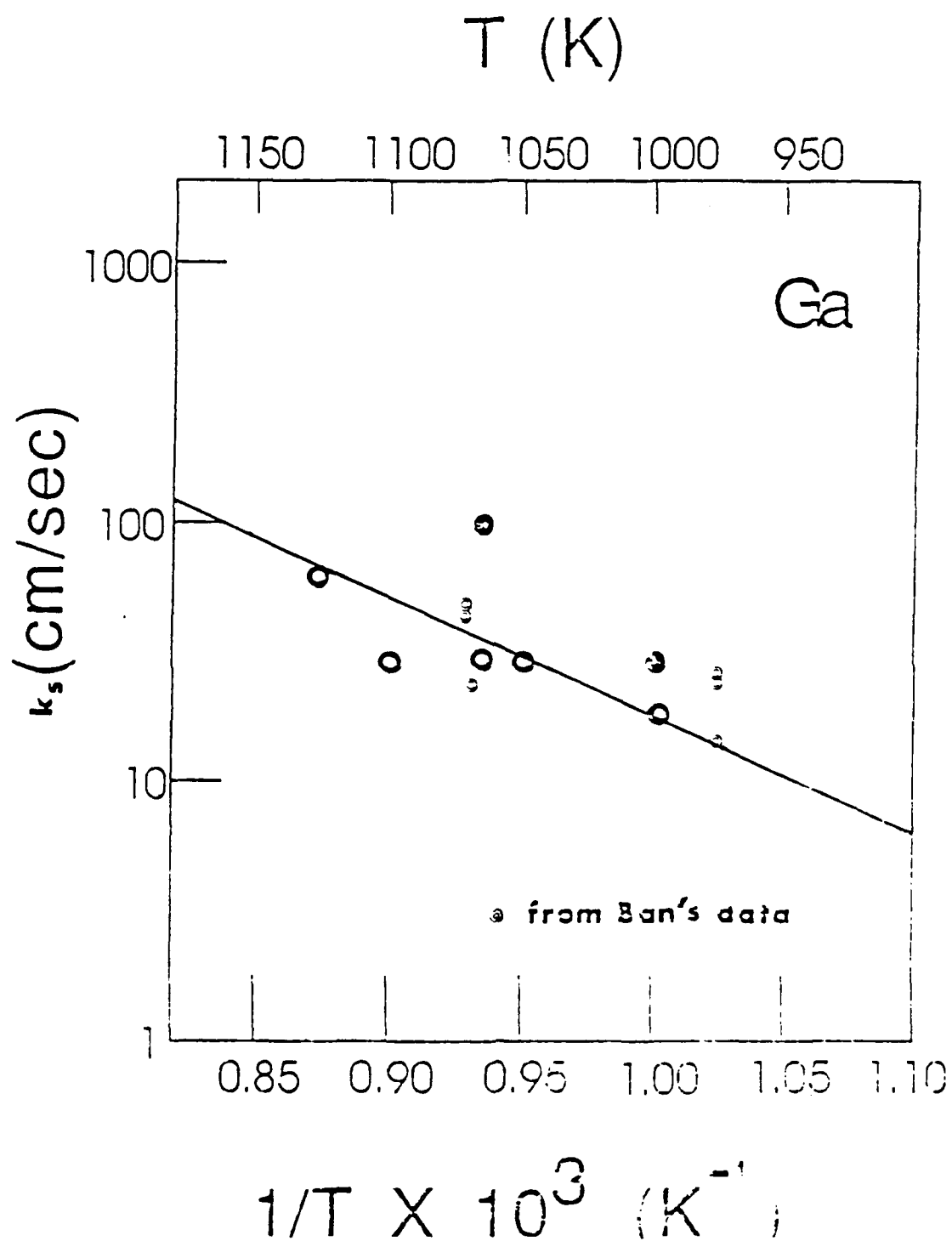


Figure C-8

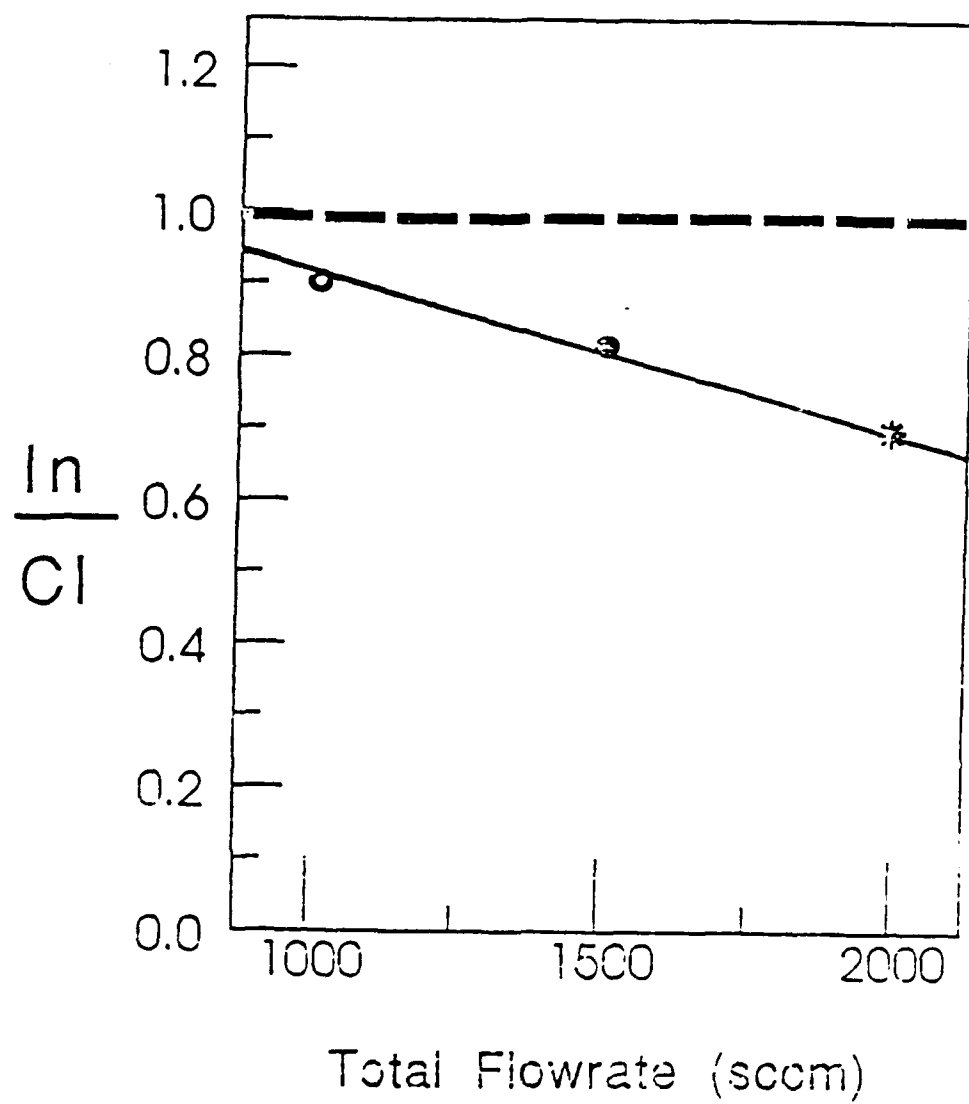


Figure C-9

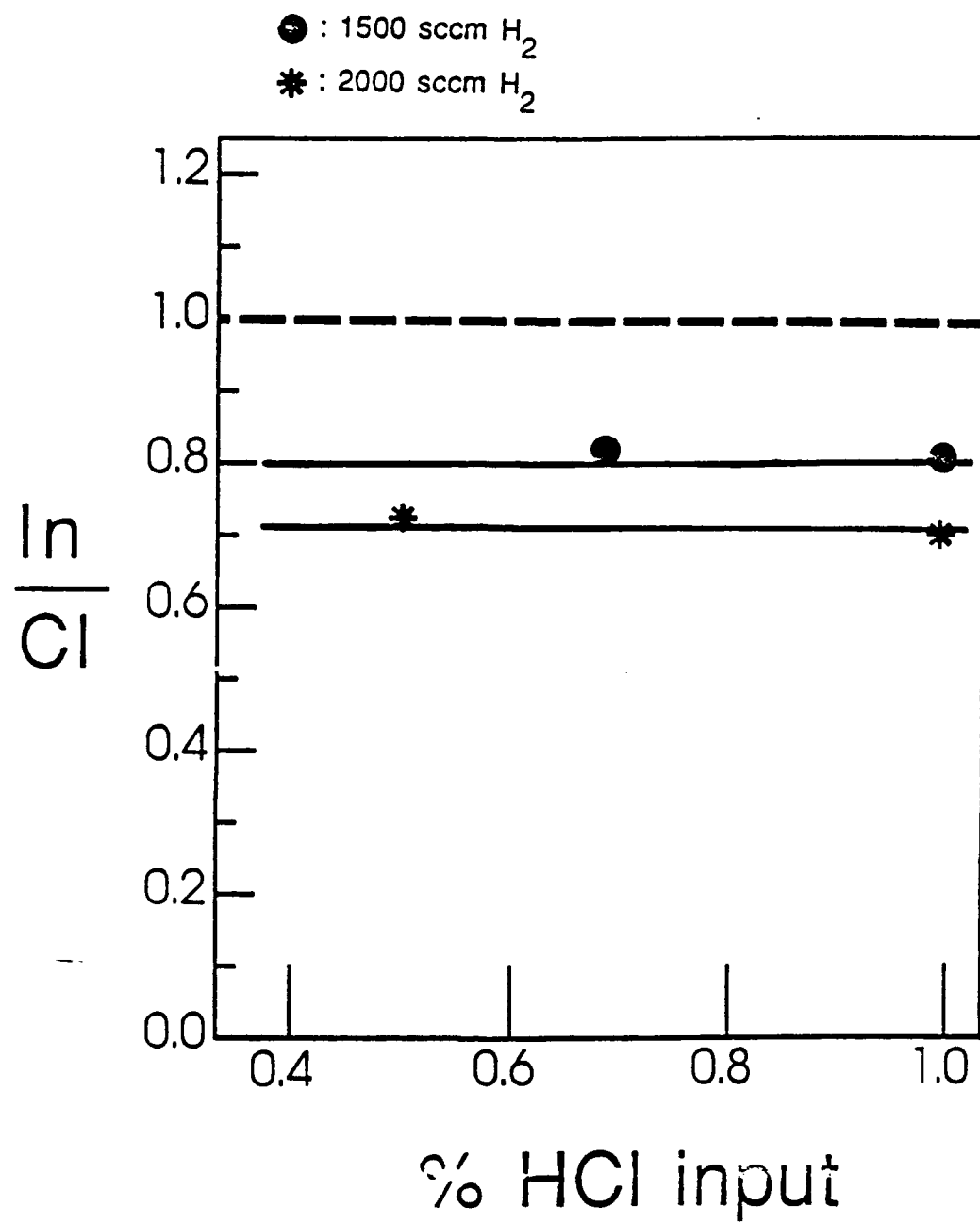


Figure C-10

○ : 1000 sccm H_2 + 10 sccm HCl

● : 1500 sccm H_2 + 10 sccm HCl

* : 2000 sccm H_2 + 10 sccm HCl

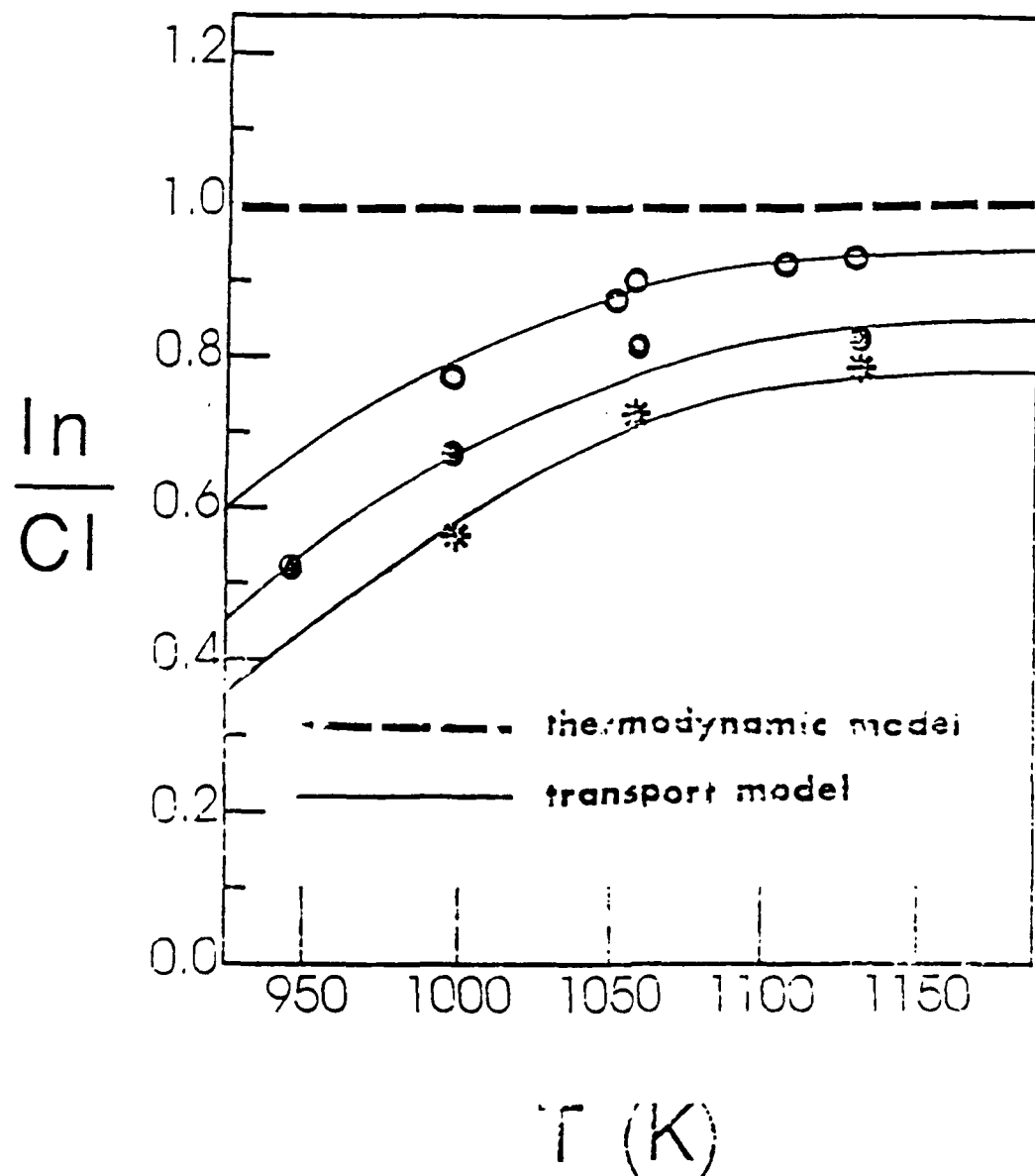


Figure C-11

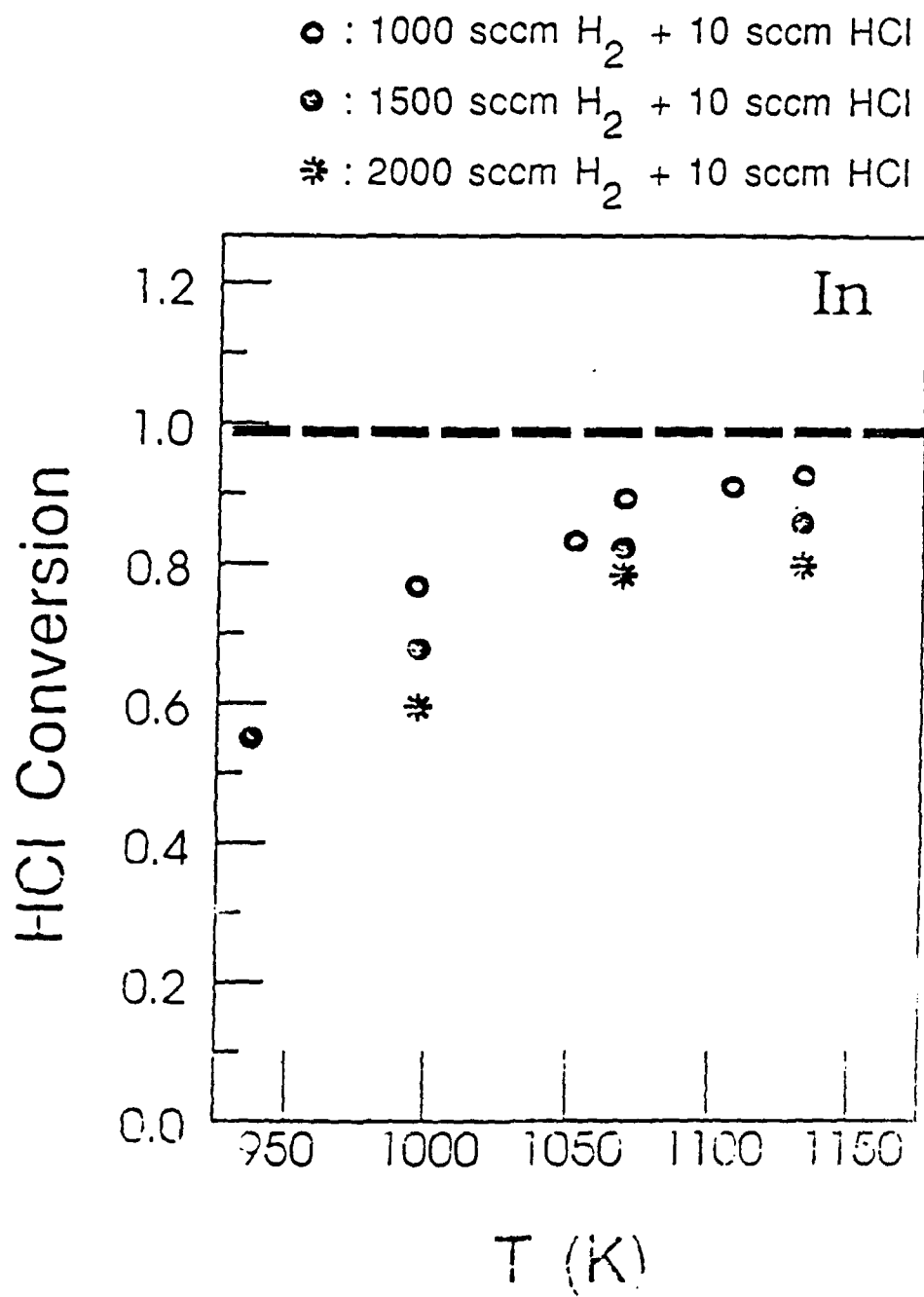


Figure C-12

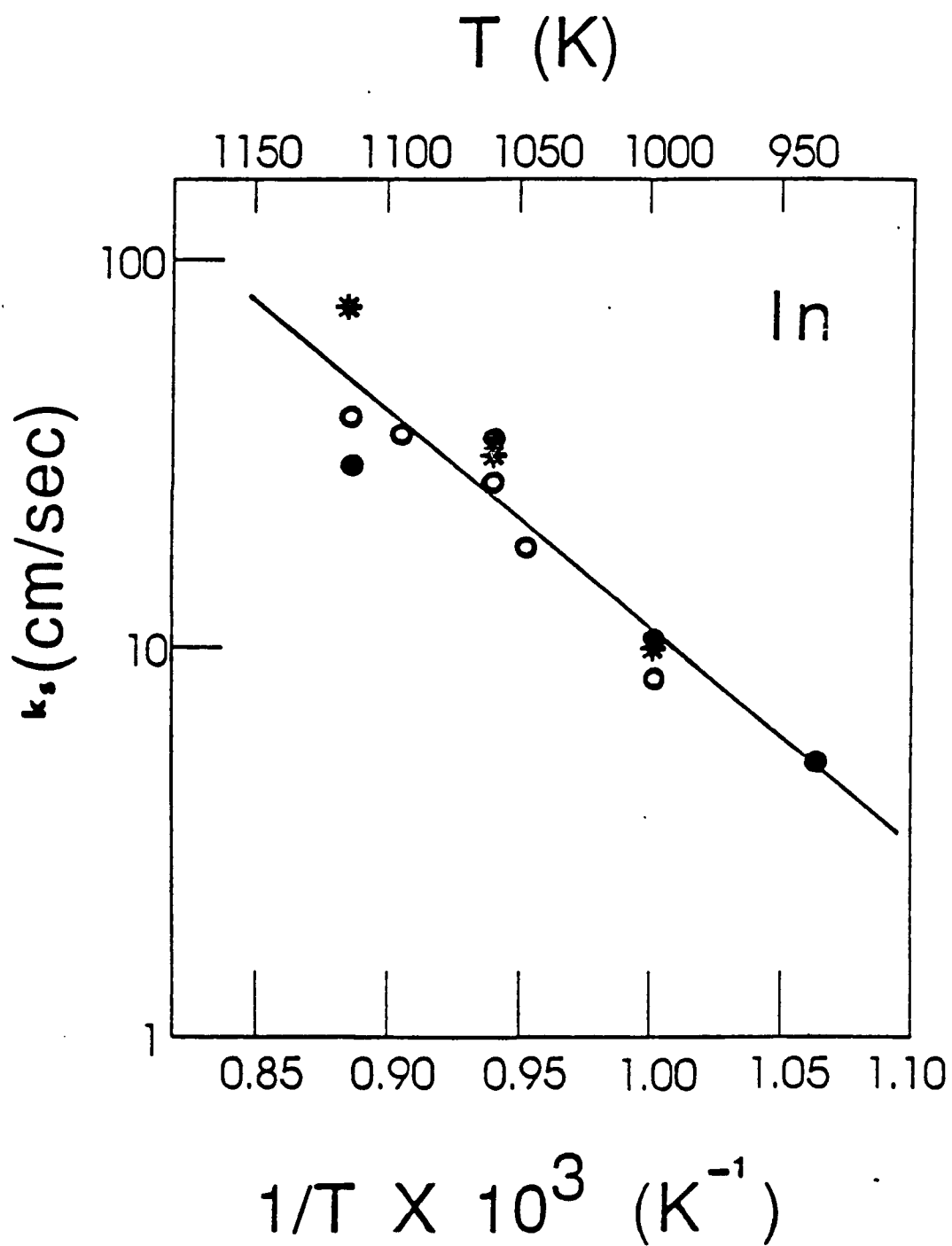


Figure C-13

Flowrates : 1000sccm H_2 + 10 sccm HCl

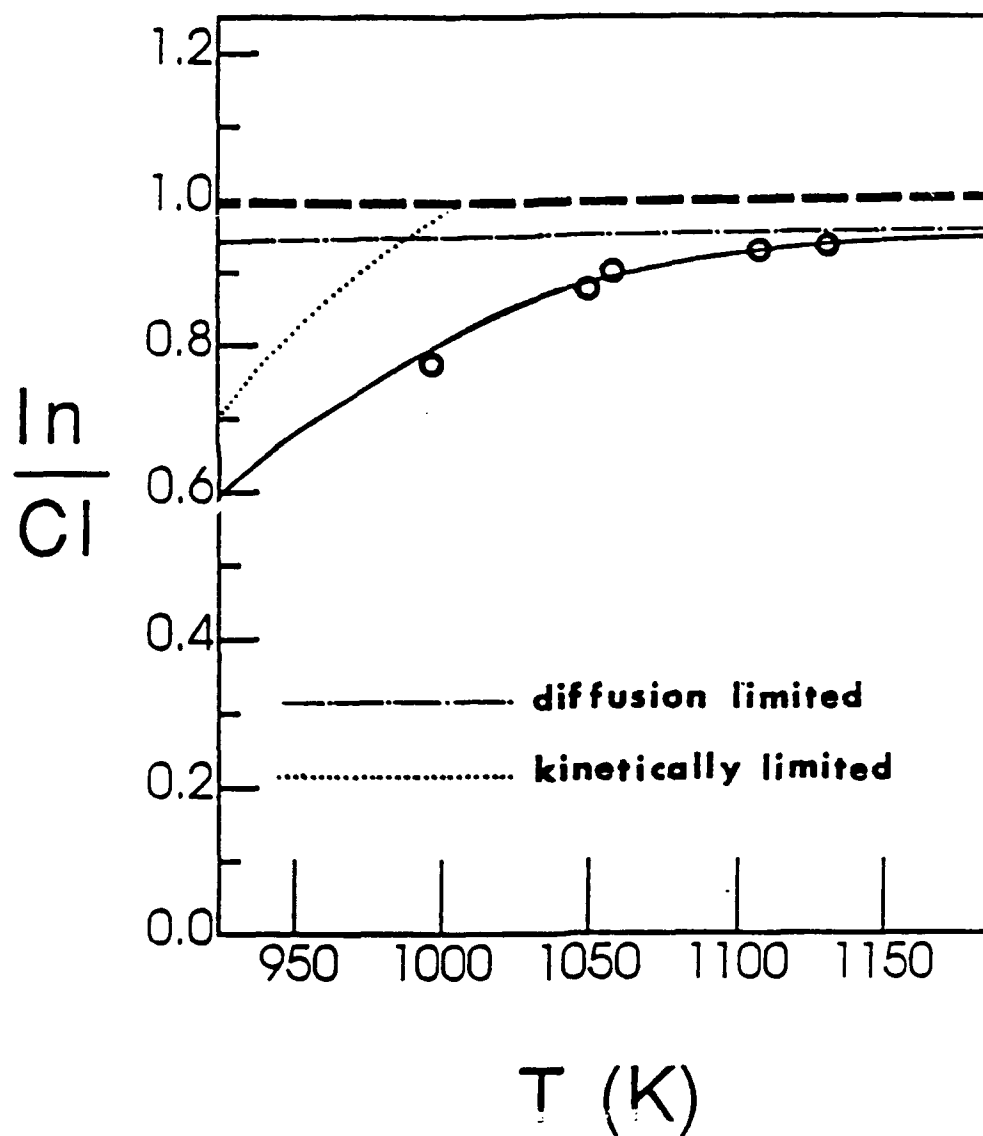


Figure C-14

Appendix D

LASER-ENHANCED SELECTIVE DEPOSITION OF GALLIUM ARSENIDE AND ALUMINUM GALLIUM ARSENIDE BY MOCVD

D.1 Introduction

The spatially localized deposition of electronic materials by laser irradiation during chemical vapor deposition is currently under investigation by many research groups around the world. Lasers are used because of their ability to provide an intense, highly directional, monochromatic source of light. In combination with chemical vapor deposition, lasers provide a means to alter the rates of chemical reactions on a very small area. The principle advantages of the technique are low temperature processing, deposition confined to the irradiated area, and deposition reaction selectivity.

Potentially this technique has many applications to microelectronics processing [38]. One possible application is in the production of optical wave guides. A wave guide is an optical pathway directing light from a source to a detector. The directing of light is accomplished by confining the light to a pathway of material with a high refractive index surrounded by a material with a lower index of refraction. All light striking the interface between the two materials is internally reflected, following the material of higher index of refraction.

Consider the fabrication of an aluminum gallium arsenide optical waveguide with the structure shown in figure D-1. To construct such a device by current methods requires several processing steps. First a layer of $\text{Al}_x\text{Ga}_{1-x}\text{As}$ is deposited over the entire substrate. Then a layer with the composition of the interior strip $\text{Al}_y\text{Ga}_{1-y}\text{As}$ is deposited. A pattern of photoresist defining the optical path is applied, and the surrounding material outside the pathway is selectively removed by etching. The pattern is next removed, and the material

surrounding the optical pathway is deposited, an $\text{Al}_z\text{Ga}_{1-z}\text{As}$ layer of a second composition.

A reduction in the number of required processing steps is possible using laser assisted chemical vapor deposition. Using this technique, the area defining the optical pathway is created by irradiation with the laser light. All processing steps to produce a thin pathway of one composition surrounded by material of another composition should be possible in a single reactor without removing the substrate.

The planar fabrication of a circuit containing many processing steps can be very time consuming. In addition, as the number of planar fabrication steps increases, the yield of usable devices decreases. It is possible that the final device does not work as predicted by theory. If the device does not perform as expected, changes are made in the device design and the planar fabrication process is repeated. For the development of prototype devices and the testing of new device designs, laser-enhanced chemical vapor deposition may be combined with laser-stimulated etching, laser-stimulated doping, and laser annealing for rapid device fabrication. Using a combination of laser stimulated techniques experimental devices may be created more rapidly than by planar techniques [39].

In this report, the use of laser-enhanced deposition of GaAs and $\text{Al}_x\text{Ga}_{1-x}\text{As}$ as a device fabrication technique is described. In the next section, the general mechanisms describing how selective deposition is achieved are reviewed. In the following section, methods are proposed for modulating the Al concentration in $\text{Al}_x\text{Ga}_{1-x}\text{As}$. Section D.4 reviews the understanding of laser-enhanced deposition of GaAs as determined by experiment previously. The experimental apparatus and the results of the laser-enhanced deposition of GaAs are described in Section D.5. Conditions under which substrate damage occurs from

laser irradiation is covered in section D.6. Experiments to selectively deposit $\text{Al}_x\text{Ga}_{1-x}\text{As}$ are described in section D.7. In order to explain the phenomena taking place in the laser enhanced deposition process knowledge of the temperature increase from the laser irradiation is important and this is calculated in section D.8. The last section of this chapter summarizes the experimental results from this study and the conclusions which can be drawn from them.

D.2 Mechanisms Involved in Laser CVD

The mechanisms by which the reaction rates are enhanced may be placed into two broad categories. In photolysis, the gas phase reactants absorb radiation which leads to a photochemical reaction. The effect which the absorbed light has on the molecule is dependent on the wavelength of light used. In the gas phase, for simple metalorganics of small alkyl groups, that is methyl and ethyl branches, electronic excitations take place at ultraviolet frequencies, corresponding to wavelengths less than 300 nm [40]. When a molecule enters an electronically excited state it may have an increased reactivity with other molecules, or it might dissociate into reactive fragments. Direct bond breaking is possible from the absorption of a single ultraviolet photon.

In contrast to electronic excitation resulting from ultraviolet radiation, absorption of infrared radiation typically induces molecular vibrational and rotational transitions. Researchers have attempted to selectively break a particular bond in a polyatomic molecule, by choosing an infrared frequency resonant with the vibrational frequency of the bond [41]. The energy a molecule absorbs from a single infrared photon is generally insufficient to cause chemical bonds in the molecule to break. If a high light intensity is used

however, several photons may be absorbed simultaneously causing multiple vibrational transitions to take place until the molecule gains enough energy to break bonds and dissociate. Selective bond breaking is a difficult process since once a photon is absorbed, the energy is rapidly dispersed from a single vibrational mode to many modes and bonds throughout the molecule [41].

In the second method of laser-enhanced chemical vapor deposition, the growth rate is enhanced by localized heating of the solid surface. In this case, the gas phase reactants are transparent and are not affected by the laser light. Only the substrate absorbs the laser light and is locally heated. The higher temperature of the irradiated area of the substrate causes the reaction to take place by pyrolysis, or thermal effects. Essentially in pyrolysis, the mechanism is similar to conventional growth but the substrate is sufficiently hot only in a small area for deposition to occur. Because the heated area is very small, however, mass transport is greatly increased, and very high deposition rates may be achieved [42].

It is possible for both photolysis and pyrolysis to take place simultaneously. Light may be absorbed by the gas phase reactants causing electronic excitation, and by the substrate, resulting in substrate heating. Depending on the wavelength of light which is used, however, one mechanism is often dominant over the other. Much lower laser power intensities are necessary for photolysis and heating of the substrate by the laser light is minimized.

There are advantages and disadvantages with both photolysis and pyrolysis. The low amount of energy necessary to initiate the reaction in photolysis results in very little temperature increase of the substrate. This is advantageous particularly if the substrate is degraded by high temperatures. A disadvantage of photolysis is that the reaction is not restricted to the

gas solid interface. Reactants may decompose in the gas phase, with the formation of clusters. When such clusters adhere to the substrate, the resulting deposited films may be porous, polycrystalline, and in general of poor quality. In addition, gas diffusion lengths are much longer than the substrate thermal diffusion lengths, the material may be deposited outside the diameter of the focused laser beam.

The high temperatures resulting from laser heating of the substrate in pyrolysis can aid in the formation of higher quality material. The higher temperatures are necessary to enhance the surface diffusion of the adsorbed molecules to form single crystal material. The gas phase does not absorb the laser light, and gas phase reactions would occur only as the gases are heated through contact with the laser spot on the substrate.

In summary, photolysis generally requires either ultraviolet or infrared light frequencies while visible frequencies are used for pyrolysis. Photolysis can deposit material on transparent substrates with very little increase in the substrate temperature. Pyrolysis results from a much larger increase in the substrate temperature and is restricted to absorbing substrates. The laser power flux necessary for pyrolysis is several orders of magnitude larger than for photolysis. Gas phase reactions occur in photolysis while for pyrolysis the reaction is restricted to the gas-solid interface.

D.3 Routes to Compositional Control by Laser CVD

Returning to the hypothetical optical waveguide, figure D-1, this structure could be fabricated in a number of ways using laser-enhanced deposition. One possibility is the modulation of the solid composition by selecting a laser wavelength which strongly increases the decomposition of one reactant, while having little effect on others. As an example of this technique, it has

been demonstrated that the composition of a nickel-iron alloy deposited by laser induced CVD can be changed from iron rich to nickel rich by shifting the laser frequency used from 193 to 337 nm [43]. This would be a primarily photolytic method.

Using a predominantly pyrolytic mechanism, the production of optical waveguides by laser-enhanced chemical vapor deposition may be accomplished by either of two routes. In the first method, the optical pathway is produced without surrounding deposition. In this case the susceptor temperature is kept low enough such that no deposition occurs except where the laser is irradiating the substrate. The layer surrounding the optical pathway is deposited in a second step at a higher susceptor temperature such that deposition occurs over the entire substrate. The second possibility for producing an optical waveguide is to simultaneously deposit the optical pathway and the surrounding material. The entire substrate is heated to a temperature at which deposition occurs everywhere. The laser is used to locally modify the composition of the optical pathway. Ideally, in this second case only the composition of the laser irradiated area is modified, not the growth rate.

To understand why the composition of the laser irradiated spot should change under laser induced pyrolysis, it is necessary to examine the change in the solid composition with temperature. At a given temperature the solid composition is determined by the relative rates of decomposition of each metalorganic group III compound present. For constant flow rates of reactants, as the temperature is changed, the rate of metalorganic decomposition changes, resulting in a difference in the solid composition. This change in the relative amount of group III element present in the solid, is controlled by the activation energy of decomposition. The decomposition of the metalorganics follows the Arrhenius expression;

$$k \propto \exp \frac{-E_a}{RT} \quad (D-1)$$

If the temperature is increased, the group III metalorganic compound having the higher activation energy will decompose to a greater extent relative to the other reactants with the resulting enhancement of that element in the solid.

As an example, it has been shown using trimethylaluminum (TMA) and trimethylgallium (TMG) with arsine to grow $Al_xGa_{1-x}As$ that for a constant flow rate of reactants, as the temperature is increased from 600 to 700°C the Al mole fraction in the solid increases by 50% [44]. This is due to the higher activation energy of decomposition for TMA, 158.6 kJ/mol, than that of TMG 119.7 kJ/mol [45].

Because the composition of the solid can be changed by an increase in temperature, it should be possible to alter the local composition at a point merely by changing the temperature at that point. By increasing the substrate temperature at a point using a laser, it should be possible to increase the aluminum solid mole fraction in $Al_xGa_{1-x}As$ when the reactants TMG and TMA are used. It should also be possible to decrease the Al solid mole fraction at a point by using triethylaluminum (TEA) instead of TMA and TMG and arsine. TEA has a lower decomposition activation energy, 84.5 kJ/mol, than TMG, 119.7 kJ/mol [45], so the decomposition rate of TMG would increase more rapidly than TEA.

If the temperature of the susceptor is so high that the metalorganics are already completely decomposed, further increases in the temperature would not change the relative amounts of Ga and Al. Selectively heating using laser irradiation would not modulate the solid Al composition. An alternative two

step technique would be necessary. In this case, it would be necessary to first deposit the optical pathway without surrounding deposition by using a low susceptor bias temperature. Then the surrounding layer would be formed in a second high temperature deposition over the entire substrate.

D.4 Review of Photon Assisted Gallium Arsenide Epitaxy

Many types of materials have been deposited by laser-enhanced chemical vapor deposition. These include metals, semiconductors, and insulators. Lasers emitting ultraviolet, visible, and infrared light have all been used successfully. The resulting deposits have included amorphous, polycrystalline and single crystal material. Many reviews have been written describing the technique [38,39,46-49].

Although many laser-enhanced chemical vapor deposition systems have been studied, relatively little work has been performed with depositing semiconductors. The majority of the studies have been with the deposition of metals. Of the semiconductor materials which have been studied, most of the work has been with depositing silicon. The laser assisted deposition studies with gallium arsenide and other III-V compounds is next reviewed.

Several researchers have demonstrated laser-enhanced deposition of gallium arsenide. Nishizawa et al. [50] used an ultraviolet laser in a chloride vapor phase epitaxy system to selectively increase the growth rate. Irradiation of the substrate was found to increase the growth rate over the temperature range from 480 to 700°C. Irradiation of the source zone decreased the growth rate at low temperatures (<600°C), and had no effect at higher temperatures. A laser wavelength of 249 nm had the most pronounced effect on the growth rate while longer and shorter wavelengths had little effect.

Roth et al. [51] used a pulsed visible frequency laser in a metal organic chemical vapor deposition (MOCVD) system to increase the growth rate locally with a susceptor bias temperature between 360 and 520°C. The resulting laser deposited material was reported to be single crystal. The morphology of the laser irradiated area was of a much higher quality than the nonirradiated portion.

Aoyagi et al. [52] used a visible frequency argon ion laser to locally enhance the growth rate of gallium arsenide by MOCVD. It was found that the temperatures for which an enhancement of the growth rate occurred were in the kinetically limited growth regime. Above approximately 600°C the reaction enters a mass transfer limited region, and no enhancement of the growth rate at the laser irradiated spot was observed. The enhancement effect was found to increase as the temperature of the substrate was decreased, down to the lowest reported temperature of 500°C.

Aoyagi et al. [52] concluded that the increase in growth rate was not caused exclusively by a temperature increase, but that a photocatalytic effect was primarily responsible. Evidence for a photocatalytic effect was proposed from a comparison between the calculated temperature of the laser irradiated spot, and the predicted increase in the growth rate due to this temperature increase. Only a small temperature increase was predicted, and the observed growth rate was much higher than that calculated from the temperature increase. In addition, the deposited spot size was found to be identical to the focused laser beam diameter, implying that deposition occurs only where the substrate is irradiated. The deposited spot did not expand outside the laser irradiated spot by thermal spreading.

Bedair et al. [53] used a scanning argon ion laser to deposit lines of GaAs, InGaAs, and GaAsP on silicon and GaAs substrates. Low temperature,

350°C for GaAs and GaAsP, and 250°C for InGaAs, were used so that deposition occurred only under laser irradiation. for GaAsP lines, the composition of P was constant across the line. From normal MOCVD of GaAsP, it was known that the incorporation of P into the solid is a function of temperature, increasing as the temperature increases. From considerations of the expected temperature distribution, it was expected that the P concentration would peak in the center of deposited lines and decrease near the line edges. Since the P distribution did not follow the temperature distribution, Bedair et al. [53] concluded that a photocatalytic process was responsible for the enhanced growth rates, concurring with Aoyagi et al. [52].

In a later paper by Bedair et al. [54], the epitaxial nature of the laser-enhanced deposition was confirmed using transmission electron microscopy. For GaAs and GaAsP lines produced using low growth rates, 2.0 nm/sec and high scan rates, 0.10 to 0.20 mm/sec the deposits were single crystal. The susceptor temperature was varied from 25 to 500°C. In this paper the phosphorus solid distribution was reported to vary across the deposited line, suggesting that the mechanism is pyrolytic.

Doi et al. [55] used a switched laser technique in combination with pulsed gas flows in a MOCVD system to achieve controllable single monolayer growth. TMG and arsine were alternately pulsed into the reactor, with the laser switched on during one or the other gas pulses. When the arsine and the laser were simultaneously on, no enhanced growth was observed. Only when the TMG and the laser were on simultaneously was enhanced growth observed. The effect of substrate doping type on the enhanced growth was also reported. The growth rate for both the switched laser and continuous irradiation followed the trend $n > i > p$.

Some work has also been undertaken to study the modulation of the material properties, that is either the doping levels or the material composition, of the film being deposited. Noteworthy in this effort is the work by Kukimoto [56], who observed an increase in the aluminum concentration of a $\text{Al}_x\text{Ga}_{1-x}\text{As}$ MOCVD deposited film under UV laser irradiation. Methyl branched organometallic sources TMG and TMA were used with AsH_3 to deposit the $\text{Al}_x\text{Ga}_{1-x}\text{As}$.

Balk et al. [57] used a low pressure mercury lamp to irradiate an entire substrate with ultraviolet radiation during GaAs deposition using TMG or TEG and AsH_3 . For the wavelength of light which was used, 254 nm, dissociation of all the reactants were expected. For both starting materials, an increase in the growth rate was observed for temperatures below 420°C for TEG and 570°C for TMG. UV radiation reduced the background carrier concentration using TEG was not effected. The UV light was proposed to aid in breaking methyl-gallium bonds resulting in lower carbon incorporation whereas the ethyl-gallium bond is already completely broken thermally.

The salient features from these experiments can be summarized. Using visible frequency lasers selective deposition was achieved as long as the deposition conditions were in the kinetically limited growth regime [51,52]. The resulting selectively deposited GaAs is epitaxial. Solid Al concentration modulation of $\text{Al}_x\text{Ga}_{1-x}\text{As}$ films has been demonstrated using an ultraviolet laser [56]. Very little electrical characterization of laser-enhanced deposited materials has reported. The limited results which have been reported [55] indicate that GaAs selectively deposited from TMG and AsH_3 contains much higher background carrier concentration levels (10^{18}cm^{-3}) than normally deposited GaAs (typically 10^{15}cm^{-3}). As yet, no devices have been produced using selective deposition of GaAs or $\text{Al}_x\text{Ga}_{1-x}\text{As}$.

D.5 Experimental Studies of Laser-Enhanced GaAs MOCVD

Laser enhanced deposition of gallium arsenide was studied as a function of temperature, laser wavelength, spot size and time. The resulting laser-enhanced spots were characterized by height, width, and overall shape. As the investigation proceeded, the experimental apparatus was changed, when it became apparent that the process could be improved.

The laser used was a visible frequency, continuous wave argon ion laser. The laser could be operated at any of several single wavelengths and powers as listed in Table D-1, or by using all lines simultaneously for power output levels up to 7.0 W.

The reactor used in the initial studies was designed to avoid attenuation of the laser beam by spurious deposition at the point where the beam enters the reactor. The horizontal reactor was arranged with the susceptor and substrate arranged in a nearly vertical position as shown in figure D-2. The laser beam entered the reactor through a flat quartz window in the endcap upstream from the susceptor. The entrance region of the reactor was long, approximately 40 cm, and deposition on the window was completely avoided. The arrangement of this reactor and the optical system is referred to as reactor configuration number 1.

As pointed out by Giling [58], this susceptor configuration can suffer from turbulent gas flow, which can result in nonuniform film thicknesses. In order to avoid this problem, the reactor was operated at reduced pressure, generally between 150 and 250 Torr. Operating at a reduced pressure suppressed the turbulence resulting in more uniform deposition. For temperatures in which the growth rate is kinetically controlled, the gas flow patterns would not affect the crystal growth rates.

In the study to determine the temperature range in which enhanced growth takes place using TMG, the laser output power was 5.0 W using all laser lines combined. Light from the laser was roughly focused on the gallium arsenide substrate (2° off 100 orientation toward the 110 orientation) using a simple lens. The flow rates of trimethylgallium (TMG) and arsine used were 1.12 and 19.5 standard $\text{cm}^3/\text{minute}$ (sccm), respectively. The total gas flow rate was 3.0 slm and the reactor was operated at a pressure of 250 Torr.

The overall deposited thickness was determined in two ways. The substrate was weighed before and after deposition, and by using the density of gallium arsenide and the substrate area, the deposited thickness could be calculated. This method gives an average thickness over the entire substrate and assumed that the mass from the laser spot was negligible. Secondly, some of the samples were cleaved and stained using A-B etch [59], and the edges were examined by optical microscopy. Average thicknesses measured in this manner were 10 to 30% smaller than those determined by mass changes. This was probably due to deposition on the edges and the backside of the substrate. Thicknesses across the substrate as determined by staining varied by about 10%.

The increase in the growth rate at the laser irradiated spot was determined using a DeK Tek profilometer. This instrument physically moves a needle across the surface of the deposited film, measuring variations in height. The instrument could easily resolve height variations as small as 20 nm. The enhanced growth rates were taken from the maximum spot height which was achieved and dividing by the deposition time.

An example of a Dek Tek trace of a laser-enhanced spot is shown in figure D-3. The spot consists of an overall enhanced growth with a basin in the center. This shape is commonly described as the volcano shape [60], because of the obvious similarities. Several mechanisms have been suggested as

Table D-1. Wavelengths and power available from the argon laser.

Wavelength (nm)	Power (W)
514.5	2.7
501.7	0.6
496.5	0.9
488.0	2.2
476.5	0.90
472.7	0.42
465.8	0.23
457.9	0.38
454.5	0.14

causing this deposit shape and these will be discussed in section D.9.

The growth rate using a TMG source as a function of the substrate temperature is shown in figure D-4 for both the laser irradiated spot, and normal thermal deposition without laser irradiation. For normal deposition, the growth rate increases exponentially with an activation energy of 99.0 kJ/mole in the low temperature kinetically controlled region. The enhancement of the growth rate was observed up to a temperature of approximately 600°C. Above this temperature, the laser irradiated spot was flush with the rest of the substrate. This temperature is the division between the kinetically controlled deposition reaction for lower temperature, and diffusion controlled deposition at higher temperature.

The dependence of the enhanced growth rate on susceptor temperature was also determined using triethylgallium (TEG) as a gallium source. Flowrates for the TEG and arsine were 7.0 and 35.0 sccm, respectively. The total flow rate used was 3.0 slm, and the operating pressure used was 150 Torr.

In figure D-5 both the laser-enhanced deposition growth rate and growth rate on the nonirradiated portion of the substrate are shown for TEG. For normal deposition at low temperature the growth rate increases with temperature with an activation energy of 87.5 kJ/mole. The upper limit of enhanced growth rate for TEG was found to be 450°C. As in the case in which TMG was used as a group III source, this corresponds to the region in conventional MOCVD that the deposition becomes mass transport rate limited. The enhancement effect was observed only in a kinetically limited growth regime.

Experiments were performed to determine the effect of laser intensity on the spot growth rate. TMG was used, at a temperature of 550°C and the laser output power was varied from 1.0 to 7.0 W. Unexpectedly, the spot height actually decreased as the laser power was increased (figure D-6). At the same

time, the area of the enhanced growth increased. This increase in the spot area with increasing laser power, has been observed by Bedair et al. [61] and was attributed to an increase in the area having a "favorable temperature for deposition". Experiments to determine the laser beam diameter indicated that the diameter increased linearly with the laser power. Dividing the laser power by the area of the enhanced growth indicated that the intensity (W/cm^2) decreased as the laser power was increased, possibly explaining the decrease in growth height.

The first problem to become apparent in the initial arrangement of the apparatus, was the large area of the enhanced growth, approximately 1.5 to 2.0 mm in diameter. The use of a lens with a long focal length, (50 cm) was responsible for the large spot size. For use as optical waveguides, it is necessary to have path widths on the order of 10 μm or less. Therefore the optical system was changed so a lens with a shorter focal length could be used. In this case, light entered the reactor through the reactor wall striking the substrate at a high angle approximately 70° with respect to the substrate normal, see figure D-7. The lens focal length used in this configuration was 14 cm. This reactor-optics arrangement is referred to as configuration number 2.

The diameter of the laser-enhanced spots in this configuration was smaller as expected. The average deposited spot diameter was 200 μm . A second observation for this configuration was the occurrence of higher maximum growth heights as compared to the previous reactor configuration. Two photographs taken with a scanning electron microscope are shown in figure D-8 and that the diameter increased linearly with the laser power. Dividing the laser power by the area of the enhanced growth indicated that the intensity (W/cm^2) decreased as the laser power was increased, possibly explaining the decrease in growth height.

Using this configuration the dependence of the deposited thickness was studied as a function of time. For this set of experiments, all laser lines were used and the power level indicated by the power meter built into the laser was 3.0 W. The temperature used in these experiments was 500°C. Growth times were varied from 1.0 to 50.0 minutes. Separate substrates were used for each laser spot. Before initiating growth, conditions were established by setting the substrate temperature, reactor pressure, and flow rates with the hydrogen and arsine flowing through the reactor and the TMG flowing to the reactor bypass. Growth was initiated by switching the TMG to the reactor and directing the laser on the substrate simultaneously.

The majority of the laser spots were oval shape, presumably because the laser was incident on the substrate at such a large angle. The average length of the deposited spot was 0.25 mm and the average width was 0.15 mm. The spot shape varied randomly with both volcano and Gaussian shapes observed (figure D-10). The deposited spots varied randomly both in the dimensions of the base, and in the spot maximum height. As shown in figure D-11 no correlation between growth time and the maximum spot height was found.

Experiments were undertaken to determine if the enhancement effect showed any dependence on the laser frequency used. The three wavelengths 457.9, 488.0, and 514.5 nm, at a laser power output of 0.37 W, were used. Different substrates were used for experiment. Measurements of the maximum height of the laser-enhanced deposited spots showed much scatter for identical conditions, as much as 300%, and no correlation between enhanced growth rate and frequency could be determined (figure D-12).

Several potential problems were apparent using the reactor in this configuration. The most serious was that the laser beam was incident on the substrate at a large angle with respect to the normal of the substrate. The amount of light which is reflected from the surface of a dielectric is angle dependent, changing slowly at small angles to the normal, and increasing rapidly as the angle approaches 90°. One possible explanation of the poor reproducibility of the maximum spot height was the slight change in incidence angle from run to run. In addition, the laser entered the reactor through a curved surface which could change the laser intensity distribution from the original Gaussian distribution.

A third reactor-optics system, shown in figure D-13, was constructed to remedy these problems. A spectroscopic window was placed directly above a susceptor on which the substrate was placed horizontally. In this configura-

tion, the laser beam could be reproducibly focused on the substrate normally. In addition, the focusing lens could be placed closer to the substrate, and a shorter focal length lens, 6.4 cm was used. An additional advantage of this reactor configuration was that the substrate could be moved so that several laser spots could be made on a single substrate. The main disadvantage of this reactor was for a susceptor temperature above 400°C deposits formed on the reactor walls and window.

Experiments were performed using the same flow rates of reactants as before, but at a lower temperature, 350°C with a laser power output of 3.0 W. It was hoped that the use of a lower susceptor temperature would reduce the temperature of the laser irradiated spot such that there would be no possibility that the spot temperature would approach the melting point of GaAs. Although this reactor and operating temperature was designed to improve the reproducibility, much scatter remained in the maximum peak height for identical conditions. The resulting maximum peak heights for identical conditions varied by a factor of 10.

A different shape of the laser-enhanced spot was also observed. Some spots produced using reactor configuration 3 had several peaks and valleys. The shape resembles a peanut butter cookie which has been cross hatched with a fork (figure D-14).

Experiments were again run to determine the change in the enhanced thickness as a function of time. A single substrate was used for several spots of different exposure times. The background thermally induced deposition rate was 0.08 $\mu\text{m/hr}$, and did not add a significant amount of material on the laser spots. In this case, the maximum spot height increased with time, but not at the same rate from substrate to substrate, as shown in figure D-15. In addition, it appeared that the sequence in which the spots were produced has

some effect. The sequence of spots produced with increasing deposition times had a more rapid increase with time than those spots produced with decreasing deposition time.

In order to determine whether the laser intensity would affect the laser deposited spot for the MOCVD of GaAs, a series of spots were produced at various laser output powers as shown in figure D-16, D-17, and D-18. TEG was used as the gallium source material, with a reactor pressure of 250 Torr, and a susceptor temperature of 350°C. The laser output power was varied from 0.2 W to 1.5 W. As may be seen from these figures, the severity of the volcano shape increases with laser intensity, until the center of the spot was almost to the depth of the substrate surface. The laser intensity at which the deposited spots became volcano shaped was approximately 0.5 W laser output power.

Two other benefits are evident from using lower laser powers. The diameter of the laser spot is reduced, and the maximum height is increased. In a separate experiment, enhanced deposition was observed at laser output powers as low as 0.05 W which resulted in a spot diameter of approximately 19 μm . The enhancement effect apparently reached a maximum at a laser output power of 0.2 W using TEG as the gallium source (figure D-16).

Improved reproducibility was obtained by depositing several laser spots on a single substrate. The overall susceptor temperature was kept low enough to avoid significant deposition outside of the laser spot. Differences still existed in growing spots under identical conditions on the same substrate. The maximum spot height increased for the same spot conditions from the first deposited spot to the next (as much as 40%). The changes, however, were much smaller than the variation associated with the same reactor conditions using different substrates (as much as 300%).

A second attempt to determine whether any dependence of the maximum height existed with the laser wavelength used. Several spots were deposited on a single substrate by moving the substrate after each spot had been deposited. The order in which the spots were deposited was changed in order to remove the small increase in the maximum height which occurred with the overall thickness of the previously deposited material. The results are shown in figure D-19 where spot height for each wavelength is plotted as a function of the maximum height on the substrate. The absolute maximum changed from substrate to substrate but the general trend was clearly evident. Higher maximum heights were observed for the shorter wavelengths at identical power levels.

D.6 Experimental Studies of GaAs Substrate Damage

Several substrates were irradiated without simultaneously growing films to determine if the substrate would become damaged. In one experiment using reactor configuration 2, a thin layer, approximately $0.6\text{ }\mu\text{m}$ of GaAs was first deposited on the substrate at a temperature of 650°C without laser irradiation. TMG was switched to bypass the reactor to halt the deposition and the substrate temperature was lowered to 500°C . The laser was switched on to irradiate the substrate at a laser output power of 2.2 W for 5 minutes. At this point the gases in the reactor were AsH_3 and H_2 . The laser was switched off and a second GaAs layer was deposited at a temperature of 500°C . Deposition was again stopped and a second spot on the substrate was irradiated at 0.8 W for 5 minutes. The susceptor temperature during both laser exposures was 500°C .

The Dek-Tek scan of the first spot produced is shown in figure D-20 and in a second scan perpendicular to the first in figure D-21. Material had been removed from below the surface to a depth of $17.1\text{ }\mu\text{m}$. At the hole edge,

material rises to a height of 9.0 μm . The Dek-Tek scan of the second spot produced at 0.8 W was similar in shape, however, material was removed to a depth of only 0.8 μm .

In a similar experiment, a plain substrate without any material deposited on it was used. In this case a hole with a depth of 2.0 μm was formed. In a third experiment, the susceptor temperature was lowered to 350°C and a substrate was irradiated. In this case, no hole was formed.

It is evident from these experiments that the substrate could be readily damaged by the laser irradiation. The extent of the laser damage was dependent on the laser irradiation. The extent of the laser damage was dependent on the laser intensity used and the background susceptor bias temperature. Using reactor configuration 2, substrate damage occurred at power levels as low as 0.8 W for background temperatures of 500°C. At 350°C, substrate damage was not observed for power levels under to 2.2 W.

D.7 Experimental Studies of Laser-Enhanced MOCVD of $\text{Al}_x\text{Ga}_{1-x}\text{As}$

Reactor configuration 1 was used to determine if $\text{Al}_x\text{Ga}_{1-x}\text{As}$ films deposited under laser irradiation had a different x value than those films deposited at the same susceptor temperature without laser irradiation. Aluminum gallium arsenide films were deposited under laser irradiation in order to determine if the solid aluminum to gallium ratio was modulated. Film compositions were measured by electron microprobe analysis (EMA). Using EMA it was possible to determine the composition of the deposited films in areas as small as 1 micron in diameter [62]. The aluminum composition was determined at points both inside and outside the laser irradiated spot.

The resulting films had a dull finish at all reactor conditions. A possible explanation for this was the relatively low purity (99.95%) arsine

which was used. Other researchers have observed film degradation with water and oxygen at ppm concentrations [63]. Both water and oxygen are believed to react with TMA to form Al_2O_3 which degrades the surface morphology.

An attempt was made to modulate the aluminum composition by providing additional heating from the laser irradiation. The aluminum composition as determined by EMA showed no variation in x between the laser irradiated spots, and the rest of the substrate for temperature from 600 to 700°C. Similar to the GaAs case, no growth rate enhancement was observed in this temperature range either.

Laser assisted deposition of $\text{Al}_x\text{Ga}_{1-x}\text{As}$ was also performed using reactor configuration 3. A new source of arsine of higher purity (99.9995%) was used resulting in a greatly improved surface morphology over previous layers produced with the lower purity arsine. Additionally, reactor configuration 3 allowed the reactor to be purged with N_2 while the substrate was loaded resulting in reduced exposure of reactor interior to atmosphere.

The effect of temperature on the solid Al composition of normally deposited (no laser irradiation) films was determined. The reactants used were TMA, TMG, and AsH_3 . The results are shown in figure D-22. Unlike the results of Kukimoto et al. [44] in which the solid Al composition increased significantly with temperature, in these experiments the Al composition increased only slightly with temperature.

$\text{Al}_x\text{Ga}_{1-x}\text{As}$ epitaxial films were deposited using laser-enhancement. Both TEG and TMG were used as gallium source materials with TMA as the aluminum source material. A susceptor temperature of 350°C was used. For the spots produced using TEG, figure D-23, x did not vary in the laser irradiated spot from the thermal background deposition on the rest of the substrate. In the case where TMG was used as the gallium source, the aluminum composition was greatly increased over that of the surrounding material (figure D-24).

D.8 Evaluation of the Temperature Increase Induced by Laser Irradiation

For enhancement of the growth rate to occur, it has been found necessary to operate the reactor in a kinetically controlled growth regime. Under kinetically controlled deposition, the deposition rate is a sensitive function of temperature, and it becomes useful to see how the laser irradiation affects the surface temperature. An expression to estimate the temperature of the substrate without crystal growth is evaluated next.

The increase in the laser irradiated spot temperature is dependent on several factors [64,65]. Certainly the power of the laser has a strong effect on the final temperature. As the laser power increases, the steady state temperature will increase proportionally. As long as the laser is operated in the TEM₀₀ mode, the power distribution from the laser beam is given by a Gaussian distribution

$$I = I_0 \exp - \frac{(r^2)}{(w_0^2)} \quad (D-2)$$

with r measured from the center of the beam and w_0 is half the diameter of the laser at an intensity of $1/e$. The maximum temperature increase will therefore occur at the center of the laser irradiated spot.

Gallium arsenide has a band gap of 1.42 eV at room temperature, and the laser energy is above this, in the range of 2.4 to 2.7 eV. The incident radiation is strongly absorbed. The intensity of the laser irradiation as a function of depth into the substrate follows Lambert's law,

$$I = I_0 \exp(-\alpha x) \quad (D-3)$$

where

- I_0 = the intensity of the beam at the surface
 α = the absorption coefficient cm^{-1} and
 x = the distance from the surface (cm).

For the frequencies used in this study, in which the photon energy exceeds the energy band gap, the absorption coefficient is on the order of $(10)^5 \text{cm}^{-1}$ [66]. Although the absorption coefficient increases as the wavelength of the incident light decreases, evaluation of the absorption expression shows that 90% of the radiation is absorbed in the first $1 \mu\text{m}$ of material in all cases. For evaluating the induced temperature increase, it is assumed that all of the radiation is absorbed at the surface.

The thermal conductivity of the material also affects the final steady state maximum temperature which is reached. The higher the thermal conductivity, the more efficiently the heat is dispersed away from the irradiated spot. As a result, the higher the thermal conductivity, the lower the resulting temperature increase of the laser spot would be. The thermal conductivity is temperature dependent, decreasing as the temperature of the solid is increased. The thermal conductivity can be approximated [67] by

$$k = \frac{A}{T - T_0} \quad (\text{D-4})$$

Where

k = the thermal conductivity of gallium arsenide (W/cm-K)

T = is the temperature

T_0 = a constant, 91 K for gallium arsenide

A = is a constant, 91 W/cm for GaAs

The thermal conductivity from this formula changes from 0.179 to 0.10 W/cm-K with a temperature change from 600 to 1000 K. For simple evaluation of the induced temperature increase, a constant average value of the thermal conductivity is used and the amount of error introduced is small in comparison to the accuracy of the calculation.

Not all of the incident laser light is absorbed by the substrate. A considerable amount of the incident radiation is reflected. The amount reflected is a minimum when the light strikes the substrate normal to the plane of the surface, and increases as the angle between the normal and the laser light increases.

The reflectivity of GaAs changes with the wavelength of light incident upon it. For the wavelengths 514.5, 488.0, and 457.9 nm the reflectivity for normal incidence is 0.395, 0.417, and 0.44 respectively [66]. For cases in which all laser wavelengths were used, an average value of 0.41 was assumed for the reflectivity.

In the case of $\text{Al}_x\text{Ga}_{1-x}\text{As}$ the reflectivity is not as well characterized as for GaAs. The general trend of the reflectivity as a function of Al composition has been determined. For radiation incident normal to the surface, the fraction which is reflected is given by [68]

$$R_f = \frac{(n-1)^2}{(n+1)^2} \quad (\text{D-5})$$

where

R_f = the intensity of incident light which is reflected.

n = the index of refraction of the substrate.

For $\text{Al}_x\text{Ga}_{1-x}\text{As}$ the index of refraction is a function of composition and is given by

$$n = 3.59 + 0.710x + 0.091x^2 \quad (\text{D-6})$$

where x is the fraction of group III which is aluminum. The reflectivity therefore as the percentage of aluminum in the solid increases.

The size of the focused laser spot also determines the maximum temperature increase. The smallest width which the laser beam can be focused is determined by the diffraction limit of the wavelength of light which is used. The size of the diffraction limited focus is generally on the order of the wavelength of light used. To obtain the diffraction limited size requires a lens with a very short focal length. This in turn requires very critical focusing.

For a collimated laser beam the diameter of the laser spot at the focal point of the laser [69] is given by

$$w = 4\lambda \frac{f}{\pi a} \quad (\text{D-7})$$

where

- λ = the wavelength of the laser light
- f = the focal length of the lens used to focus the laser on the substrate
- a = the initial beam diameter entering the focusing lens

Using this expressing to evaluate the focal length of a lens needed to obtain a 5 μm line width, the maximum focal length would be 1.0 cm. This requires that the lens be placed very close to the substrate.

For the experiments performed, it was not possible to measure the laser beam intensity at the focal point. Because the lens were not of high quality and because the laser beam was not collimated, the laser beam was not expected to be focused to the diffraction limited size. In order to calculate the temperature increase expected, it was necessary to estimate the laser spot size in another manner.

The predicted temperature distribution at the substrate surface outside the laser irradiated spot has been calculated theoretically [67]. As would be expected, thermal spreading causes the temperature distribution to be broader than the incident laser distribution. The distance at which the temperature is $1/e$ times the maximum temperature is roughly twice the distance from the center of the laser spot to the point where the laser intensity is $1/e$ times the maximum laser intensity (w_0).

Advantageously to the goal of trying to achieve high resolution, the reaction rate has an exponential dependence on the temperature. As a result, the deposited spot will always lie inside the temperature distribution and for very large temperature increases, the spot shape may lie within the laser intensity distribution. For the moderate temperature increases relative to the bias temperatures used in these experiments, it becomes reasonable to approximate the laser intensity as approximately the same dimension as the deposited spot shape. For estimating w_0 , this method should be accurate to within a factor of 2. The maximum spot diameter would not be expected to be larger than the temperature distribution which is roughly twice the light intensity distribution.

As the light leaves the laser, several losses of intensity occur before the light strikes the gallium arsenide substrate. In the present study, aluminum front surface mirrors were used to direct the laser light, each with

a reflectivity of 90%. Losses from reflection occurs as the light strikes the uncoated focusing lens, and the window in the reactor, approximately 4% each [68].

Using the assumptions given above the expected maximum temperature increase can be calculated. The simplest expression for the increase in surface temperature can be written [64]

$$T_{\max} = \frac{P(1-R_f)}{2\pi^{1/2}kw_0} \quad (D-8)$$

where

P = the power incident on the substrate (W)

w_0 = the radius of the incident laser irradiation where $I/I_0 = 1/e$,
(cm)

and the other terms as previously defined.

Application of this formula to the conditions used in reactor configuration 1 using TmG and AsH₃ to deposit GaAs give a predicted temperature increase of 65°C. This agrees well with the shift of the enhanced growth rate from the normal growth curve which is approximately 72°C. See figure D-4.

As a second example, using the parameters used in reactor configuration 2, laser output power of 3.0 W, deposited spot diameter of $5.0(10^{-3})$ cm, a temperature increase of 174°C is calculated. A temperature corresponding to the observed enhanced growth rate can be calculated from the growth rate as a function of temperature. From this calculation, a temperature increase of 214°C or 23% higher, is obtained.

The third example is taken from reactor configuration 3. The spot used for this example is shown in figure D-16. Using TEG as the gallium source, a laser output power of 0.2 W, and a spot diameter of $2.8(10^{-3})$ cm, a temperature increase of 85°C is predicted. The observed enhanced growth rate from this spot was $2.81\text{ }\mu\text{m/minute}$. Assuming that the growth rate increases in an exponential fashion at all temperatures, the temperature necessary to cause this enhanced growth rate would be 667°C .

Several conclusions may be drawn from these example calculations. For large spot sizes, those produced in reactor configuration 1, the temperature calculated agrees well with the observed enhanced growth rate. For relatively small spots, the example taken from reactor configuration 2, made with a relatively high laser intensity, the temperature calculated from theory and the temperature calculated from the observed growth rate, are also in relatively good agreement. But the small laser spot produced at a low laser intensity does not have a good agreement between the two calculated temperatures.

The above expression for the temperature increase becomes less adequate to describe the spot temperature as the spot forms. The absorbing surface no longer resembles a semi-infinite plane, and the spot can conduct heat only in the direction toward the substrate. Furthermore, convection in the gas phase can become significant in the presence of a large temperature gradient.

The optical properties of gallium arsenide are not well characterized for the high temperatures and high laser intensities used in the present investigation. Due to the creation of free electrons in the conduction band because of the high temperatures used and the high intensity of light, the semiconductor becomes more metal like, and the reflectivity increases. The energy band gap decreases as the temperature increases, resulting in an increase in laser absorption.

D.9 Discussion

The outstanding feature of laser-enhanced chemical vapor deposition processes is the variability of the results. In order to achieve enhancement effects, it is necessary to operate the reactor in the kinetically controlled deposition regime. Under kinetically limited growth, the process becomes very sensitive to temperature and surface conditions. Therefore, the reproducibility of the results becomes very difficult to achieve. In addition, as substrates were loaded and unloaded from the reactor, the reactor moved. This movement affected the optics making it difficult to have an identical optical arrangement from substrate to substrate. Changing the laser spot from one point to another on the same substrate did not cause as much movement of the reactor.

The laser process occurs very rapidly, where laser-enhanced depositions observed in some cases for irradiation times of 1.0 minute. Growth rates exceeding $9.0 \mu\text{m}/\text{minute}$ were observed in some instances. Under such high growth conditions the material deposited was of poor morphology.

The temperature which could be generated with the laser were clearly very high as observed from the substrate damage. The use of low laser intensities was advantageous as the spot shape was Gaussian shaped, and the enhanced growth rate was higher. It is possible that the adsorbed species and the deposited spot shape creates a situation where the actual temperature is much higher than predicted.

Under some conditions a volcano shaped deposit was formed. A photograph of one of these volcano shaped deposits taken with an electron microscope is shown in figure D-25. Other researchers have reported the formation of volcano shaped deposits when using a laser to locally deposit metals [60,70].

Moylan et al. has summerized the theories which have been proposed to explain the volcano shape [70].

1. Deposition in the spot center is lower than at the edges due to depletion of reactants at the spot edges. As the reactants diffuse toward the spot center, they are depleted from gas phase such that the reactant concentration at the spot center is very low.
2. The temperature of the center of the laser irradiated spot is so high that the sticking coefficients of the reactants are very low.
3. In the hot center region, reactions which are of secondary importance at the usual deposition temperatures, become significant, leaving a carbonaceous residue which interferes with deposition.
4. Strong convection from the center of the spot is produced by the creation of several gas molecules with the decomposition of a single source molecule. The deposition byproducts leaving the surface interfere with the incoming source molecules.
5. The center of the spot becomes so hot that the material melts, and may even exaporate.

In this work, the volcano shapes have also been observed for the laser-enhanced deposition of GaAs and $\text{Al}_x\text{Ga}_{1-x}\text{As}$ spots. The formation of the volcano shape has relevance to the debate on whether the enhanced growth is due to a photothermal or photocatalytic effect. The theories proposed rely on thermal effects to explain the formation of the volcano shapes. No explanation has been offered which would explain the formation of the volcano shaped deposit due to a photocatalytic effect.

Two of the suggested causes of the volcano effect are due to mass transport limitations. The mechanism requires that deposition at the laser spot is somehow controlled by the diffusion of reactants to the center of the laser

spot. The diffusion coefficient is inversely proportional to the pressure. As the pressure is lowered, the diffusion coefficient is increased, and the resistance to mass transport is reduced. If growth in the spot center is limited by the diffusion of the reactants to the center, then it would be expected that a change in the operating pressure of the reactor would have an effect on the occurrence of the volcano shape.

Using TEG as the gallium source material, a susceptor temperature of 350°C, and a laser output power of 2.0 W, the spot shape was studied as a function of pressure from 75 to 500 Torr. Such a reduction in pressure would be expected to suppress any convection occurring. All spots formed were volcano shaped, suggesting that the cause of the volcano shape is not due to mass transport limitations.

Although the laser was capable of creating conditions in which the substrate could be damaged, volcano shapes were observed under conditions in which relatively small temperature increases could be expected. It therefore seems unlikely that in the deposition of GaAs and $\text{Al}_x\text{Ga}_{1-x}\text{As}$, the volcano shaped deposits were formed by the material melting and evaporating.

The possibility that carbon deposits interfere with the deposition process also seems unlikely. Electron microprobe analysis across the laser-enhanced spot did not detect any carbon.

The most probable mechanism therefore seems to be that the spot center becomes so hot that the sticking coefficient of the reactants is less than at the edges of the spot. In normal MOCVD, it has been observed that the deposition rate of GaAs using TMG decreases as the temperature is increased above 800°C. In our experiments, using TEG the growth rate was observed to decrease above 550°C, see figure D-5. Therefore it seems possible that the volcano shaped spots are due to high temperature, and lower sticking coefficients.

The dependence of the deposition rate on the laser wavelength suggests the possibility that a photochemical effect takes place. No dependence of the growth rate on the laser wavelength used would be expected if the mechanism were purely thermal or photocatalytic. The reflectivity of GaAs increases with lower wavelengths which would suggest that the temperature and therefore reaction rate would decrease as the wavelength is decreased if the effect were caused by strictly a thermal means. The opposite trend is experimentally observed. The failure to observe the dependence of the growth rate on the laser wavelength when different substrates were used for each spot may be attributed to the poor reproducibility from substrate to substrate. The absorption spectra of the reactants may be shifted from that observed in the gas phase, to visible frequencies as the reactants are adsorbed on the substrate surface. Such a shift in the absorption spectra has been observed for dimethylcadmium absorbed on quartz [71]. Another possibility is that the partially decomposed reactants absorb light in the visible frequency range.

List of Figures

- Figure D-1. Hypothetical optical waveguide structure.
- Figure D-2. Reactor configuration 1. The focal length of the lens was 51 cm.
- Figure D-3. Dek Tek profilometer scan of a laser enhanced GaAs spot. Susceptor bias temperature was 550°C, laser output power was 5.0 W, TMG was the gallium source.
- Figure D-4. Growth rates for normal and laser enhanced deposition of GaAs using TMG vs. $1/T$. Laser output power was 5.0 W and all wavelengths were used. Reactor configuration 1 was used.
- Figure D-5. Laser enhanced (dashed curve), and normal (solid curve) growth rates of GaAs using TEG as the gallium source vs. $1/T$. Laser output power was 5.0 W and all wavelengths were used. Reactor configuration 1 was used.
- Figure D-6. GaAs deposited thickness and spot area vs. laser output power. Growth took place at a susceptor temperature of 550°C for 50 minutes, using TMG as the gallium source. Reactor configuration 1 was used. The circles indicate the spot area and the squares indicate the spot thickness.
- Figure D-7. Reactor configuration 2. The focal length of the lens was 15 cm.
- Figure D-8. SEM photograph of laser enhanced deposited GaAs spot. Susceptor bias temperature was 500°C. Laser output power was 0.38 W. TMG was the gallium source and the deposition time was 30 minutes. Maximum spot height is 28.9 microns. Reactor configuration 2 was used.
- Figure D-9. SEM photograph of laser enhanced deposited GaAs spot. Susceptor bias temperature was 500°C. Laser output power was 0.38 W. TMG was the gallium source and the deposition time was 10 minutes. Maximum spot height is 8.0 microns. Reactor configuration 2 was used.
- Figure D-10. Dek Tek profilometer scan of a Gaussian shaped laser enhanced spot of GaAs. Laser output power was 0.37 W, susceptor temperature was 500°C, and the growth time was 30 minutes. Reactor configuration 2 was used.
- Figure D-11. Maximum spot height of laser enhanced GaAs spots vs. growth time. Susceptor temperature was 500°C, laser output power was 3.0 W, and reactor configuration 2 was used.
- Figure D-12. Enhanced growth rate of GaAs vs. laser wavelength. Susceptor temperature was 500°C, laser output power was 0.37 W, TMG was the gallium source, and reactor configuration 2 was used. Circles are for 10 minutes and squares are 30 minutes of growth.

- Figure D-13. Reactor configuration 3. The focal length of the lens was 6.4 cm.
- Figure D-14. Dek Tek profilometer scan of GaAs spot produced in reactor configuration 3. Laser output power was 3.0 W, susceptor temperature was 350°C, TMG was the gallium source, and the growth period was 10 minutes.
- Figure D-15. Maximum spot height of GaAs spots by laser enhancement vs. growth time. Susceptor temperature was 350°C and reactor configuration 3 was used.
- Figure D-16. Dek Tek profilometer trace of GaAs spot. Susceptor temperature was 350°C, laser output power was 0.2 W, reactor configuration 3 was used, and TEG was the gallium source.
- Figure D-17. Dek Tek profilometer trace of GaAs spot. Susceptor temperature was 350°C, laser output power was 0.5 W, reactor configuration 3 was used, and TEG was the gallium source.
- Figure D-18. Dek Tek profilometer trace of GaAs spot. Susceptor temperature was 350°C, laser output power was 1.5 W, reactor configuration 3 was used, and TEG was the gallium source.
- Figure D-19. Maximum spot height vs. laser wavelength used to deposit the spot. Susceptor temperature was 350°C, laser output power was 0.28 W, and the growth period for each spot was 8 minutes. Each symbol represents a single substrate. Configuration 3 was used.
- Figure D-20. Laser ablation of a GaAs sample. Laser output power was 2.2 W and the susceptor temperature was 500°C. Reactor configuration 2 was used.
- Figure D-21. Laser ablation of a GaAs sample. Same spot as shown in Figure 4-20, scanning in the perpendicular direction.
- Figure D-22. Temperature dependence of the solid Al composition in normally deposited $\text{Al}_x\text{Ga}_{1-x}\text{As}$. Flowrates were 0.875, 0.7, and 12.6 sccm of TMA, TMG, and AsH_3 , respectively. Reactor configuration 3 was used.
- Figure D-23. Dek Tek scan of a laser spot and the Al solid concentration of the spot. Susceptor temperature was 350°C and TEG and TMA were the group III sources. Laser output power was 2.2 W.
- Figure D-24. Dek Tek scan of a laser spot and the Al solid concentration of the spot. Susceptor temperature was 350°C and TMG and TMA were the group III sources. Laser output power was 0.3 W.
- Figure D-25. SEM photograph of laser-enhanced deposited volcano shaped spot. Susceptor bias temperature was 350°C. Laser output power was 2.2 W. TMG was the gallium source and the deposition time was 10 minutes. Maximum spot height is > 60.0 microns. Reactor configuration 3 was used.

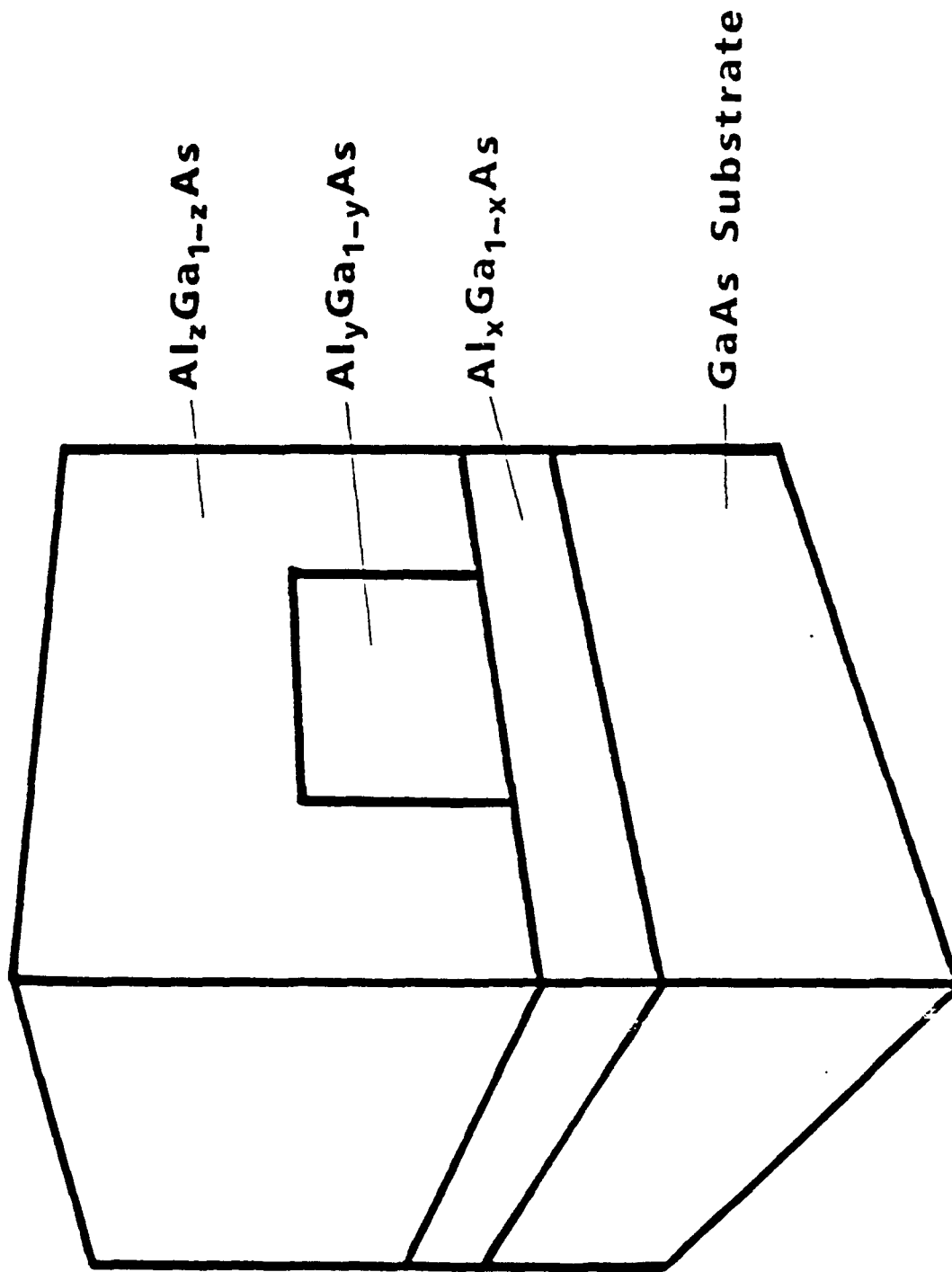


Figure D-1

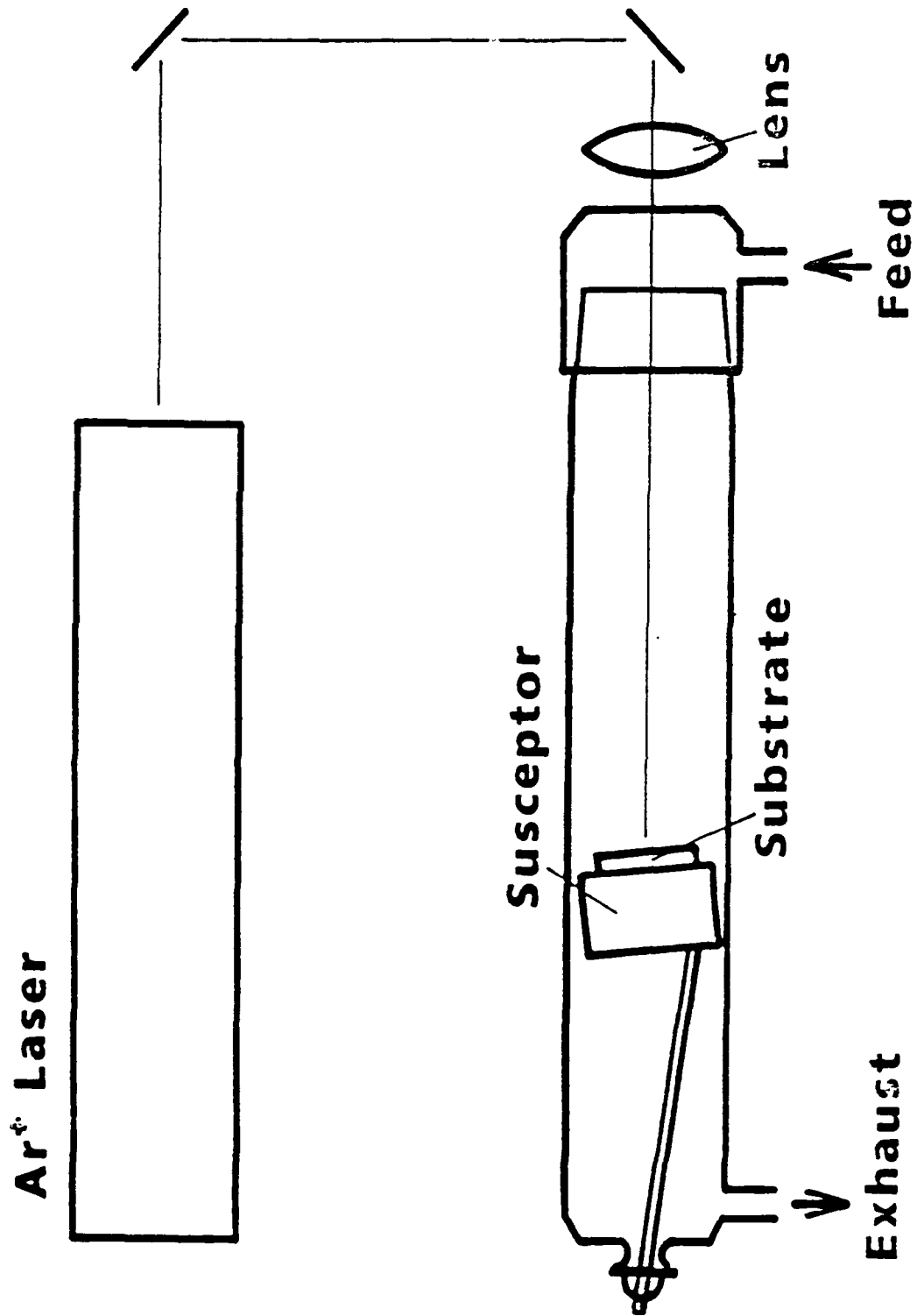


Figure D-2

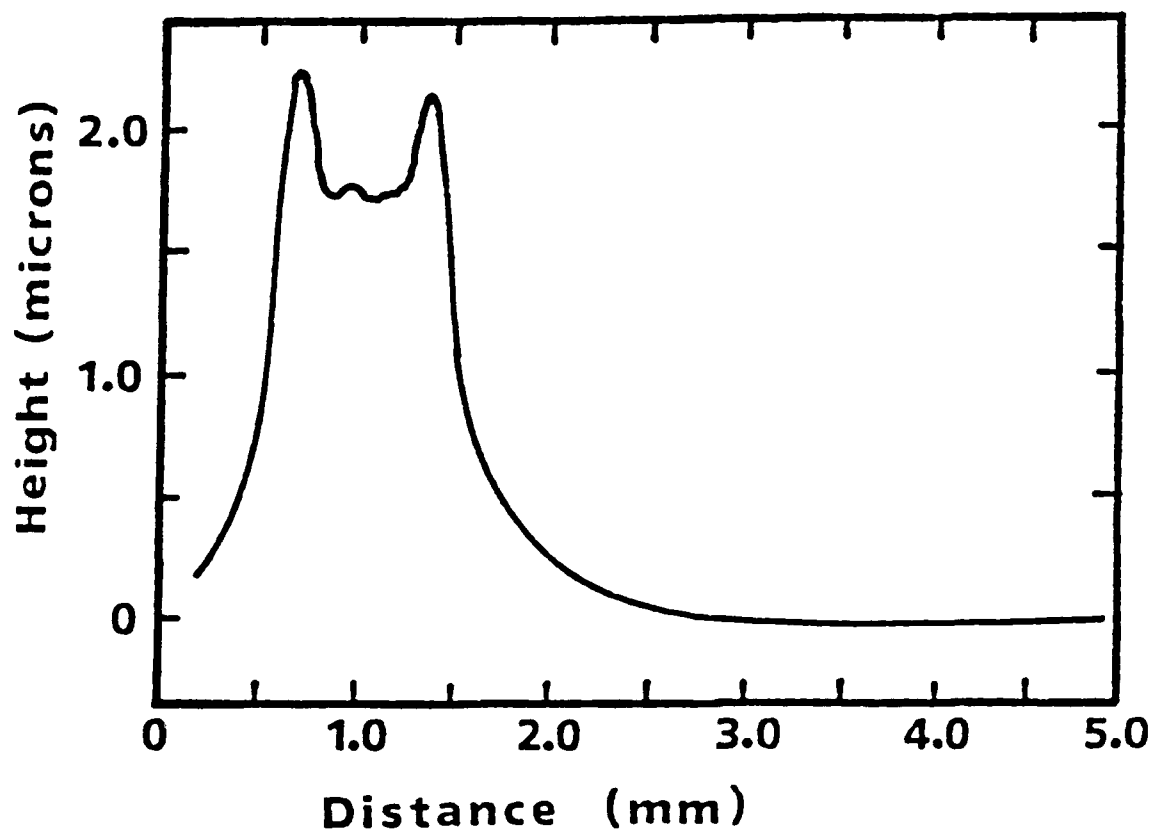


Figure D-3

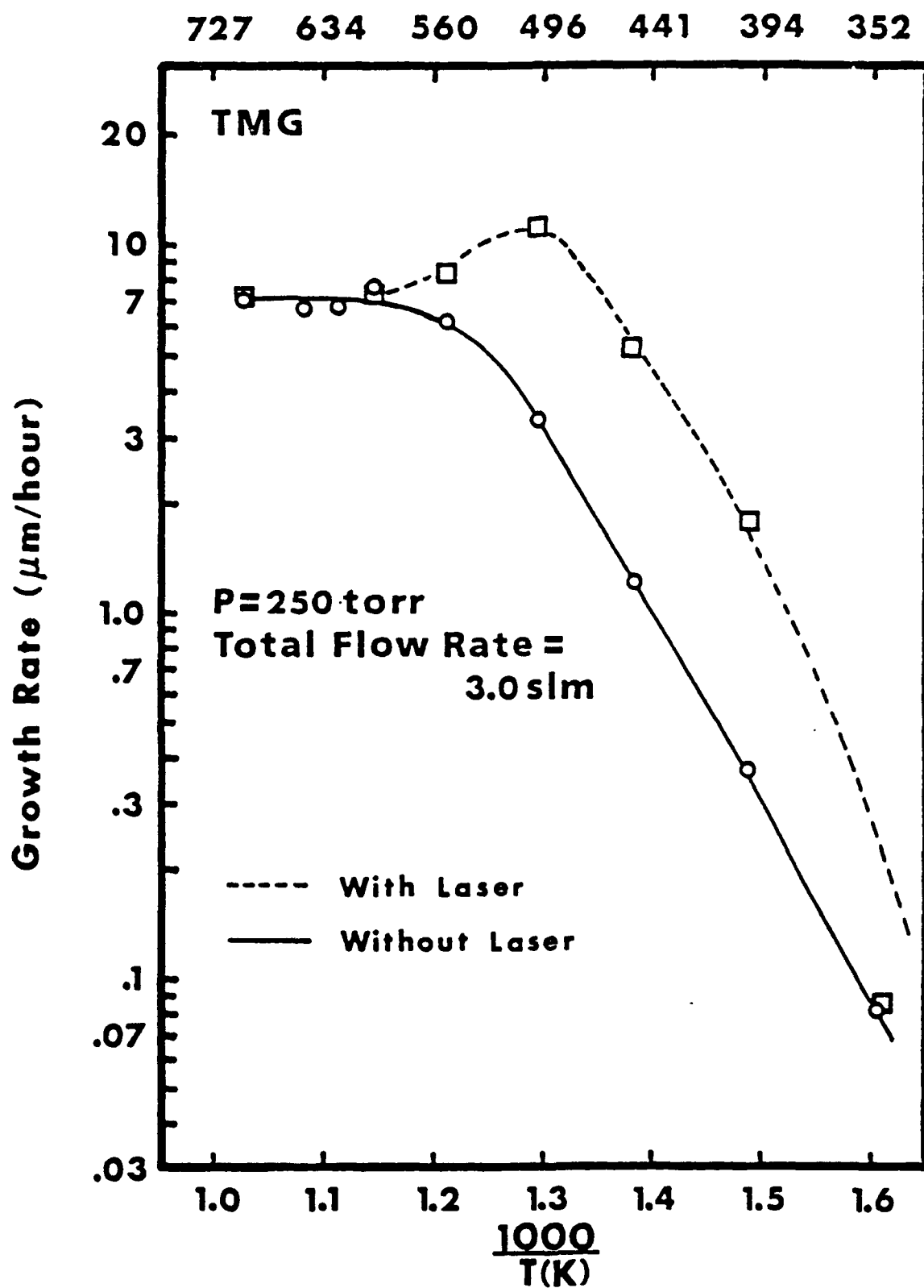


Figure D-4

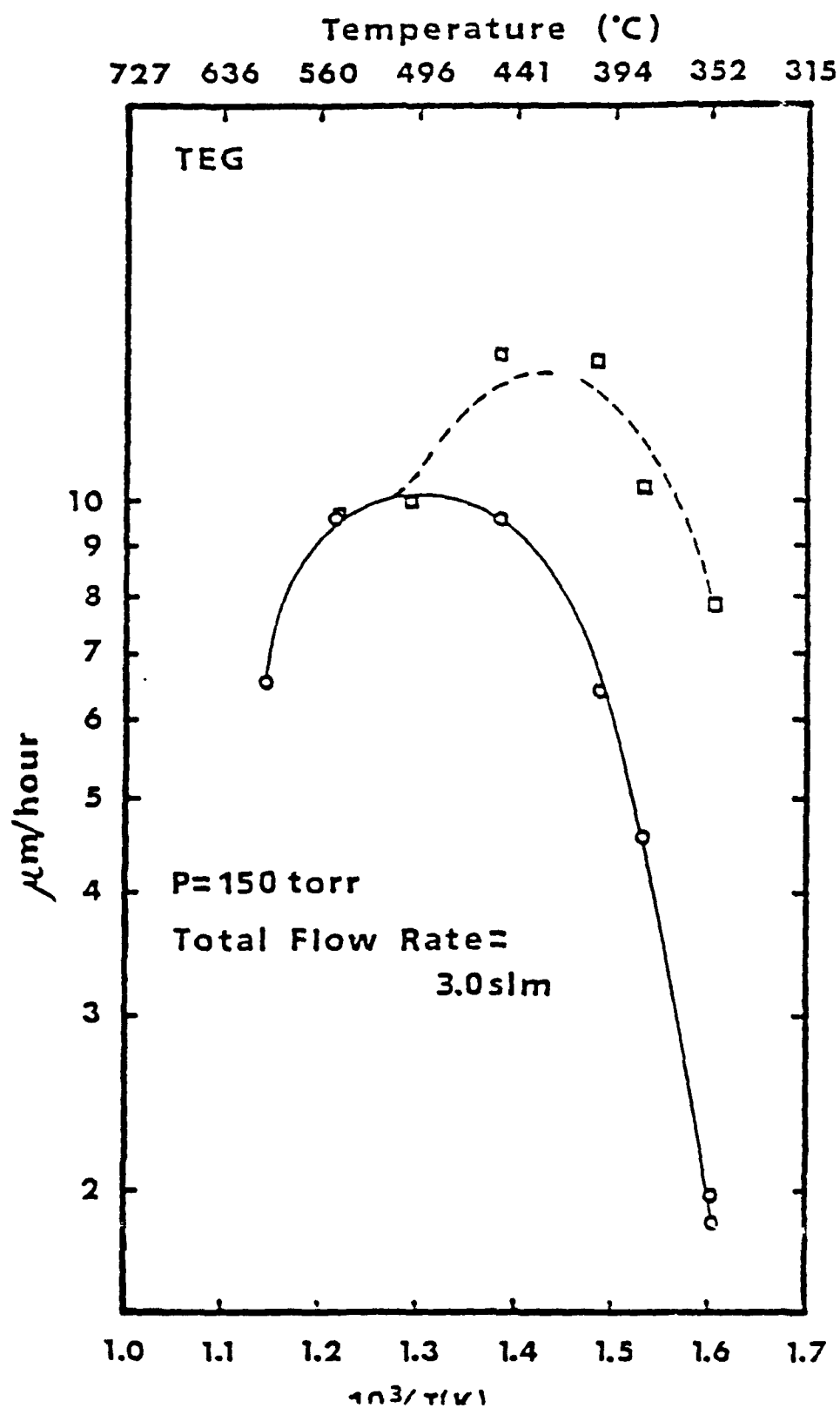


Figure D-5

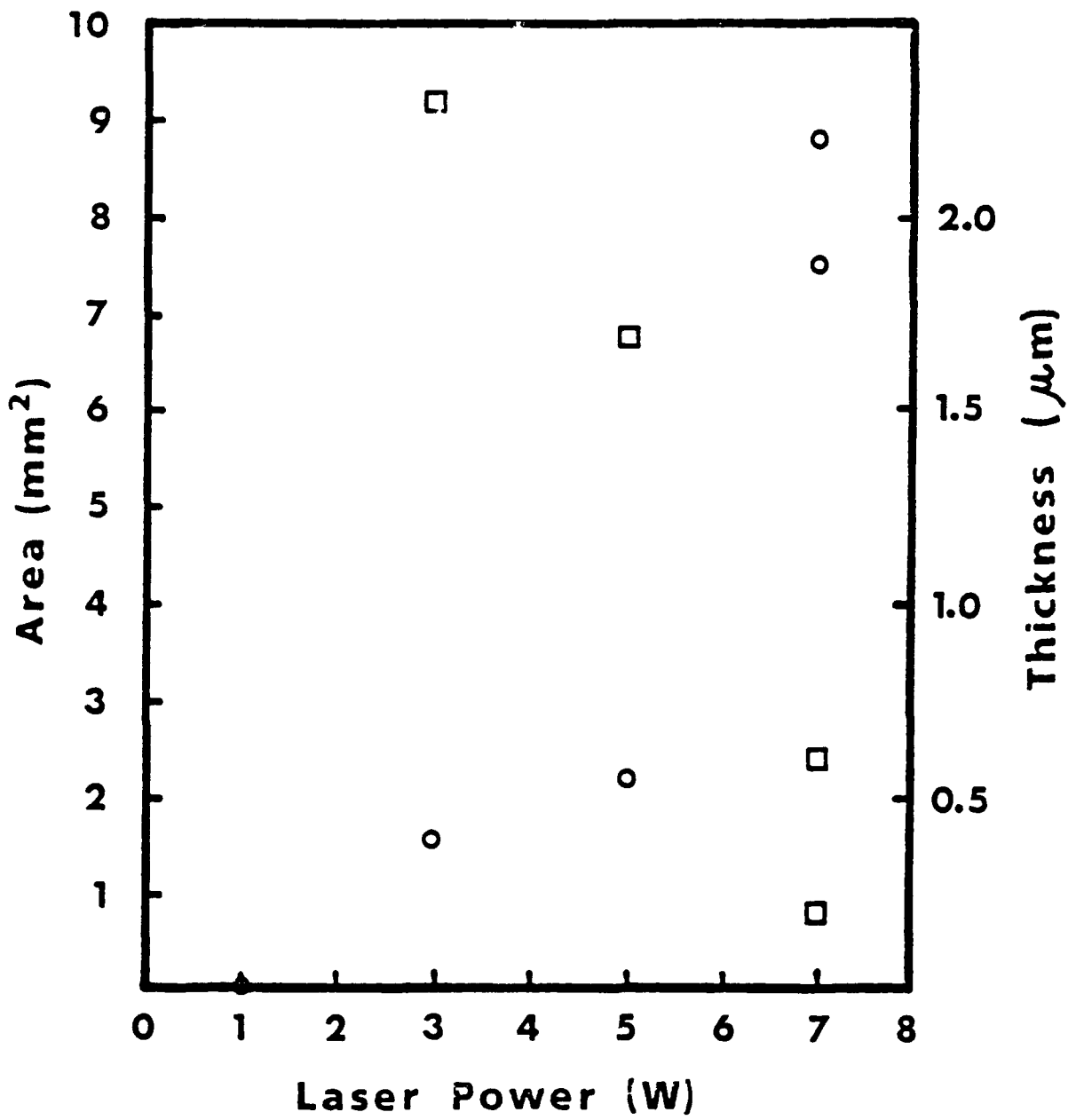


Figure D-6

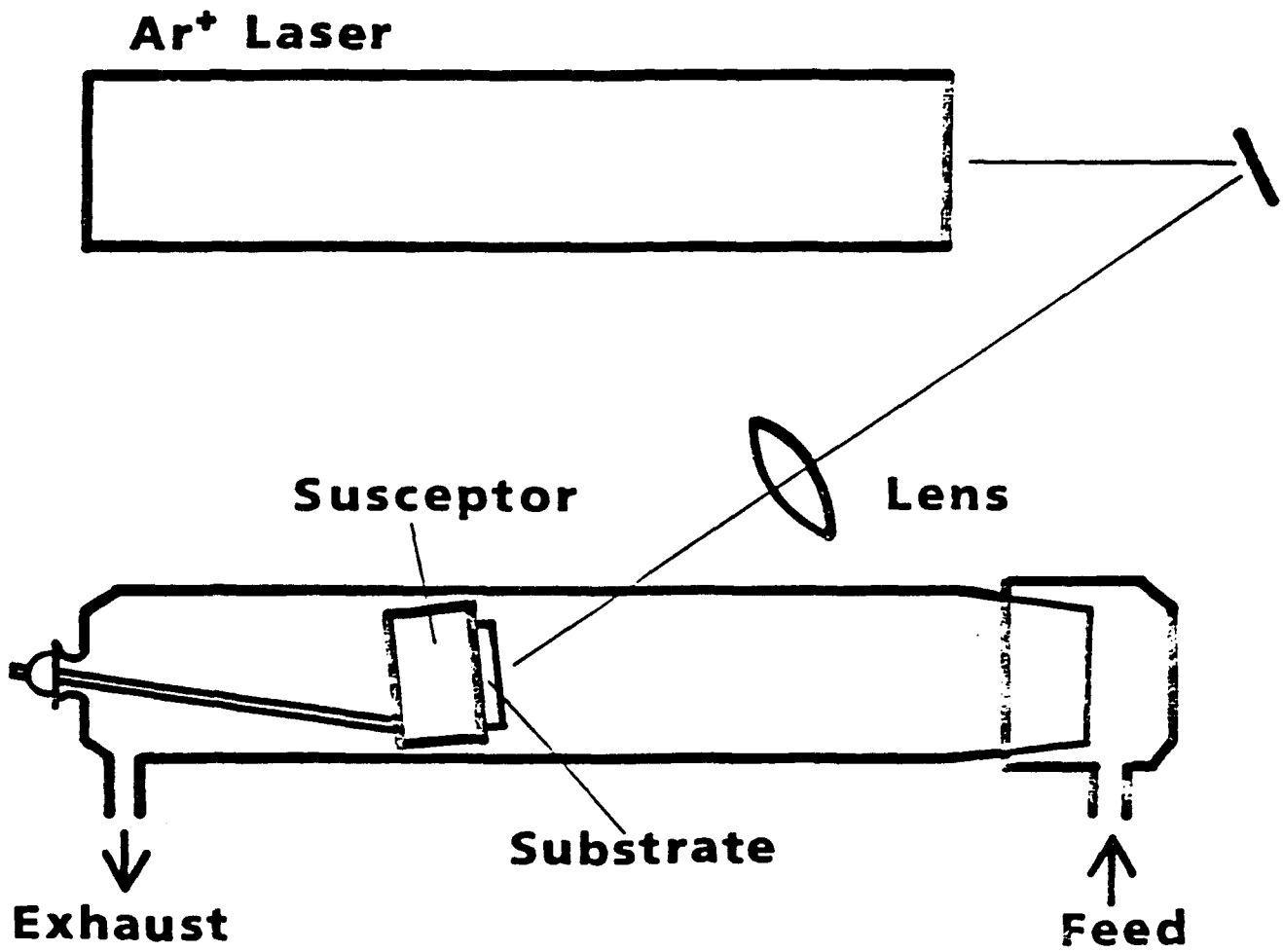


Figure D-7

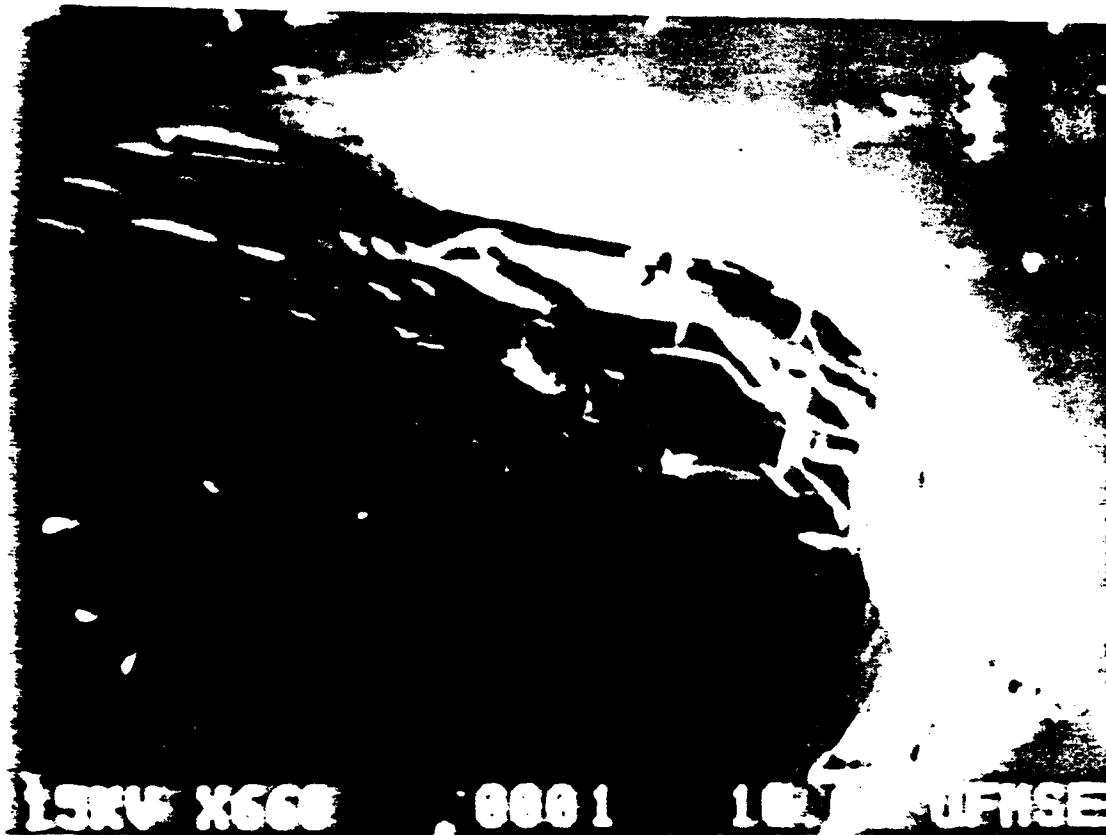


Figure D-8

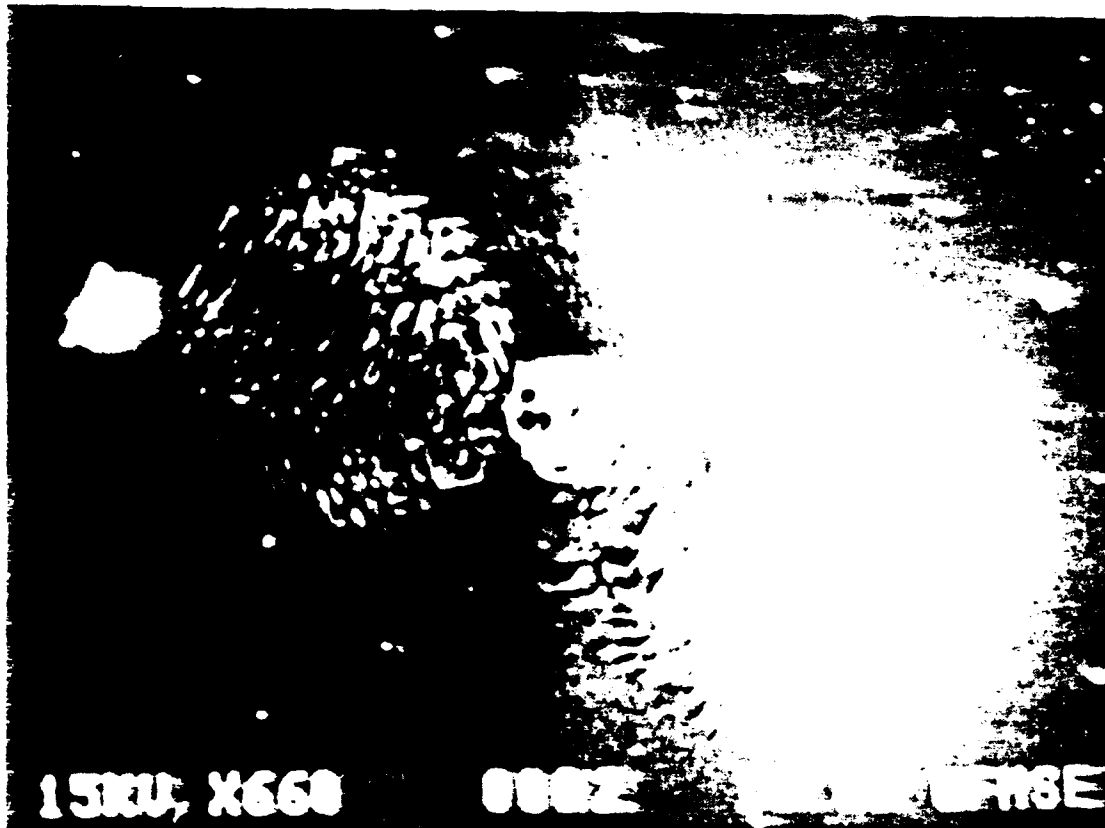


Figure D-9

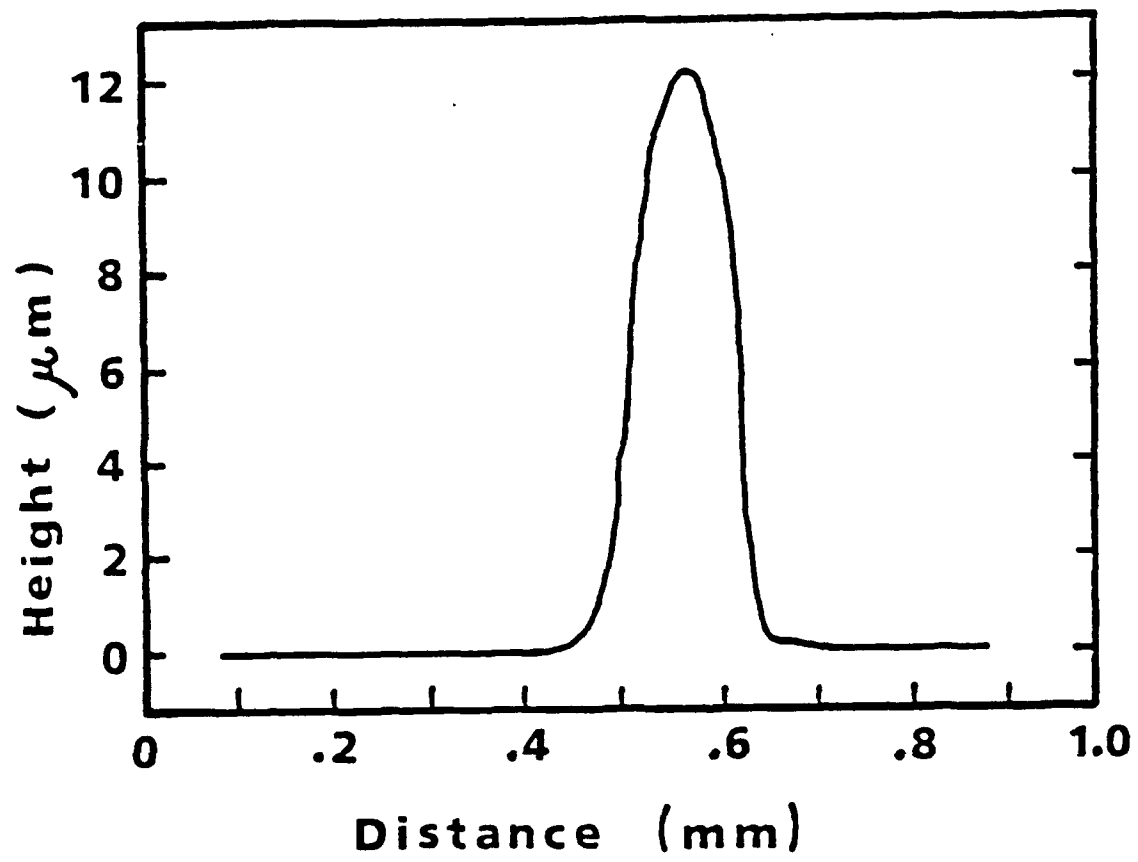


Figure D-10

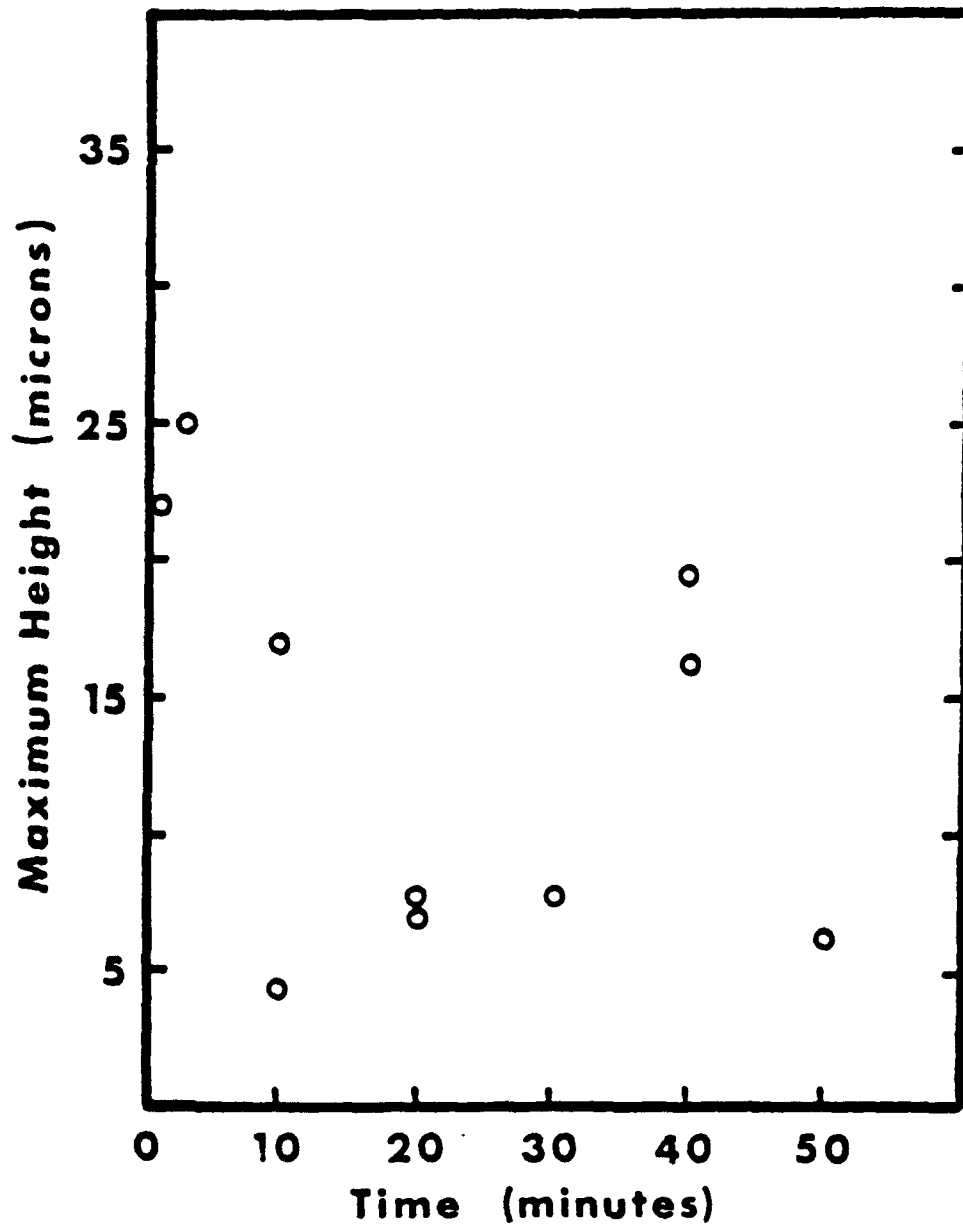


Figure D-11

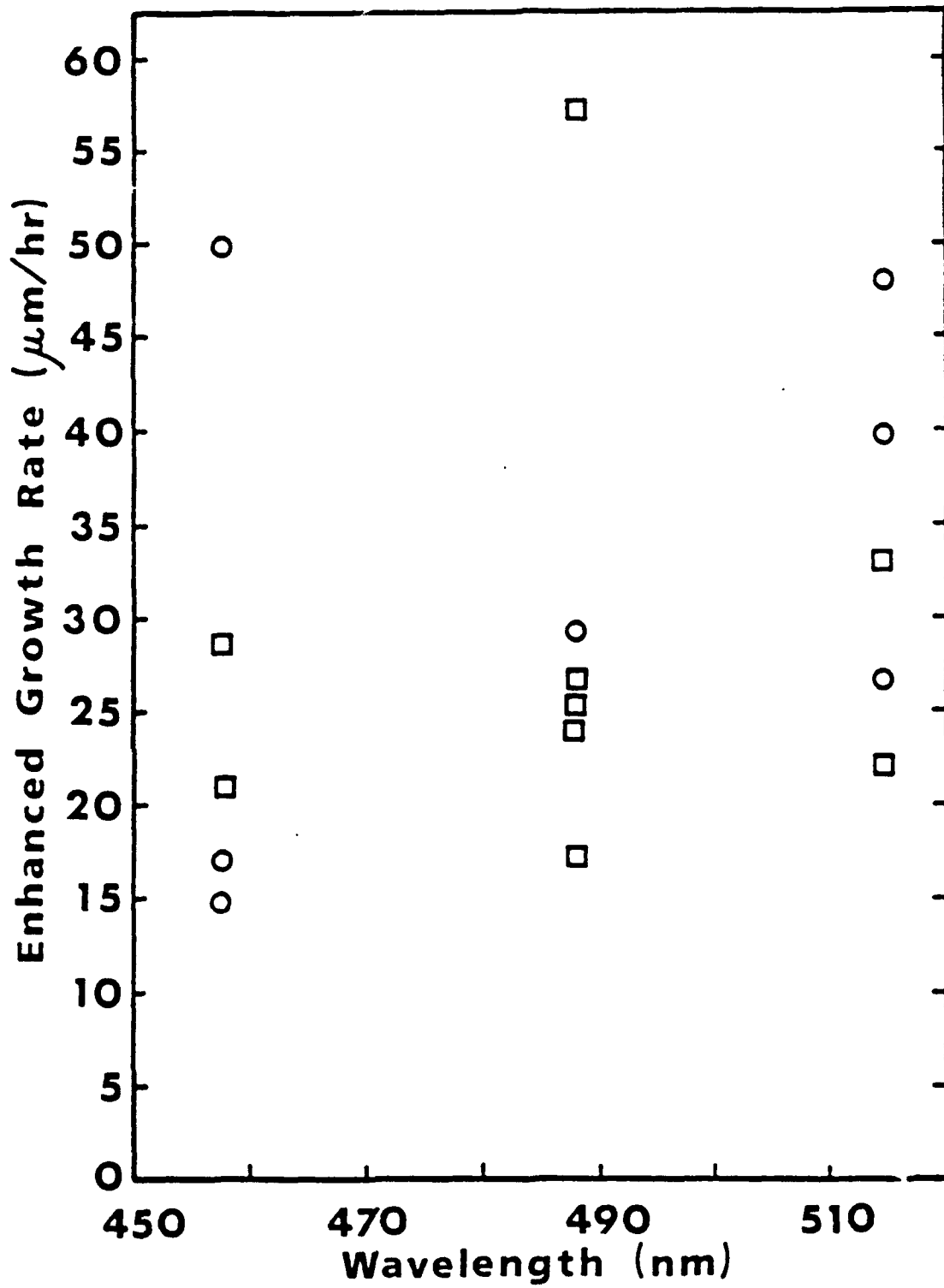


Figure D-13

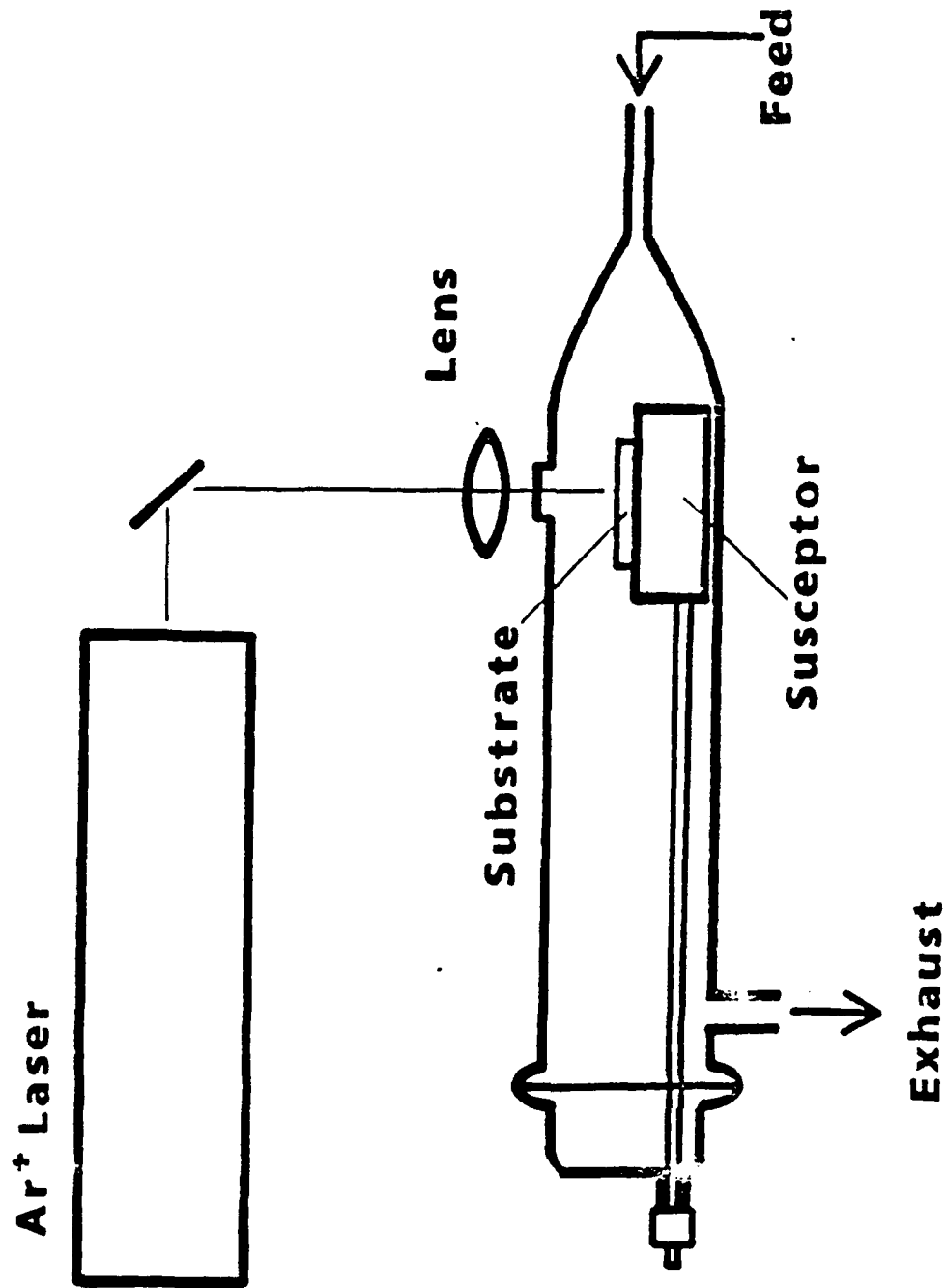


Figure D-13

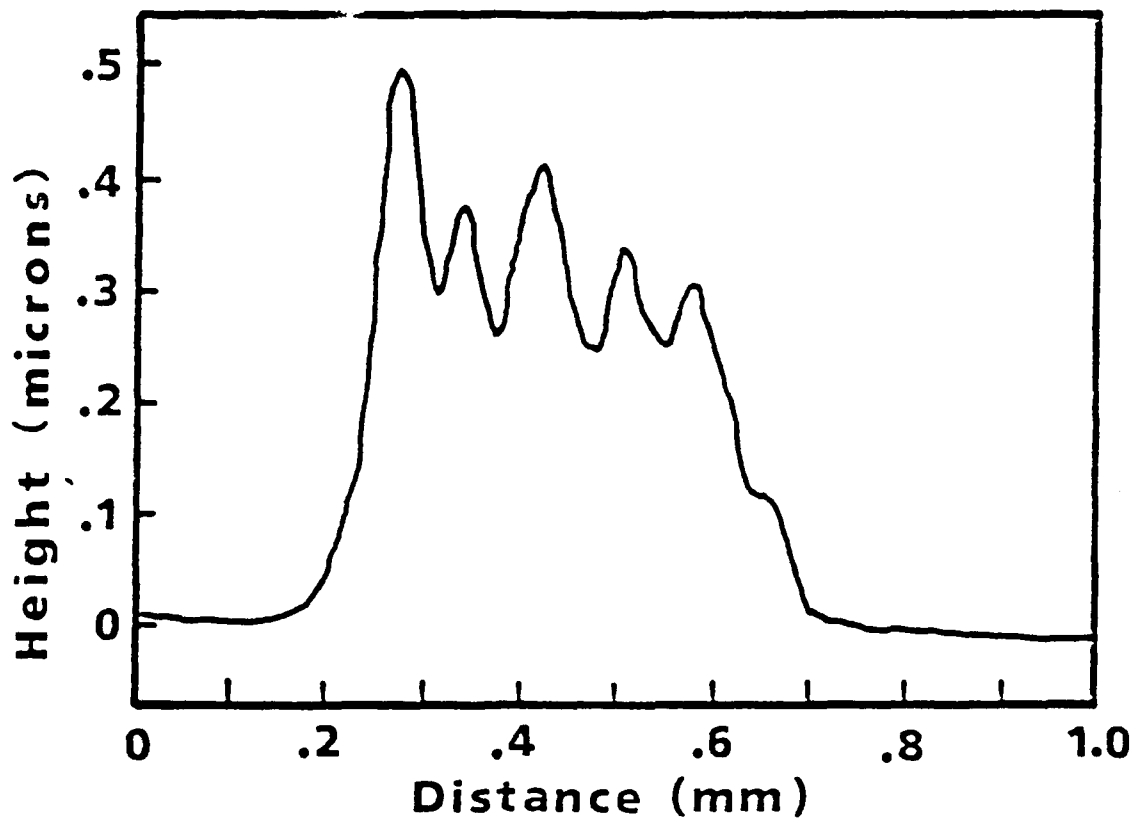


Figure D-14

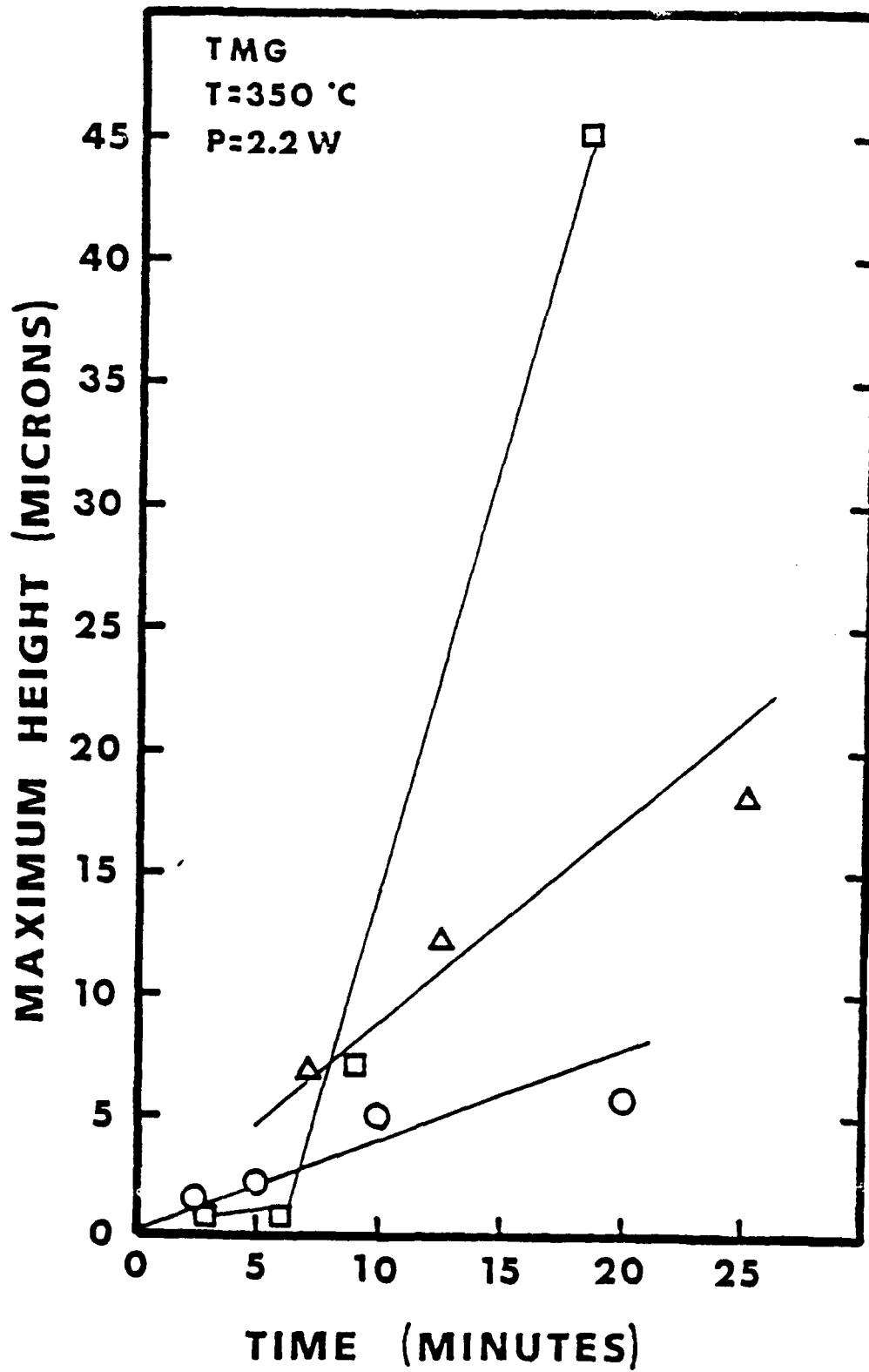


Figure D-15

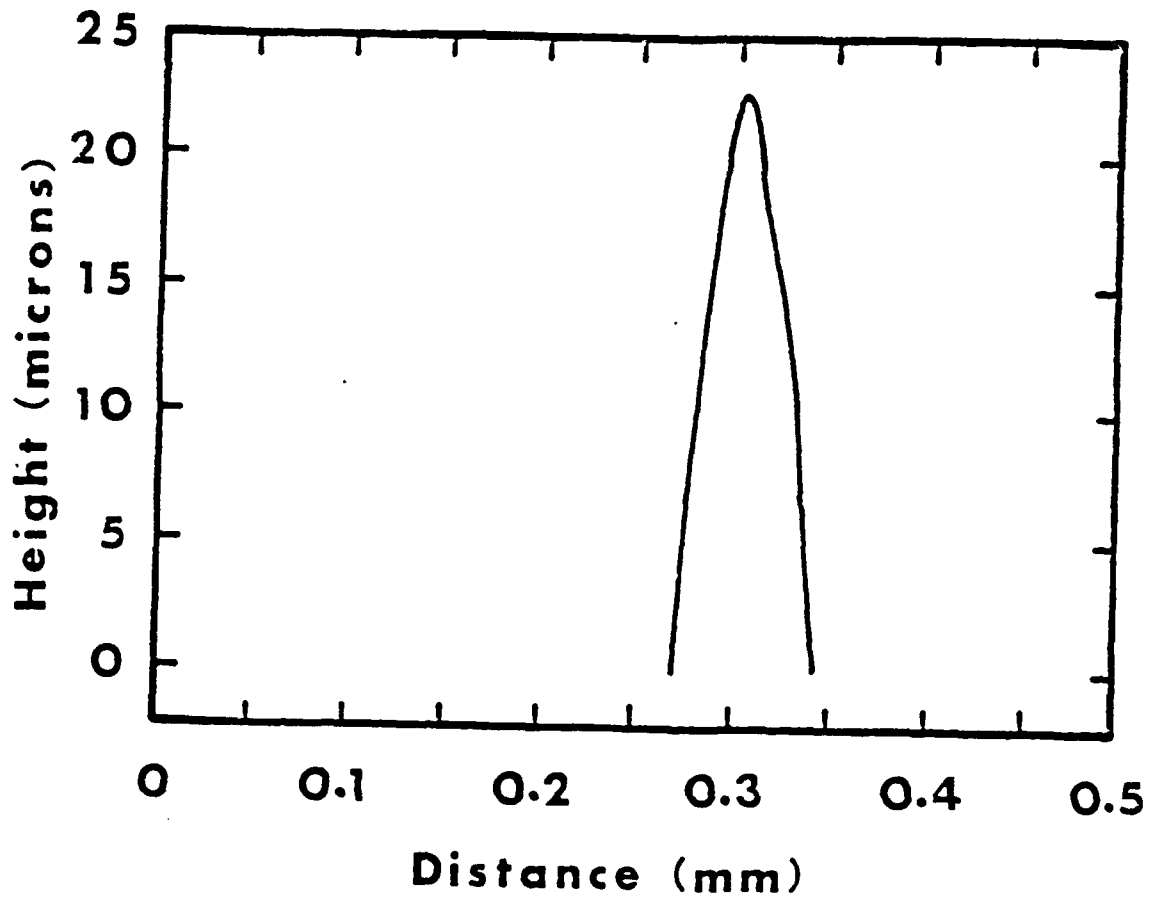


Figure D-16

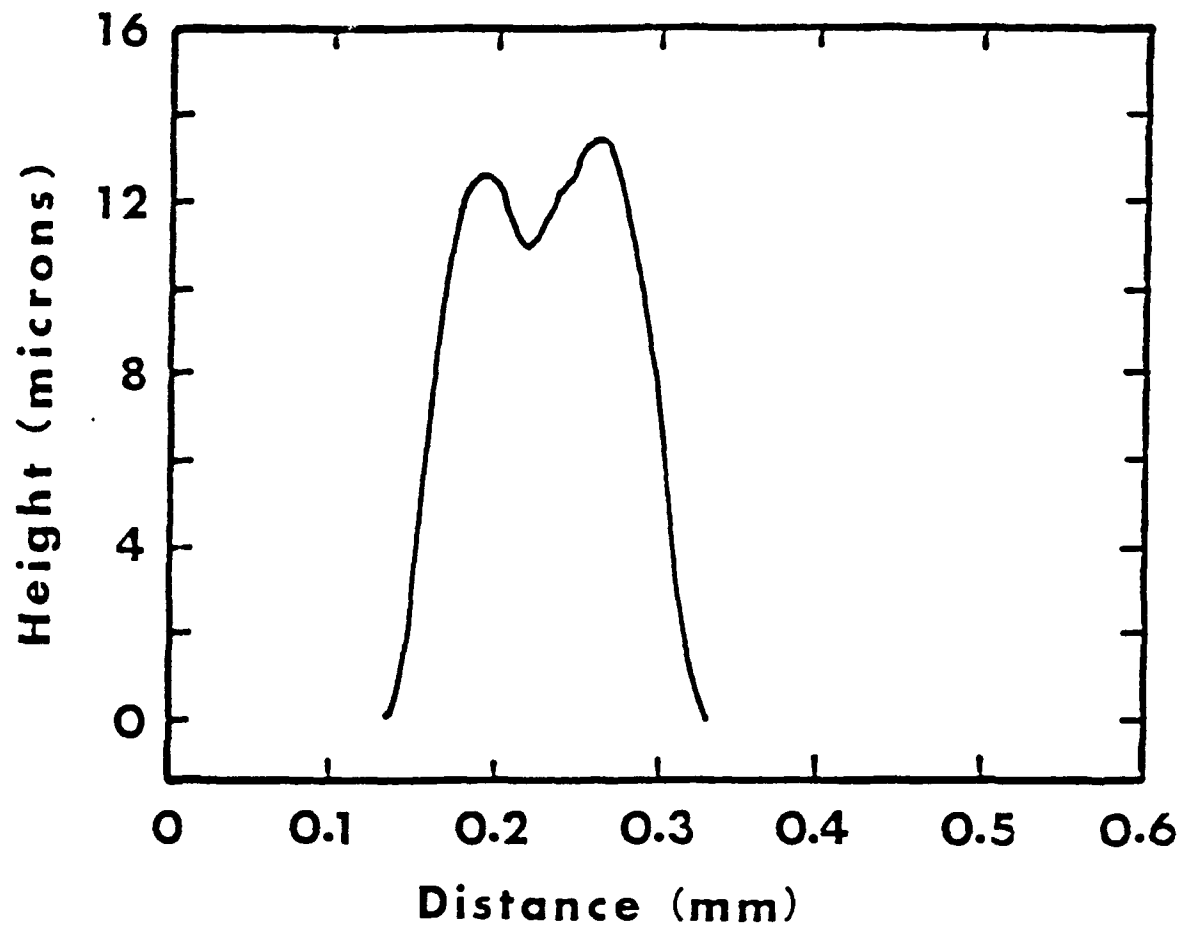


Figure D-17

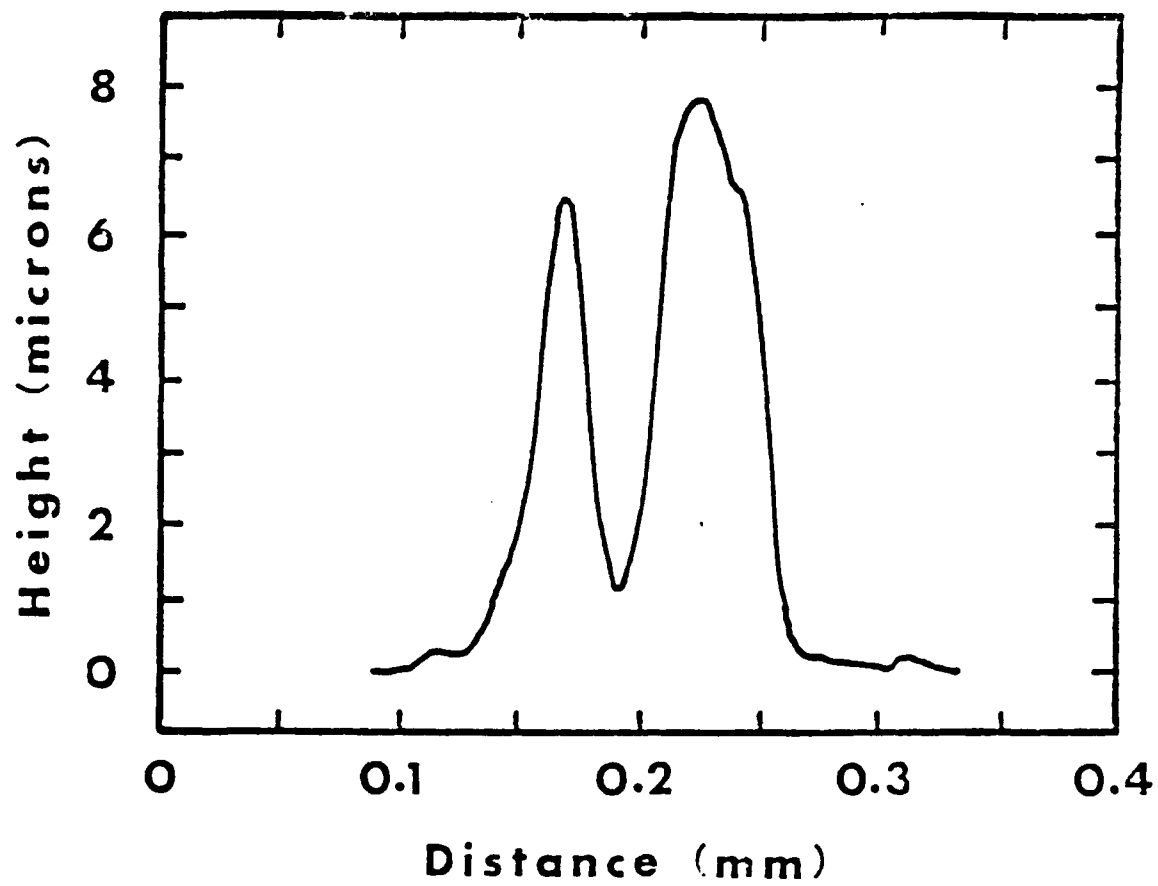


Figure D-18

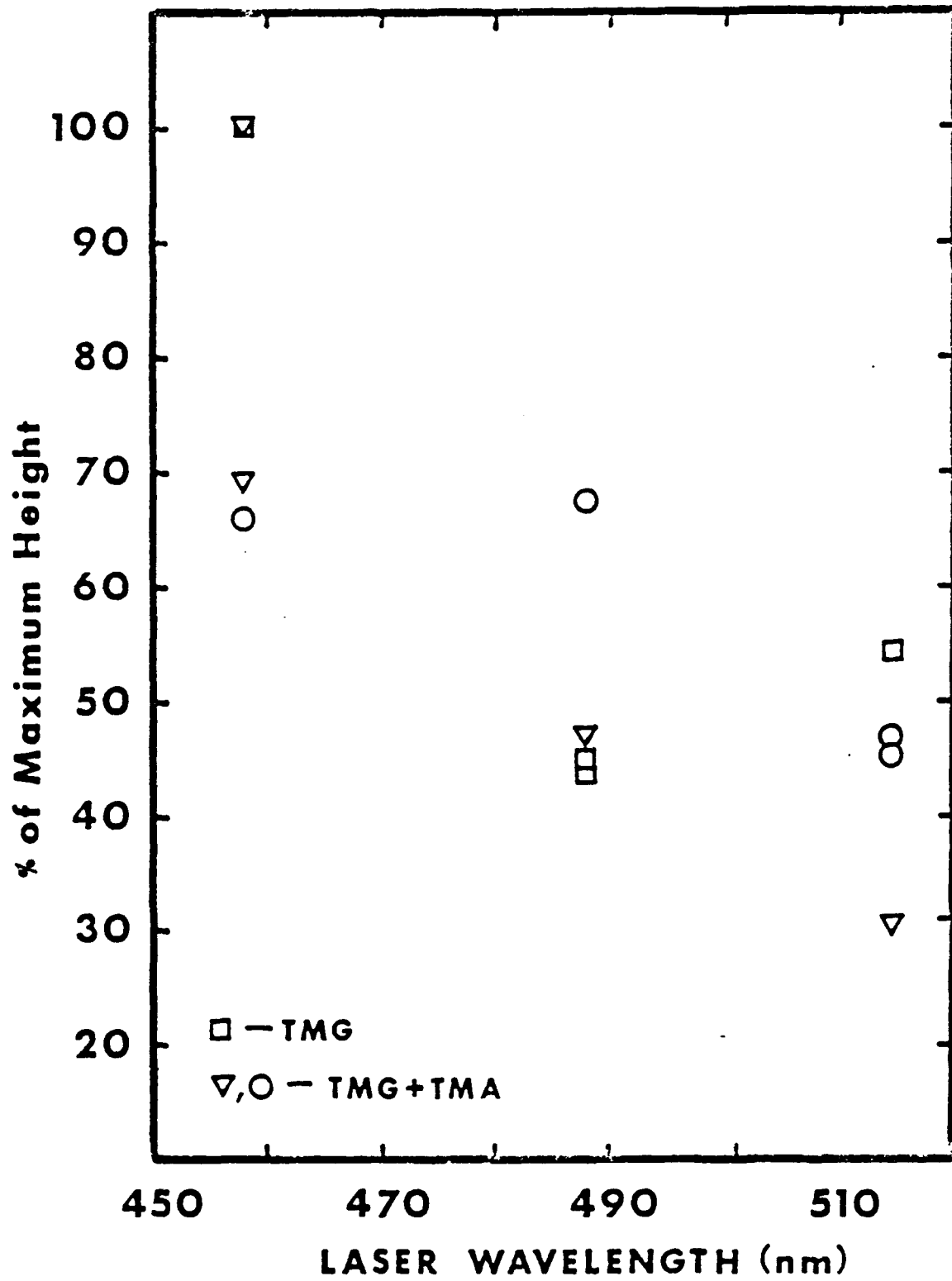


Figure D-19

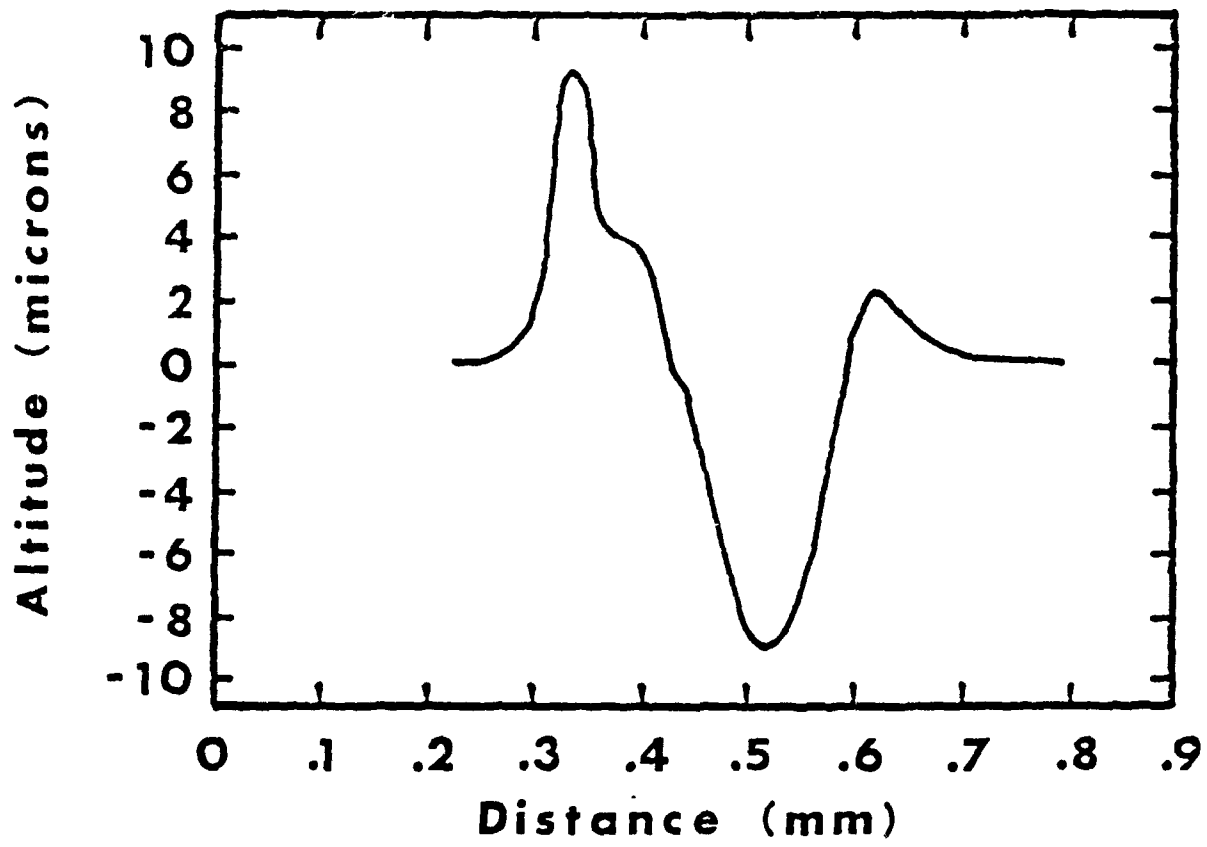


Figure D-20

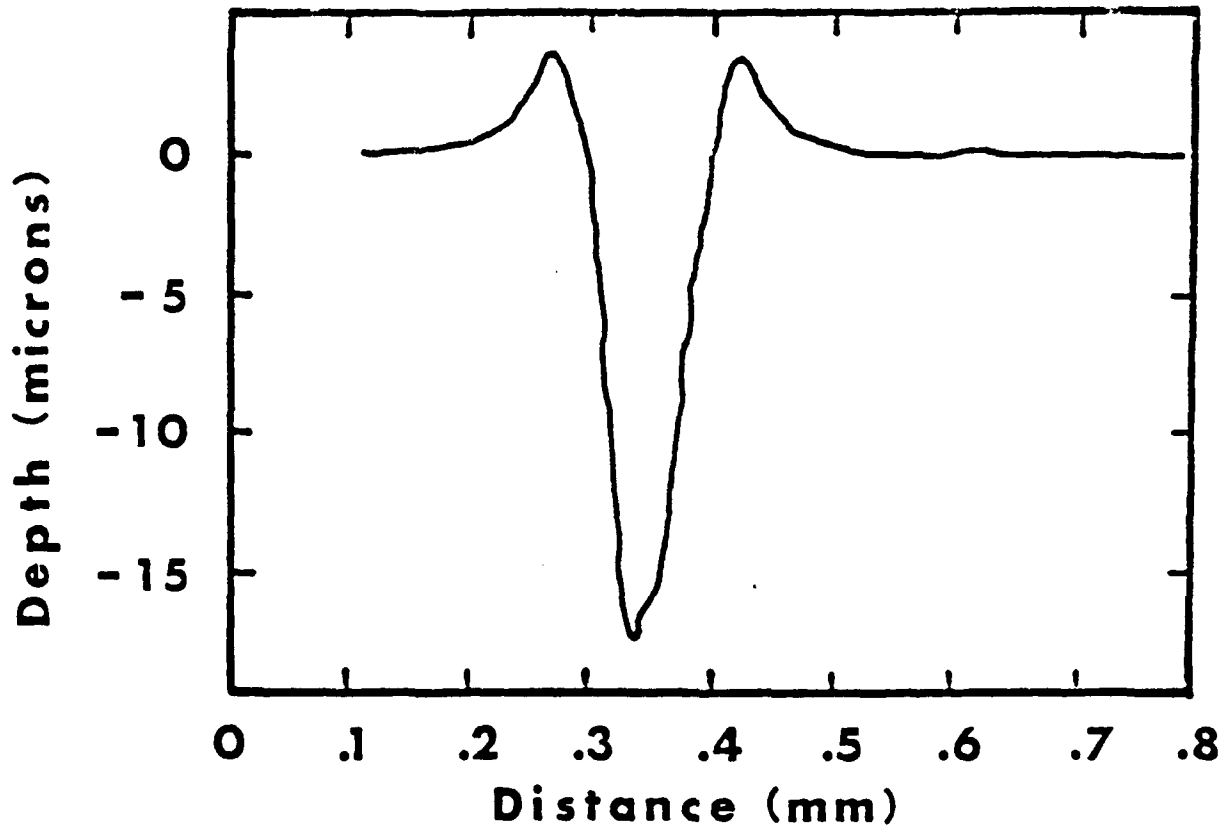


Figure D-21

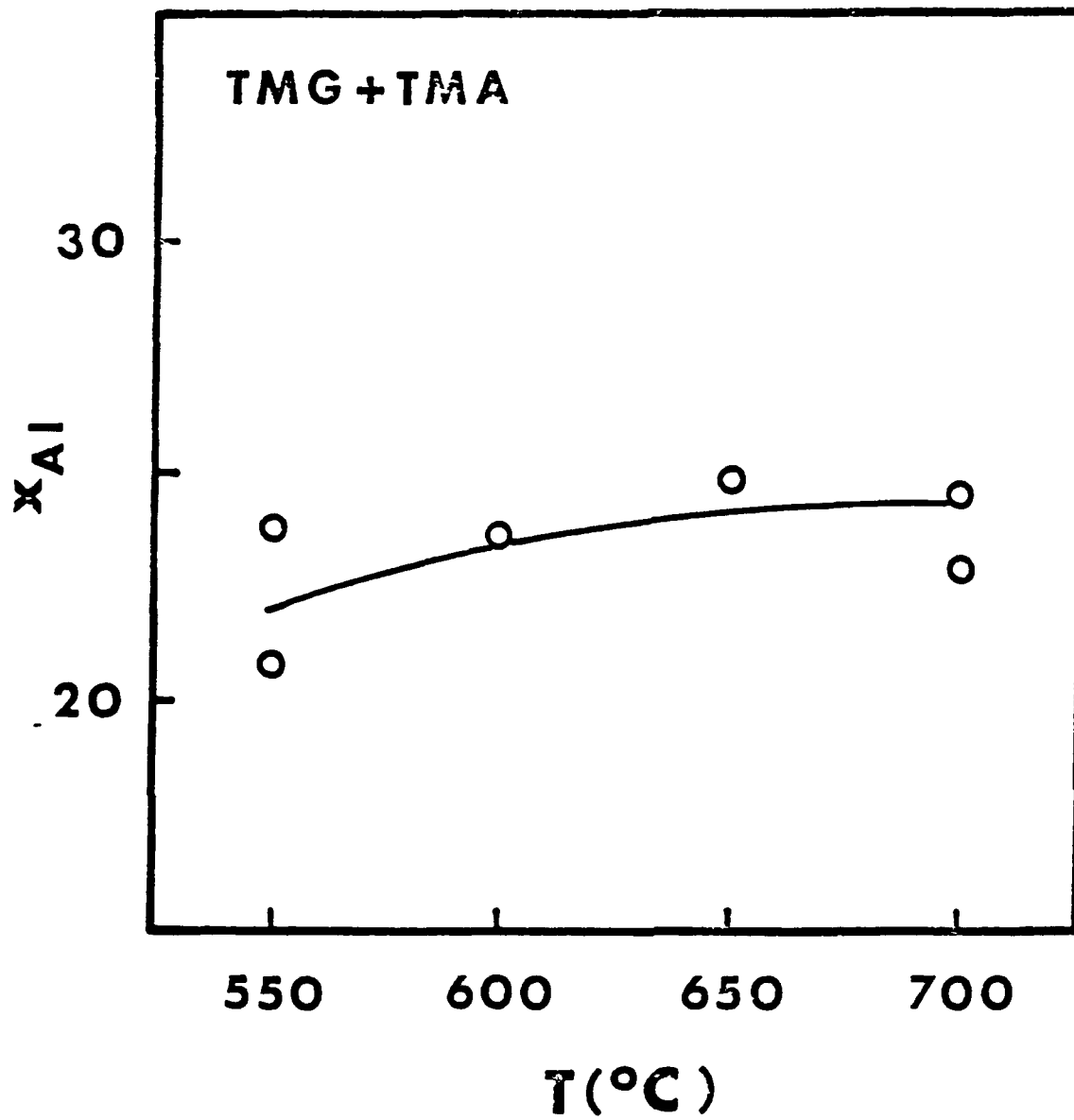


Figure D-22

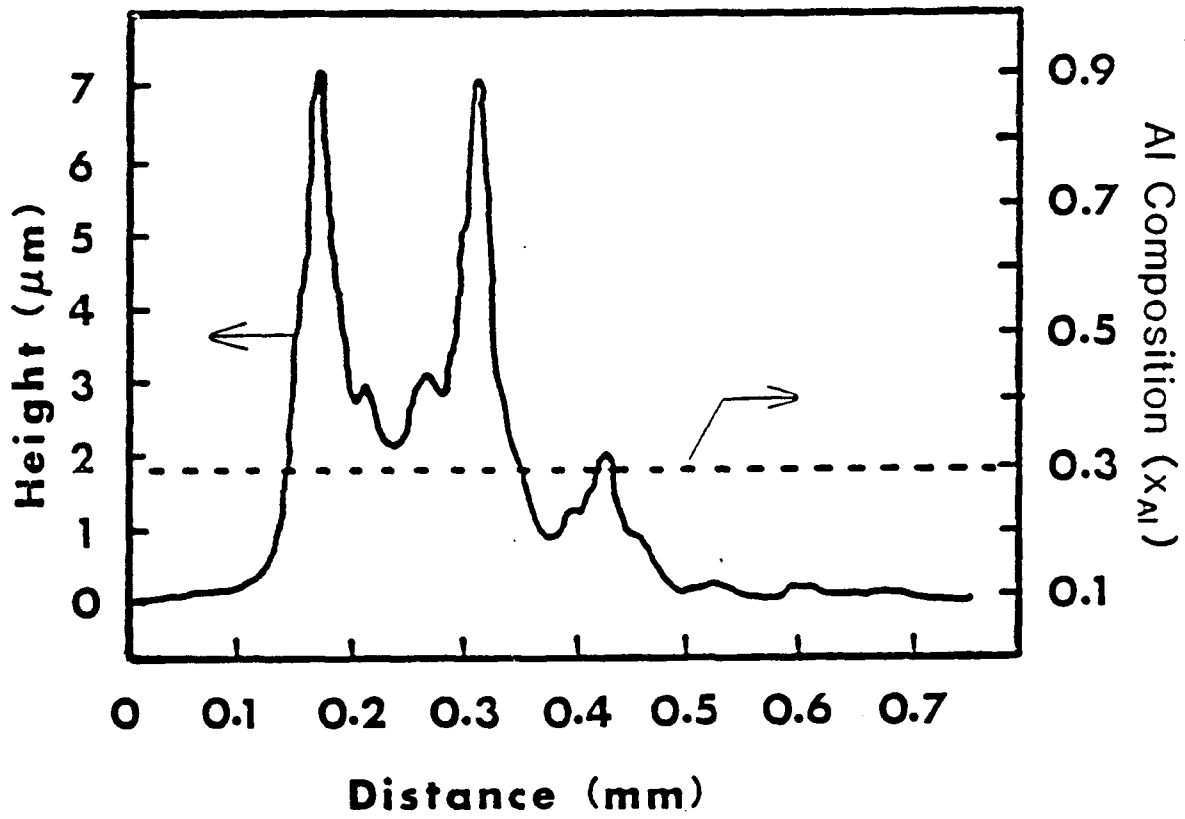


Figure D-23

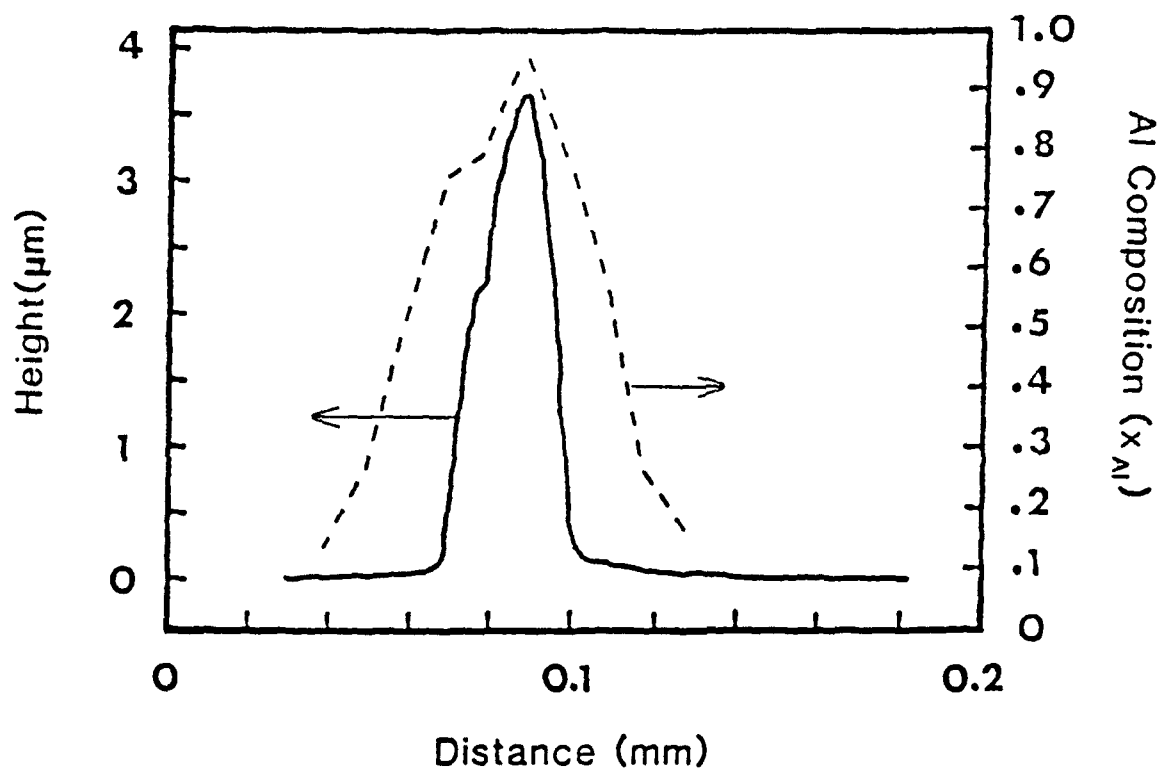


Figure D-24



Figure D-25

Appendix E

Process Characterization and Evaluation of Hydride VPE Grown $\text{Ga}_x\text{In}_{1-x}\text{As}$ Using a Ga/In Alloy Source

E.1. INTRODUCTION

Epitaxial layers of $\text{Ga}_x\text{In}_{1-x}\text{As}$ on InP substrates have properties which make them extremely attractive for a wide range of optoelectronic and electronic device applications. As an example, $\text{Ga}_x\text{In}_{1-x}\text{As}$ is used as the active layer in photodiode structures important in long wavelength optical communication technology. This active layer must have a low background carrier concentration and zero lattice mismatch to the substrate for production of quality devices. The hydride vapor phase epitaxy (VPE) technique has several advantages for large-scale production of such devices, including high purity, high growth rate, and process controllability. Since hydride VPE can be operated at conditions for which growth is limited by surface reaction, the technique is attractive for applications which require uniform growth rates and epitaxy selectivity.

In conventional hydride VPE, a HCl/H_2 gas mixture is reacted with separate Ga and In liquid sources to form volatile group III chloride species. Experimental [72] and thermodynamic calculations [73-75] indicate that the deposited film composition is very sensitive to the vapor phase molar ratio of Ga to In generated in the separate sources; this ratio must be controlled to better than 0.1% for some device applications. Since the sensitivity of film composition to the Ga/In molar ratio is highest near the condition to grow $\text{Ga}_x\text{In}_{1-x}\text{As}$ lattice matched to InP, extremely fine control of the HCl flows to both source zones is required. Equilibrium conversion of HCl is not always attained in many of the reactors [28,73,76]. Therefore, run-to-run reproducibility of the deposited film composition can be influenced by factors which alter mass transfer and reaction rates in the source zone (e.g., liquid metal height, flow velocity) [73]. Radial compositional uniformity in the deposited film is also affected by the degree of mixing of the gas streams exiting the separated source regions. Several investigators [77-83] have proposed using a binary liquid alloy source to improve the quality of the deposited layers. Although the

growth rate is affected by changes in the group III transport rate, the molar ratio of transported Ga to In or the film composition should be less sensitive to variations in the HCl flow rate or reaction efficiency with an alloy source. The Ga/In alloy source also eliminates the need for gas phase mixing of the group III species. In addition, the alloy-source technique will require less expensive reactors with simplified process operations.

The alloy source has been experimentally investigated using either HCl [78-82] or AsCl_3/H_2 [77,83] as the source of HCl with a separate flow of AsH_3 [78,80-82] or AsCl_3 [79] (chloride VPE). A full parametric study of the hydride VPE using an alloy source has not yet been reported. The reported alloy-source composition required to produce $\text{Ga}_{0.47}\text{In}_{0.53}\text{As}$ films lattice matched to InP varies from 3.2 to 12.2 at.% Ga [78-80,82]. This study reports the influence of alloy-source composition and other process parameters (e.g., inlet mole fraction of AsH_3 and HCl, deposition temperature) on the film composition and growth rate. An interesting observation by Quinlan and Erstfeld [81] is the growth of a limiting $\text{Ga}_{0.87}\text{In}_{0.13}\text{As}$ film composition by the addition of excess HCl downstream of the source zone. Similar experiments are repeated for two different source alloy compositions and the results are reported.

Operation of the group III metal source with equilibrium conversion is desirable to achieve reproducible transport rates. The present study shows that the traditional open-boat design gives non-equilibrium conversion. A modified source boat was studied and further design changes are suggested to overcome these limitations. The transport of Ga and In with an alloy source has been shown to occur by incongruent reaction, thus limiting the source lifetime [79]. It is shown in this study that the source lifetime can be increased by the gradual variation of deposition parameters to counter the run-to-run variation in the alloy composition. In addition, state-of-the-art p-i-n photodetectors were fabricated in order to demonstrate that an alloy source is capable of producing device-quality epitaxial films.

E.2. EXPERIMENTAL

The hydride VPE reactor used in this study was the double-barrel reactor design and is

described elsewhere [84-86]. Instead of using separate Ga and In source boats, a single alloy boat containing gallium and indium was inserted into one of the In source barrels. Alloy compositions of 5.35, 8.69 and 15.10 at.% Ga were studied. Excess HCl could be introduced into the mixing zone via a dopant line. The base operating conditions were the following: source zone temperature, 838°C; mixing zone temperature, 820°C; deposition temperature, 700°C; and total pressure, 1 atm. The III/V ratio was fixed at a value of two and the total volumetric flow rate in the deposition zone was held constant at 4200 sccm (25 cm/sec linear velocity). These values are based on previous work and were found to produce excellent epitaxial layer properties (e.g., surface morphology, interfacial quality, and photoelectrical properties). Study of the inlet mole fractions of HCl and AsH₃, deposition temperature, source gas velocity, source alloy composition, excess HCl and source geometry was performed around these base operating conditions.

Volatile metal chlorides were generated and transported by a stream of HCl (100%) in H₂ carrier gas. The carrier gas used was purified by Pd-alloy diffusion. Arsine or phosphine (which was used to stabilize the InP surface prior to deposition and to grow InP cap and buffer layers) was introduced as 10% mixtures of AsH₃ or PH₃ in H₂. The purity of reactant gases was at a level to give background doping of epitaxial layers routinely in the range 5×10^{14} to 5×10^{15} cm⁻³. The metals, In and Ga, were 99.99999% pure. Substrates grown by the LEC method were S or Fe doped InP, cut 2° off the (100) toward the nearest (110).

Substrates were etched in Caro's acid (5:1:1 H₂SO₄:H₂O₂:H₂O) and a 1% Br₂ in CH₃OH solution. The etched substrate, typically about 1x1 cm², was placed into the reactor load-lock chamber and flushed with H₂ prior to opening the reactor. Reactant flows were initiated about 15 minutes prior to the insertion of substrates in order to avoid significant transient effects. The substrates were preheated in a PH₃/H₂ mixture ($P_{PH_3}^0 = 3.9 \times 10^{-2}$ atm) to prevent surface decomposition and extraneous initial deposition and to promote desorption of native oxides on the surface. No deposition on the quartz wall or substrate holder was observed during most of the depositions. The alloy source was baked for 50 hrs at 838°C in flowing H₂ before deposition to insure the

complete mixing of In and Ga and to lower the background doping concentrations in the resulting films [78].

The layer thickness was measured by optical microscopy on cleaved and stained samples. The composition of $\text{Ga}_x\text{In}_{1-x}\text{As}$ epitaxial layers was determined from Vegard's law using lattice constants measured with a Siemens single-crystal x-ray diffractometer. The initial and final compositions of the Ga/In source alloy were determined by atomic absorption spectroscopy. The alloys for these analyses were remelted and rapidly quenched to 77 K to form an alloy of uniform composition [80].

E.3. RESULTS AND DISCUSSION OF PARAMETRIC STUDIES

The growth rate of $\text{Ga}_x\text{In}_{1-x}\text{As}$ was studied as a function of deposition temperature in the range 674 to 719°C, while maintaining other process parameters at the base values. An Arrhenius plot of growth rate is shown in Figure E-1. The growth rate shows two distinct segments with temperature: a strongly temperature-dependent growth rate at low temperatures and a weakly temperature-dependent growth rate at higher temperatures. At the lower temperatures, the apparent activation energy determined for the deposition of $\text{Ga}_x\text{In}_{1-x}\text{As}$ from a source alloy of 8.69 at.% Ga was 188 kJ/mol. This value is in close agreement with the values of 184 kJ/mol and 180 kJ/mol reported by Hyder et al. [87] and Erstfeld and Quinlan [80], both on (100) InP substrates. These apparent activation energies are similar to those reported for the homoepitaxy of GaAs on (100) GaAs (203.8 kJ/mol [88] and 200.0 kJ/mol [89]), while the reported apparent activation energy for homoepitaxy of InAs has a higher value of 230 kJ/mol [90]. Since the growth rate is nearly independent of deposition temperature at higher temperatures, the deposition is apparently limited by mass transfer. Figure E-1 shows that the growth is primarily limited by chemical reaction at the base temperature of 700°C.

The change in the composition of the deposited layer with the deposition temperature is shown in Figure E-2. The Ga content decreases with increasing temperatures for deposition in the reaction-limited regime (low growth temperatures). This observation is consistent with the lower

apparent activation energy reported for homoepitaxial deposition of GaAs than for InAs [88-90]. The observed change in the film composition for growth in the mass transport limited regime (high growth temperatures) is smaller.

The trends reported here in the film composition as a function of the deposition temperature are opposite to those observed by Kordos et al. [78] and Hyder et al. [87]. Both the experimental results and equilibrium analysis of Kordos et al. [78] indicate the Ga content increases with increasing deposition temperatures. Hyder et al. [87] reported HCl flow rates in the In source boat required to maintain a constant film composition of $\text{Ga}_{0.47}\text{In}_{0.53}\text{As}$ at various growth temperatures. Their results show that an increase in the HCl flow rate was required with increasing growth temperatures, suggesting the Ga content increases with increasing deposition temperatures. The reason for these differences is not apparent, though the chloride VPE study by Coronado et al. [83] at film compositions close to the lattice matched value lends support to both of these observed trends. These investigators reported a broad minimum for the Ga content at a deposition temperature near 675°C for an alloy source composition of 7 at.% Ga.

The influence of the source alloy composition on the film composition and growth rate is shown in Figure E-3. The plot shows that an alloy composition of 5.8 at.% Ga is necessary for the preparation of $\text{Ga}_{0.47}\text{In}_{0.53}\text{As}$ at these operating conditions. The Ga mole fraction in the epitaxial layer is considerably higher than the mole fraction of Ga in the alloy source. This behavior is expected on the basis of thermodynamics since the Gibbs energy of formation of InAs at the growth temperature from the monochloride is approximately 25 kJ/mol more positive than the value for GaAs [91]. Positive deviations from ideal-solution behavior in the In-rich alloy solution [92] further contribute to a distribution coefficient greater than one. The result of an equilibrium analysis using a regular solution model for the solid solution is also shown in Figure E-3 and is seen to accurately reproduce the trend in this intensive variable. The slope of the equilibrium curve is near its maximum value at the lattice-matched composition indicating this composition is very sensitive to changes in the alloy source concentration.

Figure E-3 shows the results of several other investigators using an alloy source. The

general trends are similar but the alloy composition required for lattice-matched growth varies between 3.2 to 12.2 at.% Ga. These results suggest that the composition of the film is influenced by the operating parameters and reactor design. In this study, for example, lattice-matched $\text{Ga}_{0.47}\text{In}_{0.53}\text{As}$ epitaxial layers could be grown with both 5.35 and 8.69 at.% Ga alloys by adjustment of the process parameters. Control of the film composition at the lattice-matched value by gradual adjustment of process parameters until 50% of the alloy source had been consumed. The optimum alloy composition for growth of a particular film composition should be based on other factors, such as photoelectrical properties. The observed differences in alloy composition required to grow lattice-matched layers between different investigators are consistent in sign when accounting for differences between stated operating conditions. Figure 3 also shows that the growth rate decreases with increasing Ga mole fraction in the alloy source. This decrease is consistent with the growth rates reported for the separate binary compounds [88-90].

The effect of inlet AsH_3 mole fraction, $x_{\text{AsH}_3}^0$, on the composition and growth rate of epitaxial layers grown from alloys containing 5.35 and 8.69 at.% Ga is shown in Figure E-4. The film composition shows a small increase in InAs mole fraction and agrees with the results reported by several other investigators [93-96]. The growth rate increases slightly with increasing $x_{\text{AsH}_3}^0$. These results are also consistent with the predictions of an equilibrium analysis [97] which predicts an increase in the degree of supersaturation with increasing $x_{\text{AsH}_3}^0$.

The dependence of film composition on the inlet HCl mole fraction, x_{HCl}^0 , is shown in Figure E-5, where the results for three different alloys, 15.10, 8.69, and 5.35 at.% Ga, are reported. The Ga content of the deposited layers increases with x_{HCl}^0 and exhibits a limiting value when x_{HCl}^0 is greater than 6×10^{-3} atm. The limiting film compositions of $\text{Ga}_x\text{In}_{1-x}\text{As}$ prepared from different alloy sources are 0.85, 0.74 and 0.43 for the alloy compositions 15.10, 8.69, and 5.35 at.% Ga, respectively. Increasing x_{HCl}^0 increases the group III transport rate and therefore the III/V ratio. The results shown in Figure E-4 also represent changes in the III/V ratio. The direction of change in the film composition is in agreement between the results shown in Figures

E-4 and E-5, but the magnitude of the change is greater for variations in x_{HCl}^0 than $x_{\text{AsH}_3}^0$. A thermodynamic analysis predicts an increase of Ga in the deposited epitaxial layer with increasing x_{HCl}^0 or equivalently Cl/H molar ratio. InCl is more stable than GaCl⁽²⁸⁾ and tends to remain in the vapor phase which increases the Ga content of $\text{Ga}_x\text{In}_{1-x}\text{As}$. The large increase of Ga in the grown layer may also be related to a non-equilibrium conversion in the source zone which increases the amount of unreacted HCl in the deposition zone. The extra HCl in the deposition zone reduces the degree of supersaturation, which increases the Ga concentration in the film. This aspect is discussed in the following paragraphs.

The growth rates of $\text{Ga}_x\text{In}_{1-x}\text{As}$ as a function of inlet HCl mole fraction are shown in Figure E-6. The growth-rate data exhibit a maximum for each of the three alloy compositions studied. The maxima occur at a III/V ratio of approximately one, corresponding to the stoichiometry of the film. The increase in growth rate at low values of inlet HCl mole fraction is the result of simply supplying more metal chlorides to the system. This is the region where the GaAs mole fraction is increasing in the film (Figure E-5). At high values of inlet HCl mole fraction, the growth rate decreases as the III/V ratio increases, apparently first order in x_{HCl}^0 . This result is consistent with the explanation by Shaw [99] that the deposition rate of GaAs in the kinetically limited regime is controlled by competitive adsorption between metal chlorides, HCl, and arsenic species at As growth sites. Weyburne and Quinlan [94] also observed these phenomena in the growth of $\text{Ga}_x\text{In}_{1-x}\text{As}$ epitaxial layers. They suggested that above a threshold value of GaCl partial pressure, Langmuir adsorption of GaCl probably reaches saturation and growth depends on the dissociation of GaCl from the active arsenic sites.

The effect of adding excess HCl to the mixing zone on the film composition and growth rate is shown in Figure E-7. Injection of HCl to the mixing zone has been used to reduce Si background doping, reduce the growth rate, and eliminate wall deposition. The Ga content in the deposited layers increases slightly with increasing added HCl and eventually reaches a constant value. The gallium increase is more pronounced for films prepared from the source containing the

smaller amount of Ga (5.35 at.% Ga). Quinlan and Erstfeld [81] and Buckley [96] have observed greater changes in the Ga content of the film when HCl was added to the mixing zone. The results in the present study do not show this large Ga increase since the base operating conditions gave GaAs mole fractions close to the limiting value (see Figure E-5). The decrease in growth rate with added HCl was first order. This decrease in growth rate was also observed by other investigators [81,95,96] when a threshold amount of HCl was exceeded. Jurgensen et al. [95] demonstrated that the threshold amount of HCl was dependent on source temperature. The authors showed that the decrease in growth rate occurred only after extraneous wall deposition was eliminated by sufficient HCl injection. These observations are consistent with the present work where no wall deposition was observed.

The present study showed that a limiting composition of $\text{Ga}_{0.88}\text{In}_{0.12}\text{As}$ was obtained with the 15.10 at.% Ga source alloy. This result agrees with the limiting value of $\text{Ga}_{0.87}\text{In}_{0.13}\text{As}$ reported by Quinlan and Erstfeld [81] with the use of a 11.8 at.% Ga source alloy. These authors reported the deposition of $\text{Ga}_{0.87}\text{In}_{0.13}\text{As}$ even in the etching regime of the growth curve. Similar studies with the 5.35 at.% Ga alloy in the present investigation showed no deposition in the etching regime when the layers were analyzed with sputter Auger electron spectroscopy.

E.4. SOURCE ZONE PERFORMANCE

A possible explanation for the dependence of the deposited film composition on the inlet HCl mole fraction is non-equilibrium conversion of HCl in the source zone. Experimental results [28,29,100-102] of previous investigators indicate that the reaction of HCl with liquid group III metals is not complete at all operating conditions for a tubular-shaped source zone. Ban et al. [29] reported a 78% conversion of HCl by reaction with In at 800°C with the value of P_{HCl}^0 equal to 3×10^{-2} atm. The conversion efficiency changed little with inlet HCl partial pressure in the range 3×10^{-3} to 3×10^{-2} atm. These results were recently confirmed by Hsieh [73] who showed that the reaction efficiency of HCl with Ga or In is not affected by the HCl inlet partial pressure. Though the reaction efficiency does not change with the HCl inlet mole fraction, the total amount of

unreacted HCl transported to the deposition zone does change. These observations suggest that the dependence of the film composition reported in Figure E-5 may result from incomplete conversion of HCl in the source zone.

A study was performed to demonstrate that non-equilibrium conversion of HCl occurs in this particular source-boat at typical operating conditions. Hsieh [73] demonstrated that mass transfer is the primary limitation for converting HCl to group III metal chlorides in the source zone. Therefore a change in the gas velocity in the source zone should affect the conversion of HCl if non-equilibrium conditions exist in the source. The gas velocity in the source zone was varied by changing the H₂ flow rate in the source while maintaining the flow rate of HCl at a constant value. A constant velocity in the mixing and deposition zones was maintained by adding an equivalent amount of H₂ through a dopant line in the mixing zone. Film compositions and growth rates were measured as a function of gas velocity in the source zone for two alloy source compositions, 15.10 and 8.69 at.% Ga. As shown in Figure E-8, the Ga mole fraction in the film increases with increasing volumetric flow rate in the source while the growth rate remains constant. The observed change in the film composition indicates that the gas velocity influenced the deposition process, presumably through a change in the HCl reaction efficiency. An increase in the volumetric flow rate in the source should give less HCl conversion. A decrease in the HCl conversion adds HCl to the deposition zone and produces a corresponding decrease in the group III transport rate. The variation of film compositions and growth rates with added HCl is given in Figure E-7 while the influence or changes in the group III transport rate is given in Figures E-5 and E-6. Realizing that the base operating conditions corresponds to growth with a volumetric flow rate of 1000 sccm in Figure E-8, an increase in the Ga mole fraction in the film is consistent with the results shown in Figures E-5 and E-7. The independence of growth rate with gas velocity is apparently a result of compensation between a decreasing growth rate with increasing group III transport rate (Figure E-6) and an increasing growth rate with decreasing excess HCl (Figure E-7).

In an attempt to improve the HCl conversion in the source zone a simple design change of the source boat was made. The modification made in the present study was to add a cover to the

source boat to decrease the transverse diffusion length of reactant gases to the liquid surface. The modified structure of the boat is shown in Figure E-9. The compositions and growth rates of the grown films as a function of linear gas velocity at constant x_{HCl}^0 using the modified source boat are shown in Figure E-10. The space above the cover was used to add H_2 carrier gas to maintain a constant total flow rate in the deposition zone. Although the results of the film composition indicated less than complete conversion, the increase in growth rates with gas velocity were consistent with an improved HCl conversion. Experiments with the covered boat showed that there was insufficient HCl exiting the source zone to suppress wall deposition, resulting in higher growth rates [103]. Further improvements in HCl conversion could be gained by increasing the reactant residence time (decreasing gas velocity, increasing contact length), decreasing the transverse length scale further, and increasing the diffusivity and reaction rate at the liquid surface (decreasing pressure, increasing temperature).

A disadvantage of the VPE-hydride process with an alloy source is the decrease in Ga concentration in the alloy over a series of runs [79,80]. This complication may also be resolved with boat design. A study was made of the changes of compositions and growth rates over an extended series of runs using the same alloy. Figure E-11 shows the results of the study. The abscissa in Figure E-11 represents the cumulative HCl feed where 32 standard liters (sl) corresponds to approximately 40 one-hour runs. The alloy source (300 g) was depleted by 50% after 32 sl. The results shows that the indium concentration increases in a quantitative fashion similar to the results in Figure E-3. The increase in growth rate is consistent with the observation that the InAs growth rate is greater than GaAs. Figure E-11 also shows that a constant composition of the ternary is obtained during approximately 10 runs. The decrease of Ga concentration in the alloy corresponding to the In increase in the ternary was confirmed with atomic absorption analyses of the alloy sources. The Ga depletion of the source probably results predominantly from the more efficient transport reaction of Ga than In [73,101]. A positive deviation from ideal solution behavior in the melt also contributes to a Ga-rich vapor at equilibrium if the liquid composition is less than 0.5 [92].

E.5. PHOTODETECTORS FABRICATED WITH THE VPE HYDRIDE-ALLOY TECHNIQUE

Planar p-i-n photodetectors were fabricated with 3.5 mm active layers of $\text{Ga}_{0.47}\text{In}_{0.53}\text{As}$ grown from a 6.61 at.% Ga alloy source. The growth conditions of the active layers were identical to this study except the III/V ratio was 10/7. The active layers were grown between a 3.25 mm InP buffer layer and a 1.00 mm InP cap layer on a (100) S-doped InP substrate. The photodetectors with 75 mm active diameters were fabricated using standard planar technology. The fabrication procedure has been adequately described by Forrest et al. [104].

The characteristics of the devices fabricated with the present technique compares favorably with InGaAs p-i-n photodetectors reported in the literature [105]. The fabricated photodetectors exhibited the following properties: dark current, 10 to 20 nA at -5 V; capacitance, 0.88 to 0.92 pF; responsivity, 0.84 to 0.86 A/W; and breakdown voltage, > 40 V. The data demonstrates that epitaxial layers of $\text{Ga}_{0.47}\text{In}_{0.53}\text{As}$ grown from Ga/In alloys are suitable for the production of state-of-the-art p-i-n photodetectors for fiber optic applications.

E.6. SUMMARY

The VPE-hydride process using a Ga-In alloy source has been studied in detail for the preparation of epitaxial layers of $\text{Ga}_x\text{In}_{1-x}\text{As}$. The compositions and growth rates were measured as a function of the following process parameters: source x_{HCl}^0 , $x_{\text{AsH}_3}^0$, mixing zone x_{HCl}^0 , gas velocity, deposition temperature, alloy composition, and source geometry. The results revealed that reaction kinetics and mass transfer play important roles, particularly in determining the growth-rate behavior. An equilibrium analysis, nevertheless, could explain the film compositional behavior for most process parameter changes. Table E-1 gives a qualitative summary of the effects of these parameters on the compositions and growth rates of the epitaxial layers. Lattice-matched $\text{Ga}_{0.47}\text{In}_{0.53}\text{As}$ epitaxial layers could be grown on InP substrates with alloys containing 5 to 8 at.% Ga.

The study demonstrated that the VPE-hydride method with an alloy source can be success-

fully used to fabricate high quality p-i-n photodetectors. A problem with the technique is gallium depletion in the source with continued use. This problem is related in part to non-equilibrium conversion in the source zone. Improved reactor designs for the source region with mixing zone HCl injection should extend the lifetime of an alloy source.

Table E-1. Influence of Increasing Process Parameters on the Composition and Growth Rates of $\text{Ga}_x\text{In}_{1-x}\text{As}$ Grown from Ga/In Alloys

Parameter	x_{HCl}^0 (added)	x_{HCl}^0	gas velocity	$x_{\text{AsH}_3}^0$	T_d	number of runs
Film Composition (x_{GaAs})	↑	↑	↑	↓	↓	↓
Growth Rate	↓	↑↓	↔	↑	↑	↑

Legend: ↑ : increase in x_{GaAs} or growth rate
 ↓ : decrease in x_{GaAs} or growth rate
 ↔ : negligible change

List of Figures

- Figure E-1. Arrhenius plot of growth rate of $\text{Ga}_x\text{In}_{1-x}\text{As}$ at $x_{\text{Ga}}(\text{source}) = 0.0869$, $x_{\text{HCl}}^0 = 0.0024$, and $x_{\text{AsH}_3}^0 = 0.0034$. The low temperature apparent activation energy is 188 kJ/mol.
- Figure E-2. Film compositions of $\text{Ga}_x\text{In}_{1-x}\text{As}$ as a function of deposition temperatures at $x_{\text{Ga}}(\text{source}) = 0.0869$, $x_{\text{HCl}}^0 = 0.0024$, and $x_{\text{AsH}_3}^0 = 0.0034$.
- Figure E-3. Film compositions and growth rates of $\text{Ga}_x\text{In}_{1-x}\text{As}$ as a function of Ga mole fraction in the source alloy at $x_{\text{HCl}}^0 = 0.0072$ and $x_{\text{AsH}_3}^0 = 0.0033$. Growth rates: \blacklozenge , this study. Film compositions: \circ , this study; \blacksquare , Jacobs et al. [82]; \circ , Kordos et al. [78]; \square , Erstfeld and Quinlan [80]; \diamond , Chatterjee et al. [79]. Film compositions predicted by an equilibrium analysis (regular solid solution model ($W = 12.95^{(21)}$ kJ/mol) and Redlich-Kister liquid solution model [92]), — —.
- Figure E-4. Film compositions (open symbols) and growth rates (closed symbols) of $\text{Ga}_x\text{In}_{1-x}\text{As}$ as a function of inlet AsH_3 mole fraction, $x_{\text{AsH}_3}^0$. Deposition conditions: \blacksquare , $x_{\text{Ga}}(\text{source}) = 0.0869$, $x_{\text{HCl}}^0 = 0.0036$, total flow of $\text{H}_2 + \text{HCl}$ in the source = 523 sccm; \circ , $x_{\text{Ga}}(\text{source}) = 0.0535$, $x_{\text{HCl}}^0 = 0.0072$, total flow of $\text{H}_2 + \text{HCl}$ in the source = 1045 sccm.
- Figure E-5. Film compositions of $\text{Ga}_x\text{In}_{1-x}\text{As}$ as a function of inlet HCl mole fraction, x_{HCl}^0 , at $x_{\text{AsH}_3}^0 = 0.0033$. Source alloy compositions: \square , $x_{\text{Ga}}(\text{source}) = 0.1510$; \blacksquare , $x_{\text{Ga}}(\text{source}) = 0.0869$; \circ , $x_{\text{Ga}}(\text{source}) = 0.0535$.
- Figure E-6. Growth rates of $\text{Ga}_x\text{In}_{1-x}\text{As}$ as a function of inlet HCl mole fraction, x_{HCl}^0 , at $x_{\text{AsH}_3}^0 = 0.0033$. Source alloy compositions: \blacksquare , $x_{\text{Ga}}(\text{source}) = 0.1510$; \blacksquare , $x_{\text{Ga}}(\text{source}) = 0.0869$; \bullet , $x_{\text{Ga}}(\text{source}) = 0.0535$.
- Figure E-7. Film compositions (open symbols) and growth rates (closed symbols) of $\text{Ga}_x\text{In}_{1-x}\text{As}$ as a function of added HCl mole fraction at $x_{\text{HCl}}^0 = 0.0072$ and

$x_{\text{AsH}_3}^0 = 0.0033$. Source alloy compositions: \square , $x_{\text{Ga}}(\text{source}) = 0.1510$; \circ , $x_{\text{Ga}}(\text{source}) = 0.0535$.

Figure E-8. Film compositions (open symbols) and growth rates (closed symbols) of $\text{Ga}_x\text{In}_{1-x}\text{As}$ as a function of the total gas flow rate of H_2+HCl in the source zone at $x_{\text{AsH}_3}^0 = 0.0033$. Source alloy compositions and inlet HCl mole fraction: \square , $x_{\text{Ga}}(\text{source}) = 0.1510$, $x_{\text{HCl}}^0 = 0.0072$; \blacksquare , $x_{\text{Ga}}(\text{source}) = 0.0869$, $x_{\text{HCl}}^0 = 0.0036$.

Figure E-9. Schematic of modified source alloy boat design.

Figure E-10. Film compositions (open symbols) and growth rates (closed symbols) of $\text{Ga}_x\text{In}_{1-x}\text{As}$ as a function of the total gas flow rate of H_2+HCl in the source zone with the modified source alloy boat at $x_{\text{Ga}}(\text{source}) = 0.0661$, $x_{\text{HCl}}^0 = 0.0048$ and $x_{\text{AsH}_3}^0 = 0.0034$.

Figure E-11. Film compositions (open symbols) and growth rates (closed symbols) of $\text{Ga}_x\text{In}_{1-x}\text{As}$ as a function of cumulative HCl feed at $x_{\text{HCl}}^0 = 0.0072$ and $x_{\text{AsH}_3}^0 = 0.0033$. Source alloy compositions: \square , $x_{\text{Ga}}(\text{source}) = 0.1510$; \blacksquare , $x_{\text{Ga}}(\text{source}) = 0.0869$; \circ , $x_{\text{Ga}}(\text{source}) = 0.0535$.

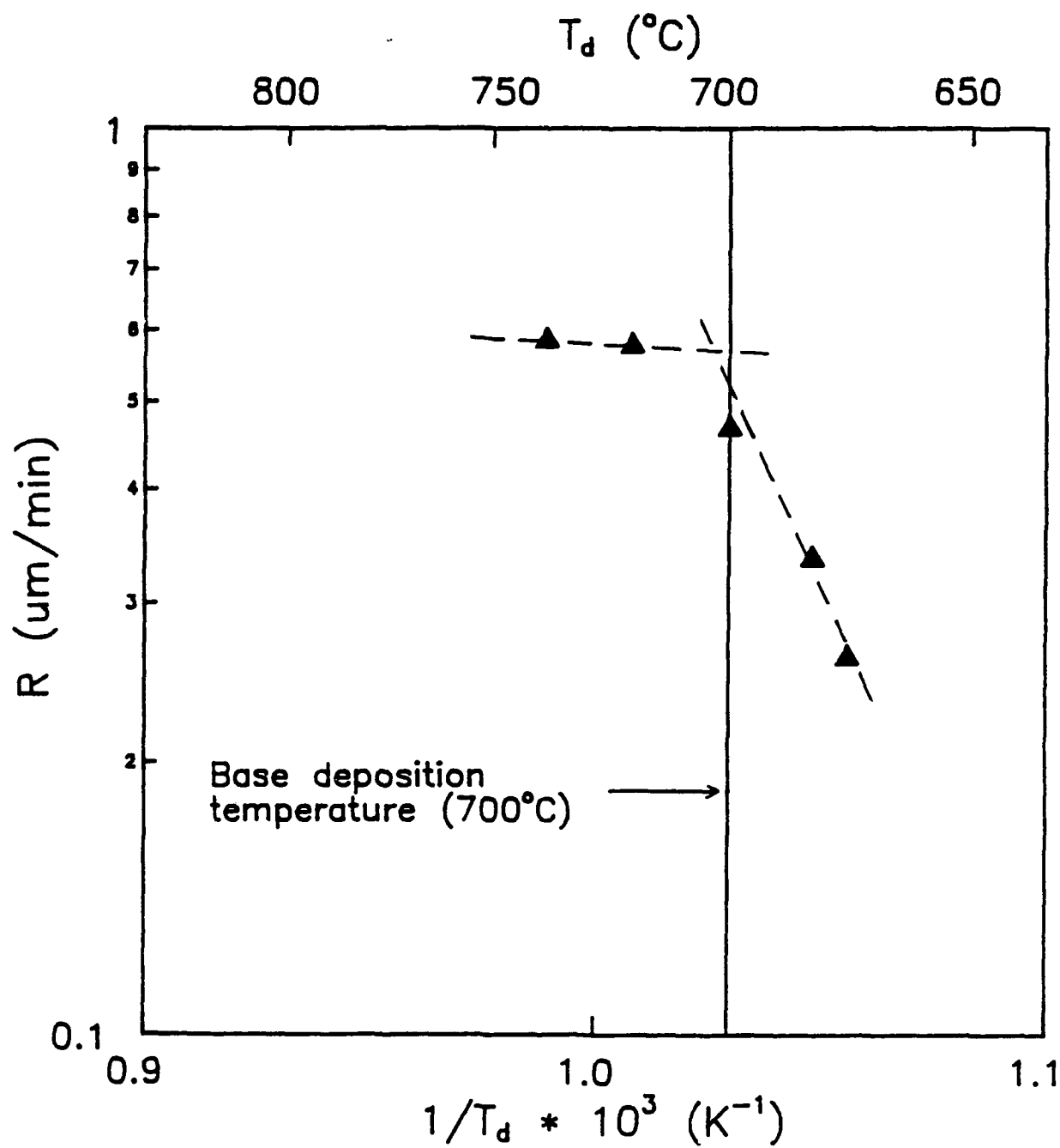


Figure E-1

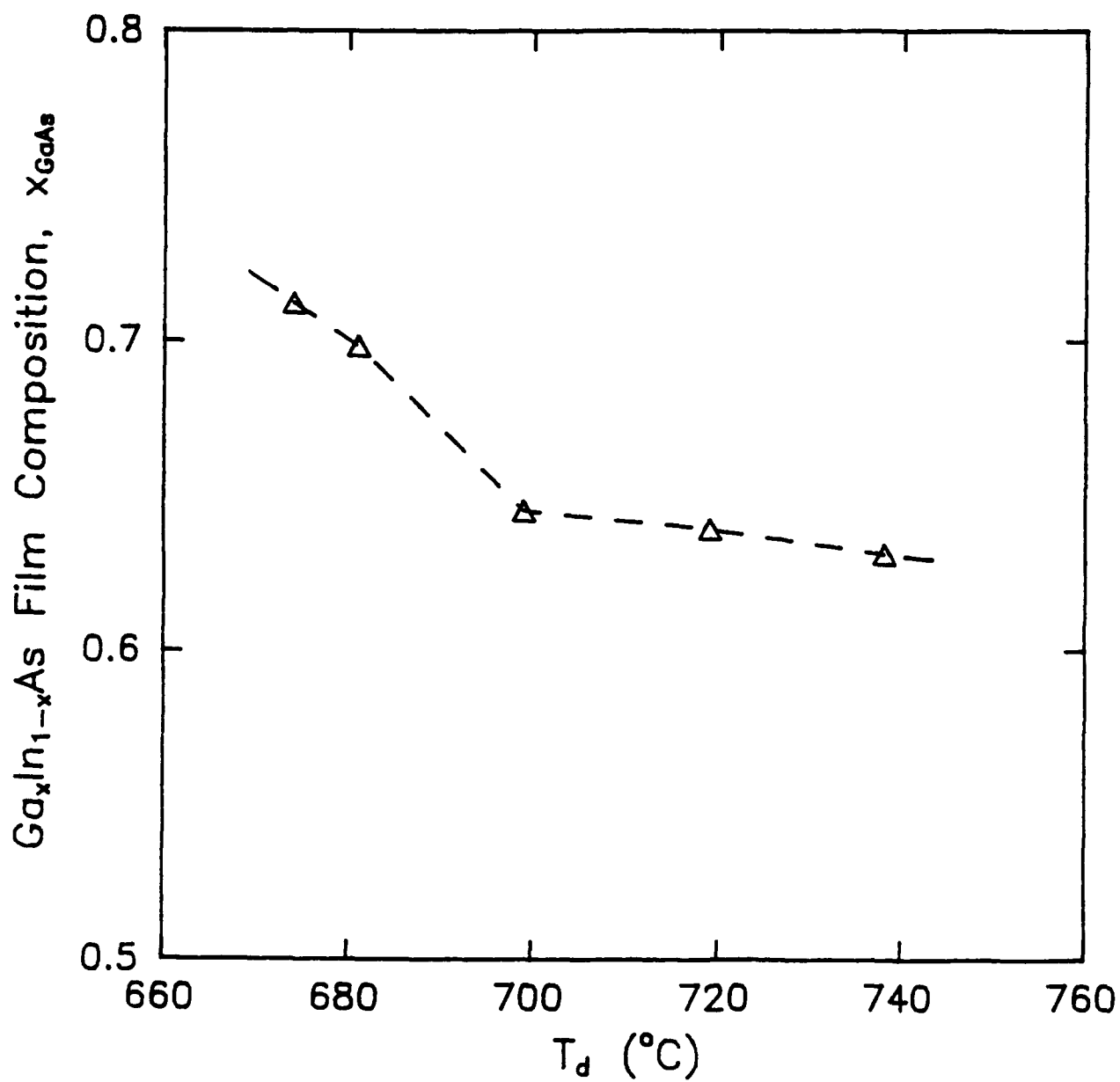


Figure E-2

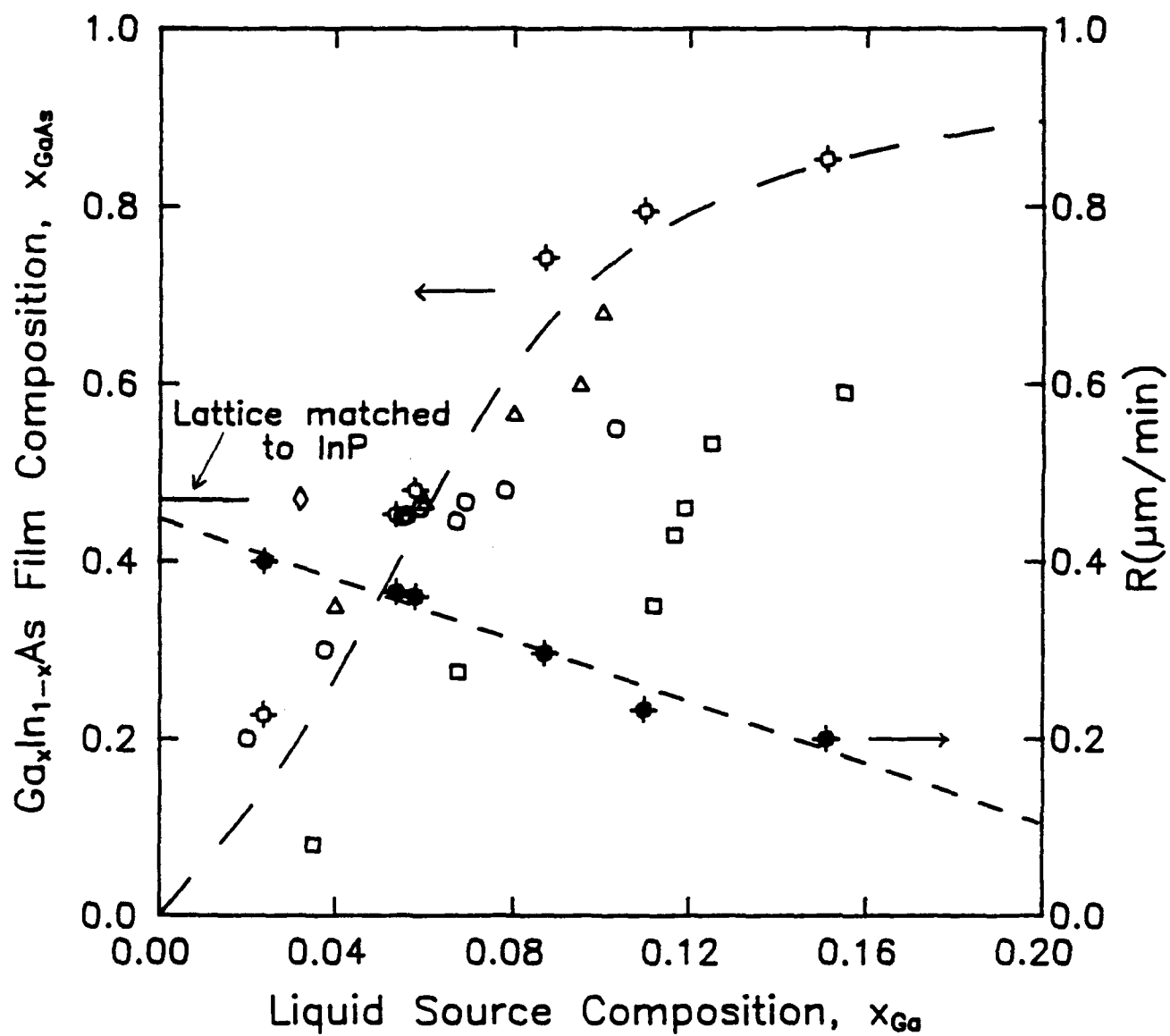


Figure E-3

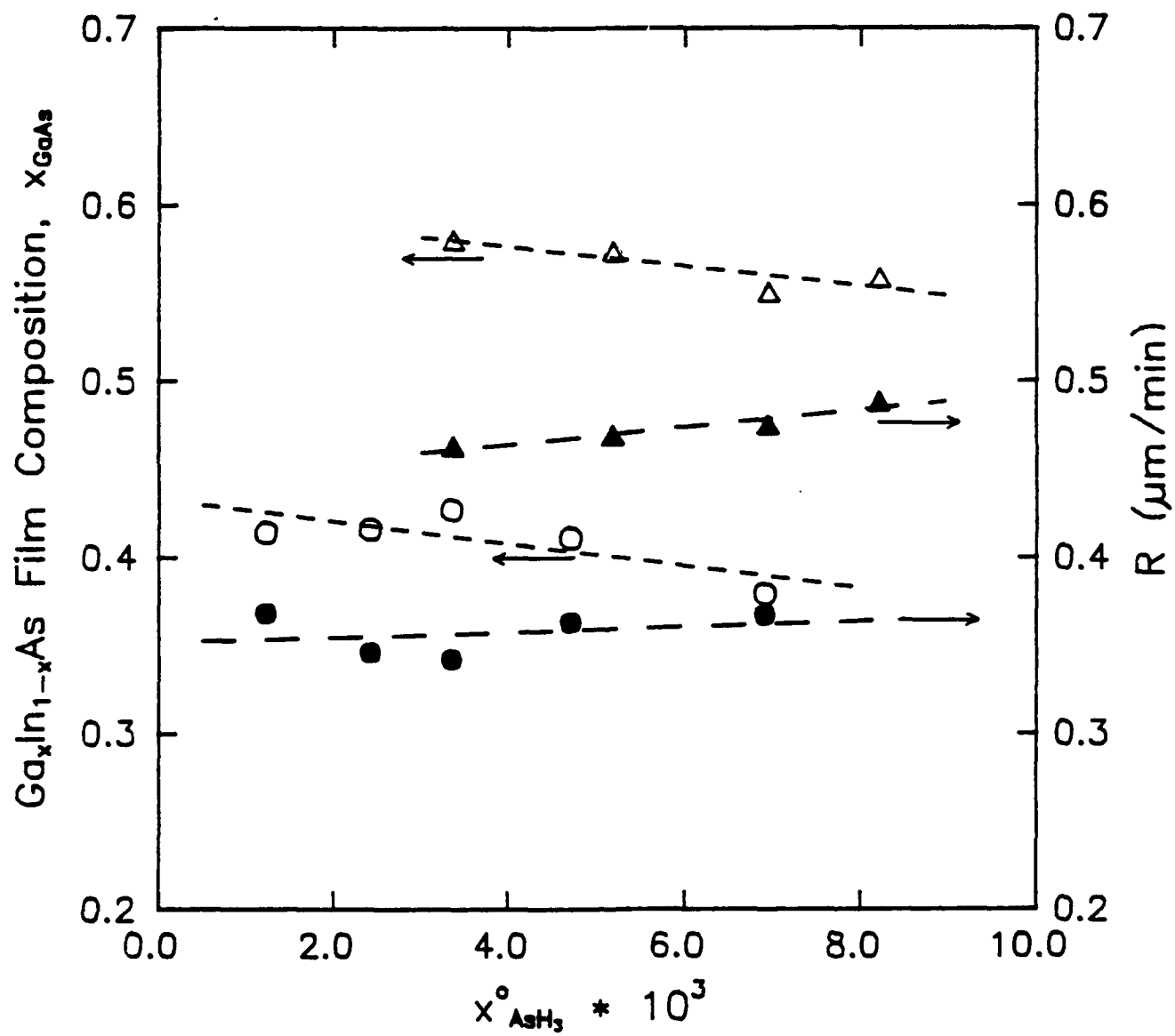


Figure E-4

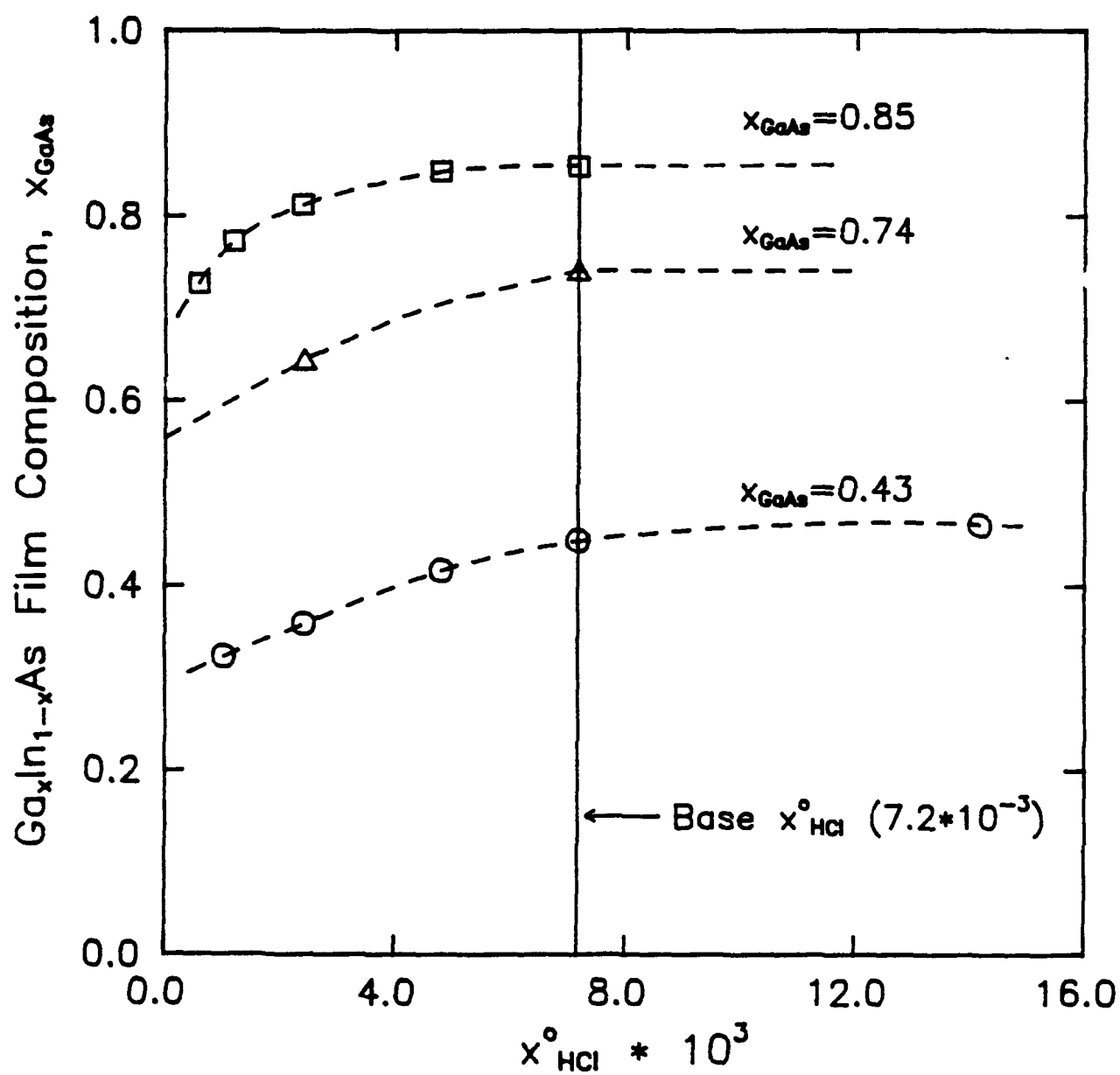


Figure E-5

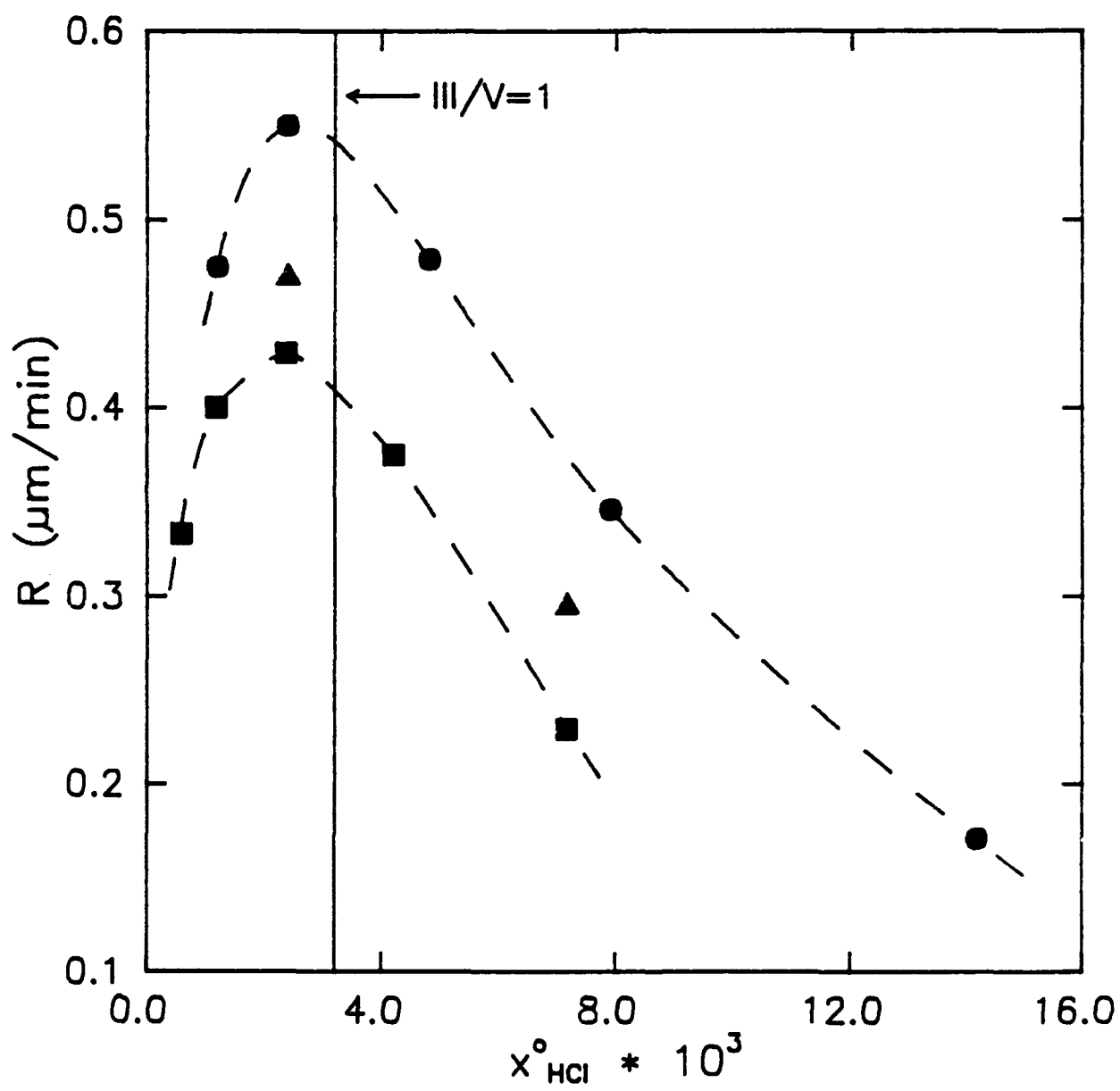


Figure E-6

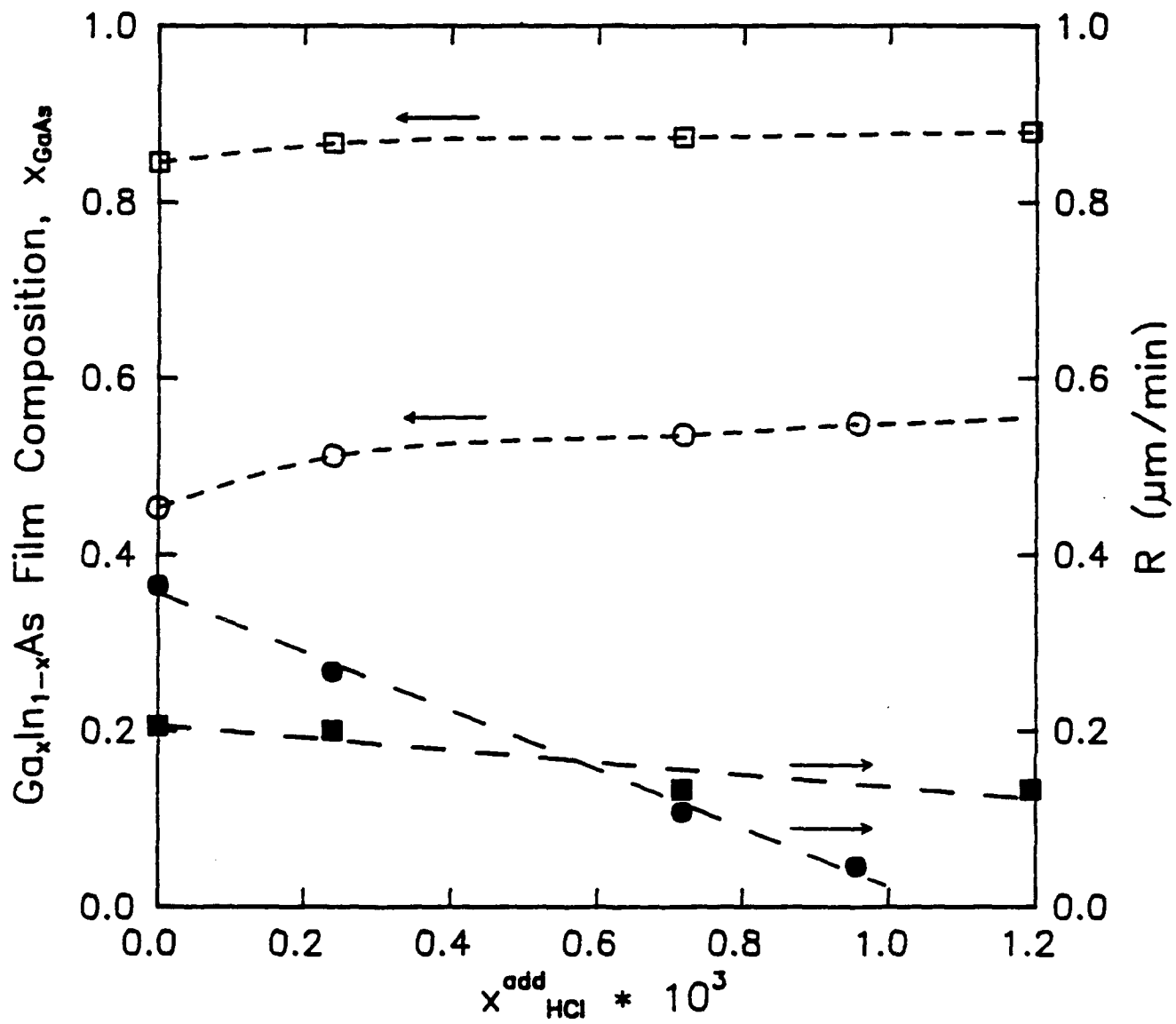


Figure E-7

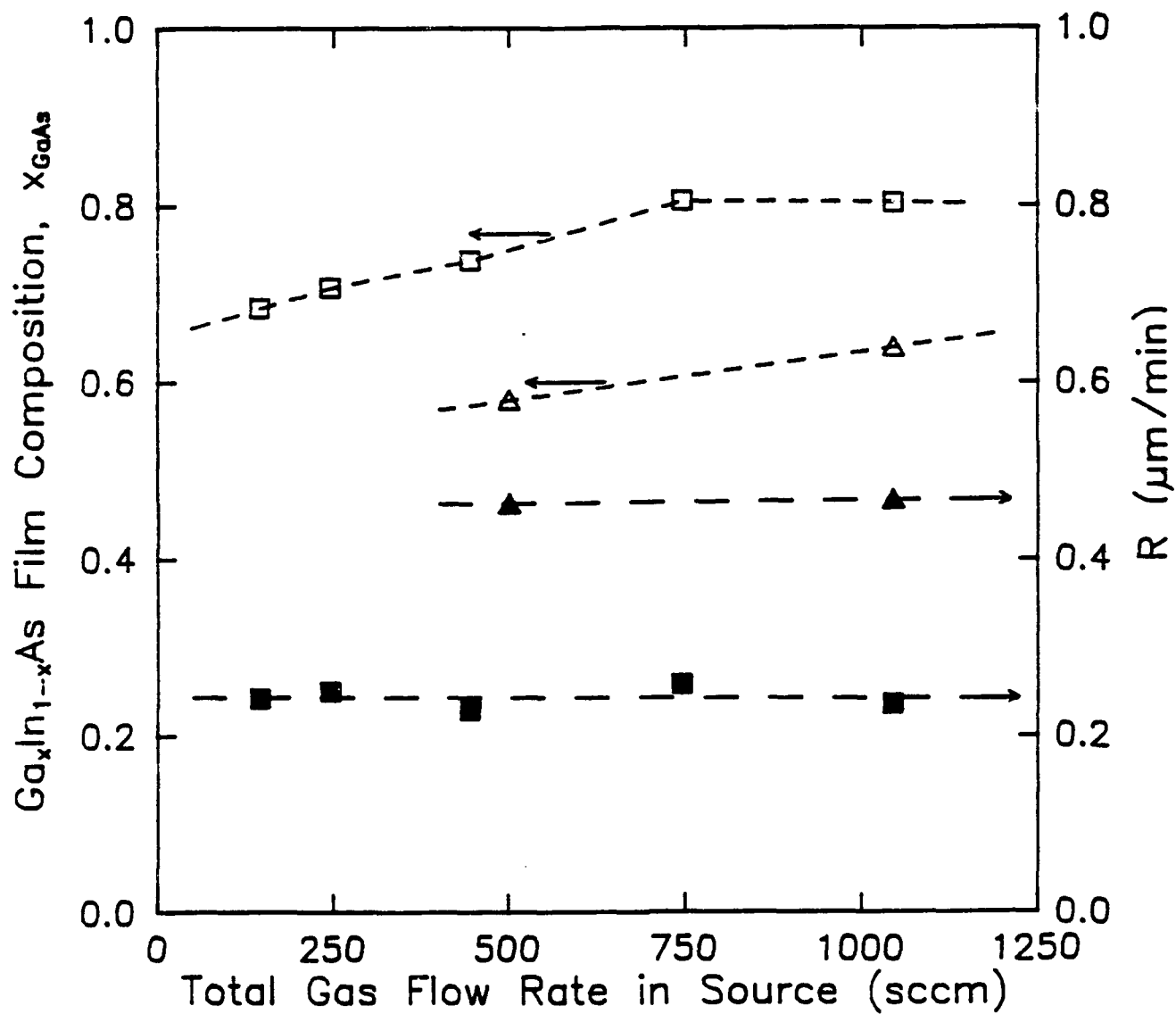


Figure E-8

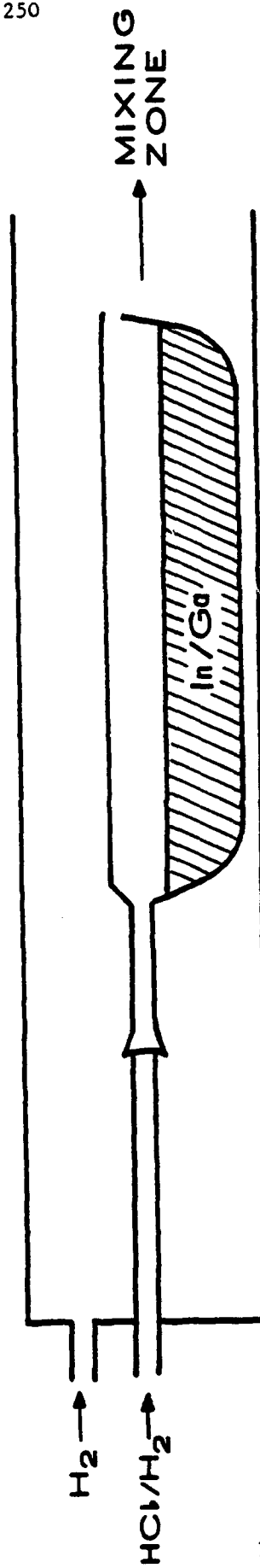


Figure E-9

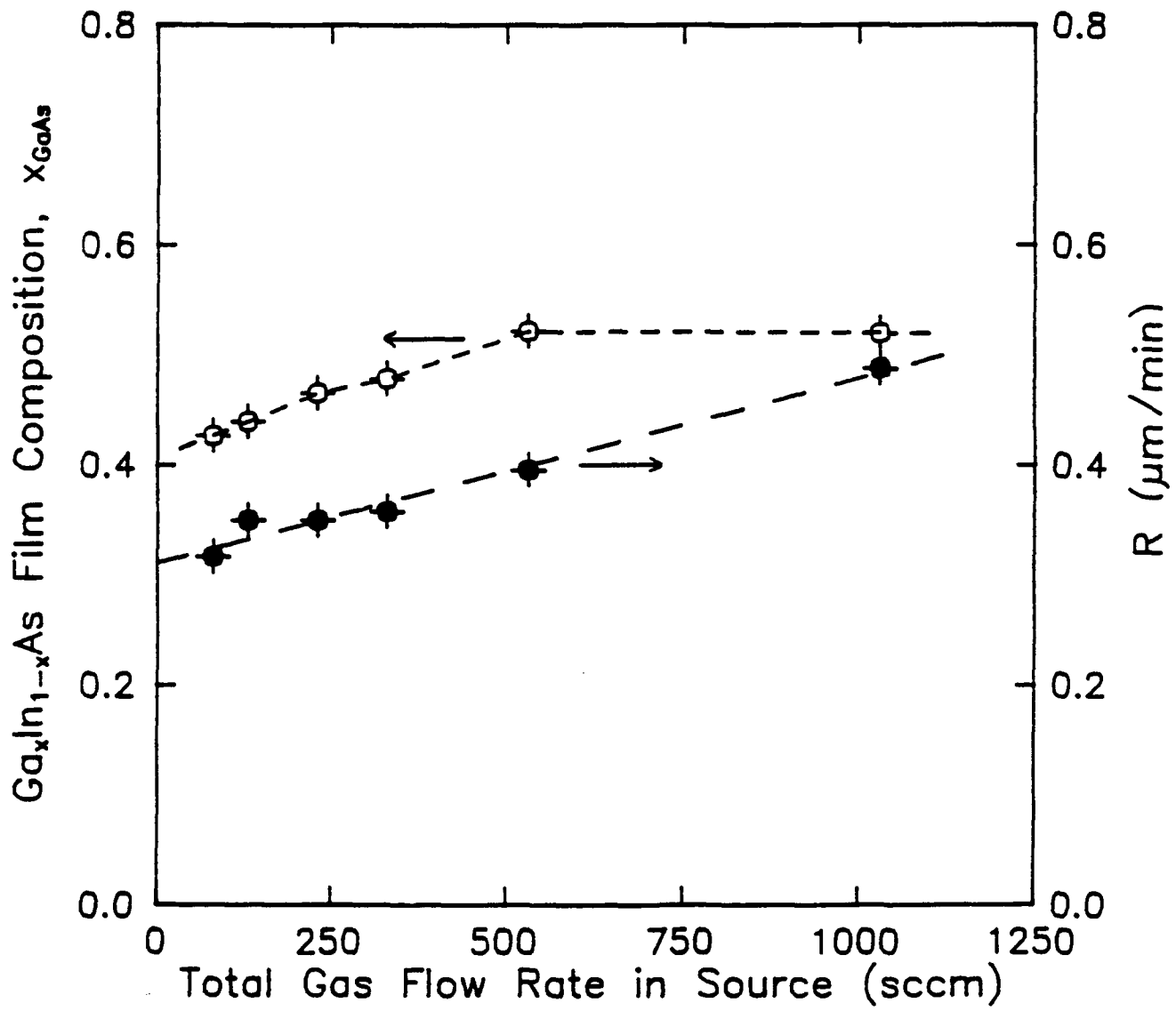


Figure E-10

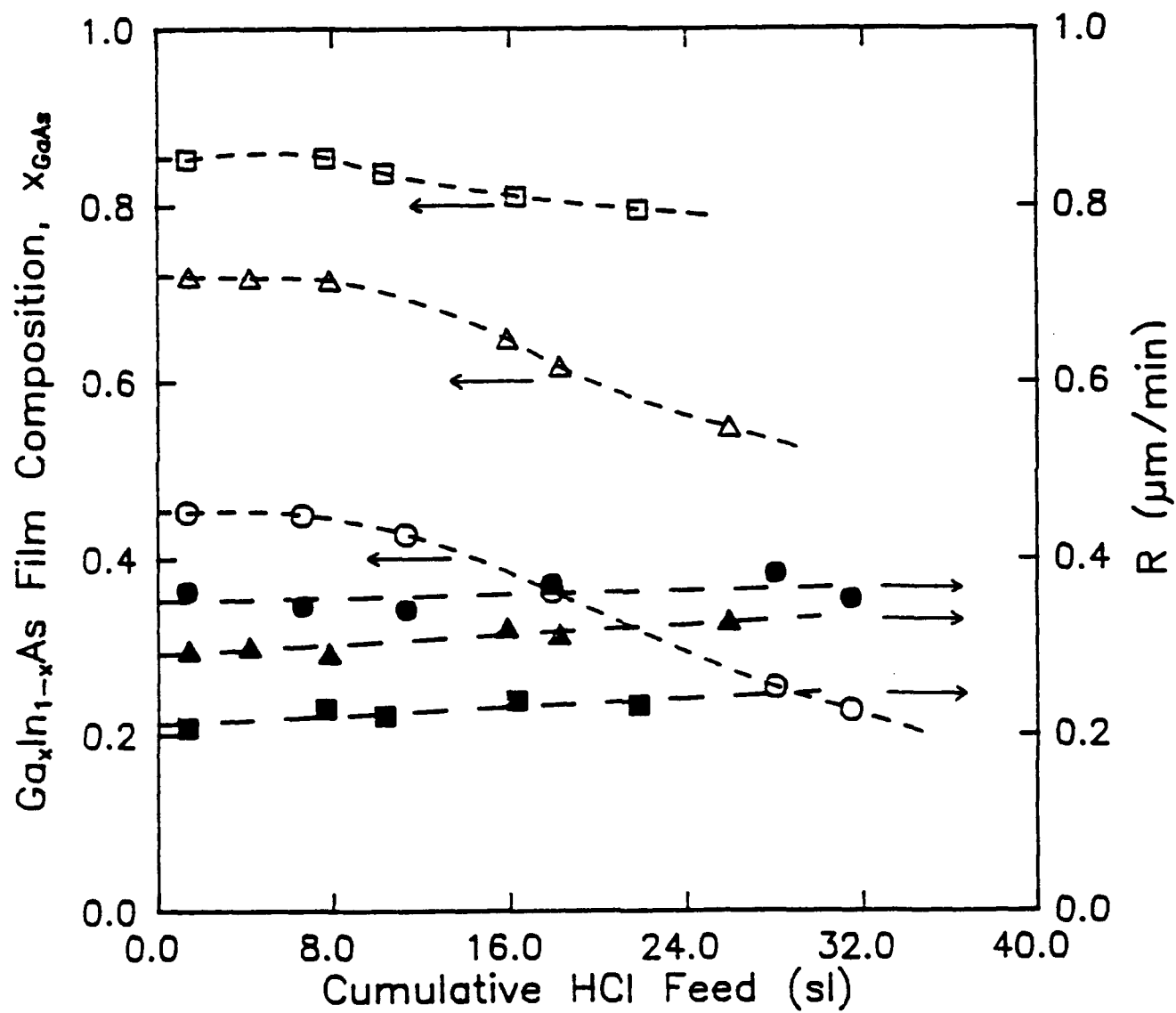


Figure E-11

REFERENCES

1. Hultgren, R., Desai, P.D., Hawkins, D.T., Geisser, M., Kelly, K.K. and Wagman, D.D., Selected Values of the Thermodynamic Properties of the Elements, Am. Soc. Metals, Metals Park, OH (1973).
2. Stull, D.R. and Sinke, G.C., Thermodynamic Properties of the Elements, Am. Chem. Soc., Washington, DC (1956).
3. Chatillon, C. and Bernard, C., J. Crystal Growth, 71, 433 (1985).
4. Shaw, D.W., J. Phys. Chem. Solids, 36, 111 (1975).
5. Shaulov, Yu.Kh. and Mosin, A.M., Russ. J. Phys. Chem., 47, 642 (1973).
6. Kuniya, Y. and Hosaka, M., J. Crystal Growth, 28, 385 (1975).
7. Meyer, D.J., Ph.D. Dissertation, Univ. of Florida (1984).
8. Tmar, M., Gabriel, A., Chatillon, C. and Ansara, I., J. Crystal Growth, 69, 421 (1984).
9. Drowart, J., Smoes, S. and Vanderauwera-Mahieu, A., J. Chem. Thermo., 10, 453 (1978).
10. JANAF Thermochemical Tables, 2nd Ed., Nat'l. Standard Reference Data Series 37, Nat'l. Bureau of Standards, U.S. Dept. of Commerce, Washington, DC (1971).
11. Tmar, M., Gabriel, A., Chatillon, C. and Ansara, I., J. Crystal Growth, 68, 557 (1984).
12. Kelly, K.K., U.S. Bureau of Mines Bulletin 584 (1961).
13. Cox, R.H. and Pool, J., J. Chem. Engr. Data 12, 247 (1967).
14. Pankratz, L.P., Rept. 6592, U.S. Dept. Interior, Bureau of Mines, Albany, OR (1965).
15. JANAF Thermochemical Tables, J. Phys. Chem. Ref. Data, 4 (1975).
16. JANAF Thermochemical Tables, J. Phys. Chem. Ref. Data, 3 (1974).
17. Mullin, J.B. and Hurle, D.J.T., J. Luminescence, 7, 176 (1973).
18. Gunn, S.R. and Green, L.G., J. Phys. Chem., 65, 779 (1961).
19. Report CODATA Task Group, J. Chem. Thermodynamics, 8, 603 (1976).
20. Wagman, D.D., Evans, W.H., Parker, V.B., Halow, I. and Bailey, S.M., Nat'l. Bureau of Standards Tech Note 270-3 (1968).
21. Jordan, A.S., J. Electrochem. Soc., 119, 123 (1972).

22. Ilegem, M. and Panish, M.B., J. Phys. Chem. Solids, 35, 409 (1974).
23. Philips, J.C. and Van Vetchen, J.A., Phys. Rev., 22,, 70 (1969).
24. Stringfellow, G.B., J. Phys. Chem. Solids, 34, 1749 (1973).
25. Onabe, K., J. Phys. Chem. Solids, 43, 1071 (1982).
26. Olsen, G.H. and Zamerowski, T.J., Progr. Crystal Growth Characterization, 2, 309 (1979).
27. Ban, V.S., J. Electrochem. Soc., 119, 119 (1972).
28. Ban, V.S., J. Electrochem. Soc., 118, 1473 (1971).
29. Ban, V.S. and Ettenberg, M., J. Phys. Chem. Solids, 34, 1119 (1973).
30. Donnelly, V.M. and Karlicek, R.F., J. Appl. Phys., 53, 6399 (1982).
31. Karlicek, R.F. and Bloemeke, A., J. Crystal Growth, 73, 364 (1985).
32. Finlayson, B.A., The Method of Weighted Residuals and Variational Principles, Academic Press, New York (1972).
33. Sir Taylor, G., Proc. Royal Soc. London A, 219, 186 (1953).
34. Danckerwerths, P.V., Chem. Eng. Sci., 1, 1 (1953).
35. Gurchenok, G.A., Russ. J. Inorg. Mat., 16, 1428 (1980).
36. Balooch, M., Siekhaus, W.J. and Olander, D.R., J. Phys. Chem., 88, 3521 (1984).
37. Skoog, D.A. and West, D.M., Fundamentals of Analytical Chemistry, 3rd ed., Holt, Rinehart, and Winston, New York (1976).
38. Ehrlich, D.J. and Tsao, J.Y., J. Vac. Sci. Technol. B, 4, 969 (1983).
39. Ehrlich, D.J. and Tsao, J.Y., in VLSI Electronics Microstructure Science, N.G. Einspruch, ed., 7, 129 (1983).
40. Gilgren, H.H., Chen, C.J., Krchnavek, R. and Osgood, R.M., in Laser Diagnostics and Photochemical Processing, D. Bauerle, ed., 225, North-Holland, New York (1985).
41. Letokhov, V.S. and Makarov, A.A., Sov. Phys. Usp., 24, 366 (1981).
42. Ehrlich, D.J., Osgood, R.M. and Deutsch, T.F., Appl. Phys. Lett., 39, 957 (1981).
43. Armstrong, J.V., Burk, A.A., Coey, J.M.D. and Moorjani, K., Appl. Phys. Lett., 50, 1231 (1987).

44. Kukimoto, H., Ban, Y., Komatsu, H., Takechi, M. and Ishizaki, M., *J. Crystal Growth*, 77, 223-228 (1986).
45. Suzuki, M. and Sato, M., *J. Electrochem. Soc.*, 132, 1684 (1985).
46. Rytz-Froidevaux, Y., Salathe, R.P. and Gilgen, H.H., *Appl. Phys. A*, 37, 121 (1985).
47. Osgood, R.M. and Gilgen, H.H., *Ann. Rev. Mater. Sci.*, 15, 549 (1985).
48. Osgood, R.M. and Deutsch, T.F., *Science*, 227, 709 (1985).
49. Ehrlich, D.J., Osgood, R.M. and Deutsch, T.F., *IEEE J. Quantum Electron.*, QE-16, 1233 (1980).
50. Nishizawa, J., Shimawaki, H. and Koike, M., *J. Electrochem. Soc.*, 132, 1939 (1985).
51. Roth, W., Krautle, H., Krings, A. and Beneking, H., in *Laser Diagnostics and Photochemical Processing for Semiconductor Devices*, H.R. Schlossberg, ed., 17, 193, North-Holland, New York (1982).
52. Aoyagi, Y. Masuda, S., Namba, S. and Doi, A., *Appl. Phys. Lett.*, 47, 95 (1985).
53. Stadelmaier, H.H., *J. Crystal Growth*, 77, 229-234 (1986).
54. Karam, N.H., El-Masry, N.A. and Bedair, S.M., *Appl. Phys. Lett.*, 880 (1986).
55. Doi, A., Aoyagi, Y. and Namba, S., *Appl. Phys. Lett.*, 48, 1787 (1986).
56. Kukimoto, H., in *Extended Abstracts of the 19th 1986 International Conference on Solid State Devices and Materials*, 423 (1986).
57. Balk, P., Heinecke, H., Putz, N., Plass, C. and Luth, H., *J. Vac. Sci. Technol. A*, 4, 711 (1986).
58. Gilling, L.J., in *Crystal Growth of Electronic Materials*, E. Kaldis, ed., North-Holland, New York (1985).
59. Abrahams, M.S. and Buiochi, C.J., *J. Appl. Phys.*, 36, 2855 (1965).
60. Allen, S.D., *J. Appl. Phys.*, 52, 6501 (1981).
61. Bedair, S.M., Whisnant, J.K., Karam, N.H., Tischler, M.A. and Katsuyama, T., *Appl. Phys. Lett.*, 48, 174 (1986).
62. Feldman, L.C. and Mayer, J.W., in *Fundamentals of Surface and Thin Film Analysis*, 236, North-Holland, New York (1986).
63. Terao, H. and Sunakawa, H., *J. Crystal Growth*, 68, 157 (1984).
64. Lax, M., *J. Appl. Phys.*, 48, 3919 (1977).

65. Bass, M., in *Physical Processes in Laser-Materials Interaction*, M. Bertolotti, ed., 77, Plenum Press, New York (1982).
66. Blakemore, J.S., *J. Appl. Phys.*, 53, R123 (1982).
67. Lietoila, A., Gold, R.B., Gibbons, J.F. and Christel, L.A., in *Semiconductors and Semimetals*, J.F. Gibbons, ed., 71, Academic Press, New York.
68. Jenkins, F.A. and White, H.E., in *Fundamentals of Optics*, 523-543, McGraw-Hill, New York (1976).
69. Rosasco, G.R. and Simmons, J.H., *Ceramic Bulletin*, 53, 626 (1974).
70. Moylan, C.R., Baum, T.H. and Jones, C.R., *Appl. Phys. A*, 40, 1 (1986).
71. Chen, C.J. and Osgood, R.M., *Chem. Phys. Lett.*, 98, 363 (1983).
72. Longeway, P.A. and Smith, R.T., *J. Cryst. Growth*, 89, 519 (1988).
73. Hsieh, J.J., Ph.D. Thesis, Dept. Chemical Engineering, Univ. of Florida (1988).
74. Quinlan, K.P., *J. Cryst. Growth*, 83, 319 (1987).
75. Quinlan, K.P., *J. Electrochem. Soc.*, 135, 2108 (1988).
76. Karlicek, R.F., Hammarlund, B. and Ginocchio, I., *J. Appl. Phys.*, 60, 794 (1986).
77. Minden, H.T., *J. Electrochem. Soc.*, 112, 300 (1965).
78. Kordos, P., Schumbera, P., Heyen, M. and Balk, P., *Proc. Int. GaAs and Related Compounds (Japan)*, No. 63, 131 (1981).
79. Chatterjee, A.K., Faktor, M.M., Lyons, M.H. and Moss, R.H., *J. Cryst. Growth*, 56, 591 (1982).
80. Erstfeld, T.E. and Quinlan, K.P., *J. Electrochem. Soc.*, 131, 2722 (1984).
81. Quinlan, K.P. and Erstfeld, T.E., *J. Cryst. Growth*, 71, 246 (1985).
82. Jacobs, K., Bugge, F. and Simon, I., *Cryst. Res. Tech.*, 21, 3 (1986).
83. Coronado, M.L., Abril, E.J., Balaguer, R. and Aguilar, M., *Jpn. J. Appl. Phys.*, 27, 1268 (1988).
84. Olsen, G.H., *Laser Focus*, 12, 124 (1985).
85. Olsen, G.H. and Zamerowski, T.J., *RCA Rev.*, 44, 270 (1983).
86. Olsen, G.H. and Ban, V.S., *Solid State Tech.*, 30, 99 (1987).

87. Hyder, S.B., Saxena, R.R., Chiao, S.K. and Yeats, R., Appl. Phys. Lett., 35, 787 (1979).
88. Shaw, D.W., J. Electrochem. Soc., 117, 683 (1970).
89. Putz, N., Veuhoff, E., Bachem, K.H., Balk, P. and Luth, H., J. Electrochem. Soc., 128, 2202 (1981).
90. Mizuno, O., Watanabe, H. and Shinoda, D., Jpn. J. Appl. Phys., 14, 184 (1975).
91. Tmar, M., Ph.D. Thesis, Institute National Polytechnique de Grenoble (1985).
92. Anderson, T.J. and Ansara, I., J. Phase Equil., 12, 64 (1991).
93. Nagai, H., J. Electrochem. Soc., 126, 1400 (1979).
94. Weyburne, D.W. and Quinlan, K.P., Report RADC-TR-85-238 (1985).
95. Jurgensen, H., Schmitz, D., Heyen, M. and Balk, P., Inst. Phys. Conf. Ser. No. 74, 199 (1985).
96. Buckley, D.N., J. Electron. Mater., 17, 15 (1988).
97. Jones, K.A. and Tu, C.W., J. Cryst. Growth, 70, 127 (1984).
98. Defoort, F., Ph.D. Thesis, Institute National Polytechnique de Grenoble (1986).
99. Shaw, D.W., J. Cryst. Growth, 31, 130 (1975).
100. Ban, V.S. and Ettenberg, M., Proc. 4th Int. Conf. on CVD, The Electrochem. Soc., 30 (1973).
101. Ban, V.S., J. Cryst. Growth, 17, 19 (1972).
102. Ban, V.S., J. Electrochem. Soc., 119, 761 (1972).
103. Mizutani, T. and Watanabe, H., J. Cryst. Growth, 59, 507 (1982).
104. Forrest, S.R., Ban, V.S., Gasparian, G., Gay, D. and Olsen, G.H., IEEE Electron. Devices Lett., 9, 217 (1988).
105. Olsen, G.H., IEEE Electron. Devices Lett., 2, 217 (1981).

**MISSION
OF
ROME LABORATORY**

Rome Laboratory plans and executes an interdisciplinary program in research, development, test, and technology transition in support of Air Force Command, Control, Communications and Intelligence (C³I) activities for all Air Force platforms. It also executes selected acquisition programs in several areas of expertise. Technical and engineering support within areas of competence is provided to ESD Program Offices (POs) and other ESD elements to perform effective acquisition of C³I systems. In addition, Rome Laboratory's technology supports other AFSC Product Divisions, the Air Force user community, and other DOD and non-DOD agencies. Rome Laboratory maintains technical competence and research programs in areas including, but not limited to, communications, command and control, battle management, intelligence information processing, computational sciences and software producibility, wide area surveillance/sensors, signal processing, solid state sciences, photonics, electromagnetic technology, superconductivity, and electronic reliability/maintainability and testability.